Imperial College London

Production of Liquid Transportation Fuels from Biomass-Derived Syngas *via* Fischer-Tropsch Synthesis

Janet Skitt

Supervised by Dr. Christopher Tighe and

Prof. Paul Fennell

This thesis is submitted for the degree of Doctor of Philosophy (PhD) at the Department of Chemical Engineering at Imperial College London of Science, Technology and Medicine

For my father,

Dr. Peter J C Skitt

(1951-2018)

Abstract

In this thesis the use of foamed iron (III) oxide catalysts for the production of liquid fuels from a carbon dioxide rich bio-syngas *via* the Fischer-Tropsch process is evaluated. Unsupported Fe_2O_3 catalysts promoted with Cu and K are generated using both a co-precipitation and a foaming sol-gel process before being characterised to study the effect of synthesis conditions on physical properties. Experiments were then performed in a purpose-built fixed bed reactor to assess the catalyst performance under industrial Fischer-Tropsch conditions. The co-precipitated catalysts, both unpromoted and promoted, were shown to have activity in the Fisher-Tropsch reaction. Promotion increased the rate of conversion of syngas to hydrocarbons and increased production of longer chain lengths. In contrast, the unpromoted foamed catalysts exhibited little Fischer-Tropsch activity. However, high levels of inherent activity are achieved once promoted. All the promoted foamed catalysts produced a comparable product range, with similar Anderson-Schulz-Flory distributions being seen. However overall rates of conversion CO and H_2 to hydrocarbons varied within the promoted foamed catalyst group. Higher calcination temperatures resulted in a dramatic loss of microporous surface area and hence lower overall hydrocarbon production rates as active surface sites were lost. Production rates over foamed catalyst pellets in excess of 300μm diameter suffered from the introduction of mass transfer limitations, thus reducing the rate.

In addition, a new dynamic model of the Fischer-Tropsch reaction was developed, accounting for variable temperature-dependant gas density and the reduction in gas velocity as the reaction proceeds. This was used to investigate the dynamic thermal response of the reactor to changes in inlet conditions, demonstrating the exaggeration of thermal responses generated when reaction contraction is accounted for. The phenomenon of wrong way behaviour over a fixed bed is also reviewed for loss of feed heating and reduced feed flow cases.

Declaration of Originality

I certify, to the best of my knowledge, that the work presented in this thesis is primarily my own and that I am the primary person responsible for the preparation of this manuscript. Any work that was the result of a collaborative effort has been highlighted and acknowledged within this thesis. The work presented was undertaken at the Department of Chemical Engineering at Imperial College London between April 2016 and September 2019. No part of this thesis has been submitted for a degree to this or any other university.

Janet Skitt, October 2020

Copyright declaration

The copyright of this thesis rests with the author. Unless otherwise indicated, its contents are licensed under a Creative Commons Attribution - Non Commercial 4.0 International Licence (CC BY-NC). Under this licence, you may copy and redistribute the material in any medium or format. You may also create and distribute modified versions of the work. This is on the condition that: you credit the author and do not use it, or any derivative works, for a commercial purpose. When reusing or sharing this work, ensure you make the licence terms clear to others by naming the licence and linking to the licence text. Where a work has been adapted, you should indicate that the work has been changed and describe those changes. Please seek permission from the copyright holder for uses of this work that are not included in this licence or permitted under UK Copyright Law.

Acknowledgements

I must offer my most profound thanks to my supervisors, Dr. Chris Tighe and Prof. Paul Fennell, as well as Dr. Matthew Boot-Handford, Prof. Fennell's replacement during the period of his sabbatical, for their hard work and patience with me. Throughout my PhD they have provided much needed guidance and insight. In particular Dr Tighe's work with the derivation of the steady state pseudo-homogeneous model and initial implementation of the dynamic heterogeneous model in gPROMS has improved the quality of this thesis immensely, as have his expert Labview programming skills.

I am also extremely grateful to Dr. Parth Shah for his assistance with generating SEM images, Dr. Clemens Patzschke for his help reviewing XRD results and sharing his continuous co-precipitation rig, and to Dr. Leah Zheng for providing samples of the iron oxide foams.

Thanks must be given to all the members of the High Pressure Industrial Systems group, Mario, Parth, Nathan and Tianyi, for their support through the good times and the bad and for all the fun times in between. I have learnt a lot from my time here, not least being never to 'drink and derive'.

To both my mother, Helen Skitt, and mother in law, Prof. Peppy Brock, I am grateful for their imperturbable proofreading and advice.

Finally, I would like to thank my parents for their unwavering support and encouragement throughout my academic journey and my husband, Dr. Oliver Joris, without whom none of this would have been possible.

Table of Contents

Abstract v

Declaration of Originality vi

Copyright declaration vi

Acknowledgements vii

Table of Contents ix

List of Figures xiv

List of Tables xvii

Nomenclature xviii

1 Introduction 23

1.1 Climate Change and Global Warming 23

1.2 Greenhouse Gas Emissions 24

1.2.1 Transportation Fuels 25

1.3 Aims and Objectives of the Project 27

1.4 Structure of the Thesis 27

2 Biomass to Liquids *via* Fischer-Tropsch Synthesis 29

2.1 Biomass to Liquids 29

2.2 Fischer-Tropsch Synthesis 29

2.2.1 Product Distribution 31

2.3 Feedstock 34

2.4 Fischer-Tropsch Reactor Types and Current Technology 36

2.4.1 Fixed Bed 36

2.4.2 Multi-tubular Fixed Bed 36

2.4.3 Fluidised Bed 37

2.4.4 Slurry 38

2.4.5 Existing Commercial Reactors 39

2.4.6 Reactor Choice 40

3 Experimental Reactor Design 41

3.1 Experimental Safety 41

3.1.1 Layers of Protection Analysis (LOPA) 41
3.1.2 Hazard and Operability (HAZOP) Study 42
3.2 Design 42
3.3 Product Analysis 45
3.4 Temperature Control of Reactor 46
3.5 Pressure Containment 46
3.6 Syngas Containment and Detection 47
3.7 Automation 48
3.8 Commissioning and Testing of Reactor 48
3.9 Reactor Operation 49
3.10 Reproducibility and Error 49
3.10.1 Reproducibility 49
3.10.2 Systematic Error 49
3.10.3 Random Error 49
4 Properties and Production Methods of Fischer-Tropsch Catalysts 51
4.1 Catalyst Base Material 51
4.1.1 Iron 52
4.1.2 Cobalt 54
4.2 Catalyst Substrate 55
4.2.1 Silica 56
4.2.2 Alumina 56
4.2.3 Titanium 56
4.2.4 Carbon 57
4.2.5 Thorium Oxide 57
4.2.6 Zeolites 57
4.3 Catalyst Reduction 58
4.4 Catalyst Particle Size and Structure 59
4.5 Catalyst Deactivation 60
4.5.1 Poisoning 61

4.5.2 Attrition 61
4.5.3 Sintering 62
4.5.4 Pore Blocking 62
4.5.5 Oxidation 63
4.6 Reaction Conditions 63
4.7 Preparation of Catalysts 63
4.7.1 Co-Precipitation 64
4.7.2 Deposition-Precipitation 64
4.7.3 Sol-Gel 64
4.7.4 Eggshell 65
4.7.5 Impregnation of Support 65
4.7.6 Other Synthesis Methods 65
4.8 Catalyst Choice 65
4.9 Reference Catalyst 66
4.9.1 Preparation 66
4.9.2 Semi-Continuous Co-Precipitation 67
4.9.3 Promotion 68
4.10 Foamed Catalyst 68
4.10.1 Foamed-Gelcasting 68
4.11 Nomenclature 70
5 Catalyst Characterisation 71
5.1 Methodology 71
5.1.1 Crystalline Phase Composition by X-ray Diffraction 71
5.1.2 Surface Area and Pore Size by N_2 Adsorption 71
5.1.3 Surface Area and Pore Size by Mercury Intrusion Porosimetry 72
5.1.4 Scanning Electron Microscopy 73
5.2 Results 73
5.2.1 XRD 73
5.2.2 BET – Co-Precipitated Catalysts 76

5.2.3 MIP – Foamed Catalysts 77
5.2.4 SEM 80
5.2.5 Grain size measurement 83
5.3 Conclusions 84
6 Fischer-Tropsch Reactions Over a Fixed Bed 86
6.1 Methodology 86
6.1.1 Fourier Transform Infrared Spectroscopy 86
6.1.2 Gas Chromatography with Mass Spectrometer and Flame Ionisation Detector 87
6.1.3 Experimental 88
6.1.4 Effectiveness Factor 89
6.2 Results and Discussion 90
6.2.1 Validation with Reference Catalyst 90
6.2.2 Foamed Catalysts 99
6.3 Conclusions 121
6.3.1 Reference Catalyst 121
6.3.2 Foamed Catalysts 122
7 Modelling the Fischer-Tropsch Reaction Over a Fixed Bed 124
7.1 Introduction 124
7.1.1 Model Types 124
7.1.2 Variable Density Reactions 125
7.1.3 Transient Responses and Wrong Way Behaviour 126
7.2 Steady State Isothermal Pseudo-homogeneous Model 129
7.3 Dynamic Model 130
7.3.1 Variable Feed Flow Modification 132
7.3.2 Model Parameters 133
7.4 Results and Discussion 135
7.4.1 Steady State 135
7.4.2 Dynamic Model Response – Temperature Variations 144
7.4.3 Dynamic Model Response – Flow Variations 151

7.5 Conclusions 157
8 Conclusions 161
8.1 Preparation of Catalysts 161
8.2 Catalyst Testing 161
8.3 Dynamic Model Allowing for Variable Velocity 162
8.4 Future Work 162
8.4.1 High Temperature Fischer-Tropsch Reactor Conditions 163
8.4.2 Catalyst Promotion 163
8.4.3 Catalyst Calcination Temperature 163
8.4.4 Extended Reaction Periods 163
8.4.5 Two Dimensional Dynamic Model 163
A Safety Reviews 164
LOPA 164
HAZOP 166
B Temperature Dependent Dynamic Model Full Derivation 172
C Temperature Dependant Dynamic Model with Feed Flow Adjustment 182
D Oscillations 186
E Published Work 187
Bibliography 191

List of Figures

Figure 1.1: Annual global anthropogenic CO_2 emissions in gigatonnes of CO_2 equivalent per year ... 23
Figure 1.2: 2018 CO_2 emissions by sector ... 25
Figure 2.1: Carbide mechanism for FTS. ... 31
Figure 2.2: Variations in ASF distributions seen experimentally. ... 32
Figure 2.3: Adiabatic fixed bed reactor and multi-tubular fixed bed reactor. ... 37
Figure 2.4: Typical fluidised FT reactor. ... 38
Figure 2.5: Typical FT slurry reactor. ... 39
Figure 3.1: Levels of tolerance to individual risk ... 42
Figure 3.2: Simplified fixed bed experimental FT reactor P&ID. ... 43
Figure 3.3: (a) catalyst bed layout, (b) three-way valve. ... 44
Figure 3.4: (a) internal reactor sealing and (b) knock-out pot internals. ... 45
Figure 4.1: Pathway for FT reaction over Fe and Co catalysts. ... 52
Figure 4.2: Steady state performance of Fe:Zn catalyst with varying K loading. ... 53
Figure 4.3: TPR profiles of Pt-promoted $CoAl_2O_3$ (15%) and unpromoted catalyst ... 54
Figure 4.4: Limiting hydrocarbon chain growth with zeolite cages. ... 57
Figure 4.5: Influence of particle size on CH_4 and C_{5+} selectivity of Al_2O_3 supported Co catalysts. ... 60
Figure 4.6: Modes of attrition and their effect on the particle size distribution ... 62
Figure 4.7: Schematic of the co-precipitation rig, used to prepare larger batches of catalyst ... 68
Figure 4.8 Schematic of preparation method for foamed catalysts ... 69
Figure 5.1: Schematic of the Bragg-Brentano geometry ... 71
Figure 5.2: XRD plot with arbitrary intensity y-axis of (A) un-calcined catalyst precursor and (B) calcined, promoted catalyst compared to reference results from the literature ... 73
Figure 5.3: XRD of foamed catalyst 950-106-P (red) and 1350-106-P (grey) ... 74
Figure 5.4: XRD of foamed catalyst 950-1000-P (red), 1350-1000-P (grey) ... 75
Figure 5.5: 1350-106-U (red), 1350-106-P (blue) ... 75
Figure 5.6: 950-106-U (red), 950-106-P (blue) ... 76
Figure 5.7: Pore size distributions of PreCat and Cat2K co-precipitated catalysts. ... 77
Figure 5.8: MIP pore size distribution for catalysts calcined at (A) 950 °C and (B) 1350 °C. ... 79
Figure 5.9: SEM images of PreCat ... 80
Figure 5.10: SEM images of Cat2K. ... 81
Figure 5.11: SEM images of A(i-iii) 950-106-U and B(i-iii) 1350-106-U ... 82
Figure 5.12: SEM images of A(i-ii) 950-106-U and B(i-ii) 950-106-P. ... 83
Figure 5.13: Distributions of diameters for 50 randomly selected particles of (A) 950-106-U and (B) 950-106-P ... 84
Figure 6.1: Schematic of gas phase FTIR. ... 86

Figure 6.2: Schematic of GC-MS/FID. 88
Figure 6.3: CO and CO_2 conversion as a fraction of total conversion possible for PreCat and Cat2K 91
Figure 6.4: C_1-C_3 alkane and water production rates for (A) PreCat and (B) Cat2K 93
Figure 6.5: Hydrocarbon mass production rates of (A) PreCat and (B) Cat2K 94
Figure 6.6: Olefin:Paraffin ratio of hydrocarbon product for co-precipitated catalysts. 95
Figure 6.7: Mass fraction of product of (A) PreCat and (B) Cat2K. 97
Figure 6.8: ASF distribution for co-precipitated catalysts. 98
Figure 6.9: (A) CH_4 and (B) H_2O production levels for the unpromoted foamed catalysts 101
Figure 6.10: CO and CO_2 conversion for (A) 950-106-P and (B) 1350-106-P. 103
Figure 6.11: C_1-C_3 and H_2O production for (A) 950-106-P and (B) 1350-106-P. 105
Figure 6.12: Mass production rates of (A) liquid and (B) wax product from 950-106-P. 106
Figure 6.13: Mass production rates for 1350-106-P. 107
Figure 6.14: Olefin:Paraffin ratio for 950-106-P liquid and wax phase products. 108
Figure 6.15: Olefin:Paraffin ratio for 1350-106-P product. 109
Figure 6.16: Mass fraction for combined liquid and wax products of 950-106-P. 109
Figure 6.17: ASF distribution of liquid and wax product phases for 950-106-P. 110
Figure 6.18: Mass fractions of product with respect to carbon number for 1350-106-P. 111
Figure 6.19: ASF distribution for 1350-106-P. 112
Figure 6.20: CO and CO_2 conversions for (A) 950-1000-P and (B) 1350-1000-P. 114
Figure 6.21: C_1-C_3 and H_2O concentrations for (A) 950-1000-P and (B) 1350-1000-P. 116
Figure 6.22: Production rates of (A) 950-1000-P and (B) 1350-1000-P. 117
Figure 6.23: Mass fractions of (A) 950-1000-P and (B) 1350-1000-P. 118
Figure 6.24: Olefin: Paraffin ratio for 950-1000-P and 1350-1000-P. 119
Figure 6.25: Double ASF model for 950-1000-P and 1350-1000-P. 119
Figure 7.1: Dynamic wrong way response to drop in inlet feed temperature, y_f 127
Figure 7.2: Schematic of dead volume of gas available for reaction on a feed trip. 128
Figure 7.3: Steady state solution of extent of reaction against DaZ 135
Figure 7.4: Effect of contraction on (A) mol fraction of hydrogen (x_{H2}) and (B) gas temperature (y) for the steady state FT reaction 136
Figure 7.5: Effect of contraction on molar fraction of hydrogen, x_{H2} during reaction 137
Figure 7.6: Varying H for M = 25 (A) dimensionless temperature, y, and (B) H_2 mol fraction, x_{H2} . 139
Figure 7.7: Varying M for H = 150 (A) dimensionless temperature, y, and (B) H_2 mol fraction, x_{H2} 140
Figure 7.8: Effect of varying β with M = 25, H = 150 on (A) dimensionless temperature, y, and (B) mol fraction of hydrogen, x_{H2} 141
Figure 7.9: Effect of varying ϕ on the isothermal effectiveness factor, $\eta(y_s)$. 142
Figure 7.10: Effect of varying ϕ with M = 500, H = 200 and β = 0.01 143

Figure 7.11: Dynamic wrong way response to a drop in inlet feed temperature 144
Figure 7.12: Wrong way behaviour due to drop in feed temperature for an adiabatic reactor with (A) $\varepsilon = 0$ and (B) $\varepsilon = -0.66$ 145
Figure 7.13: Wrong way behaviour due to drop in feed temperature 146
Figure 7.14: Maximum temperatures for M = 1-50 with H = 150 for y_{f1}-y_{f2} = 0.001-0.005 147
Figure 7.15: Maximum temperatures for H = 40-150 with M = 25 for y_{f1}-y_{f2} = 0.001-0.005 148
Figure 7.16: Maximum temperatures for β = 0.01-0.2 with y_{f1}-y_{f2} = 0.001-0.005, M=25, H=150..... 148
Figure 7.17: Maximum temperatures for ϕ_0 = 0.5-7 with y_{f1}-y_{f2} = 0.001-0.005, M=25, H=150 149
Figure 7.18: 3D plot of gradual drop in dimensionless feed temperature..... 150
Figure 7.19: 3D plot of instantaneous drop in dimensionless feed temperature. 150
Figure 7.20: Dimensionless reactor temperature, y, against dimensionless bed length, Z, at y_{max} for gradual (0.018 linearly over $\tau = 0.25$) and instantaneous y_f drop. 151
Figure 7.21: Dynamic response to 99% drop in u_f for (A) ε=0 and (B) 152
Figure 7.22: Maximum temperatures for M = 5-50 with H = 150 for u_{f1}-u_{f2} from 0.85 to 0.975..... 153
Figure 7.23: Maximum temperatures for H = 40-150 with M = 25 for u_{f1}-u_{f2} = 0.9-0.98. 154
Figure 7.24: Maximum temperatures for β = 0.01-0.2 with v_{f1}-v_{f2} = 0.85-0.975, M=25, H=150..... 155
Figure 7.25: Maximum temperatures for ϕ_0 = 0.5-7 with u_{f1}-u_{f2} = 0.85-0.975, M=25, H=150 155
Figure 7.26: 3D plot of dimensionless temperature, y, along dimensionless bed length, Z, during a gradual drop in feed velocity of 100% to 15% at $\tau = 0$ and then to 10% over $\tau = 1$ 156
Figure 7.27: 3D plot of dimensionless temperature, y, along dimensionless bed length, Z, during an instantaneous drop in feed velocity to 10%. 156
Figure 7.28: Peak dimensionless temperature profile along dimensionless bed length for instant and gradual drops in feed velocity. 157

List of Tables

Table 2.1: Typical syngas compositions (wt%) for various gasifier feeds, generated from data in reference 35
Table 2.2: Examples of current FT technologies, data taken from de Klerk and Abelló et al. [38] 40
Table 4.1: Reagents used to generate co-precipitated catalyst. 67
Table 4.2: Reagents used in foamed catalyst production. 69
Table 4.3: Descriptions and abbreviations of catalysts used. 70
Table 5.1: Summary of BET surface area, BJH pore volume and pore diameter for co-precipitated catalysts. 76
Table 5.2: MIP results for foamed catalysts 78
Table 6.1: α values for co-precipitated catalysts. 98
Table 6.2: Conversion to hydrocarbon rates of PreCat and Cat2K at steady state. 99
Table 6.3: ASF distributions of 950-106-P. 110
Table 6.4: ASF distributions of 1350-106-P. 111
Table 6.5: Conversion to hydrocarbon rates, M_W and η values of 950-106-P and 1350-106-P. 112
Table 6.6: ASF distributions for 950-1000-P and 1350-1000-P. 120
Table 6.7: Conversion to hydrocarbon rates, M_W and η of 950-1000-P and 1350-1000-P. 120
Table 7.1: Model parameters for FT reaction. 134

Nomenclature

A	Cross sectional area	m^2
C_i	Concentration of *i*	$mol\ m^{-3}$
c_i	Heat capacity at *i*	$J\ K^{-1}$
D_e	Effective diffusivity	$m^2\ s^{-1}$
D_L	Axial dispersion coefficient	
d_P	Pore diameter	μm
Da	Damkohler number	
$\overline{d}_{pore}$	Average pore diameter	nm
$(d_p)_m$	Mean grain diameter	μm
E	Activation energy	$J\ mol^{-1}$
F_i	Molar flowrate of *i*	$mol.s^{-1}$
H	Interfacial heat transfer parameter	
H'	Modified interfacial heat transfer parameter	$s\ m^{-1}$
h	Interfacial heat transfer coefficient	
h_w	Overall heat transfer coefficient at wall	$W\ m^{-2}\ K^{-1}$
k_i	Reaction rate constant with respect to *i*	$m^3\ m^3_{cat}\ s^{-1}$
k_m	Interfacial mass transfer coefficient	$m^2\ s^{-1}$
k_0	Pre-exponential factor	
L	Bed length	m
Le	Lewis number	
M	Mass transfer parameter	
M'	Modified mass transfer parameter	$s\ m^{-1}$
M_W	Wagner-Weisz-Wheeler modulus	
Pe	Peclet number - ratio of advective/diffusive mass transfer	
Pe_H	Peclet number – energy basis	
Pe_M	Peclet number – mass basis	
Pe_H'	Modified Peclet number – energy basis	$s\ m^{-1}$
Pe_M'	Modified Peclet number – mass basis	$s\ m^{-1}$
R	Universal gas constant	$J\ K^{-1}\ mol^{-1}$
r_i	Rate of conversion of *i*	$mol\ g_{cat}\ s^{-1}$
r_i'''	Rate of conversion of *i*	$mol\ m^3_{cat}\ s^{-1}$
r_p	Particle radius	m
S	Scaling factor	

S_{BET}	BET surface area	$m^2\ g^{-1}$
S_{pore}	BJH pore surface area	$m^2\ g^{-1}$
T	Temperature	K
t	Time	s
U	Heat to wall transfer parameter	
U’	Modified heat to wall transfer parameter	$s\ m^{-1}$
u	Interstitial velocity	$m\ s^{-1}$
u’	Dimensionless interstitial velocity	
UR	Usage ratio	
V_i	Volumetric flowrate of *i*	$m^3\ s^{-1}$
V_M	Molar volume	$m^3\ mol^{-1}$
V_{pore}	BET pore volume	$cm^3\ g^{-1}$
W_n	Mass fraction of chain length n	
X_i	Extent of reaction with respect to *i*	
x_i	Mol fraction of *i*	
y_i	Dimensionless temperature of *i*	
z	Reactor axial coordinate	m
Z	Dimensionless axial coordinate	

Greek Symbols

α	Chain propagation probability	
β	Dimensionless adiabatic temperature rise	
ξ	Bed voidage	$m^3_{gas}\ m^{-3}_{bed}$
ε	Expansion factor	
γ	Surface tension	$dynes\ cm^{-1}$
η	Effectiveness factor	
$\eta(y_s)$	Isothermal effectiveness factor	
ϕ_i	Thiele modulus at *i*	
τ	Characteristic time	
λ	Wavelength OR	nm
	Axial heat dispersion coefficient	$W\ m^{-1}\ K^{-1}$
σ	Standard deviation	
ρ_i	Mass density at *i*	$kg\ m^{-3}$
$-\Delta H$	Reaction enthalpy	$J\ mol^{-1}$

θ	XRD radiation angle OR	degrees
	Liquid contact angle	degrees

Subscripts

bed	Reactor bed
f	Feed or fluid
r	Reference
s	Particle surface
w	Wall
0	At Z = 0

Abbreviations

ALARP	As low as reasonably practicable
ASF	Anderson-Schulz-Flory product distribution
BET	Brunauer-Emmett-Teller
BJH	Barrett-Joyner-Halenda
BPR	Back pressure regulator
BTL	Biomass to liquids
CFB	Circulating fluidised bed
CNT	Carbon nanotubes
CRio	Compact Rio
CTL	Coal to liquids
CV	Check valve
DI	Deionised water
EDX	Energy-dispersive X-ray
EU	European Union
Exx	Petrol with xx volume % content of ethanol
IA	Instrument air
IPCC	Intergovernmental Panel on Climate Change
IPL	Independent protection layers
IR	Infrared radiation
F1	Filter 1
FAME	Fatty acid methyl ester

FC	Fail closed
FFB	Fixed fluidised bed
FIC	Flow instrument controller
FID	Flame ionisation detector
FT	Fischer-Tropsch
FTIR	Fourier transform infrared spectrometer
FTS	Fischer-Tropsch Synthesis
GC	Gas chromatography
GHG	Greenhouse gas
GTL	Gas to liquids
HAZOP	Hazard and operability
HTFT	High temperature Fischer-Tropsch
HSE	Health and Safety Executive
ID	Inner diameter
KO	Knock-out
LCB	Lignocellulosic biomass
LEL	Lower explosion limit
LOPA	Layers of protection analysis
LTFT	Low temperature Fischer-Tropsch
MIP	Mercury intrusion porosimetry
Mpg	Miles per gallon
MS	Mass spectrometer
OD	Outer diameter
PID	Proportional integral derivative
PSD	Particle size distribution
PSV	Pressure safety valve
PV	Pressure valve
P&ID	Process and instrumentation diagram
R2P2	Reducing risk protecting people
SEM	Scanning electron microscopy
STP	Standard temperature and pressure
SV1/2/3	Switching valve 1/2/3
toe	Tonnes of oil equivalent
TOF	Turnover frequency
TPR	Temperature programmed reduction
UK	United Kingdom

UN	United Nations
UR	Usage ratio
WGS	Water gas shift
XRD	X-ray diffraction

1 Introduction

1.1 Climate Change and Global Warming

The role of the atmosphere in warming the earth was first discovered by Joseph Fourier in the 1820s when he calculated that the earth's temperature, if solely heated by solar radiation, would be below freezing. Referring to an experiment by de Saussure, Fourier concluded that the atmosphere must be acting as sheets of glass, trapping heat at the earth's surface[1], and later giving rise to the term greenhouse effect.

Since these early days much has been discovered about the greenhouse effect, with the subject coming under particular scrutiny after observations of increasing global temperatures since the mid-20th century. The Intergovernmental Panel on Climate Change (IPCC) stated in their 2014 Synthesis Report that it is extremely likely that human activity is the dominant cause of the period of global warming currently occurring, with major contributors being greenhouse gas (GHG) emissions such as carbon dioxide (CO_2) and methane (CH_4) as well as changes in land use[2]. The IPCC 2018 special report Global Warming of 1.5 °C further stated that 'global warming is likely to reach 1.5 °C between 2030 and 2052 if it continues to increase at the current rate'[3].

Annual anthropogenic CO_2 emissions have increased from below 3 $GtCO_2yr^{-1}$ in 1850 to 36.2 (±2) $GtCO_2yr^{-1}$ in 2017, as shown in Figure 1.1, with emissions rising at approximately 1%yr^{-1} [4]. Current atmospheric concentrations of CO_2 and other GHGs are substantially higher than at any time in the last 800,000 years, with levels of CO_2 in the atmosphere increasing from 280-450ppm over the period 1750-2011. Half of all cumulative emissions have taken place in the final 40 years of this period[2].

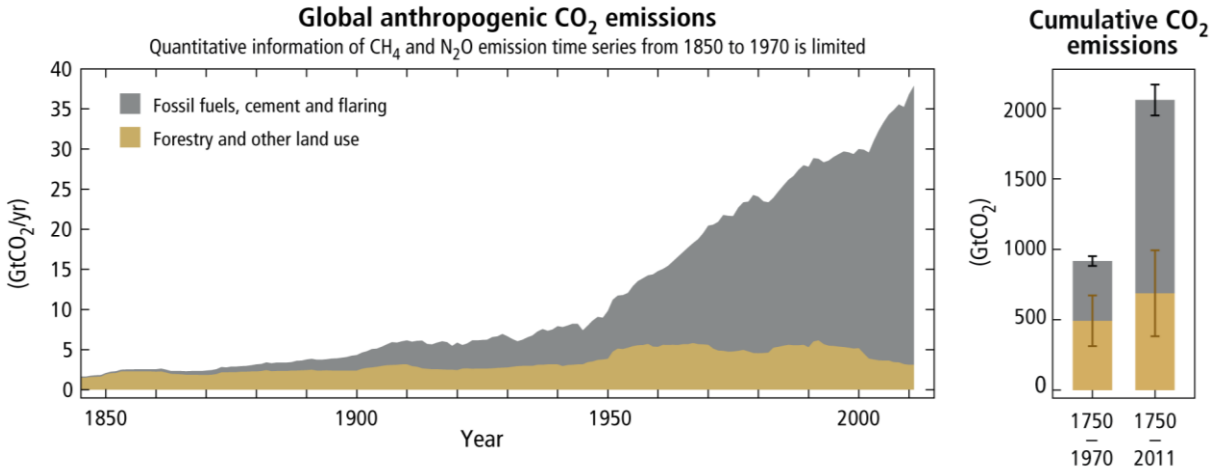


Figure 1.1: Annual global anthropogenic CO_2 emissions in gigatonnes of CO_2 equivalent per year. Cumulative emissions and uncertainties, shown as bars and whiskers, are given on the right. Reprinted from the IPCC 2014 Synthesis Report, figure 1.5[2], copyright (2014), with permission from IPCC.

These increased levels of GHGs in the atmosphere have very likely been the cause of the mean global temperature rise of 0.8-1.2 °C above pre-industrial levels. If current trends continue, the temperature will rise another 3.7-4.8 °C by 2100[2]. The generally accepted limit of 2 °C rise above pre-industrial temperatures was formalised in the Copenhagen Accord in 2009, with mean temperatures above this constituting catastrophic interference with the climate. The Paris Accord went a step further in 2015 by agreeing to aim for a 1.5 °C limit to reduce the magnitude of consequences of global warming.

Levels of global warming beyond this 2 °C 'safe limit' will have severe and lasting impacts on human life and the environment. Shrinking of glaciers and icecaps are already evident, raising the sea level and risk of flooding. This threatens those living in low-lying areas, approximately one-sixth of the current world population[5]. The rise in mean sea level will result in the salination of groundwater and underground reservoirs in coastal areas, stressing water security. Increased temperatures and sea levels will cause loss of arable land, combined with water shortages resulting in global food production ability being seriously reduced. Extreme weather and climatic events such as record temperatures, precipitation and sea levels have already been recorded and are likely to increase in frequency and severity. It is predicted that with a 2 °C rise 15-40% of species also face extinction due to loss of habitat and ocean acidification. Vector borne infectious diseases could increase as favourable tropical conditions spread[6].

All the above will increase human mortality rates through malnutrition, drought, disease, extreme weather events and mass migration. The effects of global warming will hit hardest those least able to adapt to this new world, the poorest communities, who to date have had little culpability for the anthropogenic emissions causing these changes.

1.2 Greenhouse Gas Emissions

In 2018 83% of global GHG emissions were due to the burning of fossil fuels, as shown in Figure 1.2. These fossil fuels are burnt to meet primary energy demand.

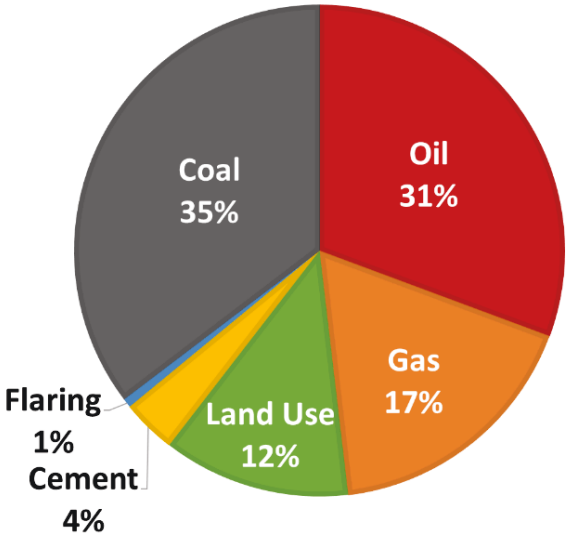


Figure 1.2: 2018 CO_2 emissions by sector. Generated from data by the Global Carbon Project[7].

Primary energy consumption has increased globally year on year by an average of 1.9% to a current high of 13865 million tonnes of oil equivalent (toe) in 2018, but the methods of production remain largely the same as in 1951. As cheap fuels with high energy densities, fossil fuels currently produce 86% of global energy demand. Despite an increase in renewable energy produced, carbon emissions from energy production increased by 2.0% in 2018, the largest increase in the previous seven years[8]. With the world's population predicted to hit 8.8 billion in 2035 the global primary energy demand is predicted to increase by an additional 34%[9]. In order to limit the mean temperature rise to 2 °C or lower, the IPCC has calculated that the total carbon budget remaining from 2018 onwards is 1170 $GtCO_2$. In the two years since the study was published, 85 $GtCO_2$ of this budget has already been emitted[3], meaning dramatic and fast acting changes to reduce GHG emissions are required.

1.2.1 Transportation Fuels

In 2017 25% of the EU's total greenhouse gas emissions were due to transportation, defined for this purpose as road, rail, air and sea[10]. As a sector, transport is over 90% dependent on oil to produce its fuel[11]. The advent of the private car during the early 20th century has rapidly expanded the number of petrol or diesel powered vehicles on the road globally, with cars and trucks now accounting for approximately 75% of total transport CO_2 emissions[12].

As part of the EU's Renewable Energy Directive, the UK has set specific measures to reduce the GHG intensity of the transport sector by 6%. Furthermore, as a UN member state, the UK is legally bound to meet, or surpass, a target of 10% usage of transport fuels from renewable sources in the transport sector by 2020[13].

However, there are currently two significant barriers to meeting these targets: i) the UK's transport sector currently only gets around 4.4% of fuels from renewable sources and ii) there is a 7% cap on the use of first generation biofuels, from crops grown on agricultural land, to preserve the sustainability of

arable land and to ensure the impact on staple food prices is minimised[12]. This means that non-food derived biofuels must be developed to surpass the 10% target, such as lignocellulosic biomass or other unwanted, organic waste. Furthermore, commercial fuel manufacturers in the EU are currently limited to an allowable fatty acid methyl ester (FAME) biofuel content of 7% (biodiesel) or 10% (bioethanol) by volume, in order to ensure fuel is compatible with current road stock[13].

In order to meet the 2020 limits either enough vehicles must be replaced with renewable fuelled counterparts such as batteries, modified to run on higher portions of biofuels, or the biofuels themselves must be improved so they are compatible with existing stock. Since there are currently more than 37 million vehicles on UK roads alone[14], it is not feasible to replace or retrofit even a small proportion of these to be electric or to run on high fractions of biofuel, by the end of 2020. Therefore, the fuel itself must be produced that can allow a 10% or higher content of renewable sources in existing vehicles.

One way of increasing the biofuel content of conventionally available fuels is to create synthetic fuels, or synfuels, from biomass. This bypasses the FAME limit of 7% since synfuels are chemically very similar to their mineral counterparts and do not pose the same problems when used with internal combustion engines.

Since the biomass for synfuels production is first thermochemically treated before undergoing conversion to synfuels, a wider variety of biomass feedstocks can be used. Many second and third generation biomass sources that don't compete with foodstuffs or would otherwise be wasted, such as stalks from food crops or wood shavings, are suitable for synfuels production. This reduces the pressure on first generation biofuels as well as improving efficiency of land use.

Several conversion methods for generating liquid fuels from biomass exist, these broadly fall into two categories. Firstly gas-to-liquids (GTL), where the feed is gasified to generate syngas, a mix of H_2 and CO, before conversion, and secondly processes utilising bio-oils generated naturally or via pyrolysis. These processes generating synfuels through indirect conversion of biomass to syngas or bio-oils are commonly referred to as biomass-to-liquids (BTL) processes. Of these conversion routes, the generation of liquid fuels from fossil fuel derived syngas *via* the Fischer-Tropsch (FT) reaction is an existing, well tested process that produces clean burning synfuels with low levels of sulphur and other impurities. Creating synfuels through the BTL *via* FT route could mean that existing coal-to-liquids (CTL) facilities could be converted to run on biomass feeds with minor alterations in catalyst type and operating conditions allowing for the higher CO_2 content common in bio-syngas. The existing operational knowledge combined with the reduction in capital input and construction time required therefore could make this route more attractive to commercial enterprises.

1.3 Aims and Objectives of the Project

Although interest in BTL has grown in the past decade the uptake of BTL processes in industry has been slow and the biofuel content of conventional petrol and diesel mixes remains similar both in volume and source of the biomass feedstock. Existing commercial synfuel production facilities, such as those operated by Sasol and Shell, focus on fossil fuel feedstocks of coal and natural gas. Smaller investigative scale plants that do use biomass or waste as feed are generally not yet economically competitive with traditional mineral fuel, with several (GreenSky, Ajos BTL, Green Biologics) having shut down in the last five years, citing lack of funding and, or governmental support.

This project aims to evaluate low cost catalysts designed for use with high CO_2 content syngas feeds for the industrial production of biodiesel suitable for use in existing internal combustion engines via the FT process. The following objectives have been specified:

- Develop an automated continuous flow reactor suitable for the assessment of FT catalyst kinetics and product distribution.
- Synthesis and characterisation of a reference catalyst from literature, and its testing in the continuous flow reactor.
- Development, characterisation and testing of a novel foamed iron catalyst.
- Modelling of the FT reaction to predict reactor responses to dynamic conditions.

1.4 Structure of the Thesis

This thesis consists of 8 chapters, covering the following content:

Chapter 1 gives an introduction to the topic, describing the issues involved with the increased use of fossil fuels to meet transport demand. It discusses the potential of using BTL technology, producing synfuels as a low carbon fuel alternative.

Chapter 2 provides a technical introduction to BTL and FT, reviewing existing technology, products and feedstocks. Within this chapter the reactor type and product range that will be used in the remainder of this research are considered and chosen.

Chapter 3 introduces the experimental section, beginning with the design of the reactor and other equipment required. Experimental safety is deliberated and the layers of protection analysis (LOPA) performed is reviewed to ensure risks are as low as reasonably practicable (ALARP). The commissioning and testing of the experimental rig are then presented and the operation summarised.

Chapter 4 discusses the properties and synthesis of FT catalysts. Desirable properties of the catalyst are detailed, and various active materials reviewed for suitability. The reaction conditions and potential deactivation routes are considered for each catalyst. Common production methods are then evaluated

before a choice of catalysts and synthesis schemes are chosen for both a reference catalyst, taken from literature, and novel catalysts to be investigated.

Chapter 5 documents the results of the catalyst characterisation, looking into crystalline phase composition, surface area and pore distribution for each of the catalysts synthesised.

Chapter 6 examines the performance of the reference and novel catalysts in the fixed bed reactor. The products generated are analysed and the findings discussed with reference to the catalyst characteristics.

Chapter 7 presents the development of a dynamic FT model allowing for the reduction in gas velocity as liquid is formed and temperature-dependent gas density, before discussing potential issues raised by exothermic, contracting reactions and how these can be simulated. Plausible industrial situations are modelled and avoidance tactics explored.

Chapter 8 summarises all the conclusions given in the previous chapters and considers future work.

2 Biomass to Liquids *via* Fischer-Tropsch Synthesis

In this chapter the process of producing liquid fuels from biomass *via* the FT reaction is introduced. Gasification of biomass is briefly discussed in the context of reviewing typical syngas compositions used as FT feeds and the effect on product composition and yields. Existing FT technologies currently available are discussed, and the reasoning behind reactor type, feedstock and targeted product choices also detailed.

2.1 Biomass to Liquids

Biomass to Liquids (BTL) is the production of synthetic liquid fuels, or synfuels, from gasified biomass. First the biomass is converted into synthetic gas (syngas), a mixture of hydrogen (H_2) and carbon monoxide (CO), through gasification. The syngas is then catalytically hydrogenated into hydrocarbon chains of varying lengths. Both petrol and diesel mixes can be generated depending on reaction conditions.

By synthesising the fuel directly from syngas compatibility issues with mineral fuels are circumvented. In particular, FAME biodiesel concentrations above 7% volume cause issues in existing diesel engines due to their relatively high cold filter plugging point temperature. The high FAME content diesel has a higher viscosity and can partially crystallise, blocking conventional diesel filters. Sulphur content and particulate matter produced from combustion of BTL fuels are lower than conventional fuel, and CO, nitrous oxides (NO_x) and hydrocarbon emissions are also reduced, making synfuels a cleaner burning alternative to mineral fuels[15]. Perhaps most important with regards to increasing the renewable content of fuel, provided the combustion characteristics of the petrol or diesel are maintained, as measured by the octane or cetane number of the product , respectively, there is no limit to the amount of biofuel that can be included without needing to modify existing internal combustion vehicles or fuel infrastructure[16,17].

In recent years the pressure to reduce carbon emissions has led to increased interest in BTL. Previously much of the biofuel production has been from first generation biomass, i.e. directly from sugars or oils in arable, usually food, crops. To reach the 10% renewable sources target required for 2020 other second generation feedstocks such as woody biomass, waste and agricultural residues are being investigated. Several demonstration plants such as the BioTfueL[18] and TRI/Velocys[19] demonstration projects are currently being built in Europe and the US in order to further this, with the aim of generating a suitable process for large-scale production without jeopardising food security.

2.2 Fischer-Tropsch Synthesis

The basis of Fischer-Tropsch synthesis (FTS) was first developed in 1902 when Sabatier and Senderens discovered that passing CO and H_2 over nickel produced methane. Further work on the hydrogenation

of CO over transition metal catalysts was done by various research groups, culminating in the production of higher hydrocarbons over an iron catalyst in 1925 by Franz Fischer and Hans Tropsch[20].

The FT reaction produces saturated and unsaturated hydrocarbons from syngas *via* a highly exothermic reaction that proceeds through a non-trivial surface polymerisation mechanism, as described in equations 2.1-2.3 below. The products are primarily straight chained alkanes, alkenes and alcohols[21,40].

Alkanes

$$nCO + (2n+1)H_2 \rightarrow C_nH_{2n+2} + nH_2O \quad 2.1$$

Alkenes

$$nCO + 2nH_2 \rightarrow C_nH_{2n} + nH_2O \quad 2.2$$

Alcohols

$$nCO + 2nH_2 \rightarrow C_nH_{2n+1}OH + (n-1)H_2O \quad 2.3$$

Side reactions also produce undesirable products such as carbon deposits, metal carbides and carbonaceous materials as well as causing catalyst oxidation or reduction.

Boudouard reaction

$$2CO \rightarrow C + CO_2 \quad 2.4$$

Carbides

$$yCO + xM \rightarrow M_xO_y + yC \quad 2.5$$

$$yCO_2 + xM \rightarrow M_xO_y + yCO \quad 2.6$$

Carbonaceous materials

$$\left(x + \frac{y}{2}\right)H_2 + xCO \rightarrow C_xH_y + xH_2O \quad 2.7$$

Catalyst oxidation/reduction

$$M_xO_y + yH_2 \leftrightarrow yH_2O + xM \quad 2.8$$

$$M_xO_y + yCO \leftrightarrow yCO_2 + xM \quad 2.9$$

Another important side reaction is the water-gas shift (WGS) reaction. This can be used to alter the H_2/CO feed ratio.

$$CO + H_2O \rightarrow CO_2 + H_2 \quad 2.10$$

Intermediary species remain bonded to the catalyst surface, allowing successive polymerisation steps to produce longer chain hydrocarbons before desorption of the final product. Although the exact mechanism is still in debate, it is agreed that growth occurs via several steps on the surface of the catalyst[21,22]:

Reactant adsorption

$$CO \rightarrow C^* + O^* \quad 2.11$$

$$H_2 \rightarrow 2H^* \quad 2.12$$

Chain initiation

$$2H^* + C^* \rightarrow CH_2^* \quad 2.13$$

Chain growth

$$R - CH_2^* + C^* + 2H^* \rightarrow R - CH_2 - CH_2^* \quad 2.14$$

Chain termination and desorption

$$R - CH_2 - CH_2^* \rightarrow R - CH_2 - CH_3 \quad 2.15$$

Van der Laan *et al*., amongst others, propose that CH_2 insertion via the surface carbide mechanism is the principle growth route for hydrocarbon formation. Figure 2.1 below gives a schematic of the chain initiation, growth and termination[22].

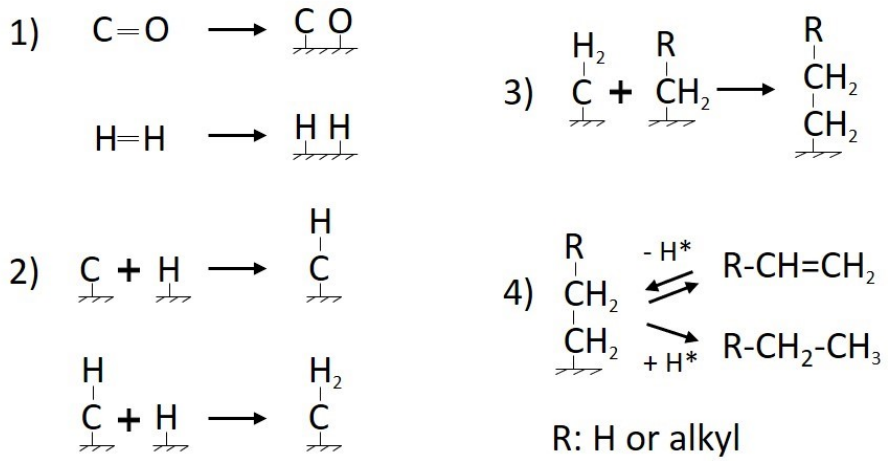


Figure 2.1: Carbide mechanism for FTS.

Pichler and Schulz suggested a CO-insertion mechanism was better suited to explain the formation of alkenes and oxygenates in a typical FTS product[23]. Several variations of the CO-insertion mechanism exist, all centring on chain growth *via* insertion of adsorbed CO. These make up the other main family of chain growth mechanisms proposed for FTS[24].

Secondary reactions can occur if products desorb and react with another forming chain. This can take the form of chain branching, isomerisation and saturation of alkenes amongst others. The nature and extent of secondary reactions taking place affects the final product composition and distribution.

Despite the increased level of research seen of late, the complexity of the final FT products mean that some details of the underlying reaction mechanisms are still uncertain, predominantly regarding chain growth. This is thought to vary with catalyst base metal[25,26]; this will be discussed further in section 4.1.

2.2.1 Product Distribution

Regardless of the catalyst type, reactor conditions and hence reaction mechanism that takes place, the product distribution comprises hydrocarbon chains from methane to high molecular weight waxes.

An approximate product distribution from literature shows that product fraction decreases exponentially with carbon number, this is typical of chain growth in polymerisation kinetics[27]. The stepwise growth process of the FT reaction means the product distribution is dependent on the probability of chain

growth, α. For true polymerisation reactions the value of α can be assumed to be independent of the chain length, and hence a simple distribution curve calculated for a given value of α.

To describe this distribution Anderson adapted the homogenous polymerisation model of Schulz and Flory to include chain branching, giving the Anderson-Schulz-Flory (ASF) distribution which is the most commonly used model to characterise FTS products.

$$W_n = n(1-\alpha)^2\alpha^{n-1} \qquad 2.16$$

Where W_n is the weight fraction of hydrocarbons containing *n* carbon atoms.

However, the probability of chain propagation for the FT reaction is not found experimentally to be independent of carbon number as it would be for a true polymerisation reaction. A local maximum is often seen at C_1 and around C_3-C_4, with a positive deviation in the higher mass fractions sometimes also experienced[28], as is demonstrated in Figure 2.2.

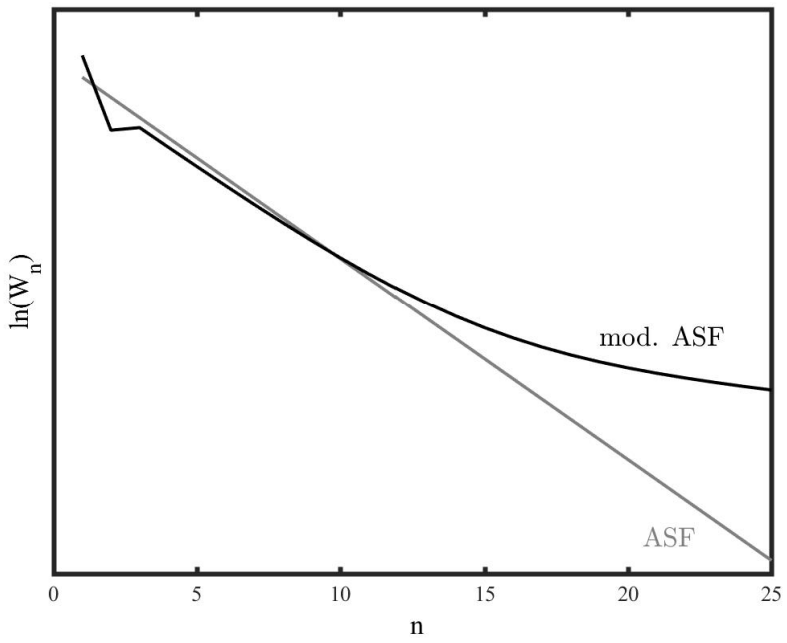


Figure 2.2: Variations in ASF distributions seen experimentally. Generated from data in reference 28.

This modified ASF distribution is frequently achieved through the use of a double ASF model, producing an α value for the elevated low chain length mass fractions and another for the higher chain lengths.

Although methane is the single largest FT product, it is generally unwanted. Increasing the value of α increases the probability of chain growth, minimising the amount of methane produced and increasing the fraction of longer chain hydrocarbons. When chain lengths become very long waxes are produced that need cracking in order to produce liquid fuels. In order to achieve the optimum product yield some

further processing will invariably be necessary, either to refine the various cuts of fuel and chemicals produced, or to further process the unwanted products into useful components.

Since it is necessary that the chain growth step take place more rapidly compared to the termination step, in order to produce longer chain hydrocarbons, α increases with reduced reaction temperatures[26]. It is also dependent on other process conditions and the catalyst used. It is deemed independent of conversion, allowing tuning of the final product distribution through choice of catalyst and reactor conditions as the reaction proceeds[29,30]. The effect of reactor conditions will be discussed later in section 4.6.

2.2.1.1 Diesel vs. Petrol

Diesel and petrol are the most common liquid fuels currently used for transportation. Both are mixes of hydrocarbons, comprising primarily of straight and branched alkanes and alkenes.

Petrol is commonly taken approximately as a mix of chain lengths C_4-C_{12}, and diesel of lengths C_9-C_{25} [31]. The differing chain lengths results in distinctive properties of each fuel, and the mix of each is adjusted to ensure criteria for the fuel is met. Although the mineral source of both fuels is the same, the chain length differences mean that the method of production of biofuels for each tends to vary. The current situation regarding renewable sources for both petrol and diesel is briefly reviewed below.

Petrol

Petrol based vehicles were the most common light vehicles in use for much of the 20th century, making up 73% of road transport fuel in 1990[32]. Ethanol from renewable sources, typically sugar cane or beet, is more miscible with petroleum based mixes than biodiesel. It contains low levels of impurities such as sulphur and is produced through a well-established reaction method. The addition of ethanol into transport fuel is common in certain areas such as Brazil where bioethanol fractions between 10-25% have been routinely added to fuel mixes since 1976 when the government made it mandatory to blend ethanol with conventional petrol[33]. In more recent years, other countries have followed suit, with the US and Germany amongst others offering a range of fuels between 10-85% bioethanol (E10-E85). Whilst not all older vehicles can run on high ethanol content petrol, due to its increased vapour pressure and hence higher octane rating, the majority of modern road vehicles are designed to run on an E10 blend.

Diesel

Whilst some countries decided to reduce their GHG emissions by increasing the renewables content of their fuel, many started giving incentives for the purchase of more energy efficient vehicles. The use of diesel was encouraged in Europe and the UK during the 1990s for the higher energy density and miles per gallon (mpg) achievable. Tax incentives on diesel fuel has meant that diesel accounted for 61% of the UKs road transport in 2014 and its share is increasing[32]. Given that the average light duty

private car has a lifespan of 10-15 years, and heavy duty vehicles longer again, it is unlikely that the proportion of diesel usage will drop significantly by 2020.

Currently the majority of biodiesel is produced via transesterification of lipids to produce fatty acid methyl esters (FAME). The composition depends heavily on the source oil or fat, and it has an approximately 10% lower energy content than an equivalent amount of mineral diesel[34].

The presence of mono and diglycerides in the fuel mean that biodiesel produced from fats can absorb water. This causes running and corrosion issues within the engine. FAME diesel also has a higher viscosity and crystallisation point, reportedly increasing injection pressures and causing blockages within the engine[35]. In order to increase the renewables content of existing diesel fuel the products must become more standardised and miscible with petroleum based diesel.

The limitations of FAME biodiesel, combined with the large market share diesel commands, means the production of synthetic diesel offers a larger opportunity for GHG reductions than that of synthetic petrol. A diesel mix of C_9-C_{25} is therefore chosen as the desired product to investigate for BTL *via* FTS.

2.3 Feedstock

FTS requires a syngas mix of H_2 and CO to proceed. Some catalysts, particularly those with WGS activity, can also utilise CO_2. Historically syngas has been produced from the gasification of natural gas or coal. Gasification converts carbonaceous materials to a gaseous mix of carbon oxides and hydrogen through controlled incomplete combustion. High quality syngas has a high heating value and hydrogen concentration, with low levels of nitrogen and other impurities. The syngas produced for FTS would ideally have a H_2/CO ratio of 2.15, to allow complete conversion to a straight chain liquid product[36]. However, this is often unachievable through stand-alone gasification, with typical production values ranging from 0.6-4, depending on feed and gasifier conditions[37].

Recently the focus on reducing GHG emissions through renewable fuels has led to increased interest in the gasification of biomass. Syngas produced from woody or lignocellulosic biomass (LCB), either directly or via bio-oils, has recently emerged as a method to produce syngas from renewable sources without competing directly with food crops[38,39]. Although the sulphur content in bio-syngas is much lower than its coal and gas derived counterparts, it can suffer from low H_2/CO ratios in the region of 1-2.2[36] as well as high water and CO_2 content[40]. Due to this steam reforming, where steam is used instead of oxygen, is typically used with direct biomass gasification to improve CO/H_2 ratios[41]. Lower temperatures required for biomass gasification can also mean that the syngas contains small amounts of methane, not usually seen in coal fed gasifiers which generally operate at higher temperatures. Table 2.1 gives an overview of the range of syngas compositions for various feedstocks.

Table 2.1: Typical syngas compositions (wt%) for various gasifier feeds, generated from data in reference 42.

Feedstock [wt%]	Mixed Biomass	Mixed Biomass	Wood	Pulp	Municipal solid waste	Coal
H_2	5-26	7-20	14.9	43.3	23.4	24
CO	13-27	9-22	46.5	9.22	39.1	67
CO_2	12-40	11-16	14.6	28.1	24.4	4
H_2O	<18	10-14	dry	5.57	dry	3
CH_4	3-11	<9	17.8	4.73	5.47	0.02
N_2	13-56	46-52	0	0	-	1
H_2/CO	0.2-1.6	0.6-1.0	0.3	4.6	0.6	0.36

A lower H_2/CO ratio can affect the products formed, giving higher alkene content and longer chain lengths due to the decreased probability of chain termination *via* hydrogenation and saturation. Dry *et al*. also found that increasing CO and CO_2 partial pressures reduces the methane split in the product, with methane selectivity being proportional to $P_H^{½} / (P_{CO} + P_{CO2})$.[43]

Altering of the H_2/CO ratio can take place via the WGS reaction where excess CO is shifted to produce H_2, shown in equation 2.10. Increased water concentration in the reactants can push this reaction towards H_2 production, however this is balanced by the CO_2 concentration on the product side.

The CO_2 content of the feed gas can also affect the extent of conversion and product distribution. Jun *et al*. state that for low H_2 content syngas ($H_2/[2CO+3CO_2] = 0.44$) CO_2 acts as an inert, with only hydrogenation of CO taking place. However, when the H_2 content is increased to stoichiometric values and beyond ($H_2/[2CO+3CO_2] = 1$) over Fe catalysts, the reverse WGS reaction becomes a factor in hydrocarbon formation[44]. The extent of CO_2 utilisation also appears to have a temperature dependence. At 508K and 513K respectively Krishnamoorthy *et al*. and Hall *et al*. found that the addition of $^{13}CO_2$ and $^{14}CO_2$ to H_2/CO ratios of 2 and 1 gave negligible ^{13}C and ^{14}C content in the product[45,46]. At an increased temperature of 543K and H_2/CO ratio of 6 ($H_2/[2CO+3CO_2] = 0.55$) Xu *et al*. detected an essentially equal amount of ^{14}C in the hydrocarbon product as in the $^{14}CO_2$ added, suggesting one ^{14}C atom was inserted in each chain[47]. It is proposed that the combination of the increased H_2 content and temperature were responsible for the uptake of CO_2, though further investigation would be required to determine the influence of each.

The use of CO_2 through the WGS in turn reduces the H_2/CO ratio of the feed, giving preferential removal of O as H_2O. This results in higher selectivity towards C_{5+} and alkene products[45]. Experiments by Jun *et al*. also found that gas composition altered the activity of Cu/K promoted Fe catalyst, with a CO_2 rich feed the activity drops sharply[44]. This is suggested to be due to increased oxidation of the Fe.

To reflect the higher levels of CO_2 concentration typical in syngas compositions from gasification of biomass, a syngas comprising of 33%, 33% and 34% of CO, CO_2 and H_2 respectively is taken as the base feed for experimentation for the experimental work performed in this investigation.

2.4 Fischer-Tropsch Reactor Types and Current Technology

There are several different types of FT reactor currently in use both commercially and in research, with variations on the core fixed bed, fluidised bed and slurry reactor designs being the main types used in industry. Each reactor type has particular characteristics that can make the design more suited to individual requirements. Since this research is focusing on testing the suitability of catalysts for industrial processes continuous reactors only will be considered.

2.4.1 Fixed Bed

In the early days of industrial FTS the majority of reactors were packed, or fixed, beds. This is an uncomplicated reactor model that allows the use of larger catalyst particles with lower mechanical strength. Operating and capital costs are low and it is easy to use in continuous operation at high conversions with catalyst poisoning being contained in the initial section of the bed. Downfalls of the fixed bed occur due to the highly exothermic nature of the FT reaction, requiring large amounts of heat removal and giving the potential for formation of hot spots. To maintain a viable pressure drop over the bed the bed void fraction must also be high. This is achieved by the use of large catalyst pellets, > 1 mm, with corresponding low porosity. Post *et al*. determined that particle diameters above 0.5 mm start to experience intraparticle diffusion limitations[120], meaning that the movement of reactant and product molecules through liquid filled catalyst pores could be rate limiting and reaction rates lower than with smaller catalysts pellets[48].

Some variations on the fixed bed were developed in Germany during the 1930s and 1940s to manage the heat removal requirements, including the addition of steam raising tubes, inter-bed cold feed quenches and high levels of inert recycle gas. The low gas space velocities required for single pass reactors give low heat transfer rates and hence require large cooling surfaces to avoid local temperature excursions and the corresponding high methane selectivity. Therefore, a fraction of the reactor outlet gas is commonly recycled, improving heat transfer but also increasing the pressure drop[49]. These factors severely limit the scaling up of fixed bed reactors from their original production rates of approx. 0.1 t/h in the 1940/1950s to the capacities required today[48]. Figure 2.3 gives a schematic of a fixed bed reactor.

2.4.2 Multi-tubular Fixed Bed

The issues of heat removal and scale up of the fixed bed reactor design are addressed in the multi-tubular fixed bed. In this design the reactor contains multiple catalyst filled tubes and a cooling medium on the shell side[50]. Each tube acts as an individual small fixed bed reactor with wall cooling, meaning the scale up is modular and relatively uncomplicated. Heat transfer rates are improved by higher velocities through the narrow diameter catalyst tubes as well as by improved contacting with the coolant on the

outside of the tubes[49]. Supported catalysts can be used, allowing flexibility in mechanical properties, though it must be ensured that changes in the catalyst dimensions through its lifespan will not cause blockages of the narrow tubes.

The benefits of product separation and the location of catalyst poisoning seen in fixed beds are retained. The use of multiple tubes however does increase catalyst loading time and complexity. Larger reactors can consist of hundreds or thousands of tubes, increasing construction costs. The significant reactor weight caused by a high number of tubes can also limit reactor size due to available transport. However, unless catalysts with very short lifespans are used, or very large single reactors are required, the increased preparation time and costs will most likely be outweighed by the improvement in operation over a traditional fixed bed reactor.

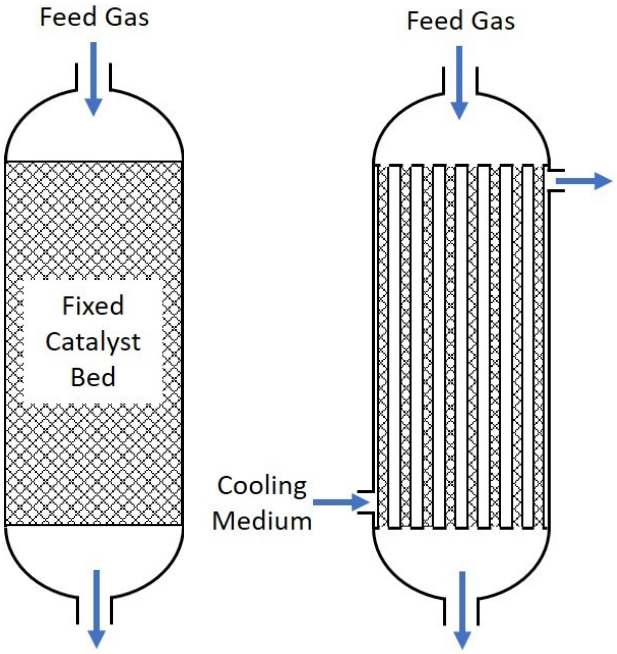


Figure 2.3: Adiabatic fixed bed reactor and multi-tubular fixed bed reactor.

2.4.3 Fluidised Bed

Fluidised beds were developed in the 1950s and 1960s, offering an improvement to the poor temperature control of the fixed bed by reducing heat transfer limitations. Two main types of fluidised bed are currently in commercial use for FTS, the fixed fluidised bed (FFB) and the circulating fluidised bed (CFB). Figure 2.4 gives a schematic of a typical FFB reactor.

The catalyst particles are fluidised by an upwards stream of fluid containing the reactants before entering a disengagement section or cyclone and being recycled back to the main bed. The movement of the bed creates high levels of turbulence which provides a more even temperature profile by improving heat transfer and prolonging catalyst activity. Intraparticle diffusion limitations are also reduced by the use of particles <1mm, as the problems of bed pressure drop are removed[48]. However,

the forces exerted on the catalyst particles mean that high strength and abrasion resistance is required to avoid dust formation and plugging. Deposition of long chain products on the catalyst surface, causing agglomeration and loss of fluidisation, must be avoided by controlling the product distribution and operating above the hydrocarbon dew point[49]. Fluidised beds are therefore best for use in high temperature Fischer-Tropsch (HTFT) at moderate pressures, with a low chain length product and an α of less than 0.7[48].

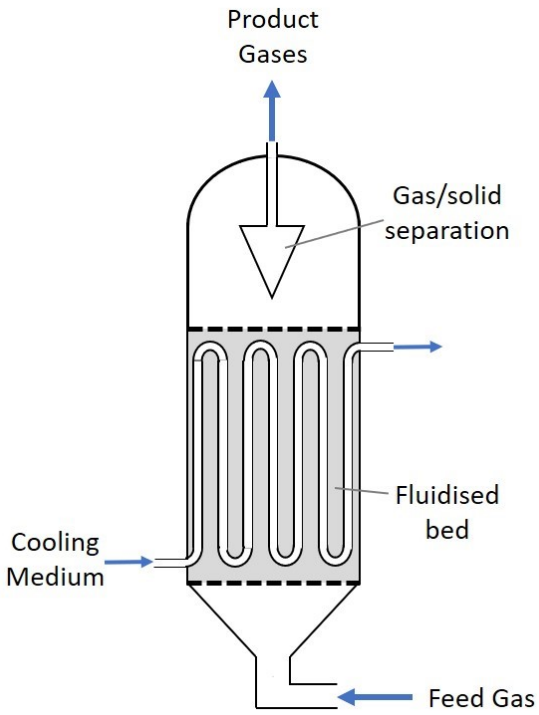


Figure 2.4: Typical fluidised FT reactor.

2.4.4 Slurry

The final reactor type most commonly used in industry is the slurry reactor. This is a three phase reactor with the solid catalyst suspended in a liquid mix of products, through which the gaseous reactants are bubbled. Slurry reactors are operated as semi-batch, or continuous processes with additional catalyst fed throughout the reaction. Two main regimes exist, homogeneous or bubble flow made up of very small bubbles and heterogeneous or turbulent flow, with large bubbles >10mm. Catalyst particles are very fine, in the order of 10-100 μm[51]. Due to the interaction between the various phases mass transfer is high and heavier products can be generated[52], although temperatures must be kept low to avoid excessive hydrocracking if a longer chain product is desired. The main issue with slurry reactors is achieving a satisfactory separation of product and catalyst, however in the 1990s Sasol introduced a more effective method of separation, allowing the successful commissioning of larger units[49].

Heat transfer in slurry reactors is good, particularly when operated with higher gas velocities in the heterogeneous regime. Heat transfer coefficients increase with increased catalyst concentration and gas

velocity, however, de Swart *et al*. found that catalyst loadings above 30 vol% causes small bubbles to coalesce[53]. As a result of these factors FT slurry reactors tend to be operated in the heterogeneous regime.

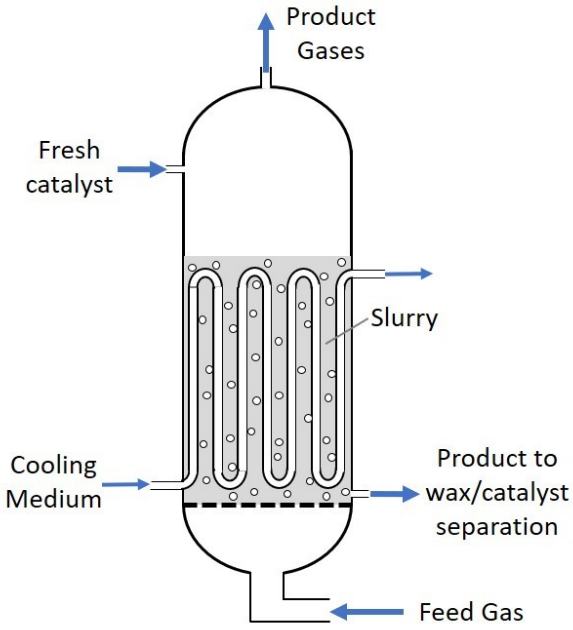


Figure 2.5: Typical FT slurry reactor.

Comparisons between fixed, fluidised and slurry reactors were made by Sasol using the fixed bed catalyst and a fused HTFT catalyst respectively. It was found that the slurry reactor matched the fixed bed conversion rates and selectivities with a third of the catalyst loading, this is believed to be due to the smaller catalyst size reducing mass transfer limitations. Compared to the fluidised bed the conversions were lower, this was taken to be due to the lower catalyst loading possible, with no benefit from decreasing particle size available[49].

2.4.5 Existing Commercial Reactors

Table 2.2 gives a brief overview of some of the existing commercial FT reactors in use, including commissioning dates where available. There is an approximately even mix between low temperature Fisher-Tropsch (LTFT) using either Fe or Co based catalysts, and Fe based HTFT. Other commercial and demonstration level plants exist, these predominately license either Sasol's Advanced Synthol or Shell's Middle Distillate Synthesis technology.

Table 2.2: Examples of current FT technologies, data taken from de Klerk and Abelló et al. [40]

Reactor	Catalyst	Type
Multi-tubular fixed bed - Arge	Precipitated Fe	LTFT
Multi-tubular fixed bed – Shell Middle Distillate Synthesis (1993)	Co-SiO_2	LTFT
Fluidised bed – Sasol Advanced Synthol (1995)	Fused Fe	HTFT
Circulating fluidised bed – Sasol Synthol (1980)	Fused Fe	HTFT
Slurry bubble column – Sasol Slurry Bed Reactor (1993)	Precipitated Fe	LTFT
Slurry bubble column (2007)	Co-Al_2O_3	LTFT

2.4.6 Reactor Choice

The type of reactor used can affect the activity of the catalyst, for example, catalyst loading limitations in slurry reactors, uneven gas contacting or temperature gradients across the bed in undiluted fixed bed reactors and catalyst attrition in fluidised beds all cause variations from optimal performance. Temperature control must be closely considered for all reactor types since the FT reaction is highly exothermic, the separation of catalyst particles and product must also be contemplated in both slurry and fluidised beds.

However, the aim of industrial reactors is to produce high yields of the desired product. Typically, industrial reactors are run at high conversions as integral reactors. These have been shown to be unsuitable for fundamental small scale reaction investigations due to concentration and temperature gradients along the bed[54]. Since the aim of this work is to review catalyst activity and performance, a differential reactor with low conversion is more suitable. For this a single tube fixed bed is chosen as it allows ease of loading and product separation, as well as flexibility in catalyst particle size, composition and reaction conditions. If required in future work, the scale up to larger pilot plant or industrial sized multi-tubular reactors is relatively simple.

3 Experimental Reactor Design

In this chapter the design and operation of the experimental apparatus built to meet the criteria specified in section 1.4 is described. For experimental simplicity and flexibility, as discussed in section 2.4.6, a fixed bed reactor has been chosen. Automatic control systems, installed to ensure safe, unattended operation over the long reaction times required, are also reviewed.

Since the production of diesel is being targeted, a suitable method of product analysis is critical. FTS produces a range of chain lengths hence it is important to be able to measure concentrations of gases, liquids and waxes. To achieve this the gaseous products are continuously sampled with a Fourier Transform Infra-Red (FTIR) spectrometer where lighter hydrocarbon content is analysed. Liquid and wax samples are taken periodically and analysed off-line using a liquid phase Gas Chromatography Mass Spectrometer and Flame Ionisation Detector (GC MS/FID). Gas samples were also periodically tested in an offline gas phase GC-MS/FID.

3.1 Experimental Safety

Risk management is an important consideration in all experimental designs, both for personnel safety and mitigating equipment damage. The use of high temperatures, pressure and a flammable, toxic feed gas must be managed in the case of FTS.

Independent protection layers (IPLs) are used during the experimental design to ensure the experimental risk is as low as reasonably practicable (ALARP). A protection layer, if successful, stops an undesirable event from occurring. However, no single protection layer can guarantee to be successful. The use of multiple, independent, layers reduces the probability of an event. If one layer were to fail it should not affect the other IPLs, which could still stop the undesirable occurrence.

3.1.1 Layers of Protection Analysis (LOPA)

The LOPA method was utilised to assess the effectiveness of the IPLs with frequency of failure values taken from literature where available. LOPA is a semi-quantative, order of magnitude method, which is commonly used to determine whether the probability of an undesired event is below a specified risk tolerance criterion, or if the risk must be reduced further by adding more IPLs. Figure 3.1 shows levels of tolerance to individual risk as presented in the HSE report Reducing Risk, Protecting People (R2P2)[55].

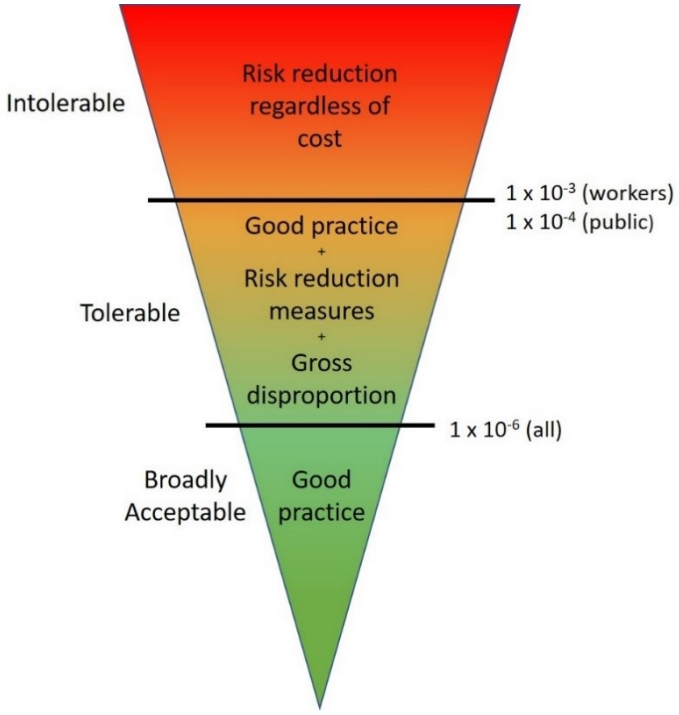


Figure 3.1: Levels of tolerance to individual risk, shown as risk of death of a single employee per year. Data taken from R2P2.

The IPLs identified for the FTS reactor were the pressure control system, CO gas detection with feed gas shutoff and the local exhaust ventilation. As LOPA was performed on the equipment design it was found that the IPLs included in the design mitigated the risk to an acceptable level of < $1x10^{-6}$ serious incidents per year. The completed LOPA assessment can be found in appendix ASafety Reviews.

3.1.2 Hazard and Operability (HAZOP) Study

The final design and subsequent updates were subjected to a hazard and operability (HAZOP) study. The HAZOP is a systematic, structured, method of identifying potential hazards within a process or operation. A set of guide words allows deviations from the original process intentions to be examined, risks discovered and actions recommended to reduce the risks suggested if necessary. The HAZOP indicated that additional layers of protection were required to mitigate the risk associated with the toxicity and flammability of the syngas feed. The full HAZOP with recommended actions can be found in appendix A.

3.2 Design

In order to test catalysts under varying setups, the reactor must be flexible enough to allow for a variety of feedstocks and operating conditions. The high CO content of the syngas feed introduces additional hazards that must be mitigated. Figure 3.2 gives a simplified process and instrumentation diagram (P&ID) of the overall reactor design.

The inlet gas mixing was designed to allow flexible mixing of one to three different gases at a combined total flowrate of up to 400 ml/min. It is important that the flowrates are independently controlled and

not affected by each other. The gas mixing has been designed to ensure that each additional gas mixes fully with the total flow at controlled flow rates. Bypasses around each three-way valve ensured that no stagnant pockets of reactant exist when not in use, see Figure 3.3 for details. A dilution gas of up to 2000 ml/min could either pass through the reactor or mix with the product downstream of the reactor before passing through the back pressure regulator (BPR). This both improved the FTIR response time and reduced the CO concentration of vent gases.

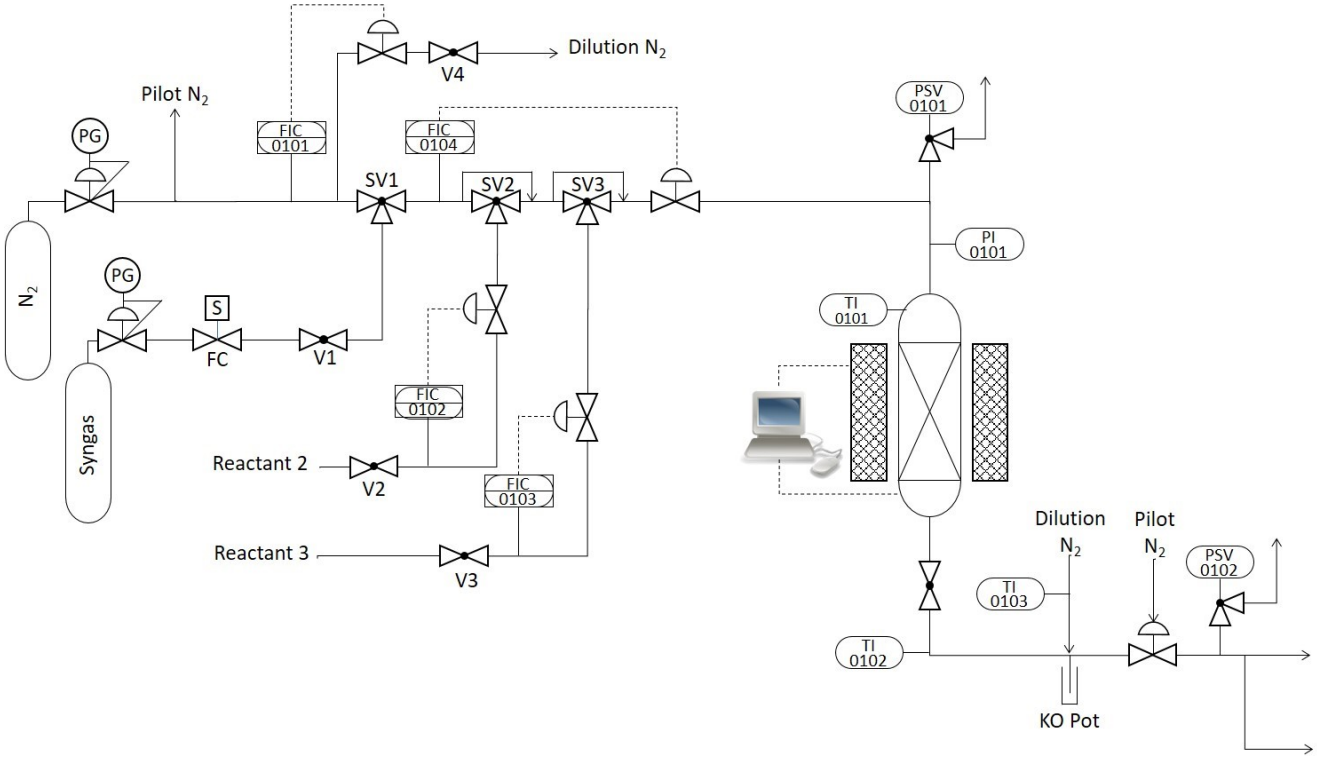


Figure 3.2: Simplified fixed bed experimental FT reactor P&ID.

As discussed in section 2.3, a typical clean syngas composition has been taken from literature of 33, 33 and 34 vol% of CO, CO_2 and H_2 respectively, and a cylinder of this composition was used as the base reactor feed. A three-way valve, SV1, was used to switch between syngas and a nitrogen purge flow through the reactor. The reactor feed can then have two more additional flows through three-way valves SV2 and SV3, these can be used to add impurities if required in future work[56]. The total reactor feed rate was controlled by FIC0104 and the dilution flow by FIC0101 (both Bronkorst EL-Flow) which control valves FV0104 and FV0101 (Badger Research Control Valves). A National Instruments Compact Rio (CRio), took measurements from the flowmeters and set the positions of the control valves according to the desired flowrates using PID control algorithms. All volumetric flows are referred to 1 bar and 20 °C. The flowmeters were calibrated at system pressure using bubble columns with either syngas or nitrogen, depending on the gas used in normal operation. Once mixed, the feed passed through a 15 µm filter and a non-return valve before it was fed into the fixed bed reactor. A pressure relief valve, PSV0101, set at 35 barg on the reactor inlet protects the system from over-pressurising. PSV0102 set at 2 barg protects the low pressure line to the FTIR.

The reactor was heated to 230 °C via a 400 W Carbolite Gero tube furnace surrounding the reactor body, the gas flow passing vertically down over the catalyst bed. The catalyst was mixed with an excess of quartz sand, sieved to contain particle sizes between 150-200µm, to dissipate heat and loaded within an 8mm ID quartz liner held within the reactor body. With the bed diameter approximately 40 particles wide it can be assumed that plug flow occurs, and the radial velocity profile is constant. Plug flow behaviour has been shown to be valid for beds more than 15 particles wide, allowing catalysts up to 533 µm to be measured under plug flow conditions in this apparatus[57]. Quartz sand was chosen as it undergoes the same thermal expansion as the liner[56]. By matching expansivities passive failure of the liner, due to the bed expanding beyond the capacity of the liner, can be avoided.

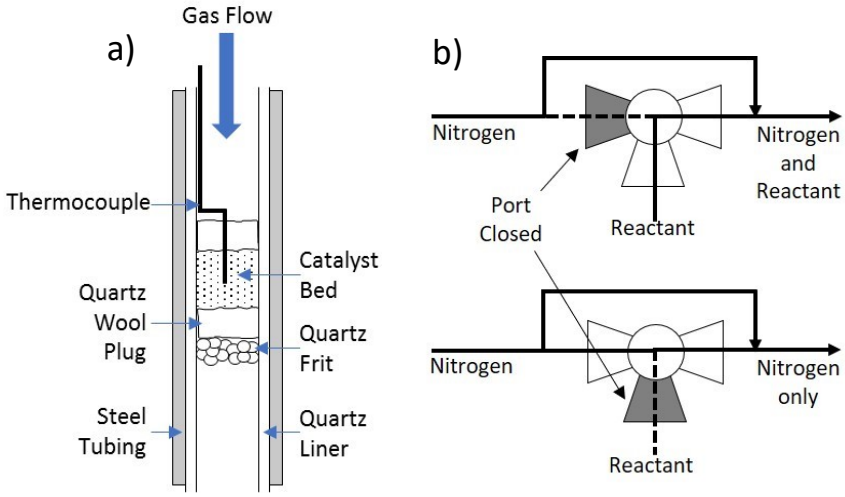


Figure 3.3: (a) catalyst bed layout, (b) three-way valve.

The catalyst bed is approximately 10 mm deep and was supported on a sintered quartz frit, topped with a plug of quartz wool to prevent catalyst particles entering the frit.

A N-type thermocouple was placed at the centre of the catalyst bed, through which a Eurotherm 3508 controller unit controlled the temperature. A K-type thermocouple measured the bed temperature at the same location and acted as a measurement check, with temperatures being recorded on the CRio. A K-type thermocouple embedded in the centre of the furnace body acted as a high temperature trip sensor for a Eurotherm 2132 controller unit, with the trip value set at 300 °C.

During in situ testing at 230 °C with 2 K-type thermocouples in different bed locations, the controller successfully maintained the set 5 °C ramp rate within 96% and held bed temperatures within +/-2 °C during soak periods. A plug of quartz wool on top secured the bed in place.

Due to the reaction conditions the whole system was made of 316L stainless steel tubing, the reactor body is ½ inch and the remainder ¼ inch tubing to minimise system volume. The quartz liner was sealed within the reactor body at the top using a Viton O-ring which seats into a groove machined into the Swagelok compression fitting at the top of the reactor body. The seal is maintained with pressure

from a spring at the base of the quartz fitting, pushing against the bottom reactor body compression fitting[58]. This arrangement allows for the system pressure to equalise in the annulus between the reactor body and the quartz liner, whilst preventing bypassing through this space. Sealing the quartz liner to the outer reactor body at both ends would result in pressure differences of up to 31 barg across the wall, which the quartz liner could not withstand. Figure 3.4 provides details of the sealing arrangement.

On exiting the reactor, the partially reacted feed entered a region heated to 120℃ by electrical heating tapes before reaching the liquid knock out pot. At this point preheated nitrogen at approximately 75℃ sweeps over the reactor outlet, quenching the gas and condensing higher boiling hydrocarbons in the knock out pot. A detailed schematic of the knock out pot internals can also be seen in Figure 3.4. The remaining gases exit the knock-out pot and passed through the electrically heated inline filter, F2, and BPR before being routed to an MKS MultiGas 2030 FTIR for online analysis. K-type thermocouples measure the temperature at the nitrogen purge and BPR inlet.

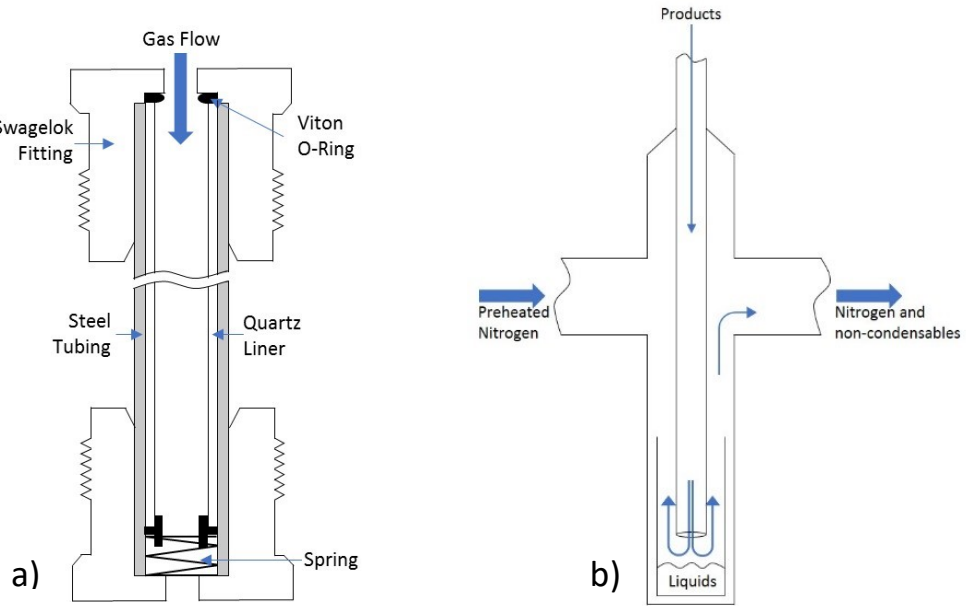


Figure 3.4: (a) internal reactor sealing and (b) knock-out pot internals.

3.3 Product Analysis

Gaseous products at atmospheric pressure pass through a secondary filter, heated to 150 °C, after which a ⅛ inch tee splits the gas for analysis. The main flow passed to the FTIR through a flexible ¼ inch line, heated to 191 °C. This ensures no condensation enters the instrument as well as preheating the gas. The FTIR is fitted with a 200 mL gas cell with 5.11 m pathlength. Exiting gas from the FTIR was vented to atmosphere in a safe space within the fume cupboard. The nitrogen dilution flow of 320 ml min^{-1} decreases the FTIR response time to changes in concentration by a factor of 9. The FTIR gas cell was maintained at a constant pressure of 1 barg and temperature of 191 °C by a pump and heater within the instrument. A continuous nitrogen purge of the volume outside the cell gives a stable background. Nitrogen was also used to purge the cell overnight before taking a background spectrum

every 6 months, providing a check on the stability of the FTIR measurements and highlighting any drift that might have occurred.

Gas samples were also taken after the BPR for offline analysis using a gas phase Shimadzu GC-17A MS/FID. This allowed confirmation of the light hydrocarbons results found through the FTIR.

Liquid and wax products could be isolated and removed via the KO pot by closing V5 downstream of the reactor, slowly venting the pressure and purging with nitrogen. The KO pot base could then be opened and the product decanted from the quartz liner before the KO pot is replaced. The liquid and wax products were removed periodically for analysis via a Shimadzu QP2020 GC MS/FID; toluene was used as the carrying solvent.

3.4 Temperature Control of Reactor

Since the reactor bed is held at a constant temperature throughout the experiment, temperatures elsewhere in the bed will be at a constant difference from the central temperature given by the thermocouple. Temperature variations through the bed were found to be well within an acceptable error of 5 °C by use of a second thermocouple at a secondary height within the bed during an isothermal run at 230 °C. K-type thermocouples have a standard accuracy of ± 2.5 °C or ± 0.75% of the temperature measured in degrees centigrade, whichever is greatest. N-type thermocouples, as used for the furnace control, are similar at 2.2 °C or 0.75% of measured temperature. Therefore, at the experimental conditions of 230 °C the expected error is less than ±2.2 °C. However, this level of accuracy is for new thermocouples only. Drift has been reported by the manufacturers for thermocouples in use, with errors particularly seen after repeated heating and cooling. In order to ensure that the accuracy of measurement doesn't degrade over time, the control N-type thermocouple was replaced every 12 months. The difference between the K and N-type bed temperature measurements was also monitored, if this became greater than 5 °C the thermocouples were both replaced. To date however, this did not occur.

For initial heating and reduction, ramp rates were kept at 2 °C min^{-1} to avoid radial temperature gradients above 5 °C in the bed. The remainder of the experiment was undertaken at a constant temperature, which was maintained at ± 2 °C by the furnace control system, as determined through temperature control testing described in section 3.2.

3.5 Pressure Containment

Stainless steel tubing from Swagelok was used for the reactor body. Individually, conditions of up to 850 °C or 288 barg can be safely reached and maintained for an operating period of 10,000 hours, however the reactor body was replaced after every 1000 hours of use to be conservative. Swagelok give a de-rating coefficient of 0.85 for design pressure at higher temperatures[59], which gives a maximum operating pressure of 234 barg at 315 °C, giving high safety margins and flexible operating conditions

for both LTFT and HTFT synthesis if required. The furnace high temperature trip was set at 300 °C, ensuring the pressure rating was well above the operating conditions.

Additional IPLs were included to further reduce the risk of a high pressure situation occurring. The dilution gas provides the pilot pressure to the BPR, ensuring that the system pressure could not exceed that of the dilution gas and that any loss of dilution pressure and hence flow, would immediately vent the reactor contents to a safe place. Two ¼" Swagelok PSVs were also fitted, one directly upstream of the reactor set at 35 barg, one immediately downstream of the BPR set at 2 barg. Both PSVs are capable of passing greater than 50 L min^{-1} (STP) at their set pressures[60], significantly above the maximum total flowrate of 2.04 L min^{-1}. The vent gas is fed to the back of the fume cupboard where gases are removed through the forced ventilation system which, in the case of loss of containment of a full syngas cylinder, is capable of reducing the CO concentration in the fume cupboard to under 30 ppm within 10 minutes.

3.6 Syngas Containment and Detection

Syngas contains CO and H_2, both toxic and flammable gases. The EU long term exposure limit for carbon monoxide is 30 ppm over 8 hours, the short term 15 minute limit is 200 ppm[61]. It is noted that the EU exposure limits were updated in January 2020, the experimental section of this work was completed in 2019 and therefore the 2018 edition is used.

Since the syngas feed contains CO levels considerably beyond these limits, it is imperative that users are not exposed to leaks and the gas is vented safely. To limit exposure to CO the main body of the apparatus is contained in a fume hood, excepting the FTIR, which was too large. Mains powered CO alarms and a flammable gas alarm were located in the laboratory with a second mains CO alarm in the fume cupboard. Additional battery powered CO alarms were located at the syngas cylinder regulator and FTIR vent. These locations were chosen as i) the site with highest potential CO flow and ii) the fitting closest to the user. The syngas feed passes from the cylinder through a fail close shut off valve in the fume hood, at minimum distance from the cylinder regulator. If the mains powered alarms detect CO at 30 ppm or above, or a flammable atmosphere, they activate, cutting power to the shut off valve and an electrical power circuit supplying the furnace and heating tape. This cuts the syngas feed to the apparatus, whilst maintaining the nitrogen dilution flow which serves to both reduce CO concentration and maintain an atmosphere below the lower explosion limit (LEL) for syngas. The electrical heating tape, filter heaters and furnace are also switched off through loss of power to the ring to remove potential ignition sources. The IA supply is independent and the CRio has an uninterrupted power supply that can last for several days in case of a power cut. This ensures that the nitrogen purge continues in case of a CO alarm, or lab-wide power loss.

The syngas shut off valve can also be closed manually whilst maintaining power to the heaters, and the high temperature trip shuts the furnace down if bed temperatures exceed 300 ℃.

3.7 Automation

Due to the long reaction times required to monitor catalyst activity in general use the experimental rig needed to be automated. This was achieved through the use of several control systems to ensure reactor conditions were maintained safely and that the system shut down if required during unsafe operating conditions.

A Eurotherm 3508 controller on the furnace maintains the bed temperature. Separate temperature controllers on the electrical heating tapes and filter body maintain the reactor outlet and filter temperatures. Flowrates were controlled by the CRio, as was the BPR pressure. The temperatures, flowrates and pressure were all logged through the CRio, the FTIR had a separate logging program.

The automation and control enable the apparatus to run safely unattended, with the only input required being topping up the liquid nitrogen in the FTIR every three days. A live web stream was run whilst the apparatus is active so that lab users could check the state of the experiment remotely.

3.8 Commissioning and Testing of Reactor

Once built, the experimental rig was commissioned and tests conducted to characterise system behaviour. Initial test runs were performed at reaction conditions, but with no catalyst bed loaded, to investigate the inherent reactor activity. No products were detected during the course of the catalyst-free runs; therefore, the experimental rig was determined to have no catalytic activity for the FT reaction. The FTIR was also used to test the off gases of the catalyst-free run for the presence of iron carbonyls. Carbonyls have been reported in some syngas feed streams, thought to have accumulated during gas storage and transport in steel containers. It is known that carbonyls can poison FT catalysts and therefore, if present, should be removed as part of the feed preparation[62]. As iron carbonyls absorb infrared radiation (IR) they can be detected at low concentrations using the FTIR, however no absorbance was seen, suggesting iron carbonyls were not present in the off gas.

Next the reactor was loaded with 0.2 g of monohydrate calcium oxalate ($CaC_2O_4H_2O$) in order to test the quartz liner seals. Under a ramped heating program, the $CaC_2O_4H_2O$ decomposes, passing through three reaction steps that can be monitored by the generation of product gases at specific temperatures; H_2O at 220 °C, CO at 550 °C and CO_2 at 750 °C. Although the experimental rig can safely reach 750 °C at atmospheric pressure, in order to reduce stresses on the reactor body the temperature was limited to 520 °C. A rise is H_2O was detected up to 250 °C, and a sharp peak in CO concentration was seen at 500 °C. This indicates that the decomposition reaction was taking place within the reactor bed, with no dead areas, and that therefore the quartz liner seal prevents significant bypassing of the bed.

Finally, the system was run at a constant temperature and pressure whilst step changes were made to the syngas feed flowrate with a constant nitrogen diluent flow. An initial plug of syngas, at experimental operating conditions and flowrates, took 17 minutes to pass through the nitrogen filled rig and be

detected at the FTIR, giving the total system residence time. Further step changes in syngas concentration using FIC-0104 took approximately 120 seconds to pass from initial to 95% of final concentration, suggesting near ideal plug flow behaviour and validating the use of the plug flow assumption.

3.9 Reactor Operation

During normal operation the reactor operated isothermally. A known mass of catalyst, typically 0.2 g, was loaded into the reactor with an equal mass of quartz sand as a bed diluent. The bed size was limited to a maximum height of 30 mm to avoid high pressure drops and the associated possibility of channelling. The catalyst was then reduced under 40 ml min^{-1} syngas at atmospheric pressure and the temperature increased at 2℃ min^{-1} to 270℃, where it was held for one hour. Off gases passed to the FTIR for analysis.

After the reduction period, the reactor pressure was increased to 30 barg through a nitrogen dilution flow of 320ml min^{-1}. The reactor bed was co-currently cooled by the N_2 flow to the operating temperature of 230℃. The bed was then maintained at 230℃ and 30 barg for approximately 100 hours, to allow the catalyst to bed in and the reaction to reach steady state.

3.10 Reproducibility and Error

3.10.1 Reproducibility

Due to long experimental run times of greater than 100 hours, measurements for each catalyst were not repeated. The reproducibility was instead determined by 3 repeats of the Cat2K and 950-106-U catalysts at the same conditions. The experimental error calculated for these runs is extrapolated to the rest of the catalysts, allowing more catalysts to be tested within the restricted time available for experimentation.

3.10.2 Systematic Error

Systematic experimental error arises from error in the gas concentration and flowrate measurements. The calibration gases used have a certified accuracy of ±5 %, as does the synthetic syngas mix used. Two synthetic syngas cylinders of the same mix were used, with approximately 50% of the tests being completed on each. The same calibration gas cylinder was used each time, resulting a systematic error of ±5 % between concentration measurements.

In addition, the flow controllers are accurate to ±5 %. The net systematic error is therefore calculated to be ±10 %.

3.10.3 Random Error

Most of the experimental error can be traced to systematic sources. The only sources of significant random error come from noise in the FTIR spectra and the operation of the BPR. The standard deviation for CH_4 measurements by the FTIR was calculated to be between 0.7-1.2 ppm, and below 0.04 % for

CO and CO_2. Since each species absorbs IR at different magnitudes the error in concentration varies with species, however over the course of the experiments, product concentrations were measured by the FTIR with deviations below 10 % (typically below 5 %). The temperature of the bed was within ±2 °C, as discussed in section 3.4.

The operation of the BPR also introduces error, as in operation it was not open continuously. The BPR would allow gas to pass once the pressure in the reaction system was above the supplied pilot pressure. This drops the system pressure below the allowed passing pressure, closing the BPR until the passing pressure was once again reached through flow from the reactor. The magnitude of the error caused by this "digital" operation of the BPR is difficult to quantify as the quantity of gas released with each opening of the BPR is not measured. However, the rate of BPR opening is regular and frequent over the entire length of the experimental run and was manifested as random "noise" in the FTIR measurements. The variations in concentration caused by the BPR opening in bursts will also be damped by the comparatively large gas space in the FTIR gas cell.

4 Properties and Production Methods of Fischer-Tropsch Catalysts

Since the initial discovery of CO hydrolysis over nickel in the early 20th century, much research has been done on FT catalysts, with the aim of increasing activity, lifespan and desired product selectivity amongst others. Different catalyst types and production methods are more suitable for varying reactor layouts, feeds and conditions, meaning an understanding of the reaction mechanisms and catalyst behaviour is important when making an informed catalyst choice.

In this chapter a literature study on the various active materials and methods of production is first made, in order that a suitable base material and production method may be chosen for the catalysts under investigation. The chosen preparation methods are then presented in sections 4.9 and 4.10, before the catalysts under test are summarised in the final section of the chapter.

4.1 Catalyst Base Material

Early FT research found that many of the transition group metals and some noble metals possess catalytic activity for hydrogenating CO. Increasing hydrogenation rates are found in the order Ir, Pt, Pd, Rh, Co, Ni, Fe, Ru[22,63,64] with Ru, Fe, Co and Rh giving the highest average molecular mass of product[40].

Low activities combined with high costs for iridium, platinum and palladium make them unsuitable as industrial catalysts. Nickel has been found to have high methane selectivity, making it unfeasible for the production of liquid fuels. Rhodium and ruthenium are not regularly used as a base catalyst, as despite higher activities and chain lengths, their rarity and high cost makes them prohibitive[21].

The general consensus is that the primary industrially viable FTS catalysts are based on iron or cobalt[65,66,67]. This review will forthwith concentrate on these two metals only.

The different base metals have different reaction pathways. When using Fe-based catalysts the oxygen in the syngas is rejected as CO_2 and H_2O, whereas Co catalysts the oxygen leaves only as H_2O, as shown in Figure 4.1 below.

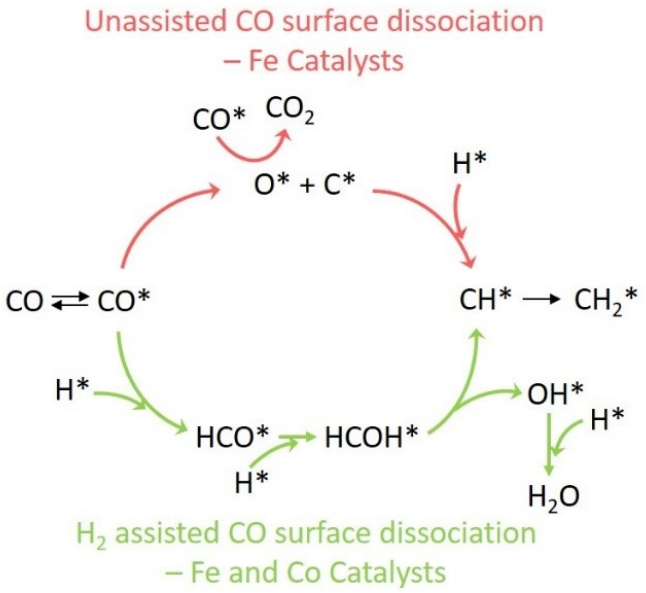


Figure 4.1: Pathway for FT reaction over Fe and Co catalysts.

Unassisted CO dissociation results in the loss of carbon atoms as CO_2, and results in a lower carbon efficiency of the reaction. However, when using a low H_2 concentration feed gas, as is common with biomass feedstock, surface-based hydrogen can be scarce. This could limit the rate of the less H_2 efficient H_2 assisted dissociation.

4.1.1 Iron

Fe is the cheapest and most abundantly available metal for FT catalysis[21]. It has a wide active temperature range of approximately 200-350 °C and is active for the WGS reaction, making it a popular choice for low H_2/CO ratio syngas sources such as coal and biomass[63]. However, Fe based catalysts are more susceptible to deactivation and carbon laydown compared to their Co equivalents[68]. The effect of the increased rate of deactivation can affect the length of life, with some sources reporting a typical industrial lifespan of 8 weeks[69], whilst others state that commercially the catalyst lifespan is not limited by deactivation[72].

The active phase of Fe catalysts for FTS is not yet agreed upon, but it has been suggested by Jahangiri *et al*. that it is the carbide phase[140], others such as Abelló *et al*. suggest it is the magnetite phase and still yet more suggesting the metallic phase[70,71]. It has also been suggested that different phases are active for different parts of the FTS reaction. To further complicate matters the WGS reaction is believed to be catalysed by the magnetite phase[71]. The uncertainty in which phase is active for FTS is caused by the ability of several oxides and carbides to co-exist whilst the FT reaction is taking place, making it difficult to identify on which phase the active site is present. However, it could be the multi-phase state itself that gives iron catalysts their activity. To date there is no accurate method of measuring the amount of active sites in Fe-based catalysts[72].

Fe catalysts tend towards linear alkenes, with some aromatics and oxygenates also being produced[73]. In order to improve stability and tune the product spectrum various promotors and stabilisers can be added. Alkalisation of the Fe via addition of group one metals, K in particular, has been shown to facilitate the activation of CO and promotes Fe_3O_4 carburisation[74]. This increases the number and rate of carbide nucleation sites during reduction, giving a higher dispersion of particles and hence, it is thought, an increased active surface area and rate of reaction[75]. Also average chain lengths are increased, as is the alkene/alkane ratio and the WGS activity[71,75]. Li *et al*. found that increasing the K surface density beyond 2 K atom/nm^2 gave no further benefit, as shown in Figure 4.2, implying the promotional effects are due to surface-based metal/promotor interactions[76].

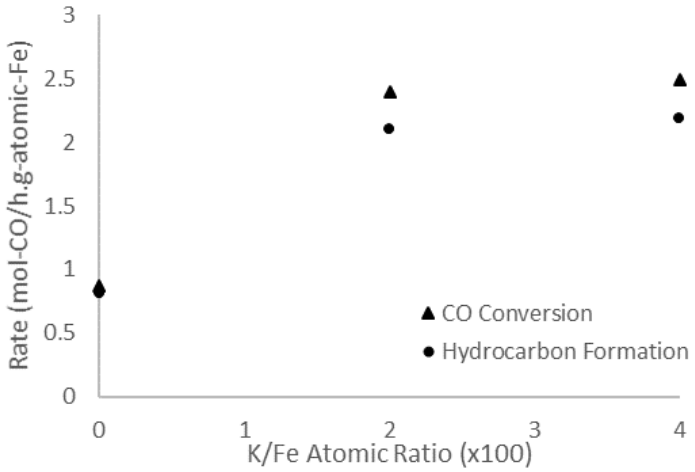


Figure 4.2: Steady state performance of Fe:Zn catalyst with varying K loading, generated from data from Li et al.[75].

The effects of Cu on activity are similar to K, with the addition of Cu aiding the reduction of Fe_2O_3 at lower temperatures, decreasing particle size and therefore increasing dispersion of active material[65,75]. The optimum surface density was found by Li *et al*. to be 1 Cu atom/nm^2.

The benefits of Cu and K are independent, with the effects of each promoter being almost cumulative, however no increase in the WGS activity is seen with Cu loading. Iglesia *et al*. replaced Cu with Ru, finding that it was more effective than Cu at decreasing particle size, but had little WGS activity[75].

Another common promotor, Zn, inhibits sintering of iron oxide at low concentrations and isolates Fe_2O_3 within a framework at higher concentrations. This gives an increased surface area once the catalyst has been activated. Zn also produces $ZnFe_2O_4$ when combined with the iron oxide pre-catalyst, this phase isn't reduced or carburised under FTS conditions. This results in intermediate Zn loadings giving increased activity without changes in product distributions[75].

Other promotors such as Mn, Mo, Ni and S have been investigated on several occasions. Mn is reported to increase catalyst surface area and reduce CH_4 production but has negligible effect on C_{5+} selectivity[77]. The addition of Ni, with its high CH_4 selectivity, unsurprisingly can encourage shorter chain formation, whilst Mo increases C_5-C_{20} selectivity[78].

Commonly catalysts generated from cheaper, less active, base metals are also promoted with small amounts of FT active precious metals in order to optimise catalyst activity and cost, such as the Ru promoted Fe catalyst discussed above. It is generally found that combinations of promotors can act together to maximise the desired properties of the base catalyst[79].

4.1.2 Cobalt

Co catalysts have higher yield of long chain products than un-promoted Fe, though they show no WGS activity so must be fed with near stoichiometric syngas to avoid high wastage rates. As can be seen from Figure 4.1, Co catalysts reject oxygen in the form of H_2O instead of CO_2, giving a higher carbon conversion efficiency. The hydrogenation activity of cobalt is also higher than that of iron, resulting in fewer oxygenates[21]. They show significantly more resistance to deactivation through irreversible oxidation and carbon laydown compared to Fe[80], with lifespans of up to five years being claimed by Shell[72,81].

However, Co is only suitable for use at lower temperatures, as methane selectivity increases with temperature and becomes unfeasible above approximately 250 °C[75]. The predominant product of Co catalysts is a mix of linear alkanes and alkenes[82].

The metallic phase is widely accepted as being the active phase for Co based FTS[123], due to this the extent of reduction is important to the catalyst activity. Particle distribution and size affect the extent of reduction achievable, with larger particles tending to agglomerate thereby reducing the number of catalytic sites available. Conversely as particle size goes below 6-8 nm the catalyst activity drops again, this is due to substrate-catalyst interactions inhibiting the catalysis[63].

The promotors used for Co catalysts varies from those most suited to Fe. A small addition of noble metals appears to improve cobalt reduction and hence activity[83]. The inclusion of 0.5 wt% Pt was found by Batley *et al*. to lower the reduction temperature of Co_3O_4. [84]

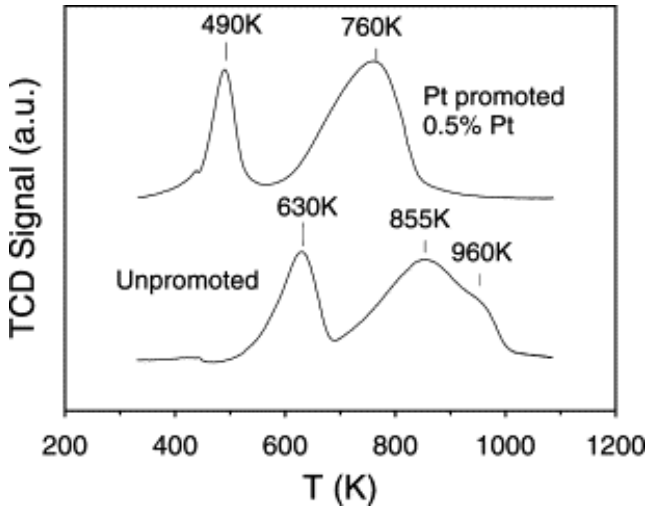


Figure 4.3: TPR profiles of Pt-promoted $CoAl_2O_3$ (15%) and unpromoted catalyst.
Reprinted from Applied Catalysis A: General, vol. 247, Jacobs et al. [85], copyright (2003), with permission from Elsevier.

Work by Jacobs *et al*.[85,86] shown above in Figure 4.3 corroborates this, however, Tsubaki *et al*. found that neither the addition of Pt or Pd affected cobalt reducibility whereas including small amounts of Ru gave dramatic improvements to the extent of reduction[87].

Other research has found noble metals such as Ru[88,89], Re[90] and Ir[91] to have positive effects, with increasing catalytic activity in the order Co, CoPd, CoRe, CoRu, CoRh, CoIr[91]. It is suggested by Khodakov *et al*. that the noble metal accumulates at the outer edge of the particles[63]. Since the noble metals are more easily reduced than Co, they bring hydrogen into the particle, encouraging it to then overflow to the neighbouring cobalt oxide.

The amplified extent of reduction has a secondary effect of improving particle dispersion, possibly through an increased number of Co metal nucleation sites. The lower reduction temperatures are also thought to reduce the probability of metal-substrate interactions and hence the amount of non-reducible cobalt oxides. Finally, Luque *et al*. state that the inclusion of noble metals can also assist with carbon removal from the catalyst surface by improving hydrogenation rates of surface based carbon[69].

The other main class of Co promotor are oxides, with ZrO_2, La_2O_3, MnO and CeO_2 being most common. These are used to adjust the physical properties of the catalyst and interactions with the substrate. Zr promotion increases Co reducibility in Si supported catalysts[92], however on Al supported catalysts reducibility was found to decrease, but still resulted in increased activity and selectivity, thought to be due to the increase in active sites due to the inhibition of the formation of cobalt aluminate[93,94].

The use of La_2O_3 in small quantities (<3 wt%) has been found to improve reaction rates as well as giving a higher selectivity to longer product chain lengths, due to its high affinity to the surface and encouraging cobalt dispersion. Increasing the La_2O_3 content beyond this however, led to significant fractions of La-Co mixed oxides forming, reducing the catalytic activity[95].

MnO promotors were found by Zhang *et al*. to improve Co dispersion and hence the CO conversion rate[96]. Experiments on TiO_2 supported catalysts suggest that the MnO interacts with the cobalt oxide phases giving a decreased Co reducibility. The increase in reaction rate despite the reduced extent of reduction are suggested to be due to Mn assisting in CO addition into forming chains[97].

4.2 Catalyst Substrate

The catalyst support, or substrate, plays an important role within the stability and activity of the final catalyst. Its primary function is to facilitate the dispersion of active particles and allow stable particles to exist in accessible areas after reduction. The substrate alters the catalyst's mechanical strength and surface area available, giving reduced pressure drops and increased longevity in industrial reactors. Since the FT reaction is exothermic the catalyst support also provides a route for heat removal in fixed bed reactors, reducing the chances of reactor hot spots or catalyst degradation[63].

Various substrates are used as the catalyst support for FTS, common industrial examples include alumina, carbon and silica. Investigations into the effect of catalyst supports have shown that the substrate chosen can alter the final catalyst activity, implying that particle-substrate interactions have a significant impact on catalyst formation. Substrate choice can also alter the effectiveness of promotors.

4.2.1 Silica

Silica has been the subject of much research as a substrate, having been in use since the very first days of FTS. It shows weak interactions with both Fe and Co[98], allowing for a good extent of reduction and increased dispersion of Fe[99]. However, these low level interactions do reduce the inherent activity compared to unsupported catalysts[100]. This reduction in inherent activity is generally compensated for by the increased surface area provided by the Si acting as a physical structural promotor[98], Si can also provide HTFT catalysts with improved thermal stability[101] and has been reported to reduce the production of methane when present in higher concentrations[99].

The effect of promotors to help increase activity is in general not altered by Si supports. Pore diameter however was found to affect the activity, with a Co catalyst on an Si support having an optimum average pore diameter of 10 nm[102].

4.2.2 Alumina

Alumina is a common substrate for many catalysts including those used in FT, where it is used to provide strength and an increased resistance to attrition during use[101]. Khodakov *et al*. state that it interacts strongly with cobalt oxides, allowing dispersed metallic Co crystallites to form[63]. If the particles are too small however these strong interactions can result in the loss of cobalt into the support and subsequent formation of cobalt aluminate spinels[103,104].

Temperature programmed reduction (TPR) studies by O'Brien *et al*. showed Fe/Al interactions caused a slower reduction of Fe[105]. However, Jun *et al*. found that alumina supports give good activity for Cu promoted Fe catalysts, this is thought to be due to an increased resistance to oxidation caused by the easier carburisation of the Fe[106].

4.2.3 Titanium

The third of the most common FT supports, TiO_2 has been shown to increase the rate of methanation and decrease conversion on several catalyst base metals, thought to be due to the formation of TiO_x layers over the active sites favouring H_2 over CO adsorption[107]. The presence of H_2O in the system has been seen to counteract this layering effect and increase conversion, with a plateau reached at approximately 30-40% CO conversion[82]. At reduction temperatures greater than 300 °C Ti supports form strong interactions with noble metals, leading to a decrease in desired product selectivity[108]. Unless there is a significant reason for use of a Ti support, such as physical conditions of the reactor, other materials are preferable.

4.2.4 Carbon

Carbon has historically been neglected in industrial FTS, as it is less stable and could gasify in H_2 rich environments. In the last 20 years high purity structured carbons have been investigated as supports, allowing good particle dispersion and low interactions, resulting in easy catalyst reducibility, even under normal FTS operating conditions[63]. High strength, high surface area carbon supports such as carbon nanotubes (CNT) are of particular appeal[109]. The use of carbon avoids the need for inorganic oxide supports which can form difficult to reduce mixed oxides with the active metal phases. Carbon supports can also be varied by the addition of surface functional groups, tuning the interactions between the carbon and metal. One such interaction between Fe nanoparticles and carbon aids iron carbide formation, thought by some to be the active phase of FTS[110].

4.2.5 Thorium Oxide

The initial catalyst developed by Fischer and Tropsch contained a small amount of thorium oxide to enhance stability. Thorium also has the benefit of supressing sintering of Fe catalysts[111]. In later years thorium oxide has largely been replaced by magnesium oxide in industrial catalysts due to its radioactivity as well as for economic reasons[112].

4.2.6 Zeolites

Solid acids, particularly zeolites with their acid-base properties, are of interest as bifunctional, one stage, FT catalysts. Surface acid sites can hydrocrack longer product molecules, maximising selectivity of the desired chain length[113]. Zeolites impregnated with FT catalysts can further tune product distribution through their shape selective nature, by providing a consistent diffusion length and physically limiting the maximum chain lengths that can develop inside the zeolite pore structure[114], as demonstrated in Figure 4.4.

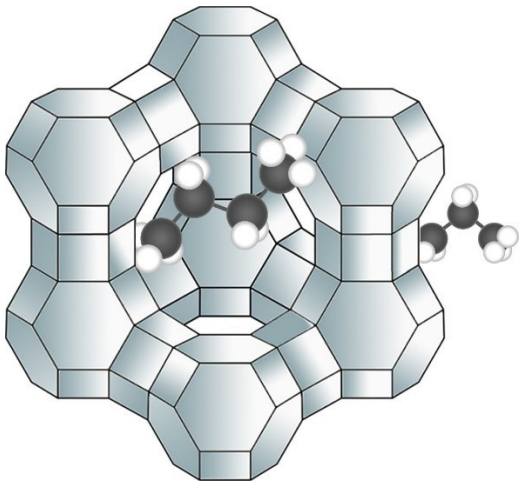


Figure 4.4: Limiting hydrocarbon chain growth with zeolite cages.

Controlling the environment within the zeolite can also limit the size distribution of metal nanoparticles supported within the structure, potentially optimising catalyst size and activity. Although research into

zeolite based bifunctional FT catalysts has taken place for several decades, they have not moved into industrial use due to prohibitive costs. With simpler, more efficient methods of large scale zeolite production becoming available this is an increasing area of FT catalysis research.

4.3 Catalyst Reduction

Both Fe and Co catalysts require reduction before use, with the extent of reduction being a significant factor in the final activity of the catalyst. The reduction of cobalt catalyst aims to produce a metallic phase. Since this is the fully reduced stage of the metal it is impossible to over-reduce. The various oxidation states of iron that are thought to be active include non-metallic and carbide phases, meaning that reduction cannot easily be tailored to produce the desired amounts of each active phase.

As has been discussed in sections 4.1 and 4.2, various factors including particle size, promotors and substrates affect the reducibility of the catalyst which in turn has an impact on catalytic activity. Increasing the extent of reduction to the active phase produces more functional catalyst sites and hence improves the activity. A lower reduction temperature is also indicative of lower amounts of barely reducible mixed oxides, suggesting more of the active phase is present. Increased metal dispersion, promotors or supports with minimal interactions can improve the ease of reduction. However even once these have been tailored to the optimum levels the reduction conditions themselves can play a part in the extent of reduction achievable.

Several groups have performed studies into the type of reduction gas used, comparing reduction in pure H_2 to pure CO or CO/H_2 mixes. Li *et al*.[115], Abelló *et al*.[71] and Pan *et al*.[116] found that reduction under CO lowered catalyst activity compared to H_2, whereas Jamala *et al*. disagree, showing an increased catalytic activity through reduction in CO for both Co and Fe catalysts[117,118]. This may be because of the low concentrations used by Jamala (5% CO in He) ensuring the reaction is mass transfer limited and minimising the amount of catalyst/substrate interactions produced, whereas the use of higher CO concentrations allow the formation of unreducible metal-carbide phases.

Work by Chun *et al*. furthered this to look at the effect of different levels of CO_2 on the reduction of Fe based catalysts. They found that increased levels of CO_2 in the reduction gas gave a higher proportion of long chain products and reduced methane selectivity. TPR of their catalysts in the various environments showed two stages of reduction, firstly the reduction of hematite to magnetite and then the reduction of magnetite and ferrihydrite either to metallic iron (H_2) or iron carbides (CO). The presence of CO_2 appears to inhibit the second stage of reduction via the reverse WGS reaction preferentially removing H_2, leaving a higher proportion of the supposed active phases, magnetite and carbides[119].

Iglesia *et al*. suggest that reducing Co catalysts in high flowrates of H_2 with a slow ramping of temperature gives increased levels of Co dispersion. This slowed reduction process appears to reduce metal agglomeration by lowering the immediate surface H_2O concentrations[69].

Although much research has been performed into the reduction of FT catalysts there is no consensus on the optimum method, or indeed a single method that suits all catalysts and reaction set ups. A slower reduction appears to be beneficial, however methods will need to be fine-tuned for each individual catalyst/substrate/promotor mix to find the most suitable method. For this investigation a slow reduction ramp rate of 2 °Cmin^{-1} to a reduction temperature of 270 °C was used. The catalyst was then held at the reduction temperature for 1 hour. Since reduction in CO_2 containing gas was found to be beneficial for liquid fuel production, the reactant feed syngas was used for reduction as well.

4.4 Catalyst Particle Size and Structure

Several studies have shown that catalyst particle size influences the final activity. In the 1980s Post *et al*. suggested that FTS in a fixed bed reactor is diffusion limited, with diffusion of reactants through the liquid filled pores being the primary reason for limited reaction rates[120]. In the interim period, methods to reduce diffusion limitations such as smaller catalyst particle size and controlled pore structure have been widely investigated.

Many groups have shown that decreasing particle size increases catalyst activity. Work performed by Shell on an Al supported Co catalyst showed that decreasing the particle size from 1.6 mm to 0.28 mm not only dramatically reduced methane selectivity but increased the amount of C_{5+} and overall conversion under various conditions[121]. As reactor types and catalyst production techniques have evolved, the ability to produce and use even smaller particles has become possible. This has improved the mass transfer enough for the FT reaction to no longer be intraparticle diffusion limited. However, the continued reduction in size introduces other influences on the catalytic activity.

Rane *et al*. found that decreasing Co particle size below 8-9 nm resulted in higher methane selectivity and reduced C_{5+} production[122], as shown in Figure 4.5.

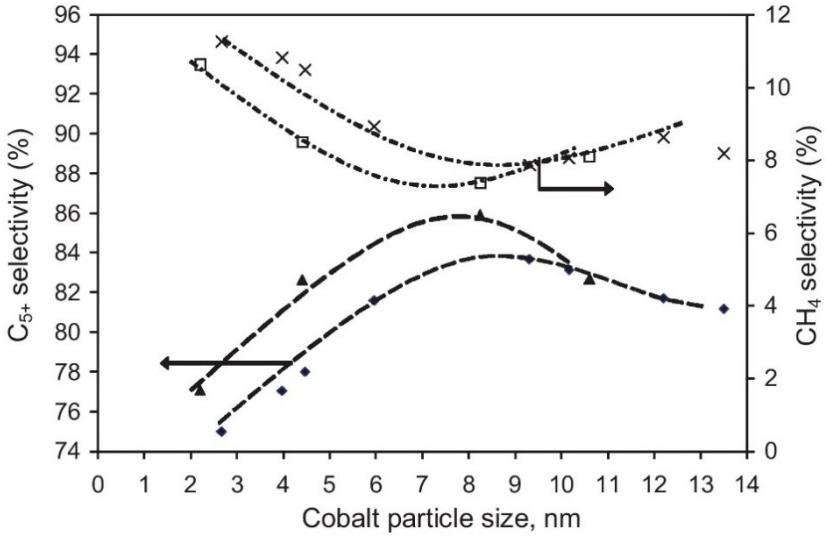


Figure 4.5: Influence of particle size on CH_4 and C_{5+} selectivity of Al_2O_3 supported Co catalysts. Reprinted from Applied Catalysis A: General, vol. 437-438, Rane et al.[122], copyright (2012), with permission from Elsevier.

The same effect was seen by Bezemer *et al*. on Co catalysts where a minimum particle size of 6-8 nm was recommended, as below this the turnover frequency (TOF), a measure of catalytic activity giving the number of catalytic cycles occurring on a unit area in a given time, and proportion of C_{5+} products both drop as well as the methane selectivity increasing. A better yield was found by increasing particle size to an optimum range of 30-40 nm. This is again thought to be due to the influence of strong substrate-catalyst interactions as the catalyst particle size decreases[123]. For Fe catalysts Abelló *et al*. state that reducing the particle size too much can cause irreversible oxidation and produce strong metal-support interactions[71]. Barkhuisen *et al*. showed that carbon and alumina supported catalysts with particle sizes lower than 7-9 nm had lower overall activities and higher methane selectivity[124].

Since there is a dependence of activity on particle size it can be determined that the FT reaction is structure sensitive. By producing a narrow distribution of catalyst particle size the product distribution can be tuned and the generation of certain desired components maximised. As discussed in section 4.2.5 the use of zeolites to support metal nanoparticles can limit the size distribution of the nanoparticles themselves, as well as providing a consistent diffusion length through the liquid filled pores. The use of regularly structured zeolites in supports or multifunctional catalysts is therefore an attractive option that requires more research.

4.5 Catalyst Deactivation

Both Co and Fe catalysts suffer from deactivation, with Co being more resistant than Fe, as shown by its significantly longer reported lifespan. Catalyst deactivation occurs via several different inherent and operational processes which all lead to the same result: loss of active sites.

4.5.1 Poisoning

Both metals are susceptible to poisoning by sulphur compounds, ammonia (NH_3), hydrogen halides and trace metals amongst others. These poisons can limit catalyst lifespans significantly, often meaning that feed gas must be purified before use.

Sulphur (S) is a common poison in syngas, known since the beginnings of FT technology. Although the S content of coal generated syngas is notably higher than that seen in gas produced from biomass, the various sources that can be used in BTL means it must still be considered. S chemisorbs onto the surface, irreversibly blocking the active sites and causing electrical modification of neighbouring atoms. This also causes small increases in secondary hydrogenation of alkenes. Fe catalysts are thought by some to be slightly more resistant to S poisoning compared to Co[69], though this is not universally agreed upon[125]. Promotion with alkali metals is reported to further increase S resistance of Fe catalysts[126]. High S concentrations (200 ppm+) have been shown to significantly decrease C_{5+} selectivity and increase CH_4 production on Co based catalysts[127]. In general, although catalyst modifications can assist in S resistance, feed gas pre-treatment is the most effective measure.

Accounts of NH_3 poisoning are contradictory, with some groups reporting that low levels (<5 ppm) of NH_3 in the feed doesn't significantly affect Co catalysts[128], whilst others have seen notable, irreversible, deactivation at all concentrations[129]. The Davis group[125] determined that maximum utilisable concentrations of NH_3 for Co and Fe were 45 ppb and 80 ppm respectively, after which overall activity drops and C_{5+} selectivity increases. Their interpretation is that this may be due to competitive adsorption resulting in an alkali surface environment and hence reduced dissociative H_2 adsorption.

Halogen compounds, usually HCl, affect Fe catalysts more than Co, encouraging substrate interactions that coat the active sites[125]. These again are irreversible, with rapid catalyst deactivation accompanying decreasing C_{5+} selectivity above concentrations of 3 ppm[130].

Gasified biomass often contains tar, a viscous mix of heavy hydrocarbons which can have a high heavy metal content[131]. These trace metals can sometimes act as promoters in low concentrations but at higher loadings impact the catalyst activity.

4.5.2 Attrition

Attrition was said by Sasol to be one of the major causes of deactivation in their Fe based catalysts[69]. The mechanical stability required varies depending on the reactor type, with slurry beds requiring high strength in particular. The particle size distribution (PSD) of the catalyst can be affected by attrition in two ways, as detailed in Figure 4.6. Firstly, via abrasion which reduces the size of the particle through the erosion of fines from the surface, producing a bimodal PSD. A secondary form of attrition, fragmentation, occurs when the particle breaks up into several smaller particles, resulting in a broader PSD with a lower mean particle diameter[132]. Smaller particles tend to undergo abrasive attrition due to a larger surface area, whereas larger particles tend to suffer from fragmentation.

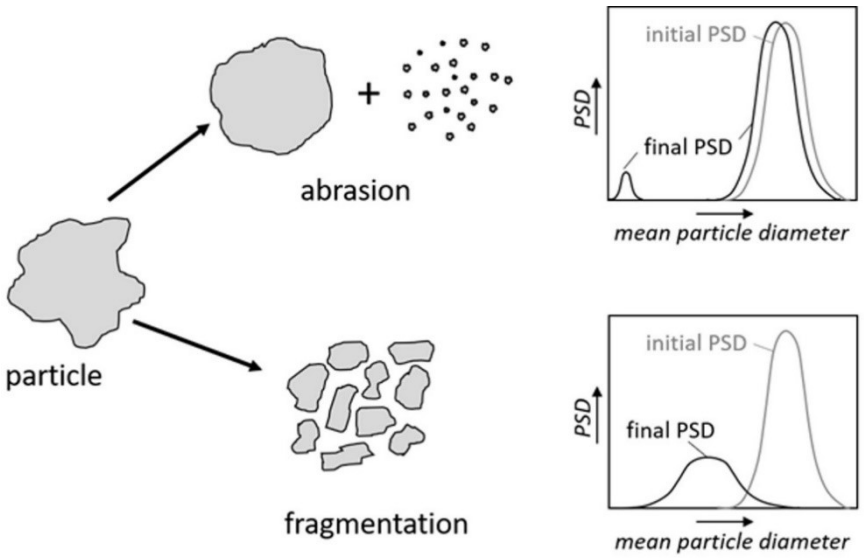


Figure 4.6: Modes of attrition and their effect on the particle size distribution, adapted with permission from C. Patzschke[147].

The change in PSD due to attrition alters the catalysts activity, as discussed in section 4.4, but also the physical behaviour of the particles in the reactor. Small particles can increase pressure drops and pass out of the reactor bed, causing not only a loss of activity, but often significant clean up requirements too. Catalyst supports can be used to avoid attrition, with alumina supports providing more resistance than Si or TiO substrates for catalysts[101].

4.5.3 Sintering

Thermal sintering reduces the catalyst surface area, as the particles agglomerate and fuse together at temperatures below the material melting point. The production of larger particles removes available catalyst surface sites and hence limits the reaction rate. Repeated cycles of reduction and oxidation as well as temperature cycling cause sintering of the particles, with higher temperatures increasing the sinter rate[133]. Like with many catalyst deactivation methods, high water content can exacerbate the process, but certain substrate interactions can increase resistance[134]. Sintering can also be reduced by physical separation or encapsulation of the active species, increasing the temperature required for sintering to take place[135]. Up to a 30% loss in activity has been found for Co catalysts[69]. HTFT Fe catalysts are particularly affected due to the more extreme reaction conditions, with weakly interacting supports and alkali promotors also increasing the sinter rate, due to the increased mobility of the Fe phase[136].

4.5.4 Pore Blocking

Tar and carbon deposits can cover catalysts, blocking pores and active sites. This is predominantly reversible by changing the gas composition and using milder conditions, however repeated regeneration cycles will lead to sintering and are not always effective enough to be industrially viable. Chemisorption and subsequent diffusion of carbon species into the catalyst can give carbide

compounds. Carburisation is mostly seen in Fe catalysts but due to the unknown active phase it is currently unsure how this affects the activity.

4.5.5 Oxidation

Oxidisation changes the catalyst composition, potentially to unreducible oxide phases causing irreversible loss of activity. Fe is much more susceptible to oxidation, with high water concentrations causing surface oxidation[69,137] . Carbide phases are thought to be more resistant than metallic Fe. Co catalyst particles above 5 nm are resistant to oxidation[138]. Some groups also suggest that re-reducing the Co oxide phases is possible under FTS conditions[139]. The extent of oxidation for both metals is dependent on the physical characteristics of the catalyst, with active particle size being the most significant factor. Mn or Al promotion can assist Fe resistance, as can control of the FTS conditions[137].

4.6 Reaction Conditions

Although it is not necessary for the reaction to proceed, FTS typically takes place at high pressure, 20-30 barg, to favour product formation. Exact conditions depend on the reactor type, product requirements and catalyst strength, but are predominately limited by capital and compressor costs. Higher pressures increase the carbon chain length, n, and reduce branching, though it is generally accepted that pressures above 30 bara lead to increased catalyst deactivation through carbon laydown. Studies into atmospheric pressure FTS have yielded comparatively low CO conversion rates[17].

The main process variable for altering the reaction is the temperature. Industrially FTS is split into two temperature groups, LTFT and HTFT. LTFT takes place between 200-240 °C[140] and favours higher chain length alkanes and waxes which can be cracked to produce diesel range hydrocarbons (C_9-C_{25}). Both the main industrial catalysts, Fe and Co, can be used for LTFT, with industrial examples including multi-tubular fixed and slurry beds.

HTFT takes place at 300-350 °C[140] and is not suitable for use with cobalt catalysts. Cobalt has been found to show increasing levels of methane selectivity with increases in temperature, meaning the production of liquid fuels becomes unfeasible at these conditions[66]. Increased carbon laydown on the catalyst can also be an issue at higher temperatures. HTFT produces predominately gaseous, shorter chain and branched alkenes, with some aromatic products[66]. These can be further processed to give petrol range hydrocarbons (C_4-C_{12}) and other petrochemicals. Typically, fluidised beds are used for HTFT[69].

4.7 Preparation of Catalysts

The methods used to synthesise catalysts are varied and widespread but each preparation technique has its own benefits and breakdowns. Synthesis can be split into two main groups, bulk and impregnated catalysts, where the catalyst is respectively active material throughout, or coated onto a support.

Material characterisation then allows the in-depth investigation of the structure and properties of the catalyst.

4.7.1 Co-Precipitation

The precipitation of solid catalyst particles from a mixture of metal solutions by controlling the pH is a well-established method that is popular in both academia and industry due to its ease of production and low cost. Control of the solution conditions, primarily temperature and pH, allows tuning of the particle size distribution. The production of bulk metal-support phases is also a possibility, depending on loadings and precipitation conditions.

It is commonly used to produce Fe catalysts from metal nitrates, allowing a controlled combination of Fe and another metal within the precipitated particle. Sasol uses co-precipitation to produce catalyst for both its LTFT fixed and slurry bed reactors[141].

Co-precipitation of Co catalysts has been undertaken by Khassin *et al*. using Co and Al nitrates, producing a highly dispersed catalyst with low reducibility and activity[142]. Chen *et al*. also found that at low Co loadings their Co-ZnO_2 precipitated catalyst gave a highly dispersed Co phase that had low levels of reduction and formed large amounts of barely reducible Co-Zn compounds. Improvements were seen as the Co loading increased, with Co-Zn compound content levelling off and metallic Co increasing.

4.7.2 Deposition-Precipitation

To circumvent the issue of producing metal-support phases during co-precipitation the deposition-precipitation method was developed. This involves the precipitation of the active phase onto a suspended support, with the precipitation being introduced slowly enough that nucleation only occurs on the support itself. This produces a highly dispersed active phase with the potential for high metal loadings, giving positive results for FTS activity. The choice of support gives flexibility in catalyst porosity, mechanical strength and bed pressure drops amongst others, making this an adaptable method for various reactor and catalyst types. Conditions must be tightly regulated and precipitation induced very gradually to avoid precipitation in the bulk solution. Deposition-precipitation can be used on both Fe and Co catalysts, with small metallic particles of 3-5 nm having been reported[63].

4.7.3 Sol-Gel

The sol-gel method involves producing a colloidal suspension of the metal components which then undergoes gelation through changes in solution composition or conditions. This produces a gel from which the solvent is removed via heat treatment. Including various promotors and modifiers allows control of pore size, surface area and particle size. The microscopic structure is highly dependent on preparation methods but is one of the easiest ways to produce a uniform structure[143].

4.7.4 Eggshell

Eggshell catalysts are used as a response to reducing diffusion limitations in FT catalysts for fixed bed reactors without increasing the bed pressure drop. By coating a near spherical support with a thin layer of active catalyst the diffusion distance is reduced, but the bed porosity maintained. Khodakov *et al*. stated that eggshell catalysts of 2 mm diameter decouple the reactor pressure drop from the characteristic diffusion distance, equivalent to pellets of <0.2 mm[63]. Both Fe and Co are suitable for catalyst production in this way.

There are several ways to fabricate eggshell catalysts, mainly involving the immersion or impregnation of substrate particles in an aqueous solution of the metal. Iglesia *et al*. found that the catalyst shell thickness affected activity and product distribution. This was attributed to the varying ease of diffusion of both reactants to active sites and reactive alkene products that could re-adsorb and react further[144].

4.7.5 Impregnation of Support

The impregnation of porous supports with catalytic precursor is a common method of producing supported catalysts, whereby a solution of the catalytic material is adsorbed onto the substrate. There are several variations on the theme. Wet impregnation involves the soaking of the substrate in an excess of solution before filtering, drying and calcining. This total immersion has the benefit of allowing high loadings in a simple procedure but involves a large amount of liquid waste.

Incipient wetness impregnation removes the waste by adding small amounts of catalyst solution to the dry support until the mixture starts showing signs of stickiness, at which point the pores are filled. The solution is drawn into the pores via capillary action, a more efficient method of drawing the active phase into the pores than diffusion. By knowing the pore volume of the substrate, a calculated loading of catalyst can be added, also making incipient wetness a useful method for the addition of promotors.

A further development is vacuum pore impregnation, where any gas in the substrate pores is removed via a vacuum. The incipient wetness method is then performed whilst still under vacuum, allowing for higher levels of catalyst loading[145].

4.7.6 Other Synthesis Methods

Dozens of other synthesis methods exist, such as chemical vapour deposition, microemulsions, fusion & alloy leaching and plasma spraying to name but a few. To go into detail on all these possible methods would be beyond the scope of this work, but further information can be found in the extensive reviews of Khodakov *et al*. and Rothenburg[63,145].

4.8 Catalyst Choice

For syngas generated from biomass the composition tends to be low in H_2 and have an excess of CO and CO_2. Despite the higher activities of Co catalysts, the WGS activity of Fe catalysts can help to avoid the need for extensive feed pre-treatment. Fe metal is also more widely available and cheaper

than Co, compensating in part for its reduced lifespan. Finally, Fe catalysts allow for more flexibility in reaction conditions and hence product variation. Simple, inexpensive, production methods that allow a relatively narrow PSD are favoured, with impregnation methods that can be scaled up simply.

With these considerations in mind, it has been decided that this research would concentrate on Fe base metals, promoted *via* incipient wetness impregnation. Reaction conditions will be kept in the milder LTFT range at first, both reducing costs and rate of deactivation but allowing for a wider range of conditions in future work.

An unsupported co-precipitated reference catalyst was initially produced to validate the experimental rig and acts as a base for comparison. A novel foamed sol-gel catalyst matrix was then introduced, promoted in the same manner as the reference catalyst. By using a foam matrix, the need for a catalyst support is removed, with the active material making up the whole catalyst structure. The aim of this is to remove any potential catalyst-substrate interactions which can cause catalyst deactivation with use. Finally, by removing the support, recycling the catalyst base material after use is simpler, making the catalyst production cycle greener.

The foamed catalyst must contain both micro and macro pores to allow efficient heat and mass transfer whilst providing a high surface area for the reaction to take place on.

4.9 Reference Catalyst

The reference catalyst, taken from the literature, was used for the initial validation of the experimental set-up. An Fe based catalyst containing 10% wt Zn, with 2% K and 1% Cu promotion, as described by Martinelli *et al*. was chosen[146]. Once the generated catalyst was confirmed as satisfactory it was loaded into the reactor and reduced at 270 °C and 1 atm using syngas at a rate of 6000 $cm^3(STP)h^{-1}g_{cat}^{-1}$. The system was then slowly moved to the operating conditions given in the reference literature of 230 °C and 31.6 barg.

4.9.1 Preparation

The reference catalyst was prepared via co-precipitation of Zn and Fe nitrates in a Zn/Fe atomic ratio of 1:10. The nitrate mixture was added to an excess of ammonium carbonate, $(NH_4)_2CO_3$, buffer solution, acidified to pH 7 with nitric acid. The solution was maintained at pH 7 ± 0.2 throughout the precipitation by feeding additional $(NH_4)_2CO_3$. After the base catalysts are produced, they were promoted with Cu and K. The reagents used during the co-precipitation are detailed below in Table 4.1. Solutions were made to the desired concentrations using de-ionised (DI) water.

During preliminary catalyst production the nitrate and carbonate solutions were added as drops, with the buffer pH being monitored with a handheld pH meter. The buffer solution was maintained at 80 °C and stirred vigorously at a constant rate using a magnetic stirrer. After addition of all the nitrate solution the stirring was stopped and the mixture left to settle for 1 hour. The liquid phase was decanted and the

remaining precipitant washed five times with 0.5 litres of DI water each time, with the mixture being allowed to settle for an hour and the clear liquid phase removed before the next wash.

Table 4.1: Reagents used to generate co-precipitated catalyst.

Reagent	Concentration [M]	Purity [%]	Supplier
$Fe(NO_3)_3.9H_2O$	3.0	100	VWR
$Zn(NO_3)_2.6H_2O$	1.4	98	Alfa Aesar
$(NH_3)_2CO_3$	1.0	100	Lab 3 Limited
$Cu(NO_3)_2.3H_2O$	1.0	99	Acros Organics
K_2CO_3	1.0	99	Alfa Aesar

The resultant precipitant was allowed to settle further overnight and another removal of liquid phase made. The slurry was then dried for 12 hours in ambient air at 120 °C. Once dried the solid catalyst was lightly crushed to reduce particle size and calcined in stagnant air at 350 °C (heating rate 1 °C min^{-1}) for 1 hour. After calcination the catalyst was crushed and sieved to produce particles in the range 212-306 μm. This gives the preliminary catalyst before promotors are added.

4.9.2 Semi-Continuous Co-Precipitation

In order to improve reducibility and reduce the amount of buffer solution required for larger catalyst batches the use of a semi-continuous co-precipitation rig developed by C. Patzschke was investigated[147]. A schematic of the semi-continuous co-precipitation rig developed is given in Figure 4.7. Alterations were made to include the use of a more accurate pH meter and an inline mixer designed to allow for rapid inline mixing of the two streams. The rapid inline mixing reduced the residence time of the fluids at precipitating conditions and ensured good mixing between the reagents, both acting to control the PSD.

A proportional-integral-derivative (PID) controller written in Agilent Vee monitored the pH of the buffer solution and controls two peristaltic pumps. During normal operation one pump is set to a standard flowrate and the other solution flow is managed by the PID controller to maintain a set pH value. Both feed solutions were also on hot plates and in this case, maintained at the same temperature as the buffer solution.

The semi-continuously co-precipitated mixture was decanted, washed and crushed in the same manner as the batch precipitated catalyst.

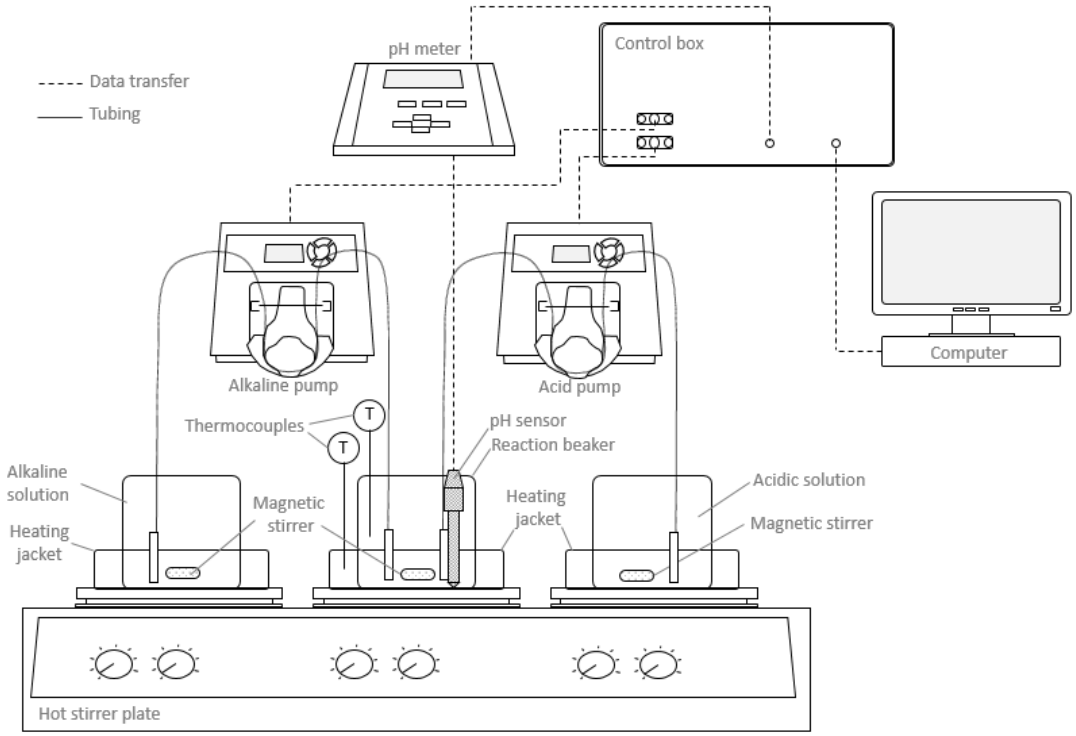


Figure 4.7: Schematic of the co-precipitation rig, used to prepare larger batches of catalyst. Reproduced with permission from C. Patzschke[147].

4.9.3 Promotion

After calcination, 50% of the precipitated catalyst was promoted with Cu and K via incipient wetness impregnation to atomic ratios of Cu:Fe = 0.01 and K:Fe = 0.02. Following each impregnation step the catalyst was dried in ambient air at 120 °C for 12 hours, before being calcined in stagnant air at 400 °C for 4 hours (heating rate 1 °C min^{-1}).

4.10 Foamed Catalyst

The foamed Fe catalyst is based on an unsupported, highly porous, Fe_2O_3 material initially developed for chemical looping. Transition metals show good activity for both FTS and chemical looping, with both reactions also requiring high levels of reduction, maintained activity and mechanical strength[148]. The Fe_2O_3 foam was produced using a foamed-gelcasting method, which, to the best of the authors knowledge, is thought to be novel in FTS catalysis.

4.10.1 Foamed-Gelcasting

The foamed-gelcasting method was based on preliminary work done at ICL by Zheng *et al*., combining gelcasting and direct foaming. Several catalysts, pre-made to the method described below and summarised in Figure 4.8, were kindly provided by Zheng *et al*. for testing under FT conditions.

Fe_2O_3 powder was first introduced into solution with DI water, dispersant, a cross linker and a solution of monomers. Bubbles were generated by the subsequent addition of foaming agent, the solution was stirred vigorously to aid regular bubble size distribution before the addition of a thickening agent,

initiator and a catalyst which cause the monomers to form a cross-linked polymer gel. This gel structure stabilises the foam, allowing the porosity to be maintained during drying. Before the gel sets the foam was poured into a flexible silicone mould. Once set it was removed, calcined and crushed.

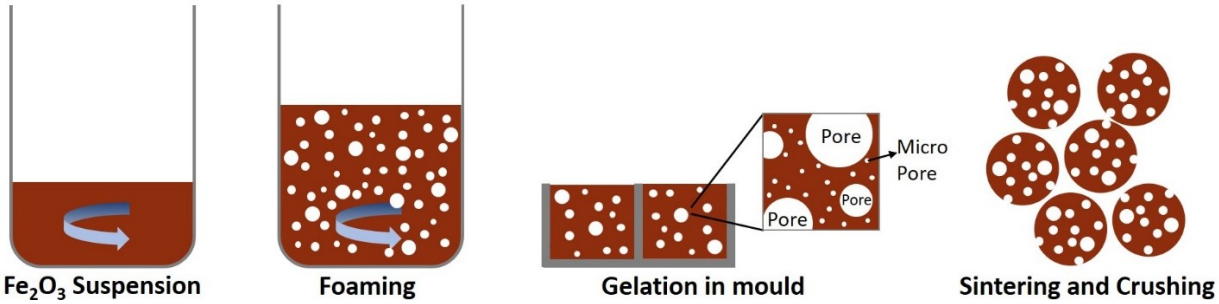


Figure 4.8 Schematic of preparation method for foamed catalysts. Adapted with permission from Zheng et al. (in press).

Various Fe_2O_3 foams were generated via this method. Varying particle size distributions were generated through graded sieving. Two of these distributions, 106-300 µm and 1000-1250 µm, were taken to investigate possible mass transfer effects, and two calcination temperatures, 950 °C and 1350 °C, to investigate the effects on catalyst structure. The reagents used are listed below in table 4.2..

After calcination the foamed catalysts were promoted in the same manner as the co-precipitated catalyst, described in section 4.9.3.

Table 4.2: Reagents used in foamed catalyst production.

Use	Reagent Used
Bulk Material	Fe_2O_3 Powder
Dispersant	Ammonium Citrate Tribasic
Monomer	N-Hydroxyethyl Acrylamide
Cross Linker	N, N'-Methylenebis(acrylamide)
Foaming Agent	Sodium n-Dodecyl Sulphate
Thickening Agent	Polyethylene Glycol
Catalyst	N, N, N', N' -Tetramethyldiaminomethane
Initiator	Ammonium Persulfate

4.11 Nomenclature

Throughout the remainder of this work the various catalysts being tested are referred to using abbreviations. Table 4.3 provides a list of the abbreviations used and a description of the catalyst being referred to.

Table 4.3: Descriptions and abbreviations of catalysts used.

Abbreviation	Catalyst description
PreCat	Unpromoted Fe:Zn co-precipiated catalyst, atomic ratio 10:1, particle size 212-306 μm.
Cat2K	Promoted Fe:Zn:Cu:K co-precipitated catalyst, atomic ratio 100:10:1:2, particle size 212-306 μm.
950-106-P	Foamed catalyst, calcined at 950 °C, particle size 106-300 μm, promoted at Fe:Cu:K atomic ratio of 100:1:2.
950-106-U	Foamed catalyst, calcined at 950 °C, particle size 106-300 μm, unpromoted.
950-1000-P	Foamed catalyst, calcined at 950 °C, particle size 1000-1250 μm, promoted at Fe:Cu:K atomic ratio of 100:1:2.
950-1000-U	Foamed catalyst, calcined at 950 °C, particle size 1000-1250 μm, unpromoted.
1350-106-P	Foamed catalyst, calcined at 1350 °C, particle size 106-300 μm, promoted at Fe:Cu:K atomic ratio of 100:1:2.
1350-106-U	Foamed catalyst, calcined at 1350 °C, particle size 106-300 μm, unpromoted.
1350-1000-P	Foamed catalyst, calcined at 1350 °C, particle size 1000-1250 μm, promoted at Fe:Cu:K atomic ratio of 100:1:2.
1350-1000-U	Foamed catalyst, calcined at 1350 °C, particle size 1000-1250 μm, unpromoted.

5 Catalyst Characterisation

This chapter describes the material characterisation of the catalysts produced in chapter 4, performed in order to determine relationships between preparation methods, material chemical and physical properties, and catalyst behaviour in the FT reactor. Properties such as chemical composition, pore size distribution, surface area and particle size are reviewed for each of the catalysts tested.

5.1 Methodology

5.1.1 Crystalline Phase Composition by X-ray Diffraction

Chemical phase composition analysis was performed on the crushed catalysts using powder X-ray diffraction (XRD). The diffraction effect of a powered crystalline substance on a monochromatic beam of X-rays result in constructive interference of the diffracted X-rays. Measuring the extent of diffraction given at a range of beam angles, 2θ, generates diffraction peaks. These peaks can be used to calculate the d-spacings of the sample and hence identify the element.

An PANalytical, X'Pert PRO instrument was utilised, using Cu-Kα radiation of wavelength λ = 0.1541 nm, generated at 40 kV and 40 mA. The standard diffraction Bragg-Brentano geometry was used, as illustrated in Figure 5.1 below. All samples were scanned in a 2θ range of 10° to 80° with a step size of 0.05°. Due to the small sample sizes available, samples were loaded on a graphite disk slide mount.

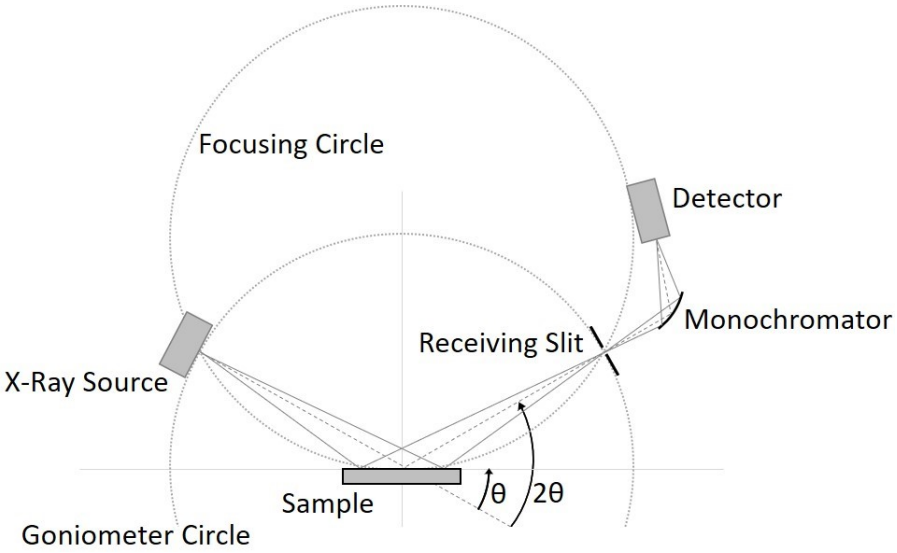


Figure 5.1: Schematic of the Bragg-Brentano geometry used.
Adapted from schematic by C. Patzschke[147] based on reference 149.

5.1.2 Surface Area and Pore Size by N_2 Adsorption

Physical N_2 adsorption experiments at 77 K were used to determine material surface area, pore size distribution and cumulative pore volume of the catalysts. Approximately 0.2 g of catalyst per sample

was first degassed overnight under a constant flow of helium at 120 °C to remove any adsorbed species from the surface before being loaded into a Micrometrics TriStar 3000 instrument.

The sample tubes are evacuated before being cooled with liquid N_2 and gradually filled with N_2 at 77 K, by recording the sample tube pressure an adsorption isotherm is produced that can be used to calculate the BET surface area, S_{BET}, via the Brunauer, Emmett and Teller (BET) method[150]. BET surface area analysis has limitations, particularly at very low or high P/P_0 values, but also through the assumption that adsorption occurs as a monolayer. In reality, N_2 adsorbs partially as multilayers, due to adsorbent-adsorbate interactions[151]. This introduces error and deviations from the true surface area, which will be accounted for in the analysis of the BET data.

The adsorption isotherms are also used to calculate the cumulative pore volume of pores between 1.7-300 nm, V_{pore}, and the surface area of the pores, S_{pore}, using the Barrett, Joyner and Halenda (BJH) method[152]. The average pore diameter, $\bar{d}_{pore}$, is then calculated by $\bar{d}_{\mathrm{pore}} = 4\,V_{\mathrm{pore}}\,/S_{\mathrm{pore}}$. Again, limitations occur due to imperfect filling of the pores with N_2, resulting from variations in pore diameters and irregular pore shape.

Instrumental measurement error for S_{BET}, V_{pore} and S_{pore} is estimated using the standard deviation of three repeated measurements of continuously co-precipitated catalyst from the same batch.

5.1.3 Surface Area and Pore Size by Mercury Intrusion Porosimetry

The combination of micro and macro pores in the foamed catalysts means that N_2-adsorption analysis is unsuitable for these catalysts, as an alternative mercury intrusion porosimetry (MIP) was instead used.

Pore diameter and volume are determined by forcing material into the catalyst pores at pressure. Since mercury is non-wetting the pore diameter, d_P, can be calculated as a function of the applied pressure and surface tension using equation 5.1, the Washburn equation which assumes straight, cylindrical pores.

$$d_P = \frac{-4\gamma\cos\theta}{P_g} \qquad 5.1$$

The measurements are taken under vacuum at 20 °C, giving a surface tension, γ, of 485 dynes cm^{-1}. The contact angle between the mercury and the solid, θ, is taken to be 130°, a value commonly used when the angle is not specifically known[153]. P_g is the externally applied gas pressure.

A Micromeritics AutoPore IV 9500 was used to perform MIP analysis on the foamed catalysts. Due to the destructive nature of MIP analysis and limited sample availability, no repeat measurements were performed and hence the measurement error is not quantified. Since MIP is not able to discern between interparticle and interstitial porosity, a proportion of the pores seen will be due to voids between the particles as they are packed into the sample tube. Pore sizes above the particle radius, r_p, are taken as interstitial porosity.

5.1.4 Scanning Electron Microscopy

The surface structure of the catalysts was studied using scanning electron microscopy (SEM) on a Zeiss Gemini 1525. A focused beam of electrons is used to scan the surface of the sample. The interactions between the sample and the electrons can be detected as scattered electrons and X-rays and used to create images of the sample surface.

Samples were loaded onto the SEM measurement tab using double sided carbon tape before being sputter coated with approximately 5 nm of gold to improve conductivity.

5.2 Results

5.2.1 XRD

5.2.1.1 Co-Precipitated Catalysts

For the co-precipitated PreCat and Cat2K XRD analysis shows peaks for the α-Fe_2O_3 (hematite) phase as shown in Figure 5.2. The number of peaks and their intensity increases after promotion and secondary calcination, with some $ZnFe_2O_4$ peaks also becoming apparent. This increase in crystallinity after promotion was also reported by Martinelli *et al*. and is possibly due to the secondary calcination step causing additional sintering and crystallisation, resulting in a stronger reflection.

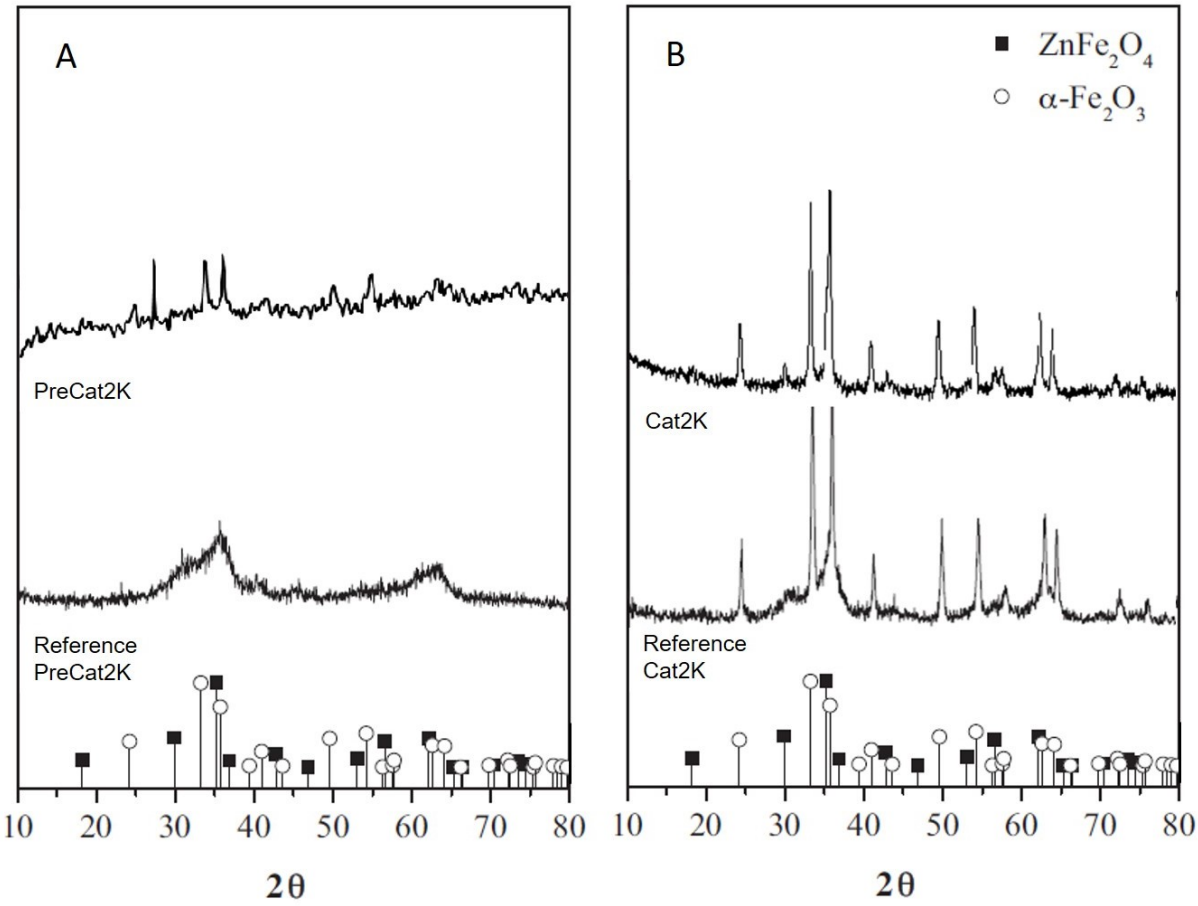


Figure 5.2: XRD plot with arbitrary intensity y-axis of (A) un-calcined catalyst precursor and (B) calcined, promoted catalyst compared to reference results from the literature[146] and reference XRD patterns for α-Fe_2O_3 and $ZnFe_2O_4$.

The peaks seen in Cat2K corelate well with those quoted in the literature for the reference catalyst, suggesting a similar phase composition, predominately α-Fe_2O_3, as expected[146].

5.2.1.2 Foamed Catalysts

XRD of the promoted foamed catalysts, given in Figure 5.3 and Figure 5.4, also show a clear crystalline α-Fe_2O_3 phase, with no other iron oxides phases seen. Peak numbers and intensity are very similar for all the promoted catalysts, indicating that the calcination temperature does not affect the base catalyst phase or crystallinity. It is not possible to say for certain what has caused the baseline shift seen in the trace for 950-106-P. However, since the peak locations and intensities remain as expected for α-Fe_2O_3, it is thought that this variation is due to the sample not being completely level within the mount.

Promotion makes little difference to the phase of the 1350 °C foamed catalyst, as shown by the very similar traces given in Figure 5.5 for 1350-106-U and 1350-106-P. The higher initial calcination temperature means the crystalline hematite phase is already formed before promotion. The secondary, lower temperature, calcination causes no detectable physical variations. The same is not found to be true for the 950 °C foams, shown in Figure 5.6, where the unpromoted 950-106-U catalyst shows additional peaks that do not correspond with α-Fe_2O_3, nor with any substance in the Hi-Score identification library available. The promotion and additional calcination stage, despite its significantly lower temperature, appears to age the catalyst and give the α-Fe_2O_3 phase seen throughout the 1350 °C samples. Similar behaviour is seen for the larger particle sizes for both temperatures.

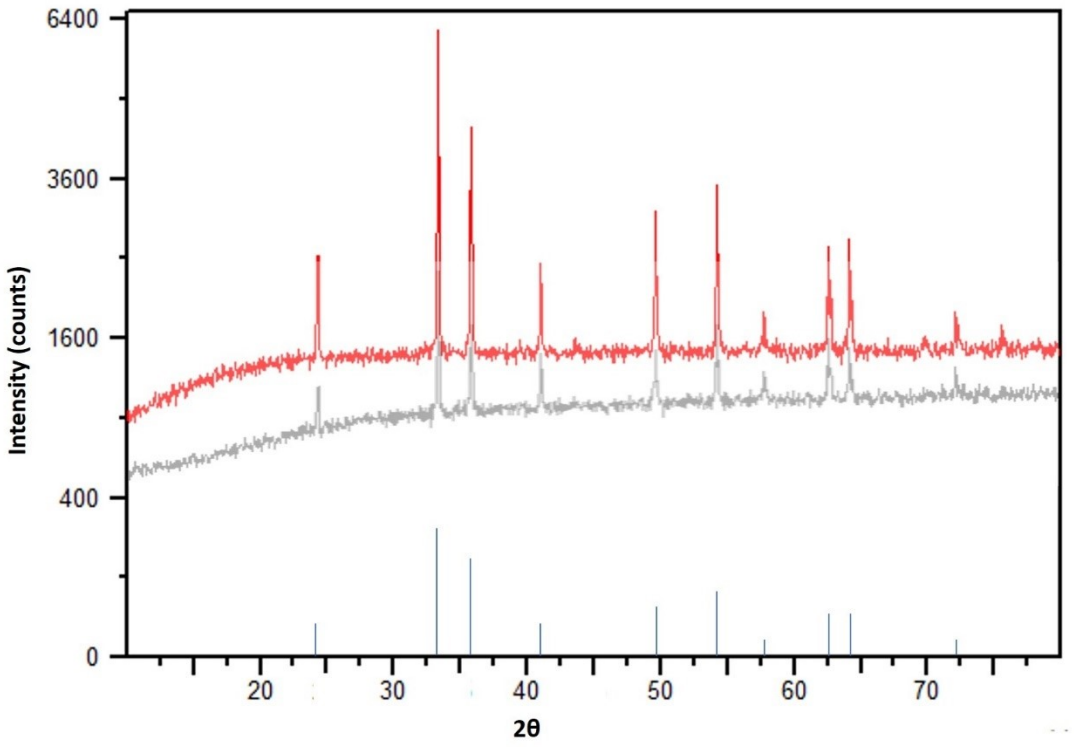


Figure 5.3: XRD of foamed catalyst 950-106-P (red) and 1350-106-P (grey) and α-Fe_2O_3 pattern (blue).

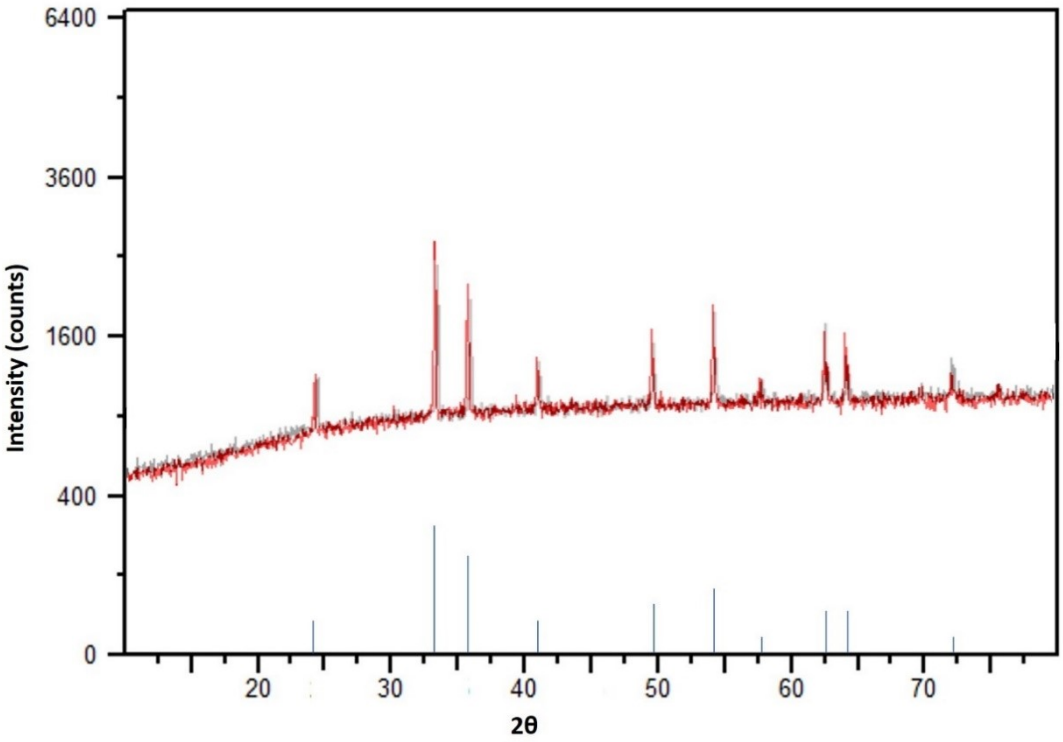


Figure 5.4: XRD of foamed catalyst 950-1000-P (red), 1350-1000-P (grey) and α-Fe_2O_3 pattern (blue).

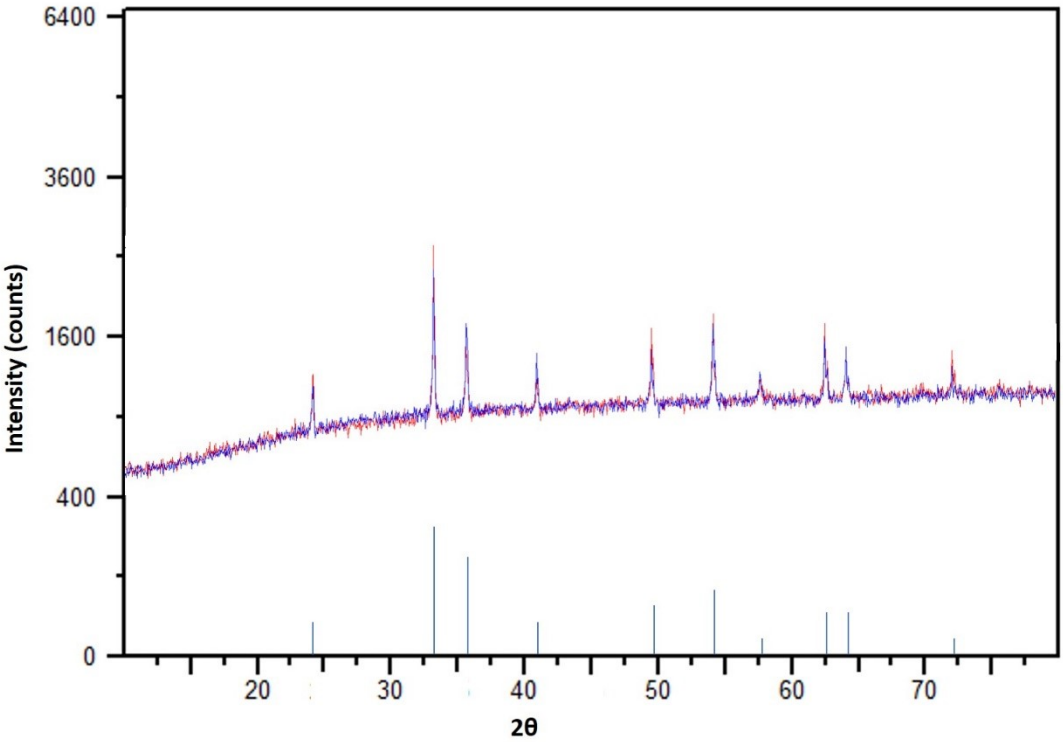


Figure 5.5: 1350-106-U (red), 1350-106-P (blue) and α-Fe_2O_3 pattern.

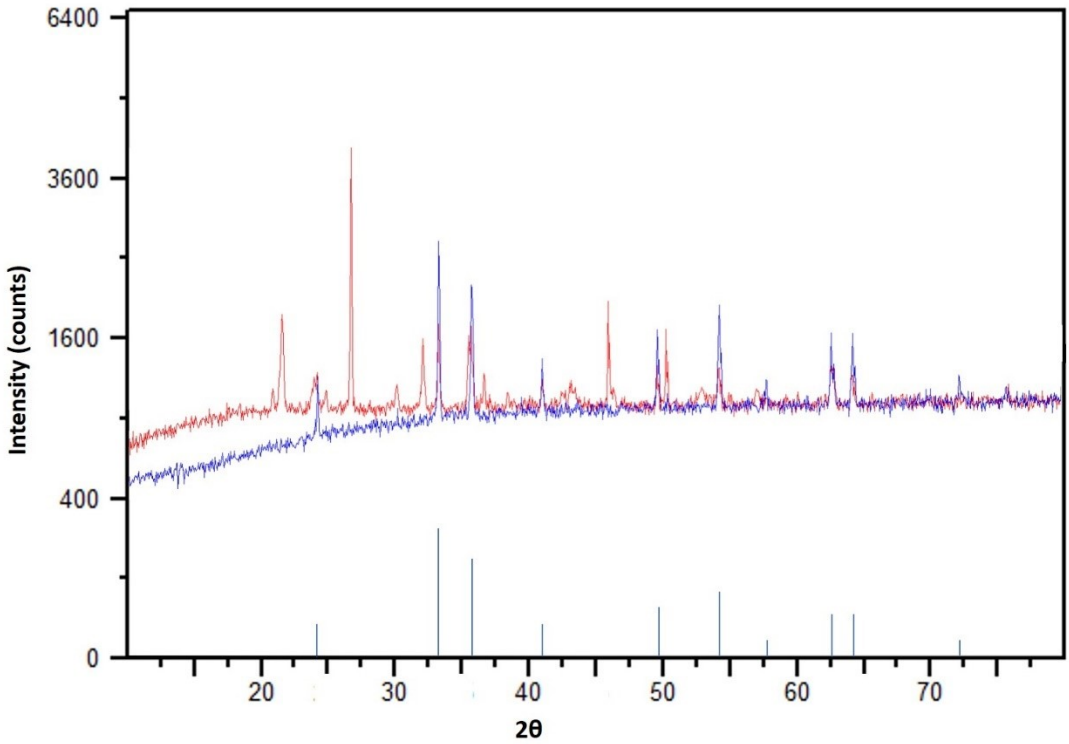


Figure 5.6: 950-106-U (red), 950-106-P (blue) and α-Fe_2O_3 pattern.

5.2.2 BET – Co-Precipitated Catalysts

From Table 5.1 it can be clearly seen that the BET surface area and BJH pore volume are significantly lower for the batch co-precipitated Cat2K samples compared to the continuously co-precipitated catalyst. This is thought to be due to the reactants being added in a less controlled manner during batch co-precipitation, resulting in a solution of varying pH and hence an altered state of super-saturation – the driving force of precipitation. It is known that the pH and hence degree of super-saturation of the solution can affect the physical properties of the particles precipitated[154]. Batch co-precipitation was therefore rejected as a preparation method for the reference catalyst after initial BET testing.

Table 5.1: Summary of BET surface area, BJH pore volume and pore diameter for co-precipitated catalysts.

Sample	S_{BET} (m^2g^{-1})	V_{pore} (cm^3g^{-1})	S_{pore} (m^2g^{-1})	$\bar{d}_{pore}$ (nm)
PreCat - literature[146]	159	0.25	208*	4.8
Cat2K - literature[146]	76	0.21	93*	9.0
Cat2K – batch	7.5	0.037	15	10.1
PreCat – continuous	45 ± 0.8	0.24 ± 0.0004	54 ± 0.3	15.3 ± 0.1
Cat2K – continuous	47 ± 0.8	0.19 ± 0.0004	59 ± 0.3	13.3 ± 0.1

* Calculated from V_{pore} and $\bar{d}_{pore}$ values using $S_{\mathrm{pore}} = 4\,V_{\mathrm{pore}}\,/\bar{d}_{\mathrm{pore}}$.

Both co-precipitation methods give lower surface areas than the catalyst from the reference literature[146], but a comparable pore volume. The larger pore diameters give this volume with a smaller surface area. Figure 5.7 shows similar pore size distributions for PreCat and Cat2K.

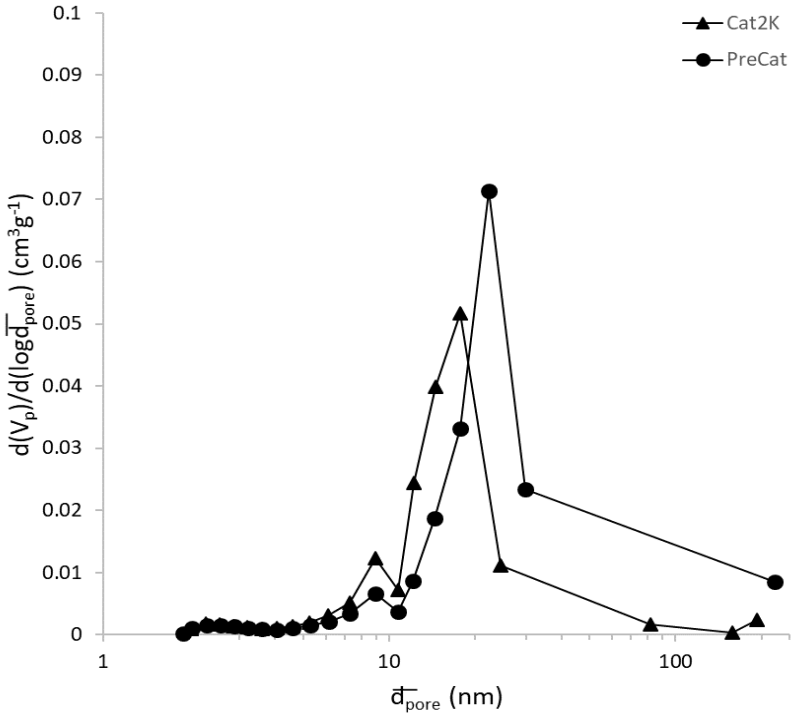


Figure 5.7: Pore size distributions of PreCat and Cat2K co-precipitated catalysts.

The continuously co-precipitated catalyst created is not a complete match with that given in the reference paper, however the method was followed closely with several repeats made, giving similar results each time. It was decided to use the continuously co-precipitated catalyst in the experimental rig in its current form as it can perform its function as a validation test.

5.2.3 MIP – Foamed Catalysts

MIP analysis indicates that the foamed catalysts have higher pore volumes and diameters than the co-precipitated catalyst, with significant levels of porosity, as shown in Table 5.2. Calcination temperature appears to influence the pore size and surface area, with the catalysts calcined at 950 °C having smaller pore diameters and a higher pore surface area. Within the catalysts calcined at 950 °C, the pore diameter also increases once promoted, resulting in a corresponding decrease of available surface area and pore volume. This promotion effect is not seen in the catalysts calcined at 1350 °C, with pore size, surface area and volume remaining approximately constant. It is speculated that the higher calcination temperature allows for more structural changes to take place in the catalyst, increasing crystal size and correspondingly reducing the number of micro pores present. After promotion the catalysts were calcined again, but at a lower temperature of 400 °C. This secondary calcination is unlikely to have caused significant change to the catalyst structure, but the promotors themselves could block the smaller pores, resulting in the increased average pore size seen. Since the

pores are already larger in the batch calcined at1350 °C the promotors do not cause any blocking, or loss of surface area.

Table 5.2: MIP results for foamed catalysts

Catalyst	V_{pore} [cm^3g^{-1}]	S_{pore} [m^2g^{-1}]	$\bar{d}_{pore}$ [nm]	Porosity
950-106-P	0.56	0.072	30648	0.55
950-106-U	0.98	1.998	1960	0.78
950-1000-P	0.29	0.17	6685	0.39
950-1000-U	0.96	2.040	1890	0.84
1350-106-P	0.64	0.021	121162	0.80
1350-106-U	0.53	0.018	116061	0.72
1350-1000-P	0.38	0.030	51174	0.57
1350-1000-U	0.33	0.026	51194	0.34

This is confirmed by MIP pore distributions shown in Figure 5.8, where the unpromoted catalysts calcined at 950 °C, 950-106-U and 950-1000-U have a bimodal pore size distribution, with peaks seen for small pores at 300 nm and at 90000 and 45000 nm respectively. The 300 nm peak relates to the micro pores inherently in the structure, whereas the peaks at 90000 and 45000 nm are in the region of the smaller particle diameter and will be a result of surface cracks and interstitial spaces as well as ‘bubbles’ within the larger catalyst particles generated through the foaming process. These ‘bubbles’, caused by the gas produced during the foam generation, are broken during crushing of the catalyst into particles of a comparable size to the ‘bubbles’ themselves.

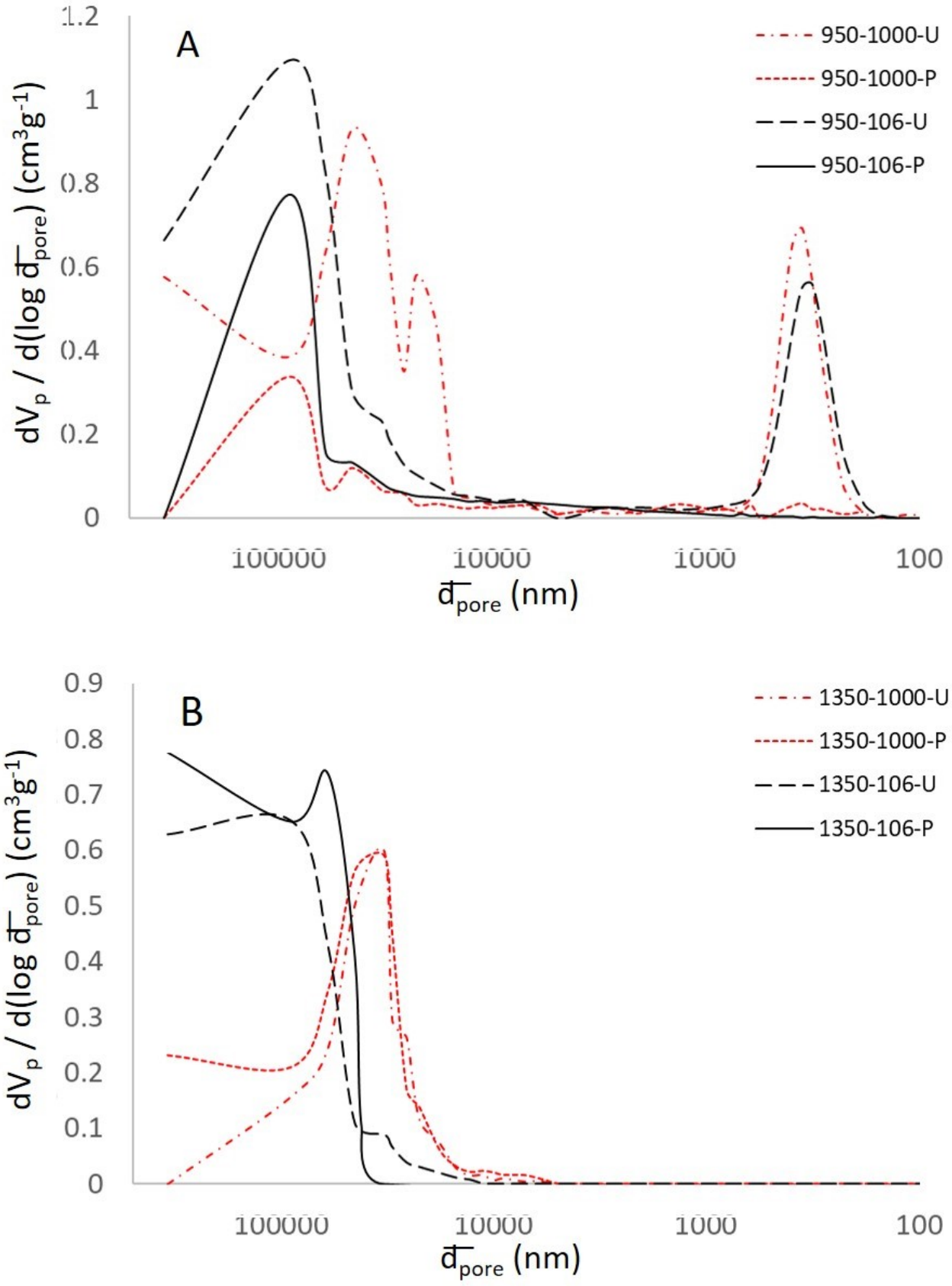


Figure 5.8: MIP pore size distribution for catalysts calcined at (A) 950 °C and (B) 1350 °C.

On promotion the small pore peak disappears for 950-106-P and 950-1000-P, again indicating that these small pores are blocked by the promoters.

For the catalysts calcined at 1350 °C no bimodal pore size distribution is seen, with only a peak for the interstitial spaces and 'bubbles' apparent. Promotion of these catalysts doesn't affect the pore size distribution, correlating well with the consistent S_{pore} and V_{pore} seen in Table 5.2.

5.2.4 SEM

SEM images of PreCat are shown in Figure 5.9, showing the irregularly shaped fractured particles. The smaller particles visible are catalyst dust caused by attrition, the smaller particles preferentially stick to the carbon tape due to their lower mass and volume. The particle surface initially appears smooth, but on magnification it appears uneven with fine grains and a microporous structure on the sub-micrometre scale. No macro pores are apparent, corelating with the BET results in section 5.2.2.

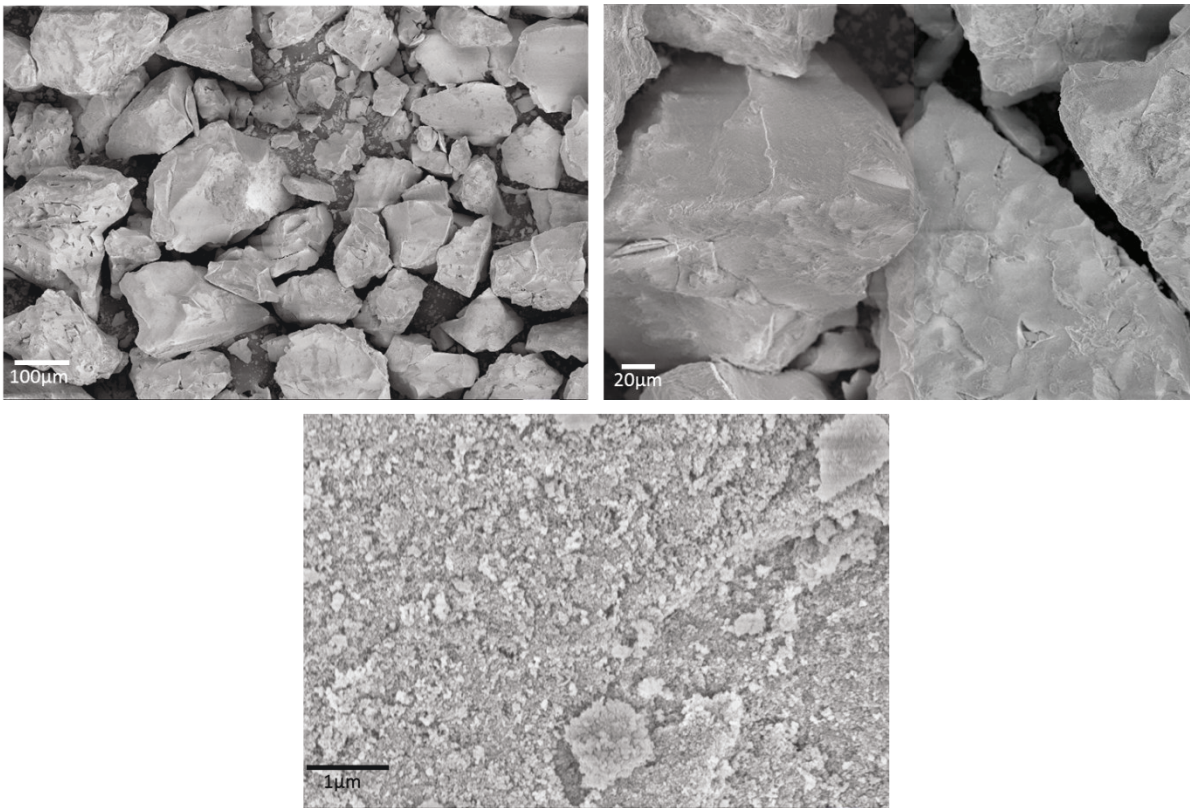


Figure 5.9: SEM images of PreCat

The SEM images of Cat2K in Figure 5.10 show that the particles do not alter noticeably with promotion. Similar irregular shapes are seen at lower magnification, with a wider spread of particle sizes than for PreCat. This spread is thought to be due to the SEM sample preparation method favouring smaller particles and is not representative of the PSD of the entire batch. Upon further magnification the microporous structure from PreCat is seen to be maintained.

Unfortunately, energy-dispersive X-ray analysis (EDX) was not available for these samples, hence the surface distribution of promotors cannot be discussed.

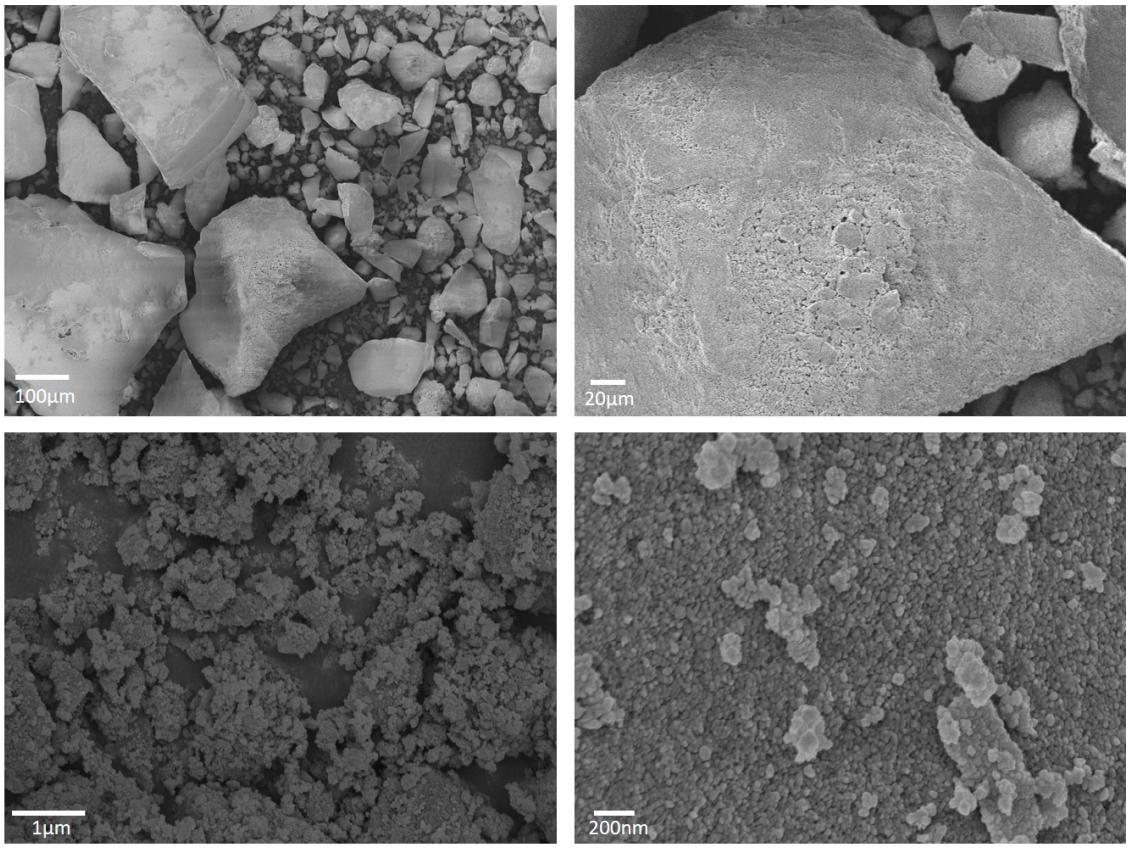


Figure 5.10: SEM images of Cat2K.

Figure 5.11 is a series of SEM images of (A) 950-106-U and (B) 1350-106-U, showing the highly porous particles with large, uniform, partially spherical pores generated during the foaming process and then fractured as the particles are crushed to size. Medium pores occasionally interconnect the larger pores, providing paths for mass transfer within the particle. On magnification the effect of calcination temperature on the macropore surface becomes apparent. For 950-106-U a rough surface is seen, with a clear microporous structure apparent at the maximum magnification, confirming the bimodal pore size distribution seen with MIP analysis. This microporous surface structure is not present in the 1350-106-U sample, where the macro pore surface is smooth and a streaked surface seen. This lined appearance is typical of glasses, indicating that the surface has sintered sufficiently for the nanometre scale grains to coalesce and the corresponding microporous structure to be lost.

Promotion of 950-106-U makes little visual difference to the structure, the surface morphology is similar and the micro pores still visible at higher levels of magnification. Blocking of these pores with promotor is not visible in Figure 5.12, however at the low Cu and K loadings on 950-106-P it is not expected to be. Due to equipment availability SEM images of 1350-106-P were unable to be produced. However, as 1350-106-U shows no microporous structure and at the same promotor loadings 950-106-P

does not appear to have pore blockage, it is unlikely that the promotion caused any significant structural changes to 1350-106-P.

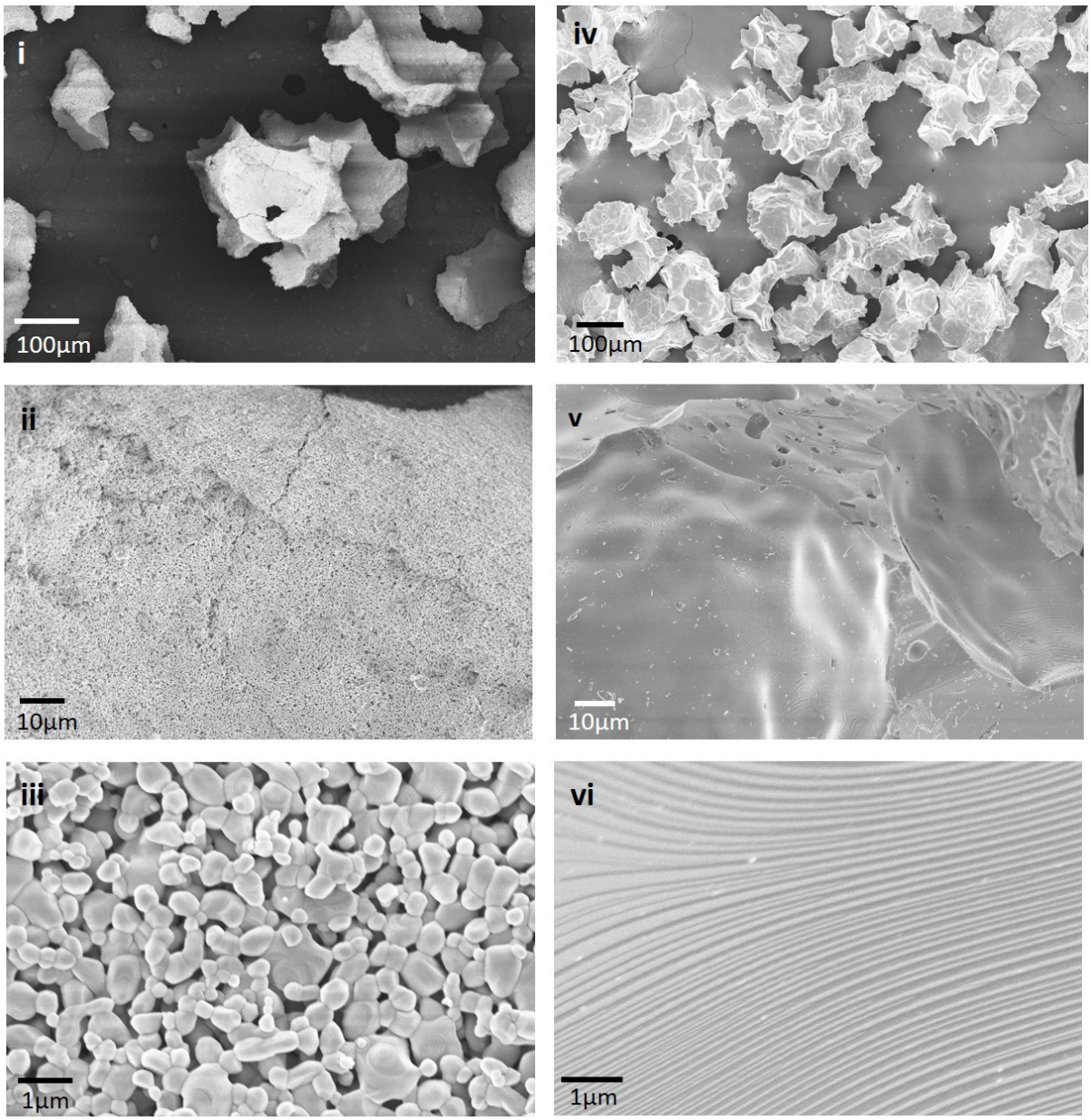


Figure 5.11: SEM images of 950-106-U (images i-iii)and 1350-106-U (images iv-vi) showing the effect of calcination temperature on the catalyst surface. The dark background in the first image of both A and B is the carbon backing tape.

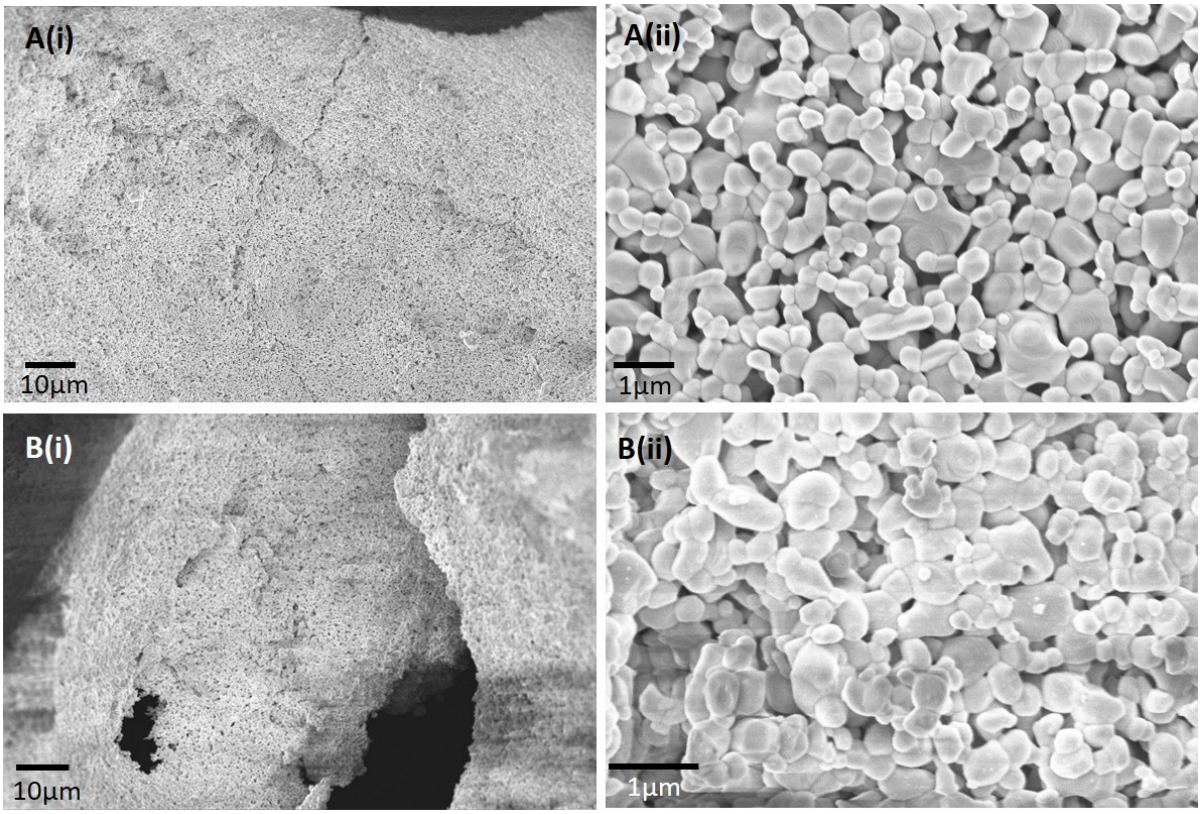


Figure 5.12: SEM images of A(i-ii) 950-106-U and B(i-ii) 950-106-P.

5.2.5 Grain size measurement

Individual grain diameters of the foamed catalyst samples calcined at 950 °C, shown in Figure 5.12 A(ii) and B(ii), were measured using an open source image analysis programme, ImageJ. The grain sizes for the co-precipitated catalysts in Figure 5.9 and Figure 5.10 are too small to give a suitable resolution with SEM to measure accurately. These are instead taken to have diameters of approximately 0.1-0.2 µm. The glassy nature of the 1350 °C foamed catalysts mean no grain boundaries are seen and hence the grain sizes cannot be analysed.

The PSD for a randomly selected sample of 50 grains of both 950-106-U and 950-106-P, as shown in Figure 5.13, were found to best fit a log-normal distribution. From this the mean grain diameter, $(d_p)_m$, of 950-106-U was determined to be 0.45 µm, with 95% confidence of falling in the range 0.40 µm < $(d_p)_m$ < 0.50 µm. The standard deviation for this sample is 0.35. For 950-106-P $(d_p)_m$ was found to be 0.55 µm, with 95% confidence of being in the range 0.50 µm < $(d_p)_m$ < 0.59 µm. The standard deviation is 0.30 for the promoted catalyst.

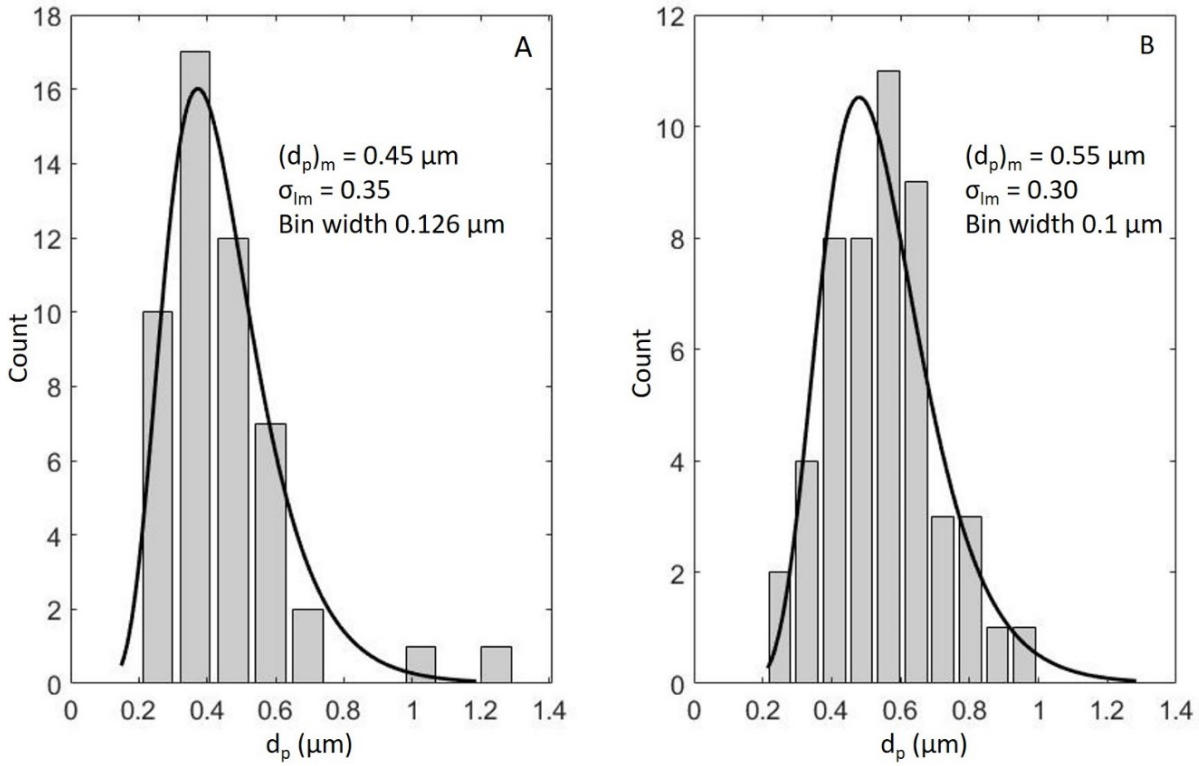


Figure 5.13: Distributions of diameters for 50 randomly selected particles of (A) 950-106-U and (B) 950-106-P, determined from Figure 5.12.

This slight increase in grain size with promotion suggests that the additional calcination time has caused grain amalgamation and growth, altering the microporous structure and hence surface area of the catalyst.

5.3 Conclusions

Thorough characterisation of the catalyst particles via various standard analytical techniques is a necessary initial step in understanding catalyst properties. This in turn can enable catalyst tuning to maximise desired behaviours and activity.

XRD analysis confirmed all the catalysts tested were composed of predominantly hematite, α-Fe_2O_3. The co-precipitated catalysts also contain smaller amounts of $ZnFe_2O_4$, correlating well with the composition and crystallinity of the reference catalyst. Promotion, and the associated additional calcination period, increased crystallinity of the co-precipitated catalysts. The higher initial calcination temperatures of the foamed catalyst appear to have imported a degree of crystallinity on the unpromoted catalysts not seen in PreCat. Additional calcination following promotion had negligible effect on the foams initial calcined at 1350 °C, which show a strongly crystalline α-Fe_2O_3 both before and after promotion. However, on the unpromoted 950 °C foams other crystalline phases are seen in addition to α-Fe_2O_3. The additional calcination period after promotion appears to age the material, and a solely crystalline α-Fe_2O_3 structure is seen for the promoted 950 °C catalysts.

The effect of the physical structure of the surface morphology of the catalysts was then investigated. N_2 physisorption experiments at 77 K on the continuously co-precipitated catalysts suggest a microporous structure with a BET surface area, S_{BET}, between 45-47± 0.8 m^2g^{-1}. Promotion causes a drop in BJH pore volume, V_{pore}, from 0.24 to 0.19 cm^3g^{-1} for a similar pore size distribution, suggesting the promotors are blocking some pores. Average pore diameters, $\overline{d}_{pore}$, remain similar for both PreCat and Cat2K at 15.3 ± 0.1 nm and 13.3 ± 0.1 nm respectively, albeit both are more than 40% larger than the reference value. The batch co-precipitated catalyst had a significantly lower S_{BET} of 7.5 m^2g^{-1}, this large deviation from the literature value meant it was not pursued as a viable production method.

The larger voids seen in the foamed catalysts mean BET analysis was unsuitable for use on these samples. MIP analysis showed the foamed catalysts all had higher V_{pore}, between 0.29 and 0.98 cm^3g^{-1}, but significantly smaller pore surface areas, S_{pore}, of less than 2 m^2g^{-1} due to larger pore diameters and interstitial voids. For the foamed catalysts pore size is dependent on calcination temperature, with peaks of 300 nm and 45-90 μm, representing the microporous surface and interstitial spaces, seen at the lower calcination temperature of 950 °C. For calcination at 1350 °C the smaller pores were no longer present. As with the co-precipitated catalysts, promotion appeared to remove the smaller pores, significantly reducing S_{pore} and removing the bimodal distribution seen for the 950 °C catalysts. The loss of pores in the region of 300 nm for the 1350 °C foams is thought to be due to changes in the catalyst structure itself rather than blocking by promotors, as suggested by the increased crystallinity seen in the XRD results for 950-106-P.

SEM imaging confirms the microporous structure seen in all the unpromoted catalysts, bar those calcined at 1350 °C, and clearly shows the larger, microporous, spherical voids generated as part of the foamed catalyst production. The SEM images were in concurrence with BET findings that the surface structure of co-precipitated catalysts does not alter significantly with promotion. For both PreCat and Cat2K samples irregular shaped particles with rough, microporous surfaces are seen. Grain sizes were estimated to be approximately 0.1-0.2 μm.

The foamed catalysts all show the macropores created by the bubbles generated during production. The foams calcined at 950 °C also show a microporous structure, with mean grain sizes, $(d_p)_m$, growing from 0.45 μm to 0.55 μm following promotion. This increase in grain size correlates with the loss of smaller pore diameters after calcination seen with MIP analysis for the 950 °C foams. This microporous surface is not seen on the 1350 °C foams, where the surface is glassy with no apparent grain boundaries. Again, this agrees with the significantly lower pore surface area, S_{pore}, seen in the MIP results.

These differences in structure and pore size of the co-precipitated and foamed catalysts will affect both the available active sites and mass transfer through the particle, an important factor in fixed bed reactors which can be diffusion limited.

6 Fischer-Tropsch Reactions Over a Fixed Bed

This chapter presents an experimental study of reaction rates and product distributions of CO_2 containing syngas over various iron oxide FT catalysts in a fixed bed reactor, as described in section 3.2. Initially the reactor rig was validated by running with the co-precipitated reference catalysts, PreCat and Cat2K, before testing of the novel foamed catalysts was performed.

The experimental equipment was run at low temperature FT conditions of 230 °C and 30 barg. Product analysis was performed using a FTIR as well as both gas and liquid GC-MS/FID.

6.1 Methodology

The design and build of the apparatus utilised in this investigation is described in chapter 3. The following analysis methods were used to characterise the products generated.

6.1.1 Fourier Transform Infrared Spectroscopy

Online Fourier Transform Infrared Spectroscopy (FTIR), as shown in Figure 6.1, was used to continually analyse the composition of the gas exiting the reactor. This technique determines the concentration of various species in a mixed gas stream by measuring the absorbance of infrared wavelengths. By analysing the absorbance over a range of wavelengths the species present and concentration can be determined by comparing against known calibrations and absorbances. A series of mirrors increase the path length of the IR through the gas sample cell to increase achievable absorbance with small sample volumes, reducing measurement response times.

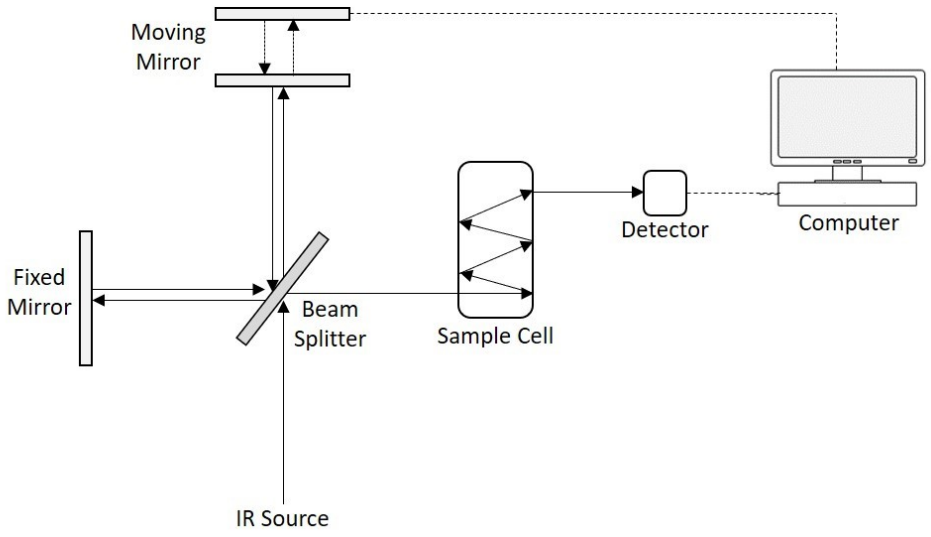


Figure 6.1: Schematic of gas phase FTIR.

A MKS MultiGas 2030 FTIR was used, with a 5.11 m effective path length and 1 Hz sampling rate. The spectral resolution was from 0.5 cm^{-1} to 128 cm^{-1}. Standard multi-point calibration curves were taken with known concentrations of a range of short chain alkanes and alkenes as well as CO and CO_2 to create a unique calibration 'recipe' of similar composition and concentration as expected to be seen

in the reactor off-gas. This calibration recipe is stored in the FTIR for use during each experimental run. A background spectrum was also taken of dry N_2, allowing the high N_2 concentration of the off-gas to be discounted in the composition calculations.

6.1.2 Gas Chromatography with Mass Spectrometer and Flame Ionisation Detector

Gas Chromatography with Mass Spectrometer and Flame Ionisation Detector (GC-MS/FID) is an analytical method for separating and identifying compounds that can be vaporised without decomposing. It is comprised of two parts, the GC and the detector, either a MS or a FID, all parts are shown in Figure 6.2.

The prepared samples are first vaporised if necessary and a small amount of the resulting vapour is injected into a stream of carrier gas, typically helium. The vaporised sample and carrier gas mixture then passes down a narrow capillary column. The relative affinities of the various components to the stationary phase in the column result in individual column retention times and the various mixture components eluting at different times. The stationary phase of the column is chosen depending on the expected sample composition. By causing the components to elute from the column separately a more accurate analysis can be made as the detector receives a purer sample, although some species do co-elute. The eluted gas is then split and a small volumetric flow sent to both a MS and a FID.

The MS ionises the gaseous sample using a stream of electrons, causing the molecules to become charged, or fragment into smaller charged molecules. The stream of ions then passes through an electromagnetic field which first accelerates the ions and then causes them to deflect from their path. Ions of differing mass-to-charge ratios deflect at different rates. The relative abundance of the various ions detected is used to identify the sample by comparing to known fragmentation patterns.

FID is often used for detecting hydrocarbon species. A hydrogen flame is used to generate ions through pyrolysis which then pass through a pair of charged electrodes. The gaseous sample stream from the GC is first mixed with a H_2 and oxidant stream before passing over the positively charged nozzle and being ignited. The reduced carbon atoms are attracted to the negatively charged detector above the flame. The number of carbon ions detected per unit time indicate the sample mass and hence the probable species.

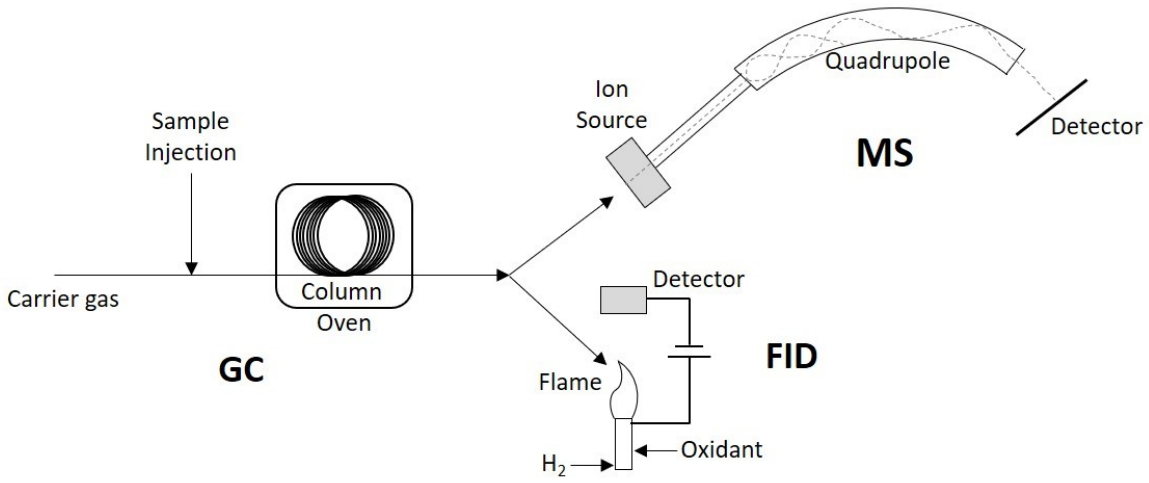


Figure 6.2: Schematic of GC-MS/FID.

The combination of MS and FID analysis can assist where there are similarities between two species, as the likelihood of both species behaving comparably in both techniques is reduced.

6.1.2.1 Liquid

A Shimadzu QP2020 GC MS/FID was used for the wax sample analysis. Toluene was used as the carrying solvent and helium the carrier gas. The column was a 80 m long 0.25 mm diameter glass column. The temperature was ramped to 380 °C over 720 minutes to allow good separation of the species. A mix of known concentration of C_7-C_{40} alkanes was used under the same program to calibrate the analysis.

6.1.2.2 Gas GC-MS

A gas phase Shimadzu GC-17A MS/FID was made available in late 2019 for testing the off-gases before the FTIR. Helium was used as the carrier gas with a 30 m 0.25 mm glass column at 320 °C over 120 minutes. A gas mix of known concentration of C_1-C_4 in N_2 and separate gas mixes of C_5, C_6 and C_7 in N_2 were used to calibrate the analysis.

6.1.3 Experimental

During the experiments a simulated biomass sourced syngas was passed over a packed bed of catalyst particles well mixed with an equal mass of quartz sand. Typical bed sizes were 0.4 g of catalyst and 0.4 g of quartz sand sieved to 200-300 µm. The catalyst mass used was limited to keep bed heights below 40mm, as longer beds resulted in undesirable pressure drops of above 1 barg across the reactor which may give rise to channelling through the bed. The quartz sand allows for a more even heat distribution within the bed. The bed was kept in place using a plug of quartz wool at either end.

Once the mixture of catalyst and quartz was loaded the reactor was re-sealed and purged with nitrogen before syngas was introduced at a rate of 6000 $cm^3(STP)h^{-1}g_{cat}^{-1}$. The bed temperature was then raised

to 270 °C at a rate of 1 °Cmin^{-1}, where it was held for 60 minutes to allow for reduction. After reducing the catalyst in situ, the bed temperature was reduced to 230 °C and the pressure was increased to 30 barg by the introduction of 48000 cm^3(STP)h^{-1}g$_{cat}^{-1}$ N_2. Once these conditions were reached the reactor was operated isothermally for approximately 100 hours to allow the reaction to achieve steady state.

To shut down the experiment the syngas flow was stopped, and the furnace switched off, allowing the reactor bed to cool naturally. The pressure was reduced gradually in 0.1 barg increments under a continuous N_2 flow in order that volatiles eluting at lower pressures could be measured. Online analysis of the off-gases was performed by FTIR. Offline gas GC-MS/FID analysis became available in late 2019 through the loan of a machine by another group and was added to later runs to check for higher hydrocarbon gases C_1-C_7.

Due to the long running time of the experiments, repeats were only undertaken of the Cat2K and 950-106-U catalyst runs.

During the run it is expected that the FTIR would predominately see C_1-C_3, as higher alkanes and alkenes are liquid at the KO pot conditions, though it is expected that some heavier hydrocarbons would be carried through by the excess N_2 flow. In order to collect heavier products from the KO pot the pressure must be reduced, causing C_4-C_6 to elute as atmospheric pressure is reached. It is therefore expected that a gap from C_4-C_6 will be seen between the on-line FTIR measurement and the off-line liquid and wax GC-MS/FID measurements. The later addition of gas GC-MS/FID was made to analyse these shorter chain length molecules.

The operation of the reactor at low conversions of CO, combined with the very long reaction times and collection of products at different points, meant that unfortunately it was not possible to calculate an overall mass balance or atomic balances on C and O.

6.1.4 Effectiveness Factor

The effectiveness factor, η, is used to indicate the extent of diffusion limitations in a porous catalyst particle. It is defined as the ratio between the observed reaction rate and the ideal rate at bulk conditions, where diffusion can be assumed to be negligible.

In order to calculate η from observed reaction rates the Wagner-Weisz-Wheeler modulus, M_W, for a spherical particle is first calculated.

$$M_W = \left({}^{r_p}/_{3}\right)^2 \frac{{}^{r_i'''}/_{C_i}}{D_e} \qquad 6.1$$

Where r_p is the catalyst particle diameter, r_i''' is the observed volumetric reaction rate, C_i the concentration of i and D_e the effective diffusivity.

The calculated M_W can then be used to determine η for each catalyst from correlations provided by Levenspiel[181], with values of M_W below 0.15 indicating diffusion free reaction and a M_W greater than 4 signifying strong diffusion resistances. The effective diffusivity is calculated by Post *et al.* based on the solubility of H_2 in liquid filled pores[120].

6.2 Results and Discussion

6.2.1 Validation with Reference Catalyst

Once the experimental equipment was confirmed inactive for the FT reaction, as described in section 3.8, the rig was run with the reference catalysts, PreCat and Cat2K. This allows comparison with the run of Cat2K from literature at the same reactor conditions. If the results are similar, within the bounds of error, then the reactor is deemed suitable for the accurate testing of novel catalysts.

Figure 6.3 shows the CO and CO_2 conversion, as a percentage CO/CO_2 converted from available CO/CO_2, of PreCat and Cat2K over the course of the experiment, once reaction conditions have been reached. It is clear that both precipitated catalysts are active for CO and CO_2 hydrogenation. CO conversion initially drops in the early stages of the reaction; however, it then starts gradually increasing again from approximately 20 hours on stream. CO_2 conversion decreases with increasing time on stream. At approximately 60 hours the rate of change in conversion for both catalysts slows, suggesting an approach to steady state. The noise seen in the CO and CO_2 conversion traces is partially due to the inherent noise of the FTIR measurements and operation of the BPR. As described in Section 3.10.3, the BPR opens periodically in small bursts to regulate the reactor pressure and can result in pulses of varying concentration in the FTIR system.

Between 60-100 hours CO conversion stabilises at 9.0 % and 16 % for PreCat and Cat2K respectively, similar to the 14.1 % steady state CO conversion reported for Cat2K in the reference literature (where PreCat is not tested). CO_2 conversion between 60-100 hours is 12 % and 7.2 % for PreCat and Cat2K respectively, again in line with the reference value of 8.9 % for Cat2K. Lower levels of CO_2 reactivity compared to CO agree with literature results for promoted catalysts[155,156]. The drop in conversion levels with reaction time is commonly attributed to the deposition of inactive surface carbon via the Boudard reaction. Surface carbon species are necessary for the FT reaction and formation of iron carbides, believed by many to be the active phase of Fe catalysts, however, inactive carbon deposition is a competing process that reduces the number of available surface sites.

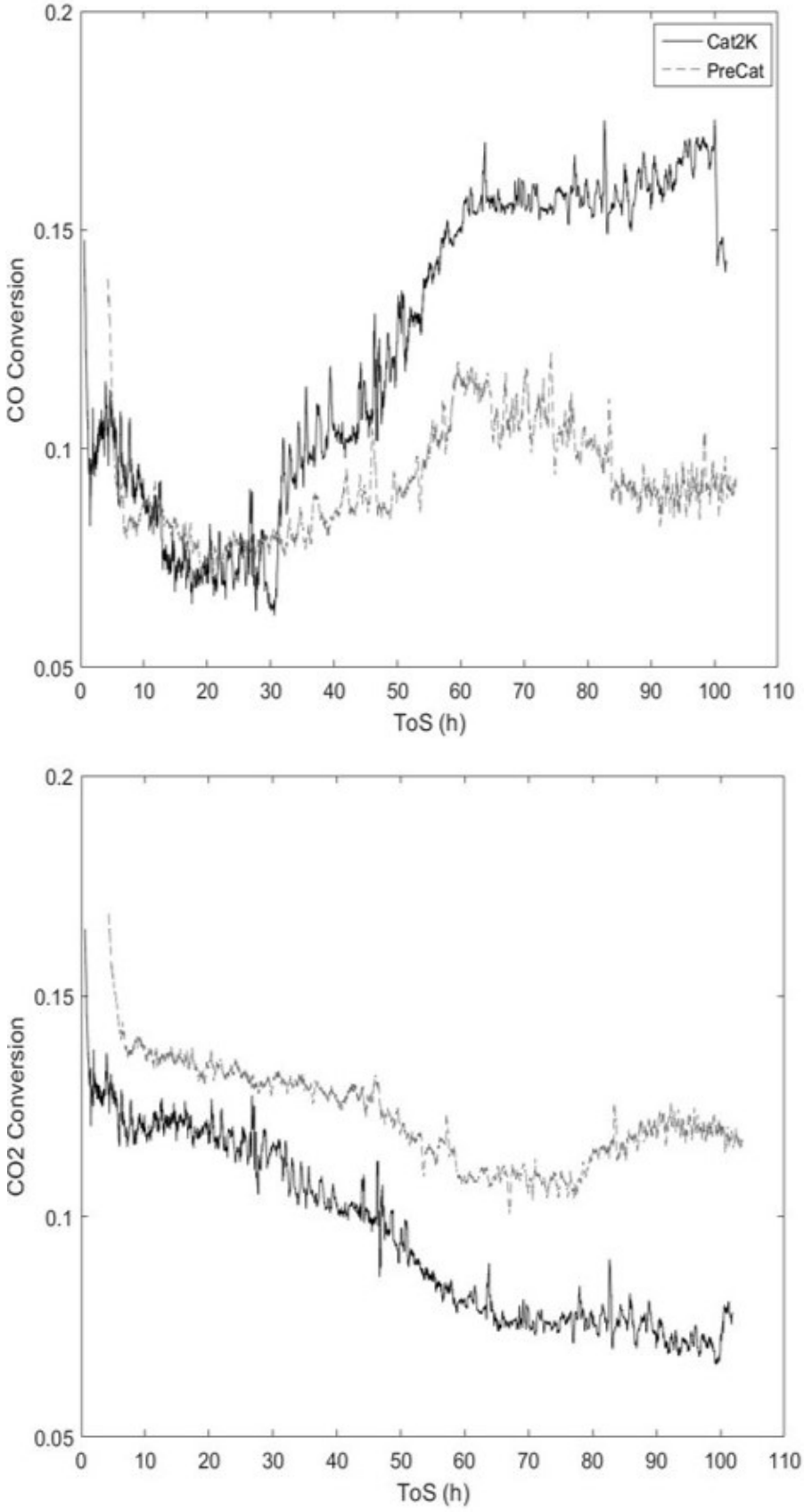


Figure 6.3: CO and CO_2 conversion as a fraction of total conversion possible for PreCat and Cat2K over a time on stream (ToS) of 0-110 hours..

As found in other studies, the CO conversion is higher for Cat2K compared to the unpromoted PreCat, however unexpectedly the CO_2 conversion is lower. The increased CO adsorption on the surface of Cat2K is attributed to the effects of the K promotion, boosting CO conversion. This increase in dissociative adsorption activity with K promotion has not been found to apply to CO_2[146], suggesting that increased CO activity for promoted catalysts results in a damped CO_2 conversion through a lack of surface sites rather than lower activity. The lower CO surface affinity of the unpromoted PreCat allows a more equal amount of CO_2 conversion to take place.

Since Fe catalysts are active for the WGS reaction it is expected that some WGS will take place, altering levels of both CO and CO_2. However, since both CO and CO_2 are present in the feed and can be utilised in the FT reaction, it is not possible to confirm levels of CO/CO_2 conversion for the FT and WGS reactions independently during these experiments.

Concentrations of C_1-C_3 alkanes and water for PreCat and Cat2K, as measured by the online FTIR, are shown in Figure 6.4. In this figure it can be seen that the concentration profile of the three alkanes follow each other closely, with methane being the most prominent hydrocarbon product for both catalysts, followed by ethane and propane. The concentration of water follows the same profile as the hydrocarbons, particularly that of methane. This is expected as water is a byproduct of the addition of CH_2 groups to growing chains or CH_4 production, and methane is the primary product in the FT reaction.

Residual amounts of water remain in the FTIR even after 24 hours of purging with nitrogen. Taking a baseline for FTIR measurements at this point resulted in a false zero for water concentrations, and increasingly negative water concentrations being measured over the long reaction times. The baseline of the measured water concentration is therefore adjusted with 'zero' being taken as the level measured at the start of the experiment after reduction, allowing for the change in water concentration to be measured. Typically this is an addition in the order of 300 ppm water, but can differ with varying causes, such as room humidity, time the rig is left inactive before the run etc. Regardless of the base level of water, Figure 6.4 shows that CH_4 and H_2O concentrations can be used as good indications of general hydrocarbon production levels.

Hydrocarbon concentrations for the PreCat run increase gradually up to a maximum of 26 ppm CH_4 at 60 hours before decreasing slowly to 15 ppm from 60-100 hours. The drop in C_1-C_3 production is in line with slight reduction of CO conversion between 60-100 hours. It is unsure whether the initial drop in ethane production in the first 5 hours of running is a real phenomenon or a measurement error. As the opening C_3 concentration is slightly negative, it is suggested that the similar absorbance spectra of the two molecules has caused the FTIR to incorrectly attribute low C_2 and C_3 concentrations solely to C_2.

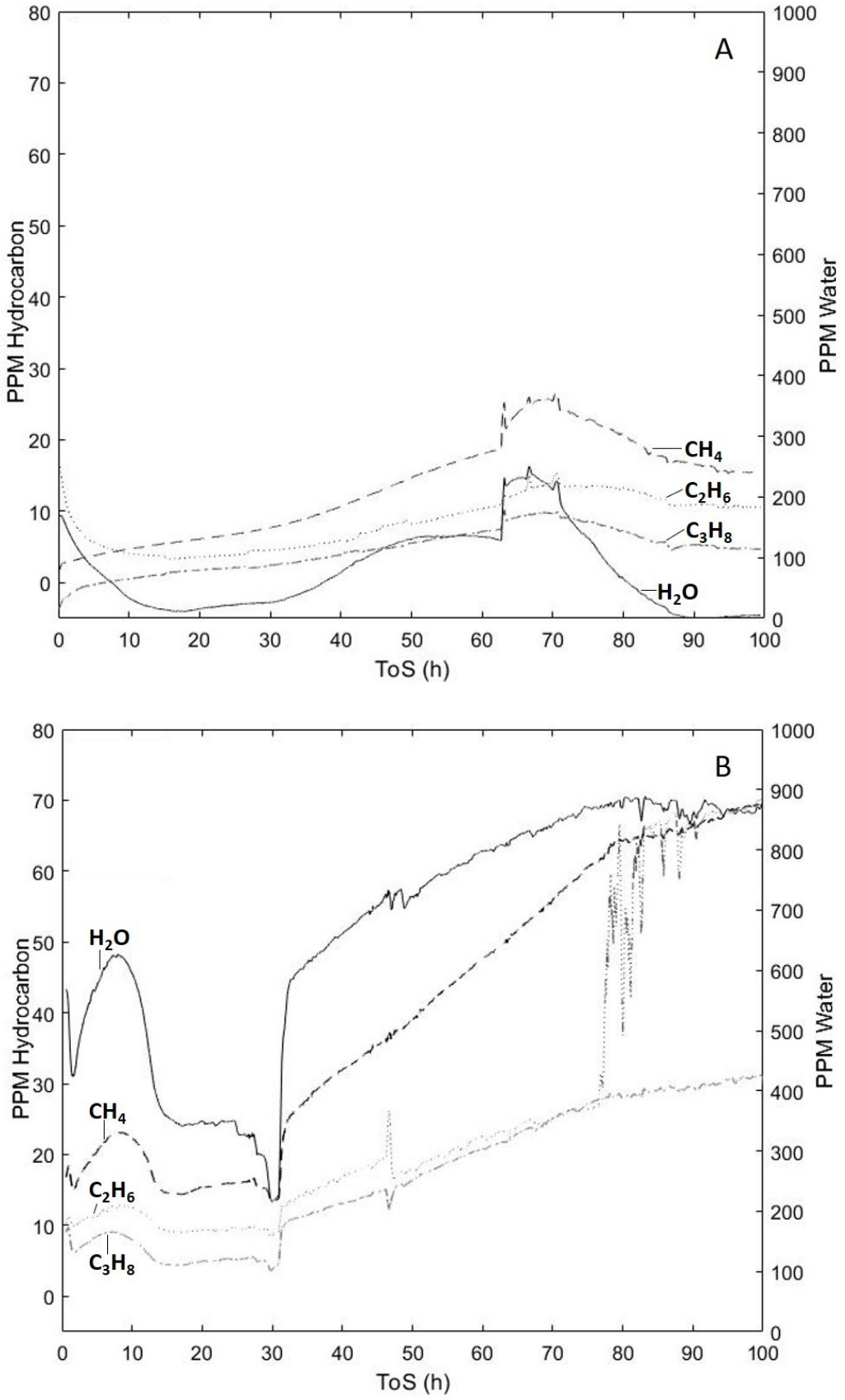


Figure 6.4: C_1-C_3 alkane and water production rates for (A) PreCat and (B) Cat2K over 100 hours.

C_1-C_3 concentrations measured for Cat2K are higher throughout than those seen in the unpromoted PreCat. The stabilisation period is longer and noisier and can be split into two segments between 0-30 hours where production levels are maintained and 30-80 hours during which C_1-C_3 concentrations rise. After 80 hours the production levels stabilise at approximately 3 times the C_1-C_3 production of the PreCat run. Noise is seen in the C_2 trace during this final stable period, again suggesting an overlap with the spectra of a similar product.

The overall mass of higher hydrocarbons produced when using Cat2K was also considerably higher than for PreCat, with 707 mg and 54 mg wax produced respectively over the 100 hour experiments. GC-MS/FID analysis was performed on the wax collected at the end of each run, the averaged production rate of each product, including data for C_1-C_3, is given in Figure 6.5.

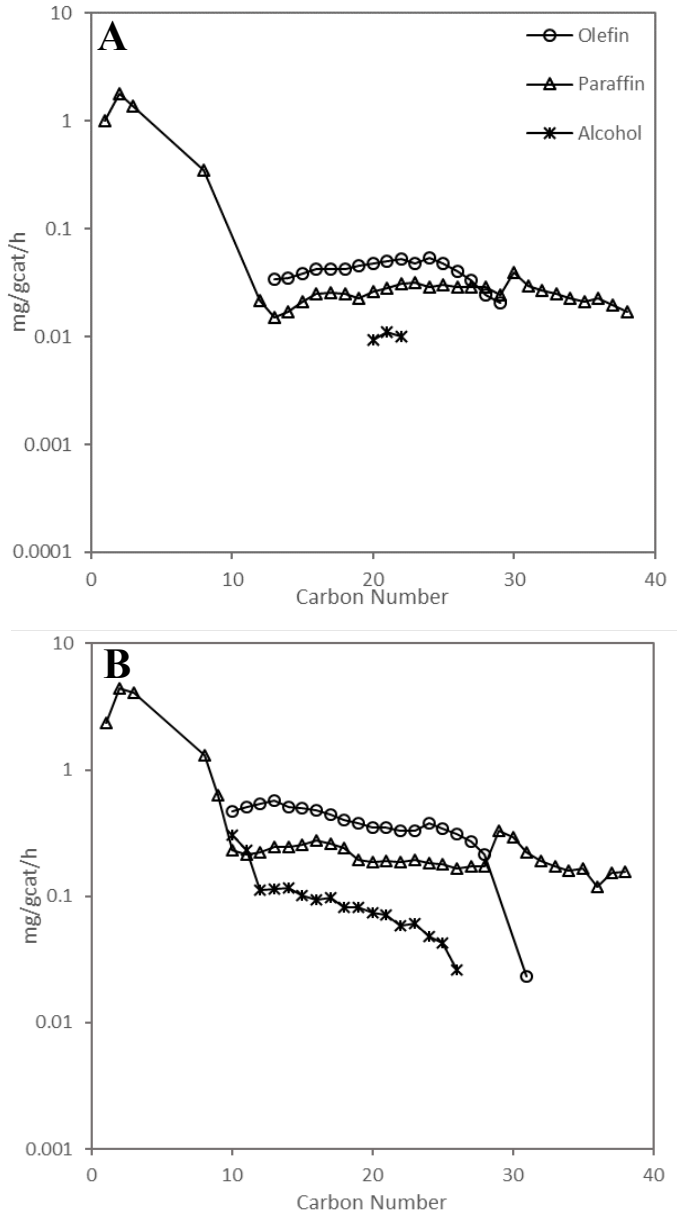


Figure 6.5: Hydrocarbon mass production rates of (A) PreCat and (B) Cat2K with respect to carbon number.

As explained in section 6.1, C_3-C_7 products evaporated during reactor depressurisation and so are not seen during GC-MS/FID analysis.

A pseudo-carbon balance was performed for each experimental run, comparing the inlet and outlet gaseous molar flowrates of C_1-C_3 species throughout. The build-up of liquid and wax products within the reactor system were not included as these were not collected continuously throughout the run, resulting in an incomplete balance. This method accounted for approximately 85-90% of the C in each experiment. The errors introduced by the exclusion of the higher C number products and low balance percentages mean the pseudo-carbon balance was not deemed accurate or appropriate to include as an analysis aid within this work and is hence not referenced in the later catalyst sections.

As seen with the C_1-C_3 alkanes, production of the higher hydrocarbons increased with promotion. This amplification in production is uniform throughout the product species and carbon chain lengths, with olefins being the overall primary product, followed by paraffins and alcohols. As the chain length increases beyond C_{25} the olefin production begins to drop and paraffins become the largest product by mass, however this drop in olefin production only occurs at the very top end of the chain lengths produced, meaning olefins are still the main product overall. This concurs with literature results for Cat2K, where olefins are the largest product mass up to approximately C_{18}, when olefin production drops below that of paraffins[146].

The range of carbon numbers over which olefins and alcohols are produced is extended for the promoted Cat2K, however the olefin to paraffin ratio remains similar for both catalysts, as shown in Figure 6.6. As the chain length increases the olefin to paraffin ratios drop for both PreCat and Cat2K, from a peak approaching 2.5 at C_8, to below 1 at C_{29}. Comparable behaviour is recorded for the literature catalyst, where olefin to paraffin ratios (g/g) drop steadily approximately from 2.3 at C_8 to 0.5 at C_{28}. [146]

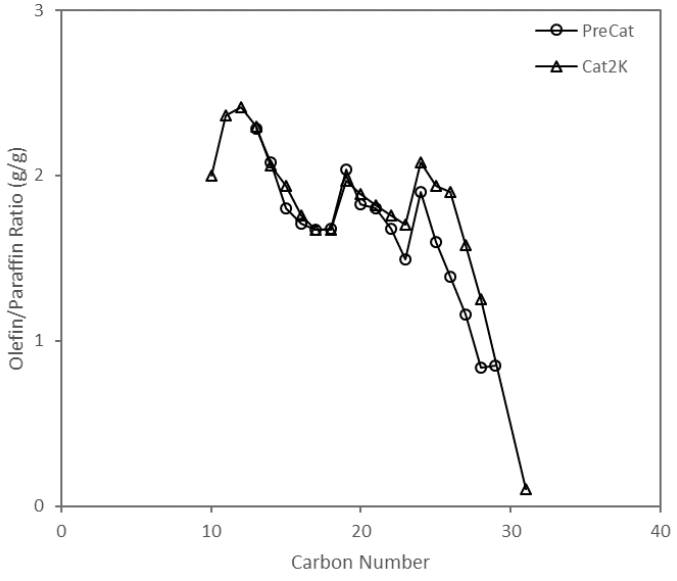


Figure 6.6: Olefin:Paraffin ratio of hydrocarbon product with respect to carbon number for co-precipitated catalysts.

As discussed in section 6.1, due to the change in conditions on wax collection it was expected that chain lengths below C_6 would evaporate before the wax sample could be tested. In actuality, even a short delay between depressurising and testing of the waxes resulted in the loss of C_6 and C_7 compounds, giving a lack of results for C_4-C_7. In order to address this and the restricted FTIR accuracy with C_4-C_6 compounds, gaseous GC-MS/FID was investigated. This became available for the PreCat run, showing the presence of C_1-C_7 in the off-gas, however, the split between paraffins and olefins could not be achieved on the column available. Since the data is not available for all runs and is qualitative not quantitative, it is not included in this analysis beyond acknowledgment of the presence of C_1-C_7 products.

The combination of the higher chain lengths and greater production rate of C_{8+} species produced with Cat2K results in lower C_1-C_3 selectivities than seen with PreCat. Figure 6.7 shows the overall distribution of mass is weighed towards the gaseous products for the unpromoted PreCat, whereas Cat2K has lower C_1-C_3 selectivities and higher mass fractions of C_{8+} products for all species.

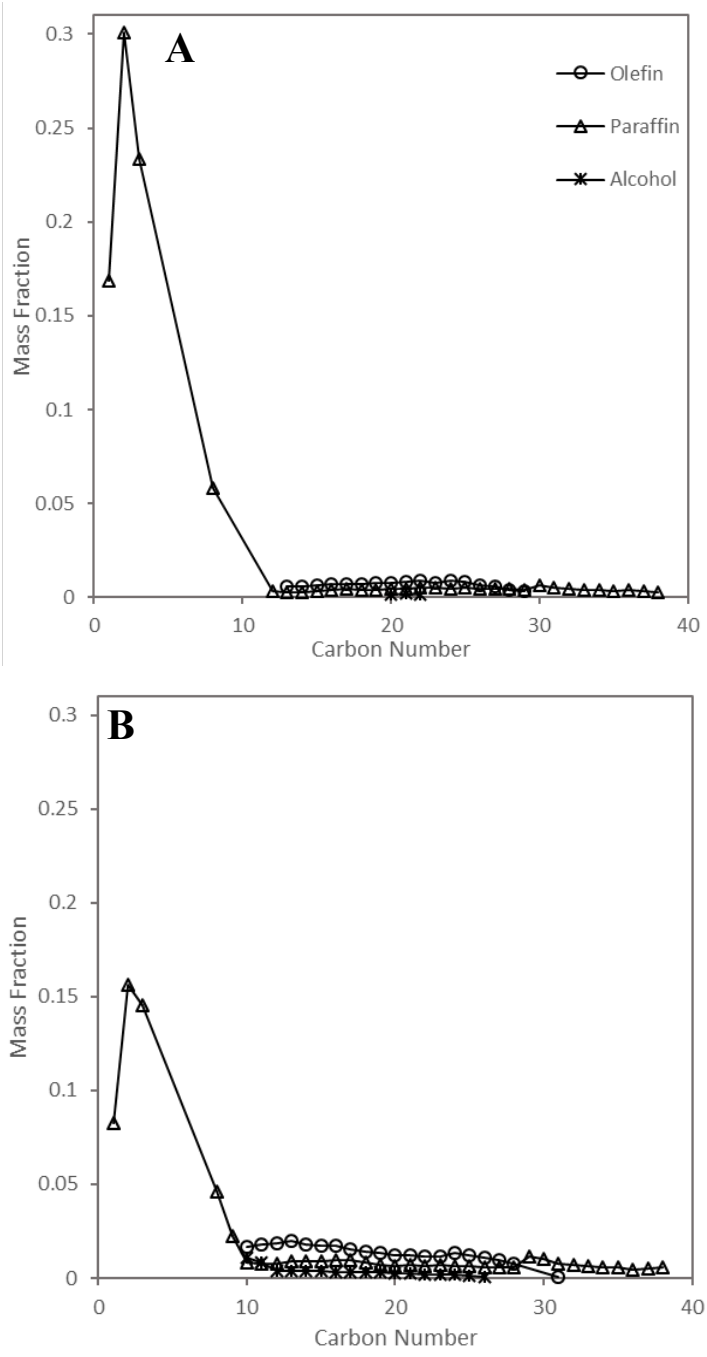


Figure 6.7: Mass fraction of product with respect to carbon number of (A) PreCat and (B) Cat2K.

The product distribution of FT product is often described using an ASF distribution, with the probability of chain growth, α, as described in section 2.2.1. The natural logarithm of α is calculated by plotting the natural logarithm of W_n, the mass fraction of chain length n, against n. The exponential of the best fit slope can then be used to calculate α. A high α means an increased chain growth probability and therefore reduced selectivity to gaseous products. Whilst this is beneficial for the production of liquid fuels, the longer chain length products produced with a high α may need further treatment to produce higher quantities of more valuable chain lengths.

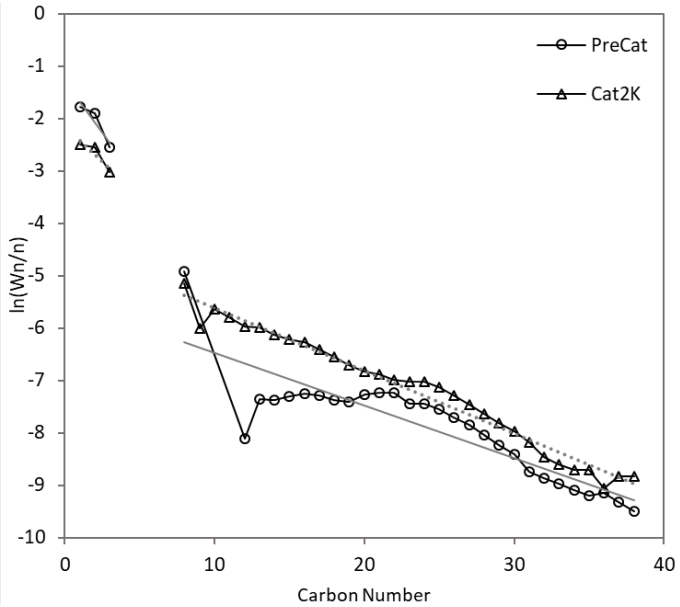


Figure 6.8: ASF distribution for co-precipitated catalysts.

As discussed in section 2.2.1 a double ASF model is commonly used to account for high levels of CH_4 and C_2H_6 production. The double ASF product distribution seems to fit best for the co-precipitated catalysts, as shown in Figure 6.8, with α_1 taken as C_1-C_3 and α_2 as C_{8+}. This double ASF fit is also seen in the reference literature for Cat2K. Table 6.1 gives the values for α_1 and α_2 calculated from the linear trend lines fitted in Figure 6.8, as well as those calculated in the reference.

Table 6.1: α values for co-precipitated catalysts.

	α_1	α_2
PreCat	0.68	0.90
Cat2K	0.77	0.89
Reference Cat2K	0.63*	0.89*

*Reference α_1 values for C_1-C_6, α_2 for C_{7+}.[146]

The overall pattern given by Figure 6.8 is similar for both PreCat and Cat2K. Promotion increases the value of α_1 from 0.68 to 0.77, agreeing with the lower C_1-C_3 selectivities seen for Cat2K in Figure 6.7 and close to the reference value of 0.63 for Cat2K. The slightly higher α_1 value calculated compared to the reference is likely due to the smaller range of carbon numbers included in the calculation for α_1. The known high selectivity of C_1-C_3 without the predicted lower production rates of C_4-C_7, causes α_1 to be larger than it would be if these values were available and included.

However, promotion makes little difference for the longer chain lengths, with α_2 remaining similar at 0.89-0.90 for both co-precipitated catalysts, equal to the reference value of 0.89 for Cat2K[146].

Although the product distributions for PreCat and Cat2K are similar more product is generated over Cat2K, as demonstrated in Figure 6.5. This results in a higher rate of conversion into hydrocarbons

over the promoted catalyst, shown in Table 6.2. The steady state PreCat rate of CO conversion to hydrocarbons is similar to that of the reference catalyst under CO and CO_2 containing syngas, whereas the Cat2K rate is almost four times this rate.

Although notably higher than the reference value, the conversion rate of CO to hydrocarbons over Cat2K is within the range of conversion rates listed for Fe catalysts in literature, where common conversion rates between 1.6 and 86 $mmolCOg_{cat}^{-1}h^{-1}$ are seen for Fe based catalysts[157, 158, 159, 67]. The particle size used for the reference catalyst work by Martinelli *et al.* is not given, the difference between the observed rates could be due to differences in experimental catalyst particle diameter with larger particles introducing rate limitations.

Table 6.2: Conversion to hydrocarbon rates of PreCat and Cat2K at steady state.

	$mmolCOg_{cat}^{-1}h^{-1}$	$mmolH_2g_{cat}^{-1}h^{-1}$
PreCat	8.0	10.6
Cat2K	34.4	41.4
Reference Cat2K[146]	9.0	-

Particle densities are not available for the co-precipitated catalysts due to equipment failures, therefore the effectiveness factor is not calculated for Precat and Cat2K.

6.2.2 Foamed Catalysts

The four unpromoted foamed catalysts, 950-106-U, 950-1000-U, 1350-106-U and 1350-1000-U, are first investigated, before the promoted foams, 950-106-P, 950-1000-P, 1350-106-P and 1350-1000-P are reviewed.

6.2.2.1 Unpromoted Foamed Catalyst

Figure 6.9 below shows the CH_4 and H_2O outlet concentrations for the four unpromoted foamed catalysts over the course of the experiments. As can be seen the levels of CH_4 detected are very low, with each stabilising below 6 ppm. In section 6.2 it was determined that production rates of methane and water can be used as indicators of catalyst activity and overall hydrocarbon production rates, suggesting that the unpromoted foamed catalysts have little FT activity.

Both CH_4 and H_2O concentrations for 950-106-U and 1350-1000-U rise slightly over the course of the experiment and end at slightly higher concentrations than the other unpromoted foams. This could suggest they are marginally more active; however, the increase is minimal and therefore cannot be taken conclusively. Negligible levels of higher hydrocarbons were detected by the FTIR and no liquid or solid product was produced, confirming a low level of activity for all the unpromoted foams.

Measured H_2O concentrations are higher than CH_4 concentrations for all four catalysts, though they remain low compared to the water seen in Figure 6.4 for Cat2K. Over the initial ten hours of the run the water concentration drops, in a manner similar to the drop seen in the first ten hours of the PreCat run in Figure 6.4, and in a smaller way, the drop over the first two hours of the Cat2K run. This drop, before stabilising at a low level in the case of 950-1000-U and 1350-106-U, or increasing slightly for 950-106-U and 1350-1000-U in line with their slightly higher CH_4 outputs, suggests the purging of residual water in the FTIR system which would normally be disguised by the production of water over a more active catalyst.

Due to the low product levels measured the unpromoted foam runs were finished earlier than the normal 100 hours, allowing time for additional catalysts to be tested. Despite the shorter experimental times it is clear that the catalyst activity is negligible, and no significant increases in productivity is expected with longer run times.

Average CO and CO_2 conversions were not calculated as there was negligible change in the inlet and outlet flows of CO and CO_2 measured. Small levels of conversion could be masked by generation of CO and CO_2 through the WGS reaction, however the variation in CO and CO_2 concentrations measured are within the scale of error of measurement for the FTIR and are therefore taken to be as zero.

The lack of gaseous products seen by the FTIR was confirmed with gas GC-MS/FID analysis performed on a sample of outlet gas for 950-1000-U, with no C_1-C_7 hydrocarbons seen.

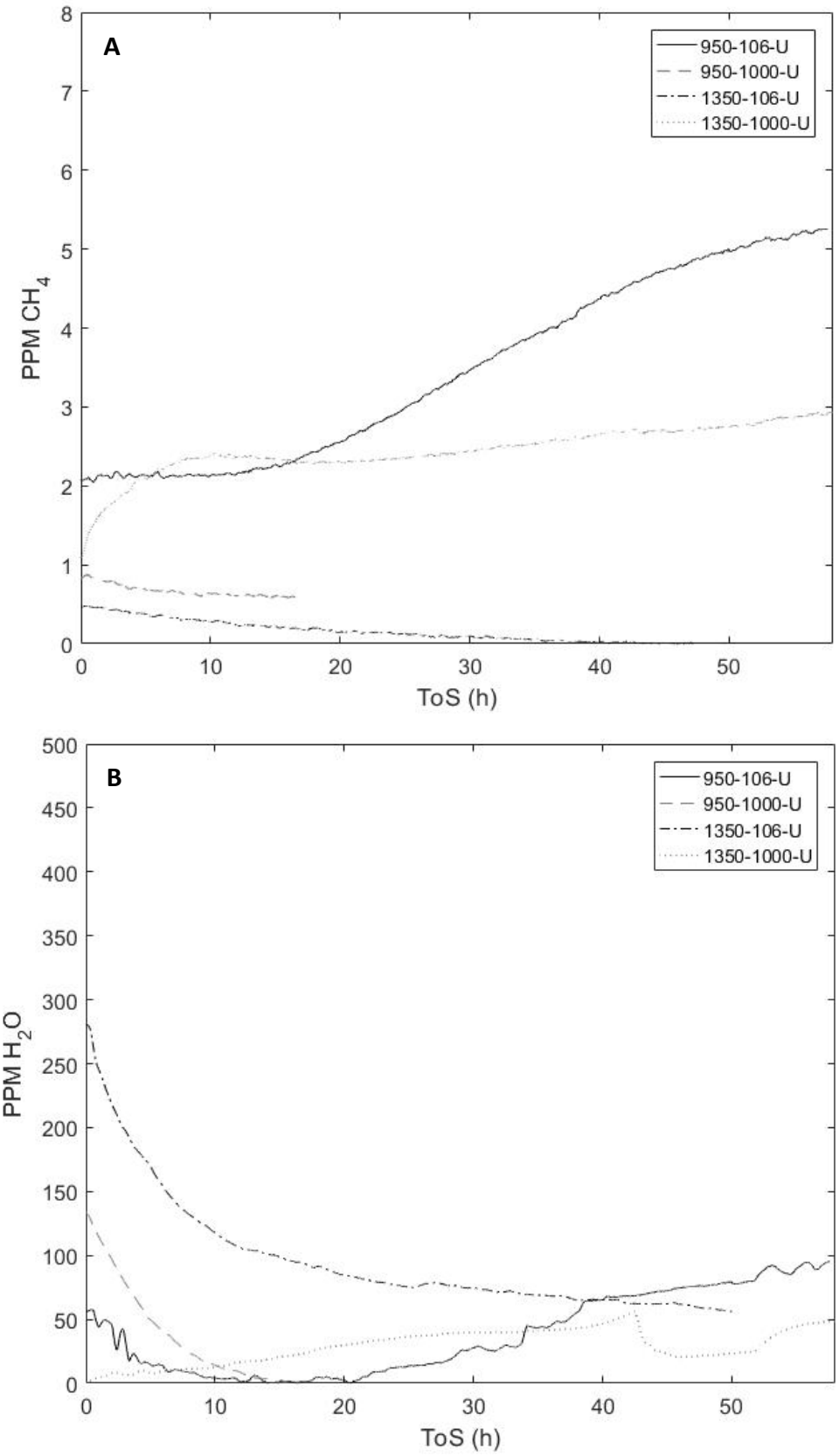


Figure 6.9: (A) CH_4 and (B) H_2O production levels for the unpromoted foamed catalysts over 60 hours on stream.

6.2.2.2 Promoted Foamed Catalyst

Unlike the unpromoted foamed catalysts, the promoted foams display a comparable level of activity to the reference catalysts, with all experimental runs also yielding solid wax products. As expected, the smaller catalyst particles, crushed to a size whereby mass transfer effects can be negated, have higher production rates than their larger counterparts.

6.2.2.2.1 106 µm pellet size

Comparing the same small particle size for the two calcination temperatures, we can see in Figure 6.10 that the 1350-106-P catalyst has lower levels of CO conversion compared to 950-106-P, but similar CO_2 conversion rates over the 100 hour run. For 950-106-P the CO conversion increases over the first 25 hours online, before stabilising at a mean conversion of 16.5 %. The CO_2 conversion drops steadily over the entire experimental period, from 16 % to approximately 10 %, in a similar manner to that seen for Cat2K in Figure 6.3.

For 1350-106-P the CO_2 conversion follows a similar pattern to 950-106-P, with a slight drop in conversion throughout from approximately 14 % to 11 %. However, despite starting at a comparable rate, the CO conversion of 1350-106-P does not increase over the course of the in the same manner as 950-106-P, remaining relatively steady at 8.5 % throughout.

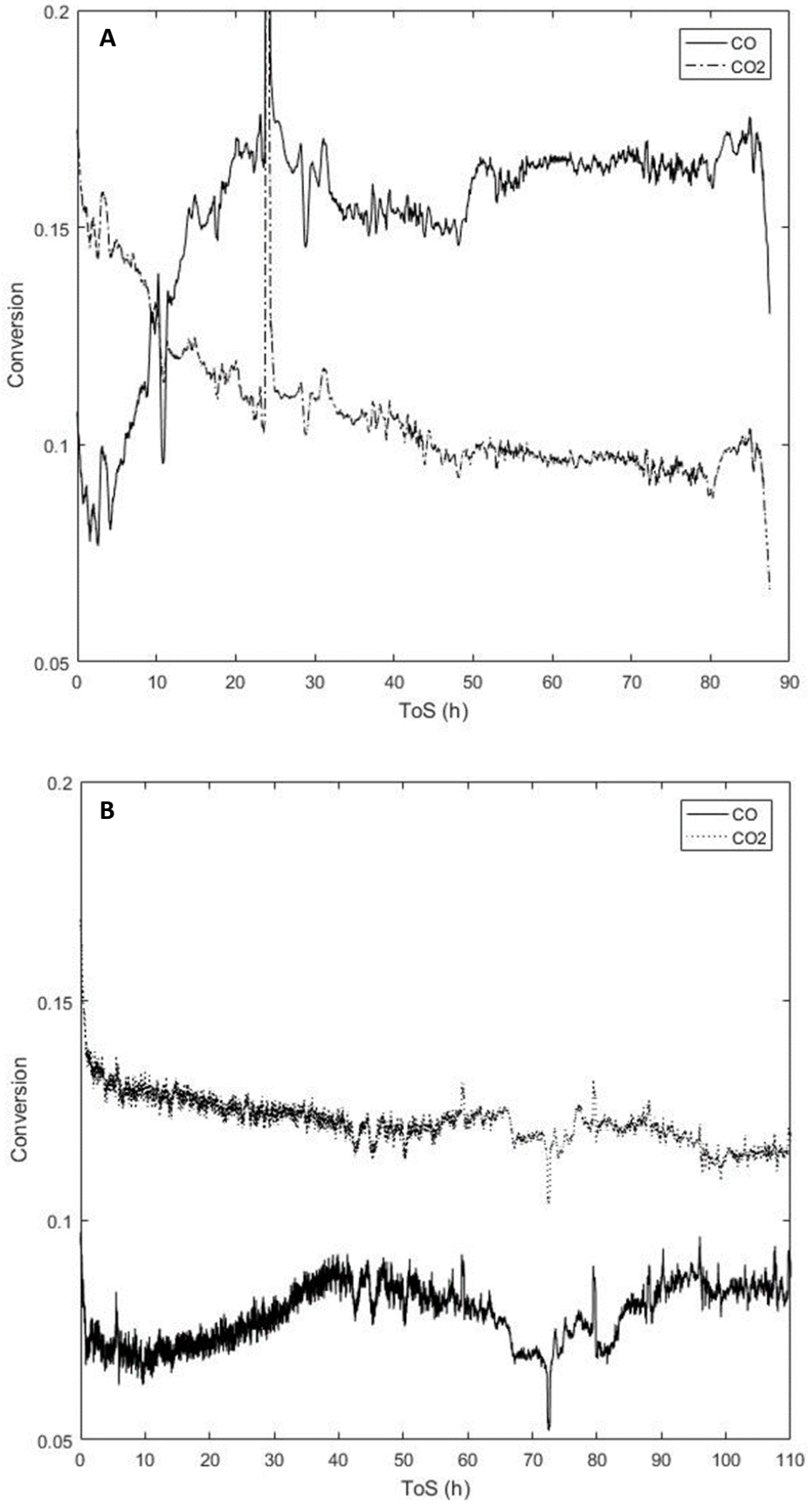


Figure 6.10: CO and CO_2 conversion for (A) 950-106-P and (B) 1350-106-P.

In section 5.1.3 it was found that the higher calcination temperature of 1350 °C significantly reduced the catalyst surface area compared to those calcined at 950 °C. SEM images in section 5.1.4 confirmed the loss of the microporous surface structure seen in the 950 °C catalysts. This loss of potential active sites is suggested to be the cause of the lower CO activity of the 1350-106-P catalyst shown in Figure 6.10.

In line with the higher CO and CO_2 conversion levels seen for 950-106-P, levels of C_1-C_3 and water measured by the FTIR are also significantly higher than for 1350-106-P. Methane is the primary gaseous product detected by the FTIR, followed by ethane and propane, as shown in Figure 6.11. Production rates increase until the stabilisation period ends at approximately 30 hours, when C_1-C_3 concentrations stabilise at 75, 70 and 30 ppm respectively. A sudden drop, followed by a peak in production of all species is seen at approximately 24 hours, this is when the KO pot was opened to check for interim liquid products, during which the reactor is isolated and the downstream system depressurised. No product was present in the KO pot at this point and after repressuring and connecting the production rates of C_1-C_3 measured by the FTIR reach similar levels to those seen before the interim product check. It was decided, due to the disruption to the trace and lack of product within the KO pot, to avoid interim product checks for the remaining experimental runs.

As discussed above, levels of C_1-C_3 and water are lower throughout the 1350-106-P run, with a maximum CH_4 concentration of 12 ppm reached. The catalyst stabilisation period is slightly shorter, with C_1-C_3 production levels levelling out at approximately 20 hours. As previously noted in Figure 6.4 for PreCat, the initial C_3 concentration in Figure 6.11B is negative and the primary measured product C_2 instead of the expected C_1. This is again thought to be due to C_3 absorbance being incorrectly attributed to C_2 at low concentrations.

Interestingly the H_2O concentration for 1350-106-P drops between 70-110 hours despite there being a steady production of C_1-C_3. It is suggested that this is due to the removal of the last of the low level H_2O from the FTIR gas chamber, known to take several days of continuous running with dry gas. With higher H_2O production rates this slow drop could be missed, as it is negligible in scale compared to the concentration of H_2O generated. A similar phenomenon was seen for PreCat in Figure 6.4.

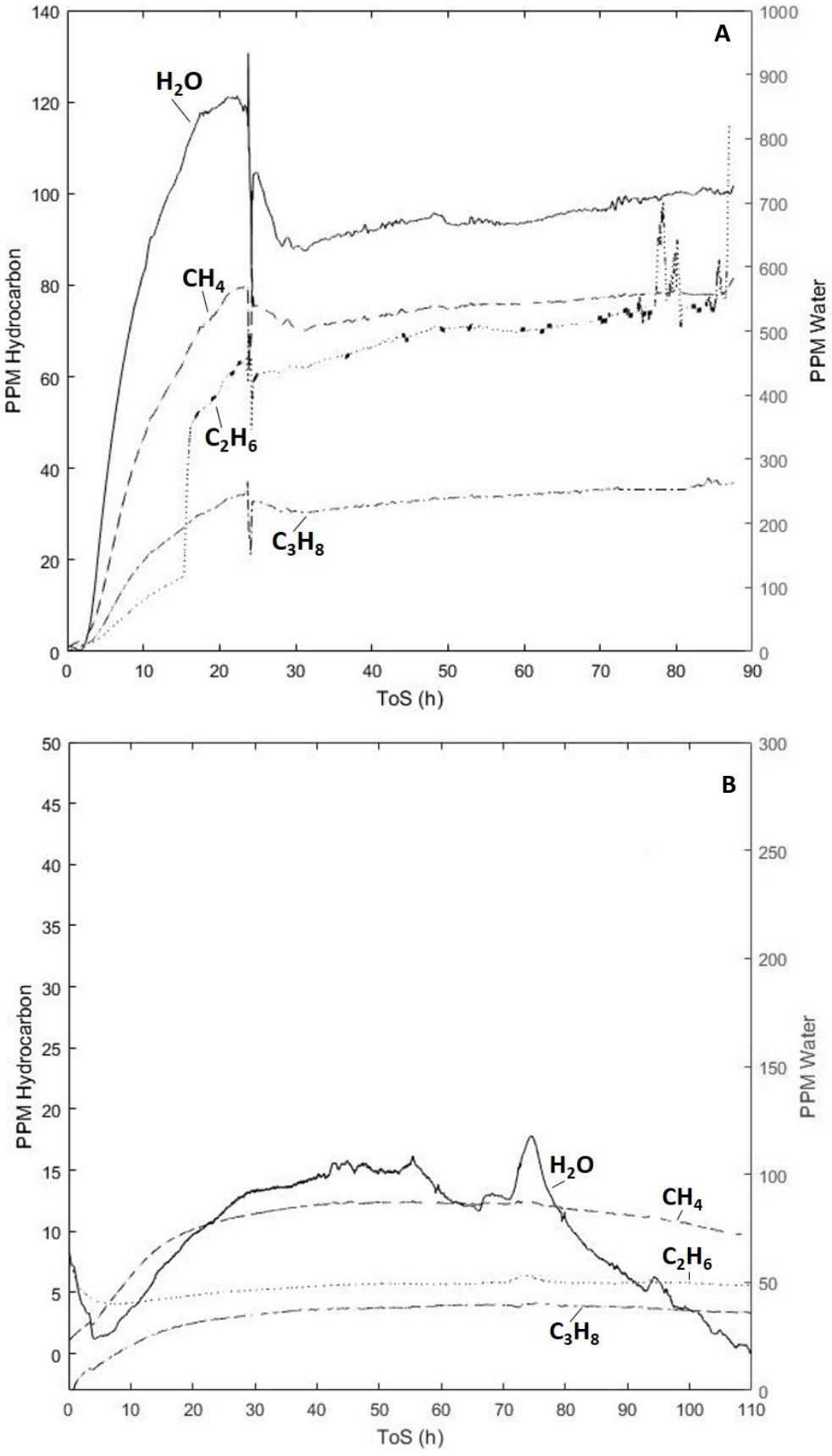


Figure 6.11: C_1-C_3 and H_2O production for (A) 950-106-P and (B) 1350-106-P.

Although no interim product was found during the 950-106-P run, 210 mg of liquid and 1265 mg of wax product was collected at the end of the experiment. It was the only experimental run for which a liquid product was seen. Some soft wax solidified in the liquid phase after collection, this was dissolved back into solution before testing in the liquid GC-MS/FID. The reconstituted liquid and solid phases were analysed separately.

Figure 6.12 shows that the gaseous C_1-C_3 products are still the most prevalent by mass, but high levels of paraffins and olefins are seen in both liquid and solid product. The liquid product also contains a range of alcohols.

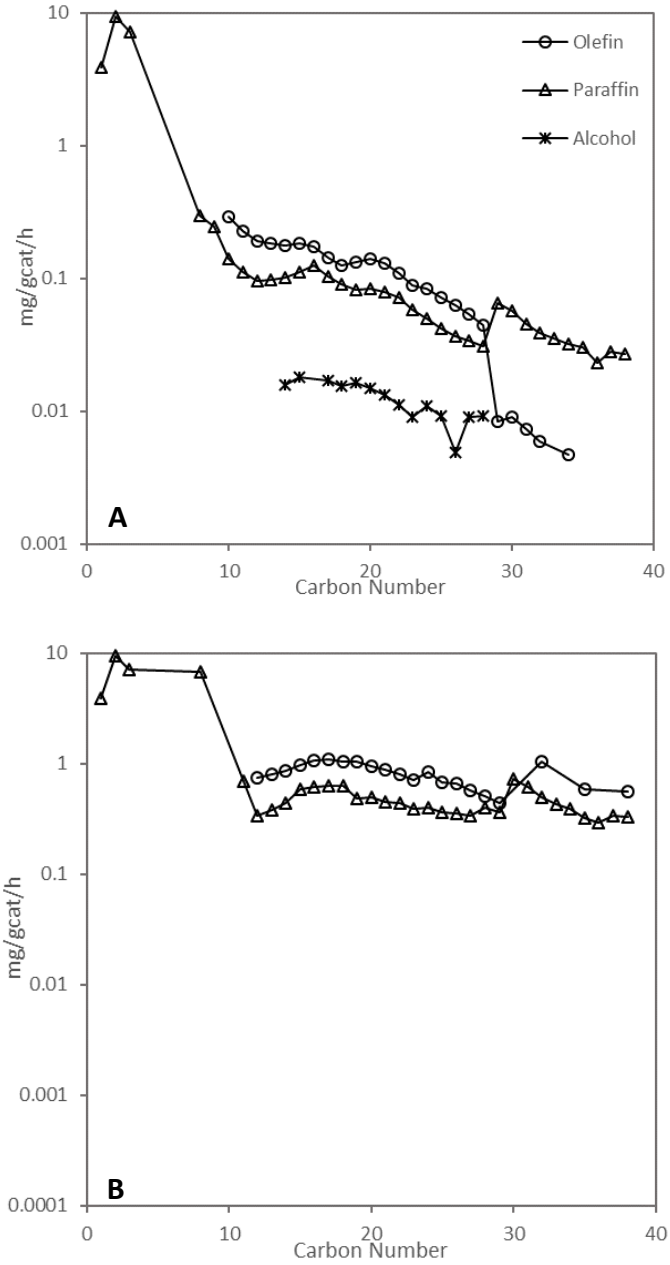


Figure 6.12: Mass production rates of (A) liquid and (B) wax product with respect to carbon number from 950-106-P.

The quantity of liquid product produced drops off with increasing carbon number, as expected due to the increasing melting points of the higher carbon number products causing these products to solidify into the wax phase. In the wax sample the mass of product is similar throughout the carbon range, suggesting a high probability of chain growth. It is likely that higher carbon number products exist in this sample but are unable to be seen on the GC-MS/FID trace due to the temperatures required for them to elude being higher than the GC-MS/FID column allows.

Interestingly only the liquid sample contains any alcohols, this is suggested to be due to the increased miscibility of alcohols in water due to the OH group. The liquid phase would have had a reduced amount of aqueous and organic separation compared to the solid wax phase, meaning the liquid product has a higher water, and hence alcohol, concentration than the wax phase.

Several other peaks were seen in the GC-MS/FID trace for the liquid sample, grouped in batches around the double olefin/paraffin peak associated with each carbon number. It was not possible to confirm the species responsible for these additional peaks as matching calibration mixes were not available, however, from the species search function on the GC-MS/FID it is likely they are from other branched hydrocarbons of the same carbon number and varying levels of saturation.

By contrast, the production rates for 1350-106-P are an order of magnitude lower than for 950-106-P, as expected with the lower C_1-C_3 concentrations seen in Figure 6.11B. A total of 7.3 mg of wax was collected at the end of the run. A similar range of chain lengths is seen, with again olefins being the main product species followed by paraffins and alcohols.

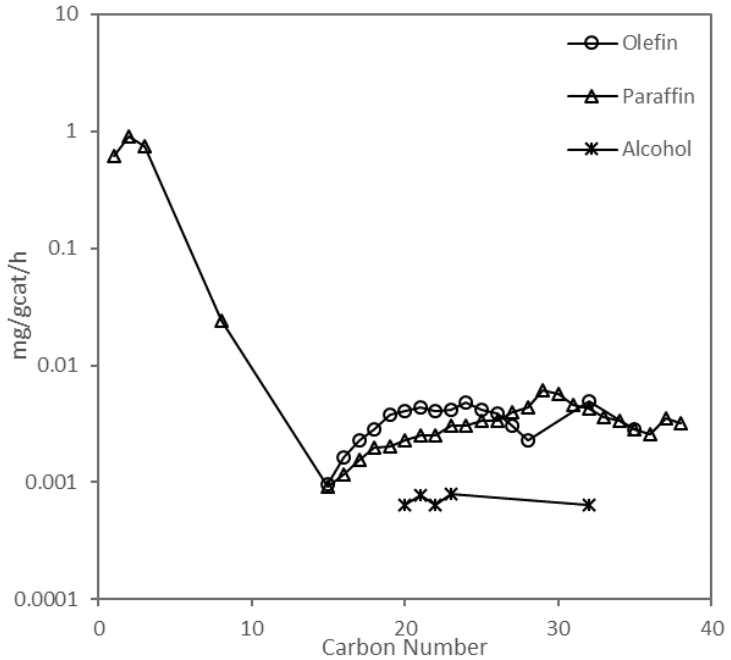


Figure 6.13: Mass production rates with respect to carbon number for 1350-106-P.

This suggests the differences in production rate are not due to altered characteristics of the catalyst, but to overall catalytic activity. The significantly lower available surface area of 1350-106-P compared to 950-106-P, as seen in chapter 0, is likely the cause of this reduced activity.

Figure 6.14 shows that the olefin to paraffin ratio for both liquid and wax phases of 950-106-P remains between approximately 1.5 and 2.1 until C_{29} of the liquid phase is reached, when the fraction of olefins produced, and hence ratio, reduces. This behaviour matches that seen by both PreCat and Cat2K in Figure 6.6, where olefin production above C_{28} also drops significantly. The fraction of higher chain length olefins remains constant for the wax phase, suggesting a high catalyst α, with heavier products in the wax phase that cannot be detected by the GC-MS/FID.

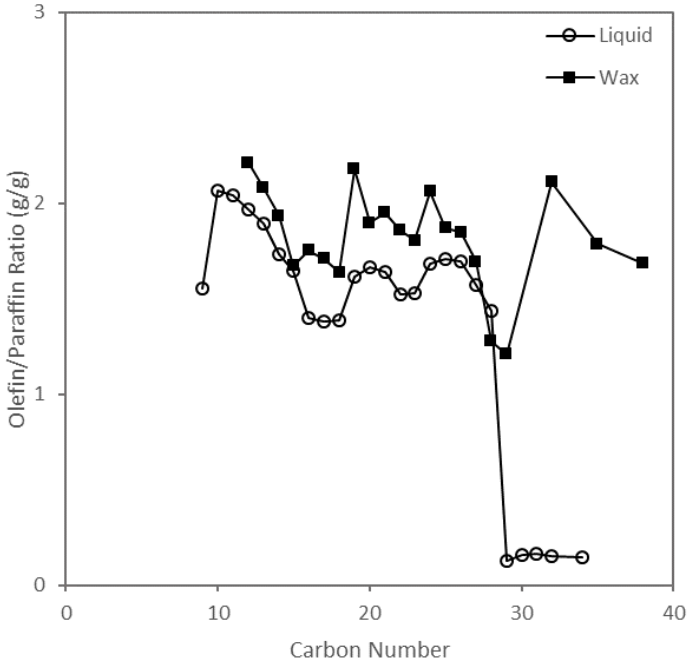


Figure 6.14: Olefin:Paraffin ratio for 950-106-P liquid and wax phase products.

The olefin:paraffin ratio of 1350-106-P, shown in Figure 6.15 is between 0.5 and 1, marginally lower than that of 950-106-P. It follows more closely the pattern seen in Figure 6.6 for the co-precipitated catalysts, where the fraction of olefins decreases as the carbon number increases.

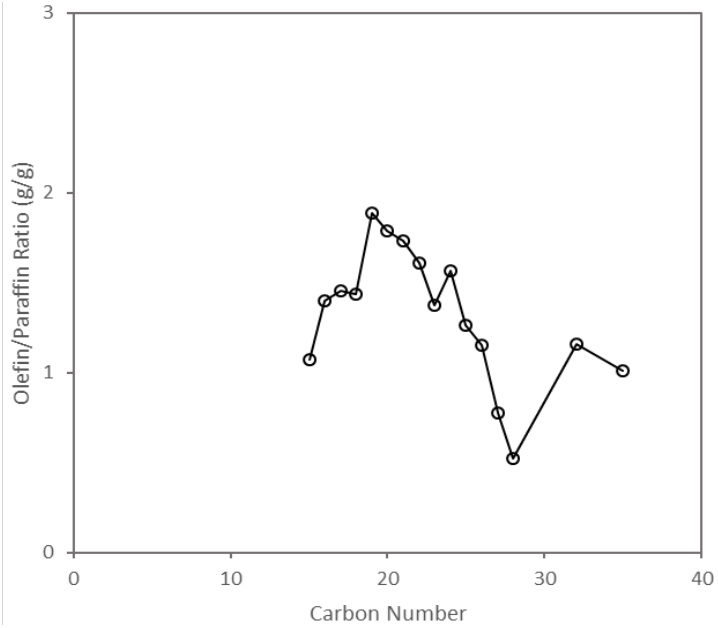


Figure 6.15: Olefin:Paraffin ratio for 1350-106-P product.

Figure 6.16 gives the mass fraction of each product for the combined liquid and wax phases of 950-106-P. The high production rate of the higher alkanes, alkenes and alcohols results in relatively low mass fractions of C_1-C_3 products of 6, 15 and 11 % respectively. These figures are comparable to those seen for Cat2K, with correspondingly larger fractions of the higher hydrocarbons seen.

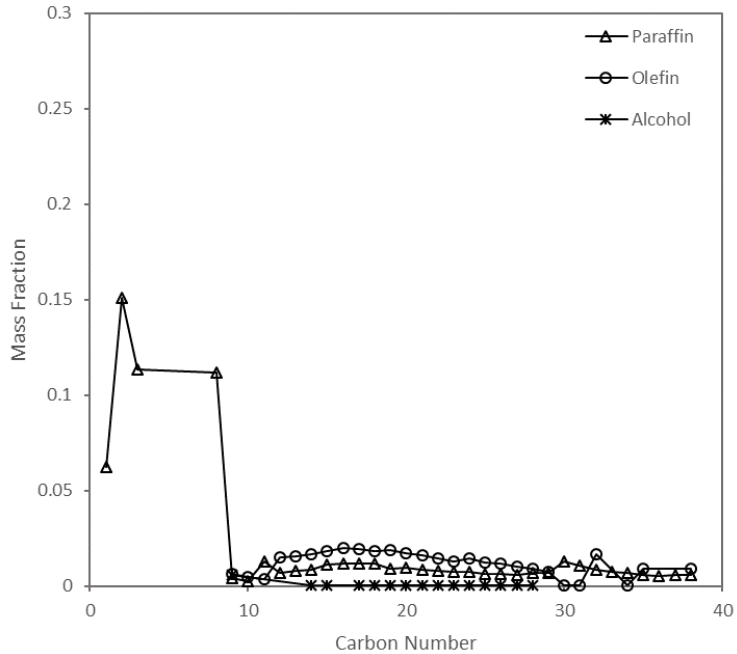


Figure 6.16: Mass fraction for combined liquid and wax products of 950-106-P.

These large mass fractions of higher chain length product unsurprisingly results in high α values for 950-106-P, as shown in Table 6.3 and Figure 6.17, where α_1 is again taken as C_1-C_3 and α_2 as C_{8+}.

Table 6.3: ASF distributions of 950-106-P.

	α_1	α_2
950-106-P Liquid	0.78	0.86
950-106-P Wax	0.78	0.91

The probably of growth for C_1-C_3 matches the reference catalyst, Cat2K, where α_1 is 0.77. The value of α_2 increases for the wax product as expected, due to the heavier components it contains. This α_2 of 0.91 is again very similar to the Cat2K α_2 of 0.89.

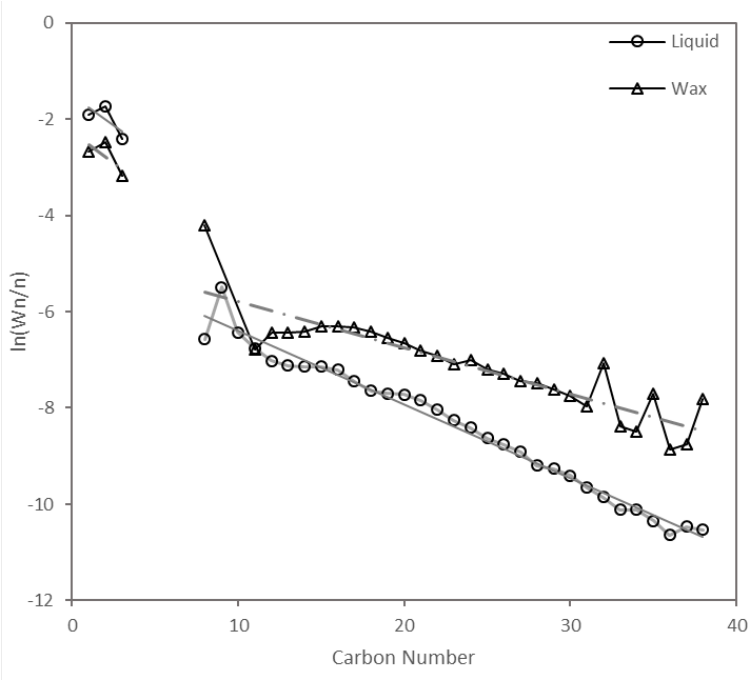


Figure 6.17: ASF distribution of liquid and wax product phases for 950-106-P.

In contrast, the 1350-106-P mass fraction of C_1-C_3 products shown in Figure 6.18 is significantly larger than for 950-106-P, with correspondingly low fractions of higher species. This high selectivity towards C_1-C_3 is expected, given the low production rates of higher hydrocarbons shown in Figure 6.13.

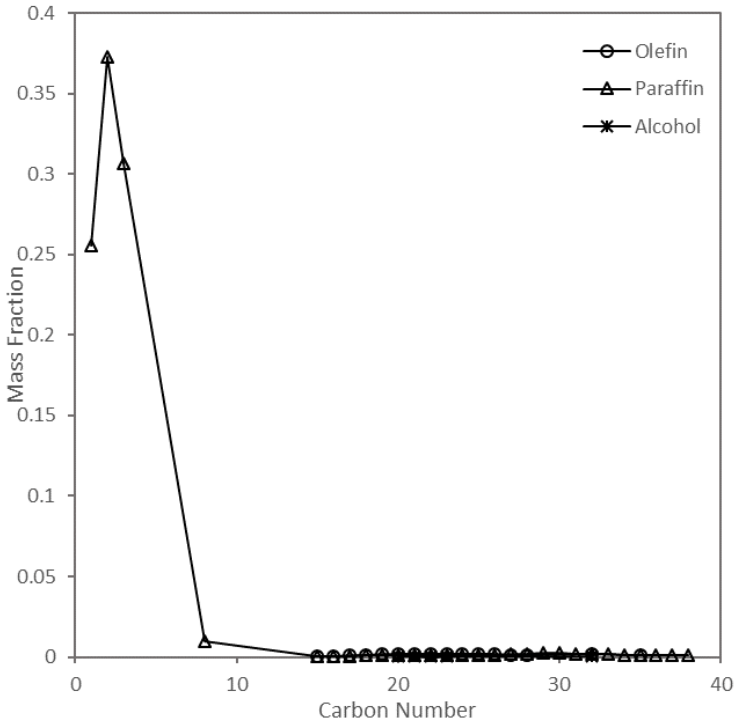


Figure 6.18: Mass fractions of product with respect to carbon number for 1350-106-P.

As expected with reduced production of the higher hydrocarbons over 1305-106-P, the value of α_1 calculated from Figure 6.19, shown in Table 6.4, is lower at 0.63 than the other catalysts tested.

Table 6.4: ASF distributions of 1350-106-P.

	α_1	α_2
1350-106-P	0.63	0.94

Unexpectedly however, the value of α_2 is higher than both Cat2K and 950-106-P at 0.94. This high α_2 value, despite the low masses of hydrocarbons produced, again suggests that the low levels of production are due to a lack of active catalytic sites rather than an alteration in the inherent catalyst activity.

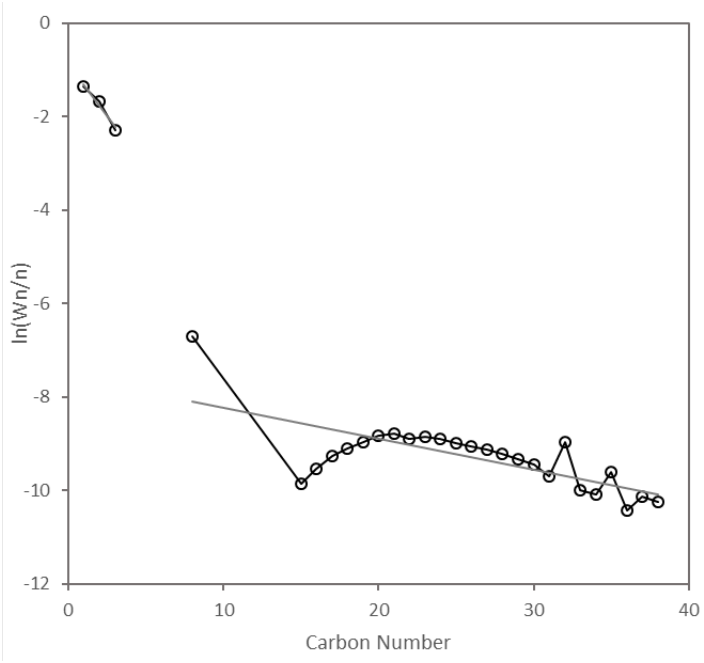


Figure 6.19: ASF distribution for 1350-106-P.

As expected with the higher chain growth probabilities and overall production rates of 950-106-P the conversion to hydrocarbon rates of 950-106-P are over an order of magnitude higher than 1350-106-P. The CO conversion of 950-106-P is over twice that seen with the co-precipitated Cat2K at the same conditions and in the top bound of the region found in literature for Fe catalysts in similar reaction conditions, suggesting that the macropore structure created by the foaming process increases production by reducing product transport limitations.

Table 6.5: Conversion to hydrocarbon rates, M_W and η values of 950-106-P and 1350-106-P.

	$mmolCOg_{cat}^{-1}h^{-1}$	$mmolH_2g_{cat}^{-1}h^{-1}$	M_W (H_2)	η
950-106-P	73.3	86.0	0.368	0.95
1350-106-P	3.1	4.4	0.019	1.00

The same equipment failure that prevented measurement of the co-precipitated catalyst density precluded densities of the foamed catalysts being taken. Work by Zheng *et al.* (in press) on the foamed particles however provided a measured porosity of 79.8% for particles calcined at 1050 °C, calculated using bulk mass, volume and Fe_2O_3 density. These were used to give an assumed foamed catalyst density of 1061 kg m^{-3}. The assumed density was used to calculate M_W and hence η of each foamed catalyst. The porosities measured using MIP in section 5.2.3 were not suitable for this calculation as they do not account for internal pore volume.

Table 6.5 shows that both 950-106-P and 1350-106-P catalysts have low or negligible diffusion resistances, indicated by η values approaching 1. The absence of small pores present in catalysts calcined at 1350 °C, as shown in 5.2.3, is partially responsible for the lack of pore diffusion seen in

1350-106-P, however the low diffusion resistances seen in 950-106-P suggests that the particle size also a factor.

6.2.2.2.2 1000 µm pellet size

The foamed catalysts were produced with the aim of improving heat transfer and activity in an industrial bed by removing the need for a support material and instead using the catalyst as monolith pellets. For this to be viable in an industrial environment without large pressure drops across the bed, the pellet size must be increased, invariably introducing mass transfer limitations. In order to test the foamed catalysts in more realistic industrial conditions the pellet size was increased to be between 1000-1250 µm.

As with the smaller catalysts discussed in section 6.2.2.2.1, a lower CO conversion is seen in Figure 6.20 for 1350-1000-P compared to 950-1000-P, but CO_2 conversions are similar.

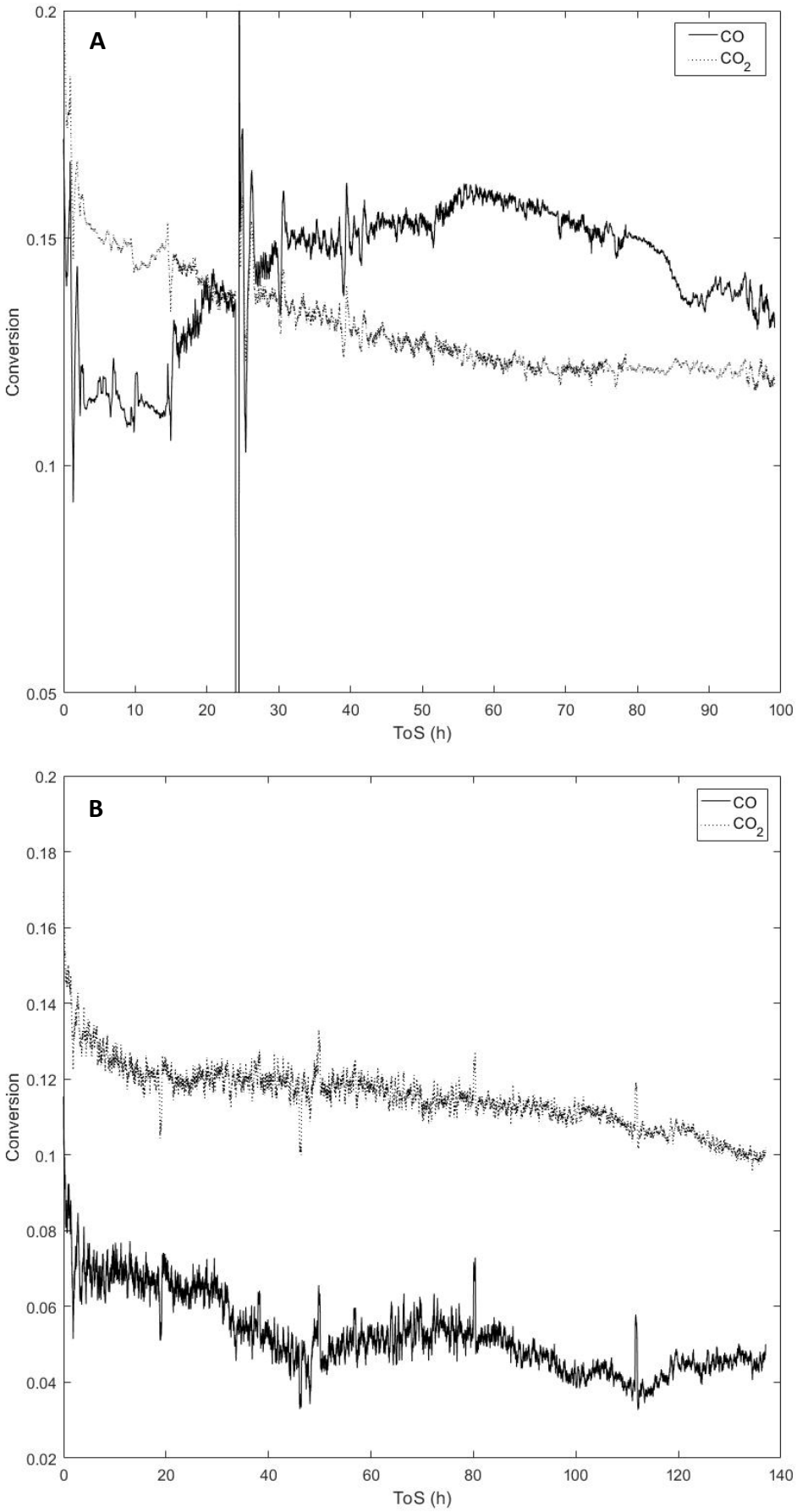


Figure 6.20: CO and CO_2 conversions for (A) 950-1000-P and (B) 1350-1000-P.

As with 950-106-P in Figure 6.10, 950-1000-P shows an initial increase in CO conversion to a maximum of 16 % at approximately 60 hours on stream, close to the estimated intrinsic maximum of 16.5 % seen for 950-106-P. Interestingly, despite initially following a similar pattern, the level of CO conversion is not maintained over 950-1000-P and drops from 16 % at 60 hours to 13 % at 100 hours. This indicates that the catalyst activity is reducing over the course of the reaction. As with 950-106-P, the CO_2 conversion drops throughout the experiment from 16 % to 12 %, once the catalyst has stabilised it remains lower than the CO conversion.

Both CO and CO_2 conversions over 1350-1000-P drop very gradually over the entire reaction period, as seen in Figure 6.20. CO and CO_2 conversions are lower than those over 950-1000-P throughout the run. The conversion profiles imitate those seen for 1350-106-P in Figure 6.10, with CO conversion dropping from 9 % to 5 %, and CO_2 conversions from 15 % to 10 %, and the CO_2 conversion higher than that of CO throughout. This suggests the mass transfer limitations introduced with the larger catalyst pellets are not the limiting factor for this catalyst.

Although the C_1-C_3 concentrations for 950-1000-P and 1350-1000-P shown in Figure 6.21 concur with the indications made by the CO and CO_2 conversions in Figure 6.20, with 950-1000-P generating approximately double the concentration of hydrocarbons compared to 1350-1000-P, the H_2O concentration profile does not follow the C_1-C_3 profiles in the same way as for the smaller catalysts in Figure 6.11. In both cases the H_2O concentration remains below 300 ppm throughout, considerably lower than the 700-900 ppm generated by both 950-106-P and Cat2K. The profile is also variable throughout the reaction, including significant peaks that are unrelated to C_1-C_3 concentration changes. This suggests that over these larger catalyst particles the generation of H_2O through hydrogenation of CO and CO_2 is no longer the determining influence on H_2O concentration. Offline GC-MS/FID analysis of the gas produced from 950-1000-P confirmed the presence of C_1-C_8 hydrocarbons.

At the end of the runs 8.7 mg of wax was collected for 950-1000-P and 101.4 mg for 1350-1000-P. Despite the slightly lower C_1-C_3 production levels for 1350-1000-P shown in Figure 6.21, the distribution of solid products from C_{10+} are similar for both catalysts as shown in Figure 6.22. The C_1-C_3 production rate for 950-1000-P however is significantly higher than that of 1350-1000-P, as expected from Figure 6.21.

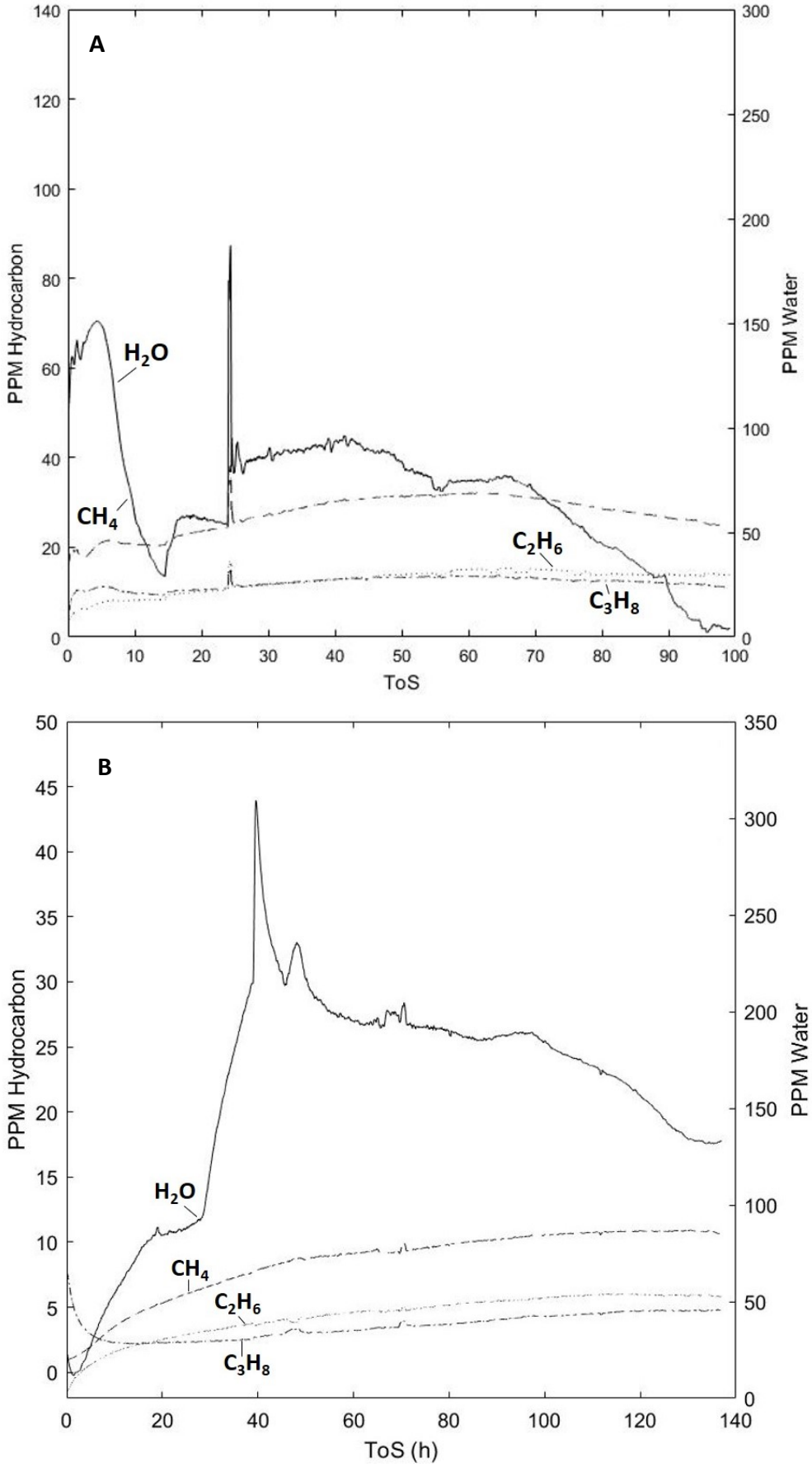


Figure 6.21: C_1-C_3 and H_2O concentrations for (A) 950-1000-P and (B) 1350-1000-P.

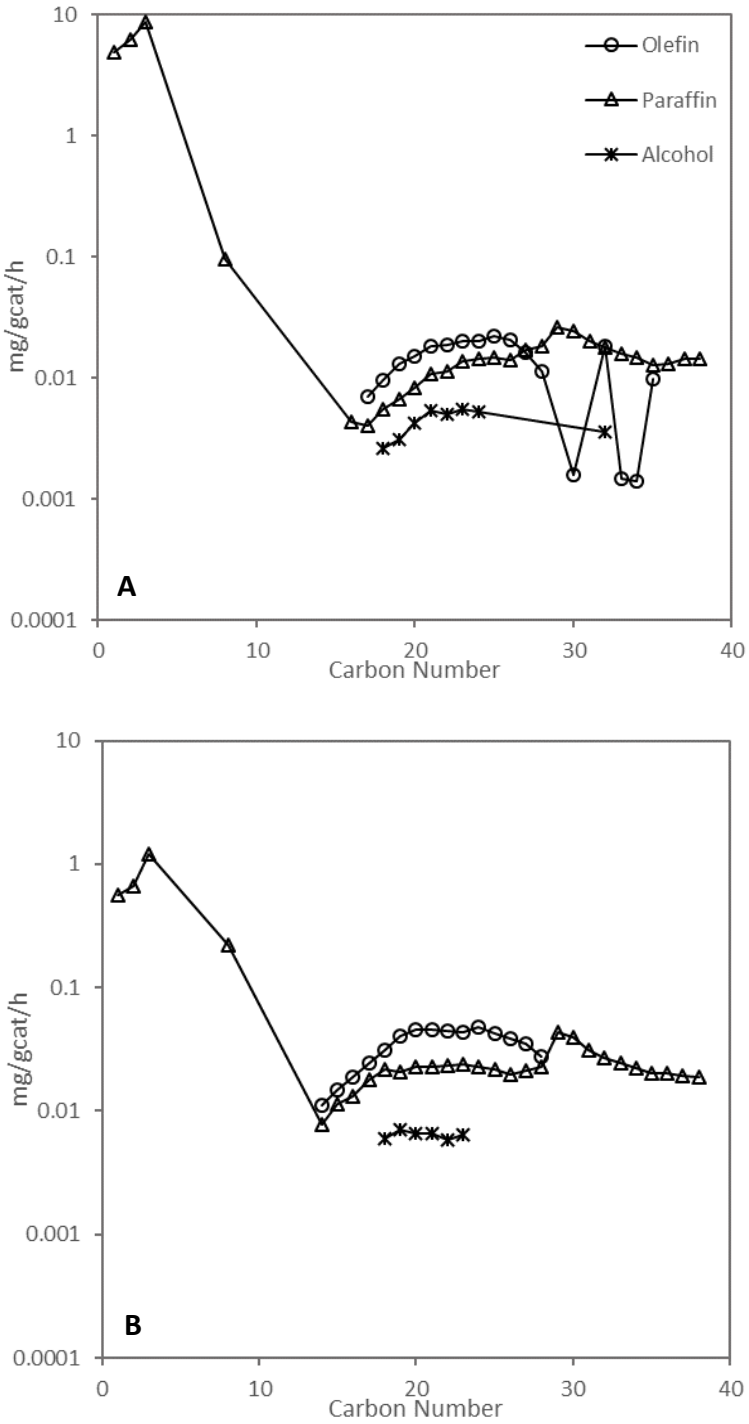


Figure 6.22: Production rates with respect to carbon number of (A) 950-1000-P and (B) 1350-1000-P.

As with all the other catalysts tested, for both 950-1000-P and 1350-1000-P, olefins are initially the primary product, followed by paraffins and alcohols. As carbon number increases the ratio of olefins to paraffins begins to drop. Beyond C_{30} the measured production rate for olefins becomes noisy, with values for C_{32} and C_{35} notably higher than expected with the previous trend exhibited. It is suggested these two results are due to noise between the olefin and paraffin peaks at these higher chain lengths, causing false high readings of olefin production.

The higher production rates of C_1-C_3 over 950-1000-P result in a depression of mass fraction of the higher hydrocarbons compared to 1350-1000-P, as shown in Figure 6.23. The largest product fraction is C_3 for both, for the smaller catalyst particles the main product by mass was C_2.

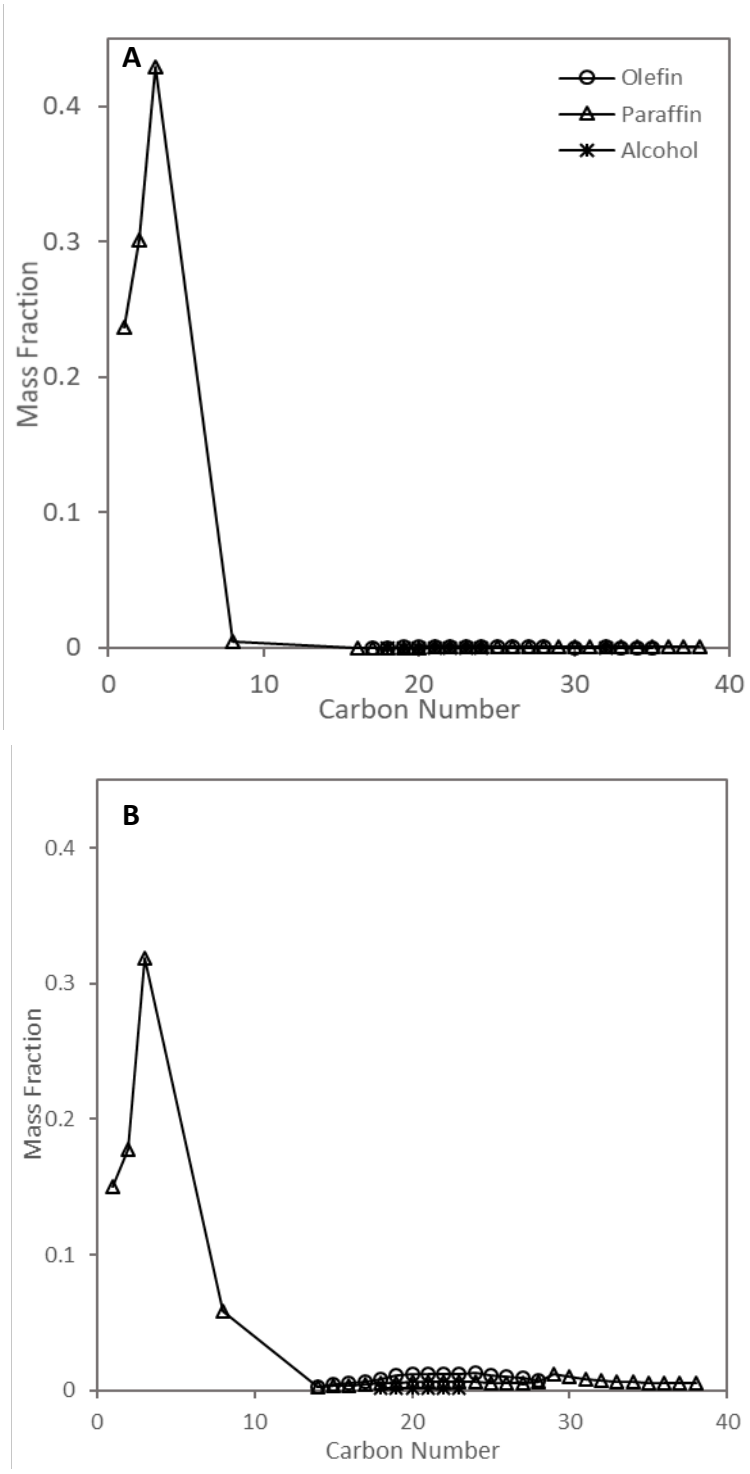


Figure 6.23: Mass fractions of (A) 950-1000-P and (B) 1350-1000-P.

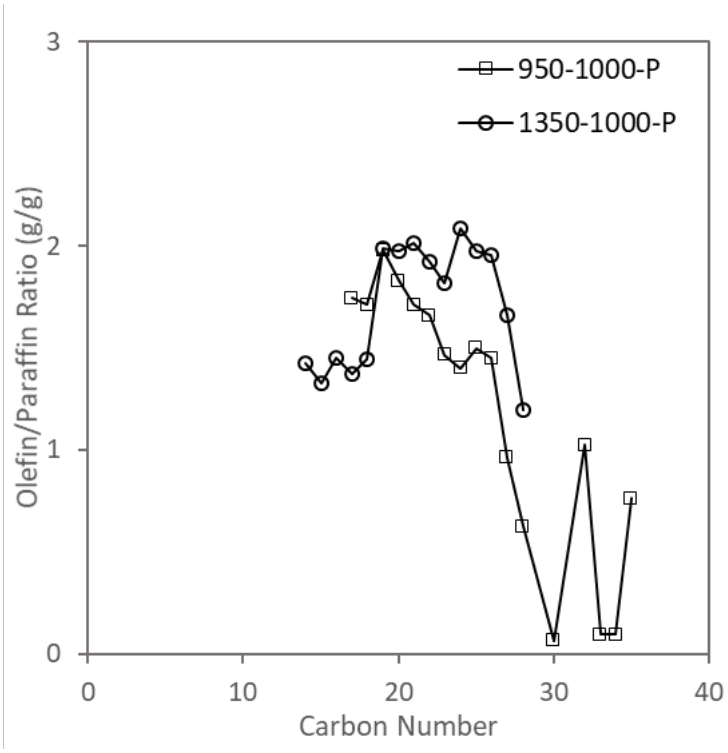


Figure 6.24: Olefin: Paraffin ratio for 950-1000-P and 1350-1000-P.

The similar product distribution of 950-1000-P and 1350-1000-P results in comparable olefin to paraffin ratios between approximately 1 and 2 for chain lengths between C_{10}-C_{30}, as shown in Figure 6.24. Longer chain length olefins are not seen for 1350-1000-P, and olefin production levels for carbon numbers of 30+ over 950-1000-P drop significantly, as was previously seen for 1350-106-P and the co-precipitated catalysts seen in Figure 6.15 and Figure 6.6 respectively. The noise seen for 950-1000-P above C_{30} is due to the variations in olefin production rate discussed with Figure 6.22.

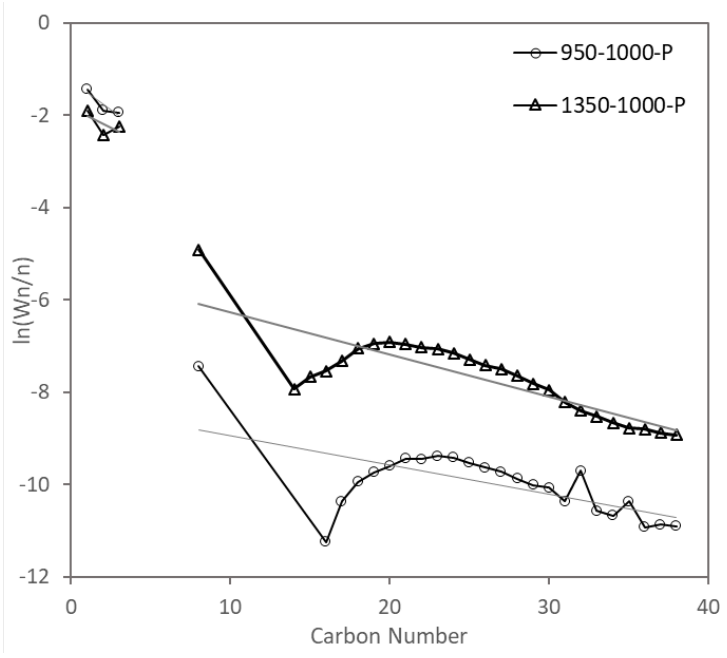


Figure 6.25: Double ASF model for 950-1000-P and 1350-1000-P.

The probabilities of growth, α_1 and α_2, are calculated for 950-1000-P and 1350-1000-P from Figure 6.25 and shown in Table 6.6.

The short chain value, α_1, of 950-1000-P is similar at 0.78 to that of both 950-106-P and the co-precipitated catalysts at 0.77 and 0.78 respectively. The value for 1350-1000-P is higher at 0.84, consistent with the larger mass fractions of higher hydrocarbons seen in Figure 6.23, compared to 950-1000-P. This increased probability for 1350-1000-P is not maintained for the longer chain lengths though, with 950-1000-P having a slightly higher α_2 value of 0.94 to that of 1350-1000-P at 0.91.

Table 6.6: ASF distributions for 950-1000-P and 1350-1000-P.

	α_1	α_2
950-1000-P	0.78	0.94
1350-1000-P	0.84	0.91

These variations are within the limitations of the calculation technique, particularly as Figure 6.25 shows it is uncertain whether the measurement for C_8 should be included in the calculation for α_1 or α_2. For continuity the carbon ranges for α_1 and α_2 have been kept at C_1-C_3 and C_{8+} respectively, as used for the other catalysts tested. Allowing for the slight variations, values of α_1 and $\alpha_{2\ for}$ both 950-1000-P and 1350-1000-P match reasonably well with those calculated for 950-106-P and Cat2K.

Again, with the higher chain growth probabilities and overall production rates of the 950 °C catalyst, the conversion to hydrocarbon rates of 950-1000-P are almost an order of magnitude higher than 1350-1000-P. The larger 1000-1250 μm particles of promoted foamed catalyst show a lower conversion than their 106-300 μm counterparts, suggested to be due to the introduction of mass transfer limitations with the bigger catalyst pellets

Table 6.7: Conversion to hydrocarbon rates, M_W and η of 950-1000-P and 1350-1000-P.

	$mmolCOg_{cat}^{-1}h^{-1}$	$mmolH_2g_{cat}^{-1}h^{-1}$	M_W (H_2)	η
950-1000-P	28.9	39.4	5.33	0.19
1350-1000-P	5.9	7.3	0.99	0.85

The calculated values of η in Table 6.7 and Table 6.5 show that the diffusion resistances of both 950-106-P and 1350-106-P catalysts have increased significantly, with 950-1000-P experiencing strong pore resistance. As discussed in section 6.2.2.2.1, the higher value of η for the foams calcined at 1350 °C is due to the absence of small pores in these particles. However, clearly the larger particle size introduces diffusion limitations for both calcination temperatures.

6.3 Conclusions

6.3.1 Reference Catalyst

Initial tests with the reference catalysts, PreCat and Cat2K, show that the co-precipitated catalysts both have activity for the hydrogenation of CO and CO_2. After a preliminary settling in period of approximately 20 hours the CO conversion increases before becoming steady at approximately 60 hours at 9.0 % and 16 % respectively, indicating that the catalyst is reaching a steady state of activity. The CO_2 conversion slowly drops with time for both PreCat and Cat2K to 12 % and 7.2 % at the conclusion of the 100 hour run. Literature values for steady state CO and CO_2 conversions over the reference catalyst Cat2K at the same reactor conditions are given as 14.1 % and 8.9 %. These values are considered to be within the scope of error calculated in section 3.10, particularly when the lower surface area of Cat2K compared to that quoted in the reference paper is considered. The increase in CO and CO_2 conversion rates with K promotions also correlates with the higher conversions recorded in literature for a rise from 2% K to 4% K promotion.

FTIR traces for the lower hydrocarbons, C_1-C_3, and H_2O confirm that the increased CO and CO_2 conversion with catalyst promotion translates into increased hydrocarbon generation. For both PreCat and Cat2K it is apparent that the pattern of production of these 4 species are closely related. This allows the concentration of the two main products, CH_4 or H_2O, to be used as initial indicators of hydrocarbon production and catalyst activity.

Offline analysis of the total product shows that promotion increases the production rate throughout the range of hydrocarbons produced. As found in the literature results, CH_4 has the largest product mass fraction for both catalysts, and olefins are the primary product species overall. Olefin to paraffin ratios of approximately 2.5 for both PreCat and Cat2K at C_8 compare well with the reference value of approximately 2.3 at C_8. Both experimental and reference ratios then drop as carbon number increases, to below 1 at C_{28}.

A double ASF model is used to fit the product distributions for both catalysts tested, with α_1 taken as C_1-C_3 and α_2 as C_{8+}. Although α_1 increases upon promotion, from 0.68 to 0.77, α_2 values remain similar at 0.90 and 0.89 respectively. These closely match the probabilities of growth in the reference of 0.63 for α_1 (C_1-C_6), and 0.89 for α_2 (C_{7+}). Conversion rates of CO and H_2 to hydrocarbons show that the promoted Cat2K has a significantly higher conversion to hydrocarbons rate of 34.4 mmolCO g_{cat}^{-1} h^{-1} compared to 8.0 mmolCO g_{cat}^{-1} h^{-1}.

In conclusion, promotion of the co-precipitated PreCat is shown to increase CO and CO_2 conversion and hydrocarbon production rates without significantly altering the range of hydrocarbons produced. Experiment results for the Cat2K run give similar production rates to reference data in literature for Fe catalysts. Production patterns and probability of growth factors are deemed within experimental

variation. The reaction rig is therefore regarded to be a suitable testing environment for further FT catalysts.

6.3.2 Foamed Catalysts

The four unpromoted foam catalysts, 950-106-U, 950-1000-U, 1350-106-U and 1350-1000-U, show little CO or CO_2 hydrogenation activity with conversion rates approaching zero. Small amounts of CH_4 were detected, with only 950-106-U reaching above 5 ppm CH_4. Higher hydrocarbons were not detected through FTIR or gaseous GC-MS/FID analysis, and no liquid or solid product was produced for any of the unpromoted foams. It is concluded that the unpromoted foamed catalysts have little FT catalytic activity and that the physical variations in the catalysts, e.g. pellet size and calcination temperature, have little effect on the unpromoted catalyst behaviour.

The promoted foams, 950-106-P, 950-1000-P, 1350-106-P and 1350-1000-P, all demonstrated some level of FT activity. CO conversion rates are higher over the catalysts calcined at 950 °C, with maximum conversions of 16.5 % and 16 % reached for 950-106-P and 950-1000-P respectively. The slight loss of CO conversion for 950-1000-P is attributed to the larger pellet size causing mass transfer limitations within the catalyst particle, as shown by the reduction in effectiveness factor with increasing particle size. CO conversions over the 1350 °C catalysts are notably lower, remaining below 10 % throughout for both 1350-106-P and 1350-1000-P. This reduced CO conversion over the 1350 °C foams is unsurprising considering the findings in chapter 0, where the increased calcination temperature has resulted in the loss of the microporous structure and hence a significant reduction in surface area. Since the CO must dissociatively adsorb onto the surface, the loss of potential active sites causes a decrease in CO conversion.

CO_2 conversions remain similar for all four promoted foams, showing a steady decrease in conversion over the experimental period. Initial CO_2 conversions are slightly higher for the 950 °C foams at approximately 16 %, compared to those seen over the 1350 °C foams of approximately 14 %. This is again attributed to the higher surface area of the 950 °C catalysts. The closing rates of CO_2 conversion at the end of the experiments are all similar, in the region of 10-12 %. No discernible difference is noted between the small and large pellet sizes, suggesting that CO_2 hydrogenation is not mass transfer limited. This concurs with findings by Martinelli *et al*., who determined that CO_2 conversion is low in an excess of strongly adsorbing CO[146].

As expected from the CO and CO_2 conversions above, higher concentrations of C_1-C_3 and H_2O were measured for the 950 °C foams compared to the 1350 °C foams at both particle sizes. Increasing the pellet size approximately halved the C_1-C_3 concentrations for each temperature group. Only 950-106-P matched the C_1-C_3 production of the reference Cat2K, which was maintained from approximately 30 hours. For the other promoted foamed catalysts, the H_2O concentration measured was less than 50 % of that generated with 950-106-P. For these a gradual drop in H_2O concentration is seen in the final

30 hours of the experiment. It is thought that this is due to residual H_2O being slowly removed from the FTIR gas chamber.

As the increased C_1-C_3 concentrations suggest, 950-106-P generated significantly more higher hydrocarbons than the others. It was also the only catalyst for which a two-phase liquid/wax product was seen. Production rates of C_1-C_3 were higher for both the 950 °C catalysts, however C_{8+} production remained largely similar for all except 950-106-P which was 2 orders of magnitude higher. This led to a notably larger selectivity to C_{8+} products over 950-106-P compared to all the other catalysts. The higher C_1-C_3 production for 950-1000-P, despite generating a similar quantity of higher hydrocarbons to 1350-1000-P, resulted in higher CH_4 selectivity. The high overall activity of 950-106-P resulted in CO and H_2 to hydrocarbon rates over double that of the validation catalyst, Cat2K, at 73.3 mmolCO g_{cat}^{-1} h^{-1} and 86.0 mmolH_2 g_{cat}^{-1} h^{-1}. The effectiveness factor for 950-106-P was found to be 0.95, indicating that this particle size had low diffusion resistances and gives a close to intrinsic reaction rate. Rates were also high for 950-1000-P, matching the Cat2K values at 28.9 mmolCO g_{cat}^{-1} h^{-1} and 39.4 mmolH_2 g_{cat}^{-1} h^{-1}, despite being larger particles and displaying transport resistances as shown by a reduced effectiveness factor of 0.19, indicating strong pore diffusion. This suggests the promoted foamed catalyst calcined at 950 °C has an inherent activity over four times that seen in the reference Cat2K.

All catalysts generated olefins as the primary product, followed closely by paraffins and alcohols. Olefin to paraffin ratios began to drop for chain lengths above C_{28}. A double ASF model was used to fit the product distributions for all the catalysts tested, with α_1 taken as C_1-C_3 and α_2 as C_{8+} as per the reference catalysts in section 6.2. The four promoted catalysts gave similar probabilities of growth, with α_1 in the range of 0.77-0.84 for all bar 1350-106-P which was low at 0.63. This lower value is probably due to the lack of measurement points from which to generate a best fit line. Values for α_2 were all in the range 0.86-0.94. These values of α are close to that measured over the reference catalyst, where α_1 was 0.77 and α_2 0.89. The lack of change with pellet size and calcination temperature suggests that the reaction mechanism and intrinsic catalyst activity is not drastically altered by these features. Far more limiting is the reduction in surface sites on catalysts calcined at 1350 °C, and mass transfer limitations introduced with larger pellet size.

7 Modelling the Fischer-Tropsch Reaction Over a Fixed Bed

In order to design and operate a reactor optimally, knowledge of the reaction itself, and how it will respond, is required. Mathematical models can allow predictions of reactor behaviour to be made before finalising the design or making operational changes.

This chapter presents two reaction models for FTS over a fixed bed, allowing for contraction of the gas phase and consequent reduction in velocity during reaction. The initial model is a simplified pseudo-homogeneous isothermal reactor, assuming steady state. The model is then expanded to include solid catalyst particles, temperature variations and allow the investigation of dynamic responses to reactor conditions.

7.1 Introduction

7.1.1 Model Types

Many models of the FT reaction currently exist, covering a variety of features, reactor types and complexities. For fixed bed reactors however, there are several basic classes of model with varying complexity. Some types of existing FTS models are briefly reviewed below.

The simplest model is the one-dimensional pseudo-homogeneous model, in which the effects of heat and mass transfer are assumed to be common for the reactants, products and catalyst. Temperature and concentration differentials are only considered in the axial direction, usually with no axial diffusion accounted for. The kinetics employed here vary from simple power laws[160], to more complicated FTS specific rate expressions such as the Yates-Satterfield model[161]. Since these models do not account for the catalyst phase or axial diffusion they are often used when the temperature profile of the reactor is not important or mass transfer limitations are deemed insignificant. This allows the models to solve quickly and means different reactor types can be compared under the same model[161]. They are useful to validate reaction kinetics; however, they lack accuracy due to the assumption that reaction properties are independent of temperature and reactor location.

The addition of a second, radial, dimension to the pseudo-homogeneous model increases the accuracy of the heat and mass transfer predictions, however without considering the catalyst phase this benefit is limited and does not always account for diffusion of heat and mass in either or both directions[162]. The common use of simple expressions for reaction rate also limits the gain from the second dimension[163].

Next is the inclusion of separate mass and energy balances for the solid catalyst to produce a heterogeneous model. The temperature and concentration within the particle can either be assumed to be constant, taking account of interfacial gradients only, or integrated in the balances giving interfacial and intraparticle gradients. Although this gives a more realistic representation of the variations in concentration and temperature, the models are still limited by the accuracy of the reaction kinetics, such

as the simplified power law[164]. Radial variations are not accounted for and therefore reactors designed to validate these models must be designed so that radial flow profiles are close to ideal[165].

Finally, the inclusion of a second dimension to the heterogeneous model gives yet more detail. The most complex models account for axial and radial diffusion of heat and mass, as well as intraparticle transfer limitations. The additional complexity can make the model cumbersome and unwieldy, particularly if dynamic responses are of interest. Often to reduce the processing power and time required the reactions kinetics are simplified, meaning these models are perhaps better suited to evaluating thermal behaviour than for validating kinetic models.

7.1.2 Variable Density Reactions

Other considerations to account for when choosing a model are the reaction type, phase and conditions. These affect the reaction behaviour and can result in different aspects of the model, e.g. heat transfer, being of particular interest. In this case, the FT reaction is a polymerisation reaction, with dissociatively adsorbed CO and H_2 reacting on the catalyst surface to produce chain initiators (CH_3) and methylene monomers (CH_2) which insert into growing hydrocarbon chains. In order to produce a single alkene molecule of carbon length n, 3n reactant molecules are required. Although the ratio for a mix of hydrocarbons is slightly different, the overall result is that FTS is a contracting reaction, with fewer moles of product generated than moles of reactant consumed. Condensation of products, as is common in a gas-to-liquids reaction like FTS, further exacerbates this volume reduction, as the liquid specific volume is negligible to that of the gas. The extent of the contraction is dependent on the type of product and the chain length of the final hydrocarbon produced. In a fixed bed reactor with plug flow this results in a reducing gas velocity down the reactor bed

Since the FT reaction is also highly exothermic, the reduced volumetric flowrate means that the heat generated through the reaction is concentrated in a smaller section of the bed. This concentration of heat can cause hot spots within the bed, this can both damage the catalyst but also alter the highly temperature sensitive product distribution. In extreme cases, runaway reactions can develop as the reactor temperature profile becomes unstable. Levenspiel described a graphical design method accounting for variable density in gaseous systems using the expansion factor, ε, and using a key reactant to model the conversion[181]. The expansion factor can be calculated by

$$\varepsilon = \frac{v_{final} - v_{initial}}{v_{initial}} \qquad 7.1$$

Where *v* is the volumetric flowrate. It has been suggested that the added complexity and need for design charts means that the density variation is often ignored in industry[166]. In the course of an extensive literature review only the Turek group were found to utilise an FT model accounting for contraction on reaction. The Turek model was used to review novel reactor types and does not address dynamic reactor behaviour or temperature excursions[167].

Density variations can cause changes in reaction rates, temperature and therefore product distributions for an exothermic, temperature sensitive reaction such as FT. It was therefore decided to produce a model that accounts for contraction and allows a dynamic assessment of the response to reaction conditions.

7.1.3 Transient Responses and Wrong Way Behaviour

Packed bed reactors can undergo interesting transient responses to changes in conditions that can only be investigated through dynamic analysis. Of particular interest is the inverse response of bed temperature to a sudden change in an inlet variable, known as wrong way behaviour.

The occurrence of wrong way behaviour in packed beds has been studied since 1966 when Crider and Foss first predicted the inverse response[168]. The shift is caused by differences in the transfer speeds of temperature and concentration changes down the reactor due to the high thermal inertia of the bed. This causes the mass front to propagate more quickly along the bed than the thermal front, resulting in an isothermal pseudo-steady state at the inlet of the bed which slowly develops into the true steady state response. Evidence of wrong way behaviour in a fixed bed was later observed experimentally by Sharma and Hughes for the oxidation of carbon monoxide[169] and Doesburg and De Jong in the methanation of carbon monoxide and carbon dioxide[170], amongst others.

A typical example of wrong way behaviour is shown in Figure 7.1, where the dynamic response to a drop in dimensionless inlet feed temperature from y_{f1} to y_{f2}, is modelled by the one dimensional heterogeneous model described by Luss *et al.*[182]. The progression of the temperature transient along the dimensionless axial position is clearly visible, as is the wrong way behaviour, where a drop in feed temperature produces a temperature peak higher than that seen in the original steady state. This peak moves along the bed axially as dimensionless time, t, increases and the new steady state is reached.

The wrong-way behaviour develops as the entry section of the bed is cooled by the lower temperature feed, giving a reduced extent of reaction in that section of the bed. This results in a higher concentration of reactants moving along to areas where the bed has not yet cooled, heating the unreacted feedstock and igniting reaction. Since the reaction begins with a higher concentration of reactants than normally seen in that area of the bed, the change in temperature due to reaction is more extreme and gives a temperature peak in the case of exothermic reactions. This temperature peak moves along the bed with the concentration front, the thermal front caused by the cooled feed follows at a slower velocity, moving the bed to its new steady state.

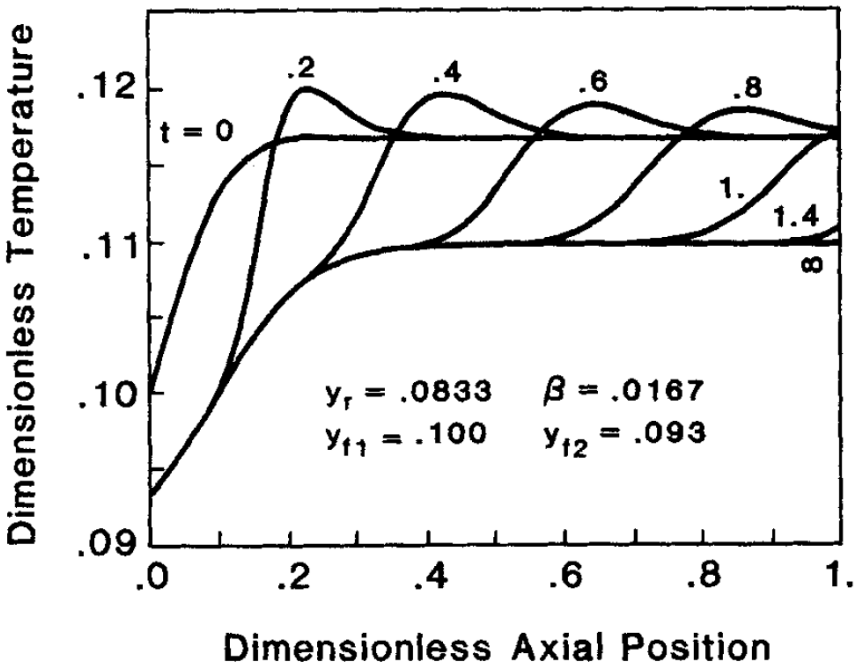


Figure 7.1: Dynamic wrong way response to drop in inlet feed temperature, y_f, as modelled by Luss et al. Reprinted from AIChE Journal, vol. 35, 7, Luss et al.[182], copyright (2004), with permission from Wiley.

Sinai and Foss later showed that the transient response of a packed bed is determined by the ratio of the thermal wave velocity to the fluid velocity[171], which was expanded upon by Kulkarni and Dudukovic to explain that a short characteristic heat transfer time relative to the characteristic reaction time allows the reactants to heat appreciably before any significant reaction takes place[172].

The differences in the propagation speed of these fronts within the bed have implications for the operation of fixed beds during transient periods such as start-up, shut down and feed alterations[173]. This is particularly true for gas-solid reactions common in industry where the solid phase often has a heat capacity three orders of magnitude higher than that of the gas phase[164].

Luss *et al*. have produced extensive work on the influences of wrong way behaviour, investigating the benefits of heterogeneous over pseudo-homogeneous models, the effect of interphase transport[182], reaction type[177], subsequent reactions and reactant/support interactions[174]. Chen and Luss also looked at the effect of intraparticle resistances[176], Almeida-Costa *et al.* investigated intraparticle conversion[175], whilst Dudukovic *et al*. looked at heterogeneous reactions taking place in both the solid and gas phase[164]. The work done by Luss *et al*. on dynamic responses of packed beds found that a one dimensional heterogeneous model accounting for axial diffusion allowed accurate predictions of transient behaviour even in reactions that experience multiple steady states[176], with a second dimension significantly increasing computational complexity without particularly altering temperature profiles. This assumption remains valid for small diameter beds, where the radial temperature gradient is negligible compared to the axial variations.

Changes in several inlet variables can give rise to an inverse temperature response, including feed temperature, concentration and flowrate[161,162]. The following sections will focus on the more common occurrences in industry, loss of feed heating or feed flow. These situations are encountered regularly during start up, shut down and whilst varying conditions during normal operation.

7.1.3.1 Temperature Variation

The most common cause of wrong way behaviour documented in literature is a drop in feed temperature. Under certain conditions this can cause a high temperature peak to travel down the bed as a plug of unreacted feedstock gains sufficient heat from the hot bed downstream to begin reacting, before the new steady state profile is eventually reached. Key parameters affecting the magnitude of the inverse response to a sudden inlet temperature drop were found by Mehta *et al*. to be the adiabatic temperature rise, wall temperature, activation energy, heat transfer and the magnitude of the temperature drop[177].

7.1.3.2 Loss of Feed Flow

The majority of the literature looking into wrong way behaviour focuses primarily on changes in feed temperature, however a well-known dangerous operating point for exothermic reactions over fixed beds is when the reactor is shut in, for example during a reactor block-in trip or unexpected shutdown. When this happens the feed gas is largely stationary over a still hot bed, allowing for overheating and reaction of the stagnant feed, and can result in localised temperature excursions. To exacerbate matters, the feed valve is often significantly upstream of the reactor, giving a dead volume of unreacted feed gas upstream of the catalyst bed, as demonstrated in Figure 7.2. This volume of unreacted gas enters the reactor slowly as it mixes and expands due to heating, and in the case of contracting reactions, the downstream pressure falls. Tight shut off in large industrial scale upstream valves is also difficult to obtain and so often a small flow of feed will leak through to the reactor. Typical leakage rates expected in industry can range from 1-10% of design flow depending on the valve specifics.

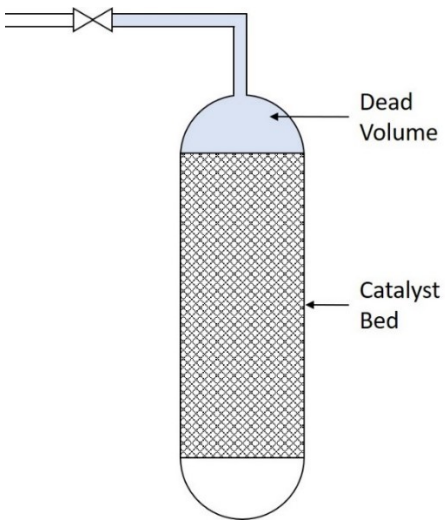


Figure 7.2: Schematic of dead volume of gas available for reaction on a feed trip.

In industry pilot plant experiments are usually performed to determine the extent of any temperature changes[178]. The level of testing required to accurately predict reactor behaviour is expensive and time consuming, a suitable model can reduce the number of, intensity, and hence cost, of live testing required.

Although many of the studies into wrong way behaviour reviewed above looked at heterogeneous catalytic systems, none considered the effect of variable velocity seen in many gas phase and gas to liquid reactions such as FT that are common over fixed beds.

This chapter aims to remedy this by examining the effect of contraction on dynamic responses to inlet conditions over fixed beds using a dynamic model derived for the purpose. The dynamic model refers to work done by Luss *et al*. and is extended to allow for temperature-dependent gas density and gas contraction during reaction[176].

7.2 Steady State Isothermal Pseudo-homogeneous Model

A simplified homogeneous one dimensional model of the FTS reaction was initially derived, estimating the steady state concentration profile within the bed and modelling the effect of contraction. Pseudo-first order kinetics were assumed, taken from work by Post *et al*. on fixed bed FTS limitations which gives the rate equation below[179].

$$-r_{CO} = k_{CO} C_{H2}^{1} C_{CO}^{0} \qquad 7.2$$

Where k_{CO} is the rate constant with respect to CO ($m^3.m^{-3}cat.s^{-1}$) and C_i the concentration of *i* ($mol.m^{-3}$). Since the rate is independent of C_{CO} the model only need feature C_{H2}.

Ruthven describes a non-isothermal axially dispersed fluid, packed bed, steady state plug flow model for species *i* [180], as shown in equation $0 = -\frac{\partial}{\partial z}(uC_i) + \frac{(1-\xi)}{\xi} r_i$ 7.3.

$$0 = -\frac{\partial}{\partial z}(uC_i) + \frac{(1-\xi)}{\xi} r_i \qquad 7.3$$

Where z is segment length (m), u interstitial fluid velocity ($m.s^{-1}$), ξ the bed voidage and r_i the rate of generation of *i* ($mol.m^{-3}cat.s^{-1}$).

Since the pressure drop down the bed is negligible compared to the inlet pressure, it is assumed that the reaction pressure is maintained during the reaction, meaning the volumetric flow will reduce as the gaseous reactants are converted to significantly denser liquid products. Levenspiel gives X_i, the extent of reaction, as a factor of molar flowrates in and out of a segment, which can then be described using volumetric flowrates and hence interstitial velocities[181]. Rearranging this to include the expansion factor, ε, gives C_i as a function of ε_i:

$$C_i = C_{i,0} \frac{(1-X_i)}{(1+\varepsilon_i X_i)} \qquad 7.4$$

The derivative of equation 7.4 is used to modify the terms of equation 7.30 $= -\frac{\partial}{\partial z}(uC_i) + \frac{(1-\xi)}{\xi} r_i$ 7.3 to be in terms of X_i.

Simplifying the resulting equation, neglecting axial diffision and defining the characteristic length, Z, then gives the complete, dimensionless model.

$$0 = -\frac{(1+\varepsilon_i X_i)^2}{(1+\varepsilon_i)}\frac{\partial X_i}{\partial Z} - \frac{L}{u_0}\frac{(1+\varepsilon_i X_i)^2}{(1+\varepsilon_i)}\frac{(1-\xi)}{\xi C_{i,0}} r_i \qquad 7.5$$

Where the dimensionless axial length is described as follows, with L as the total bed length (m).

$$Z = \frac{z}{L} \qquad 7.6$$

Post *et al*. described the rate of H_2 consumption in the FT reaction in terms of the usage ratio, UR, of H_2/CO, which allows the conversion between k_{H2} and k_{CO} [179].

$$r_H = -URk_{CO}C_H = -URk_{CO}C_{H,0}\frac{(1-X_H)}{(1+\varepsilon_H X_H)} \qquad 7.7$$

$$0 = -\frac{(1+\varepsilon_H X_H)^2}{(1+\varepsilon_H)}\frac{\partial X_H}{\partial Z} + \mathrm{Da}\frac{(1+\varepsilon_H X_H)(1-X_H)}{(1+\varepsilon_H)} \qquad 7.8$$

Where Da is the Damköhler number, relating the reaction rate to the mass transport rate:

$$Da = \frac{L}{u_0}\frac{(1-\xi)}{\xi} URk_{CO} \qquad 7.9$$

The model can be further manipulated to portray the extent of reaction down the reactor bed at steady state by simplifying and integrating equation 7.8 with respect to Z. The result is given in equation 7.10.

$$DaZ = -ln(1-X_H)\left[(1+\varepsilon_H X_H) + \varepsilon_H(1-X_H)\right] - \varepsilon_H X_H \qquad 7.10$$

7.3 Dynamic Model

In order to give a more complete, dynamic, analysis, the pseudo-homogenous model was further developed to produce a one dimensional, heterogenous model including axial diffusion.

Since the heat transfer within the catalyst particle is rapid compared to the interphase transfer, the particle is considered isothermal. Concentration changes within the particle are also faster than both concentration and temperature changes in the bulk, so the particle concentration is also assumed to be in a pseudo-steady state with respect to temperature. An isothermal effectiveness factor is therefore used to model the particle concentration profile, and the particles are modelled as spherical pellets[182].

The variation in the volume of a plug of gas as it passes down the bed, and hence interstitial velocity, u, of the plug is taken into account by including an equation describing the variation of u with respect to both reaction and reactor temperature, assuming ideal gas behaviour and constant fluid heat capacity.

Assuming a first order, irreversible, surface-based reaction that experiences expansion, ε, the following mass and energy balances referencing the hydrogen mol fraction can be derived.

$$\frac{d\left(\frac{x_{H_2}}{V_M}\right)}{dt} = -\frac{1}{\xi}\frac{d\left(\frac{x_{H_2}u}{V_M}\right)}{dz} + \frac{D}{\xi}\left(\frac{1}{V_M}\frac{dx_{H_2}}{dz}\right)\frac{1}{dz} + \left(x_{H_2S} - x_{H_2}\right)\frac{k_m 3(1-\xi)}{\epsilon r_p V_M} \quad 7.11$$

$$\frac{dT}{dt}\left(\rho_f c_f\right) = \frac{-\rho_f c_f}{\xi}\frac{d(Tu)}{dz} + \frac{\lambda}{\xi}\frac{d^2T}{dz^2} + (T_s - T)\frac{3h(1-\xi)}{r_p\xi} + (T_w - T)\frac{2h_w}{r\epsilon} \quad 7.12$$

$$k_m\left(\frac{x_{H_2S}}{V_M} - \frac{x_{H_2}}{V_M}\right)(1-\xi)\frac{3}{r_p} = \eta(y_s)k_0\frac{x_{H_2S}}{V_{Ms}}e^{\left(\frac{-E}{RT_s}\right)} \quad 7.13$$

$$\frac{d}{dt}\left(\rho_p c_p T_s(1-\xi)\right) = h(T - T_s)\frac{3(1-\xi)}{r_p} + \eta(y_s)k_0\frac{x_{H_2S}}{V_{Ms}}e^{\left(\frac{-E}{RT_s}\right)}(-\Delta H) \quad 7.14$$

$$-\frac{d\left(\frac{u}{V_M}\right)}{dz} = fk_m\left(\frac{x_{H_2S}}{V_M} - \frac{x_{H_2}}{V_M}\right)\frac{3(1-\xi)}{r_p} \quad 7.15$$

To assist with modelling purposes these equations are then non-dimensionlised to produce the mass and energy balances used in the model, below.

$$\frac{1}{Le}\frac{d\left(x_{H_2}\frac{y_r}{y}\right)}{d\tau} = -\frac{1}{u_F'}\frac{d\left(x_{H_2}u'\frac{y_r}{y}\right)}{dZ} + \frac{1}{Pe_M}\left(\frac{y_r}{y}\frac{dx_{H_2}}{dZ}\right)\frac{1}{dZ} + \left(x_{H_2S} - x_{H_2}\right)M\frac{y_r}{y} \quad 7.16$$

$$\frac{1}{Le}\frac{dy}{d\tau} = -\frac{1}{u_F'}\frac{d(yu')}{dZ} + \frac{1}{Pe_H}\frac{d^2y}{dZ^2} + (y_s - y)H + (y_w - y)U \quad 7.17$$

$$\frac{M}{y}\left(x_{H_2S} - x_{H_2}\right) = \eta(y_s)\frac{x_{H_2S}}{y_s}e^{\left(\frac{1}{y_r} - \frac{1}{y_s}\right)} \quad 7.18$$

$$\left(1 - \frac{1}{Le}\right)\frac{d}{d\tau}(y_s) = (y - y_s)H + \beta'\frac{y_r}{y_s}\eta(y_s)x_{H_2S}e^{\left(\frac{1}{y_r} - \frac{1}{y_s}\right)} \quad 7.19$$

$$\frac{d\left(u'\frac{y_r}{y}\right)}{dZ} = \frac{u_F}{u_r}MS\frac{y_r}{y}\left(x_{H_2} - x_{H_2S}\right) \quad 7.20$$

$$\eta(y_s) = \frac{3}{\emptyset_s^2}(\phi_s coth\phi_s - 1) \quad 7.21$$

Where the dimensionless groups are described as follows;

$$y = \frac{RT}{E} \qquad Z = \frac{z}{L}$$

$$\tau = \left(\frac{u_F t}{\xi L}\right)\frac{1}{Le} \qquad Le = 1 + \frac{(1-\xi)\rho_s c_s}{\rho_f c_f \xi}$$

$$M = \frac{3k_m L(1-\epsilon)}{r_p u_F} \qquad H = \frac{3hL(1-\xi)}{r_p u_F \rho_f c_f}$$

$$\beta = \frac{R}{E}\frac{(-\Delta H)}{V_{Ms}\rho_f c_f} \qquad Pe_M = \frac{Lu_F}{D_L}$$

$$Pe_H = \frac{Lu_F\rho_f c_f}{\lambda_a} \qquad U = \frac{2h_w L}{r_p u_F \rho_f c_f}$$

$$\frac{k(y_r)}{k_0} = \frac{u_F}{Lk_0} = e^{-1/y_r} \qquad u' = \frac{u}{u_r}$$

$$\beta' = \beta \frac{y_s}{y_r} \qquad \emptyset_0^2 = \frac{r_p^2 k(y_r)}{D} = \frac{r_p^2 u_F}{DL}$$

$$\emptyset_s^2 = \emptyset_0^2 e^{1/y_s - 1/y_r}$$

A full derivation of the dynamic model is given in appendix B.

As per the dynamic modelling work of Chen and Luss, the dimensionless mass transfer, internal and external heat transfer and reaction parameters are taken as M, H, U, and β' respectively[182]. The effectiveness factor, $\eta(y_s)$, describes the concentration profile within the particle.

The subscripts, s, 0, F and f refer to the particle surface, initial reference, feed and fluid respectively. A reference dimensionless temperature, y_r, is chosen where $k(y_r) = u/L$ in order to simplify the particle balances and scale the exponential term in the Arrhenius equation for computational ease.

Since the mass and energy balances refer to the mol fraction of hydrogen, x_{H2}, the overall mass balance in equation 7.15, which describes the dependence of gas velocity on temperature and extent of reaction, must contain a scaling factor, S, which relates the consumption of the reference reactant to the overall change in the number of moles. For a general reaction containing inert gases, I, $aA(g) + bB + iI \rightarrow cC + iI$, where the reaction is described with respect to component A, the scale factor, S, is given by:

$$S = \frac{(c+i)-(a+b+i)}{a} \qquad 7.22$$

Inclusion of non-participating components is important as although not active in the reaction, they affect the fractional change in total mols as reaction takes place, and hence the density variation. The scaling factor is related to the contraction through the feed mol fraction of the reference component, in this case x_{Af}, where $S = \frac{\varepsilon}{x_{Af}}$.

The boundary conditions are derived using Danckwerts' criteria, specifying diffusion and convection at the inlet and a zero-slope condition at the outlet[183]. This gives the following boundary conditions:

$$\frac{u_0'}{Pe_M} \frac{\partial \frac{x_{H_2,0}}{y_0}}{\partial Z} = \frac{u'_0 x_0}{y_0} - \frac{u'_f x_f}{y_f} \qquad \text{at} \quad Z = 0$$

$$\frac{u'_0}{Pe_H} \frac{\partial y_0}{\partial Z} = u'_0 y_0 - u'_f y_f \qquad \text{at} \quad Z = 0$$

$$\frac{\partial x_{H_2}}{\partial Z} = \frac{\partial y}{\partial Z} = 0 \qquad \text{at} \quad Z = 1$$

7.3.1 Variable Feed Flow Modification

In order to replicate a reactor block-in trip, equations 7.16 to 7.20 need to be re-dimensionalised with respect to time to access the feed velocity term. This results in the use of modified pseudo-dimensionless parameters, M', H' and U', also with feed velocity removed, giving a single

variable, u_F that can be suddenly reduced at $t = 0$ in the model to simulate the trip. A full derivation is given in appendix C.

$$\xi L \frac{d\left(x_{H_2} \frac{y_r}{y}\right)}{dt} = -u_r \frac{d\left(x_{H_2} u' \frac{y_r}{y}\right)}{dZ} + \frac{1}{Pe_{M'}} \left(\frac{y_r}{y} \frac{dx_{H_2}}{dZ}\right) \frac{1}{dZ} + \left(x_{H_2 S} - x_{H_2}\right) M' \frac{y_r}{y} \quad 7.23$$

$$\xi L \frac{dy}{dt} = -u_r \frac{d(yu')}{dZ} + \frac{1}{Pe_{H'}} \frac{d^2 y}{dZ^2} + (y_s - y) H' + (y_w - y) U' \quad 7.24$$

$$\frac{M'}{y}\left(x_{H_2} - x_{H_2 S}\right) = \eta(y_s) \frac{x_{H_2 S}}{y_s} e^{\left(\frac{1}{y_r} - \frac{1}{y_s}\right)} \quad 7.25$$

$$\xi L (1 - Le) \frac{d(y_s)}{dt} = (y - y_s) H' + \beta' \eta(y_s) k_0 L x_{H_2 S} e^{\left(-\frac{1}{y_s}\right)} \quad 7.26$$

$$u_r \frac{d\left(u' \frac{y_r}{y}\right)}{dZ} = \frac{\varepsilon}{x_f} M' \frac{y_r}{y}\left(x_{H_2} - x_{H_2 S}\right) \quad 7.27$$

$$\eta(y_s) = \frac{3}{\emptyset_s^2}(\phi_s coth \phi_s - 1) \quad 7.28$$

Where the modified pseudo-dimensionless parameters are as follows;

$$M' = \frac{3 k_m L (1-\xi)}{r_p} \qquad H' = \frac{3 h L (1-\xi)}{r_p \rho_f c_f} \qquad U' = \frac{2 h_w L}{r_p \rho_f c_f}$$

$$Pe'_M = \frac{L}{\mathrm{D}} \qquad Pe'_H = \frac{L \rho_f c_f}{\lambda_a}$$

The boundary conditions also needed updating for use with the pseudo-dimensionless parameters.

$$\frac{u_r u'_f x_f}{y_f} - \frac{u_r u'_0 x_0}{y_0} = \frac{-1}{Pe'_M} \frac{d\left(\frac{x_0}{y_0}\right)}{dZ} \quad 7.29$$

$$u_r (u'_f y_f - u'_0 y_0) = \frac{-1}{Pe'_H} \frac{d(y_0)}{dZ} \quad 7.30$$

7.3.2 Model Parameters

Typical FT reaction conditions of 250 °C and 30 barg over an insulated, fixed catalyst bed result in the model parameters listed below in Table 7.1, assuming the reaction is irreversible first order as described by Post *et al*. as in section 7.2. In some instances, the parameters are varied from the below values to more clearly illustrate the dynamic behaviour being discussed.

The additional complexity of the dynamic model merited the move to modelling in gPROMS ModelBuilder 5.1.1. A backwards finite difference method (BFDM) discretisation method of second order with 1000 elements. Computational difficulties with the variable feed flow model meant that lower values of contraction were used as the typical value of -⅔ led to conversion difficulties.

Table 7.1: Model parameters for FT reaction.

Parameter	Value	Source
ξ	0.5	Froment *et al*. [184]
ρ_f	18 kgm^{-3}	Calculated
c_f	1429 $Jkg^{-1}K^{-1}$	Calculated
ρ_s	5240 kgm^{-3}	ThermoFisher [185]
c_s	824.7 $Jkg^{-1}K^{-1}$	NIST webbook
Le	169	Calculated
L	12 m	Speight [186]
k_m	0.00043 m^2s^{-1}	Nassr [187]
r_p	0.005 m	Nassr
h	287.5 $Js^{-1}m^2K^{-1}$	Nassr [187]
M	1	Calculated
H	20	Calculated
h_w	900 $Wm^{-2}K^{-1}$	Odunsi *et al*. [188]
$-\Delta H$	152000 $Jmol^{-1}$	Odunsi *et al*.
U	0 / 84	Assumed adiabatic / Calculated
R	8.314 $Jmol^{-1}K^{-1}$	
E	92000 $Jmol^{-1}$	Nassr
β'	0.13	Calculated
D_L	0.005 m^2s^{-1}	Calculated
Pe_M	4800	Calculated
λ	51.2 $Wm^{-1}K^{-1}$	Calculated
Pe_H	97582	Calculated
y_r	0.05	Chosen as similar to y_f
y_w	0.04	Chosen as 170 °C
y_f	0.045	220 °C
u_f	2 ms^{-1}	Simons **Error! Bookmark not defined.**
u_r	2 ms^{-1}	Chosen as v_f
ϕ_0	7	Calculated
x_{H2F}	0.66	For $CO/CO_2/H_2$ feed
ε	-2/3	Calculated for typical FT

7.4 Results and Discussion

7.4.1 Steady State

The effect of gas contraction is first investigated using the pseudo-homogeneous model at steady state as described in section 7.2. The results of equation 7.10 for both a gas contraction of -⅔, stated by Post *et al*. as typical for a H_2:CO feed ratio of two with liquid hydrocarbon products[179], and a constant velocity system with no contraction are plotted in Figure 7.3.

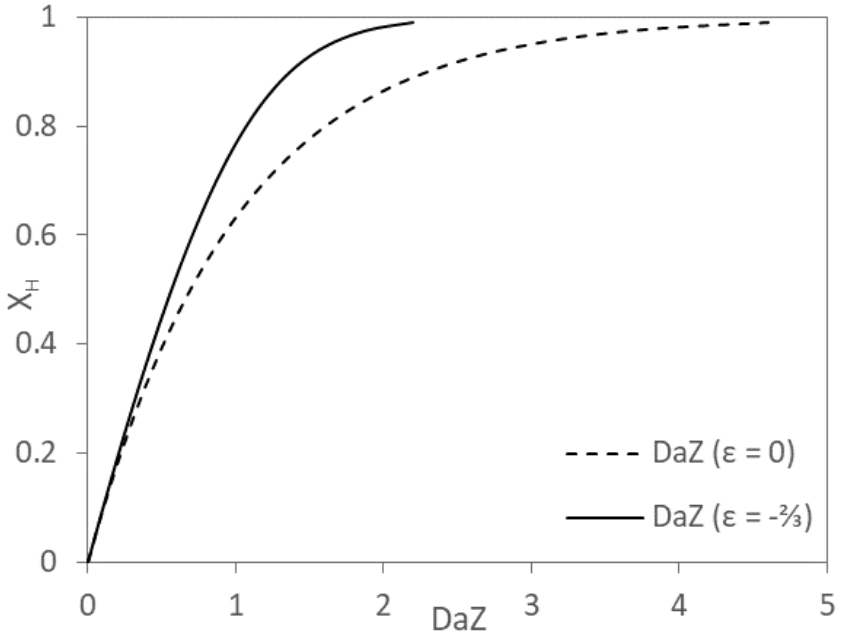


Figure 7.3: Steady state solution of extent of reaction against DaZ for FTS model with varying gas contraction

As seen in Figure 7.3 the reaction reaches completion in a smaller bed length when $\varepsilon < 0$ (i.e. contraction), due to the increasing residence time as the gas contracts and the plug velocity drops.

Although this is a simple isothermal model it illustrates the general reactor behaviour. The compression of the exothermic reaction into a smaller volume will result in higher bed temperatures in that section. This in turn can affect the heat and mass distribution as well as the rate of reaction, potentially leading to spikes in reaction, hot spots and possible runaway reactions.

The steady state solution of the dynamic FT model is expected to follow the same contracting trend as the steady state pseudo-homogeneous model, although the inclusion of the energy balance will influence the conversion. The use of combined heat and energy balances and inclusion of a solid phase in the dynamic model means the two methods cannot be compared directly, however the extent of reaction, X_{H2}, and change in hydrogen mol fraction, x_{H2}, can be used to evaluate the change in reaction profile due to contraction.

The effect of contraction at steady state on the mol fraction of hydrogen, x_{H2}, and dimensionless temperature, y, is therefore investigated in the dynamic model to ensure the same behaviour is exhibited as for the steady state pseudo-homogeneous model.

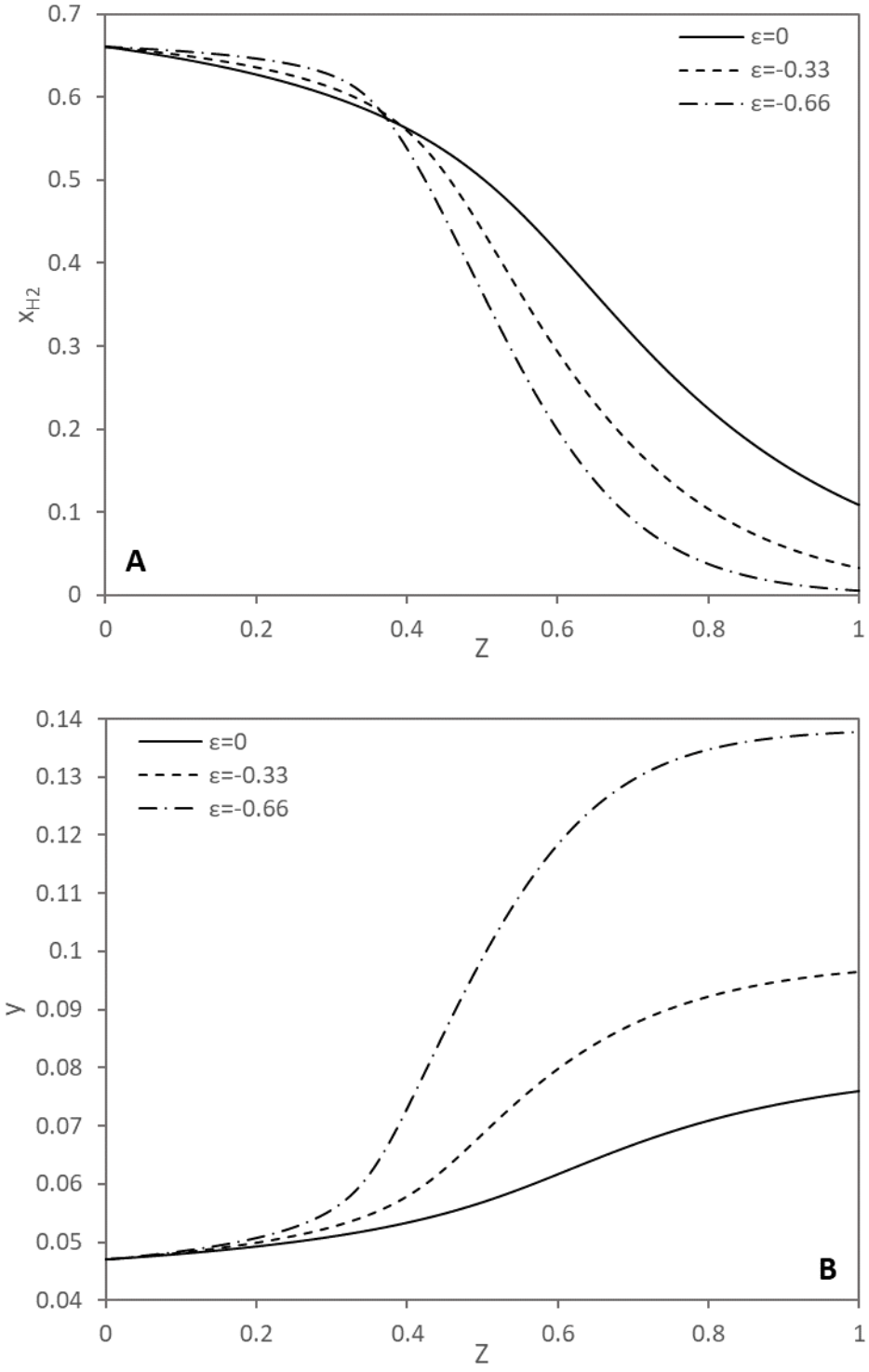


Figure 7.4: Effect of contraction on (A) mol fraction of hydrogen (x_{H2}) and (B) gas temperature (y) for the steady state FT reaction. Parameters as given in Table 7.1.

As is clearly shown in Figure 7.4 the dynamic model at a steady state shows the same behaviour as the pseudo-homogeneous model shown in Figure 7.3, with the FT reaction progressing further within a

fixed bed volume when contraction is considered, with ε = -0.66 being a typical value for a stoichiometric feed and ε = -0.33 the value calculated for the feed composition used in chapter 3 of this thesis. Figure 7.4A shows higher conversions of hydrogen in the same volume of bed with increasing contraction. Figure 7.4B confirms that temperatures increase in line with the higher extents of reaction.

Interestingly, although the temperature increase in Figure 7.4B is consistently higher for the contraction cases, the hydrogen mol fraction, x_{H2}, at the start of the bed in Figure 7.4A reduces more slowly when $\varepsilon < 0$. This is due to the reduction in total gaseous mols that takes place during a reaction with contraction. If there is no change in the number of mols between the reactants and products of a gaseous reaction, i.e. $\varepsilon = 0$, the total number of mols at any point in the reaction is taken to be equal to that of the feed and the change in reactant mol fraction varies linearly with the extent of reaction.

However, when expansion or contraction are accounted for, there is a change in total number of mols in the gas phase as the reaction progresses. The total number of gaseous mols will therefore vary during the course of the reaction, influencing the relation between x_{H2} and X_{H2}. For contracting reactions, the total number of gaseous mols decreases as the reaction progresses. Since the number of H_2 mols decreases with extent of reaction, the mol fraction of H_2 is thus higher than if the total number of mols remained constant. The opposite is true for expanding reactions.

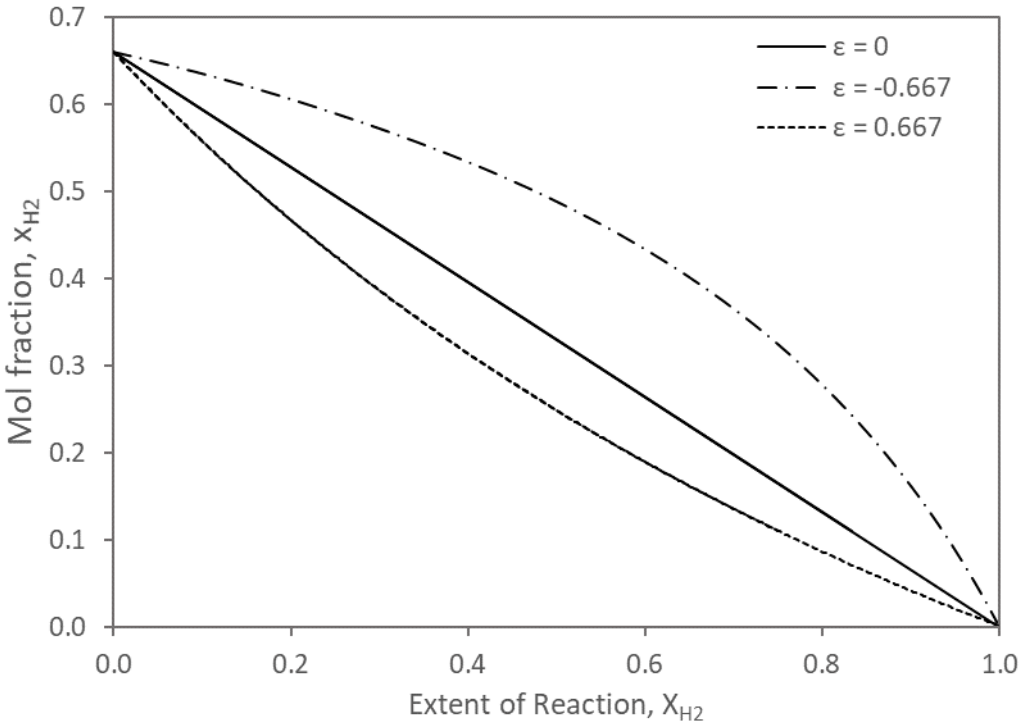


Figure 7.5: Effect of contraction on molar fraction of hydrogen, x_{H2} during reaction.

Figure 7.5 illustrates this for both contracting and expanding reactions using the dynamic model. The total number of mols in the system at time *t* is first calculated using x_{H2} and ε, this then allows the extent of reaction at *t* to be determined as the fraction of H_2 to have reacted at this point.

$$X_{H_2} = \frac{mols\ H_2\ reacted}{mols\ H_2\ in\ feed}$$

This non-linear variation of x_{H2} when $\varepsilon \neq 0$ was not seen in the pseudo-homogeneous isothermal model reviewed in section 7.2. This is because the isothermal equation models the change in superficial velocity with extent of reaction of hydrogen, and hence is not affected by the overall change in mols through reaction. The heterogenous model utilises the mol fraction of hydrogen which varies as the reaction progresses and total number of mols changes.

The significant levels of temperature increase seen for the different contraction cases in Figure 7.4B are also important to note. Re-dimensionalising these y values shows the substantial temperature increases that take place once contraction is included. In this case the actual temperature increases shown in Figure 7.4 are 322 K for $\varepsilon = 0$, 549 K for $\varepsilon = -0.33$ and 1004 K for $\varepsilon = -0.66$, highlighting the need to account for contraction in exothermic reactions. This matches well temperature rises modelled by Zhu et al. for a fixed bed, constant velocity system undergoing catalyst reduction, where the catalyst temperature increase exceeded that of the adiabatic temperature rise by a multiple of 2 or more at approximately 340 K [173].

Although the dimensionless groups given in Table 7.1 are typical for FT over a fixed bed, they will vary as the heat and mass transfer resistances are altered by reactor design and conditions. The effect of fluctuating conditions is demonstrated in Figure 7.6 and Figure 7.7, giving changes in concentration and temperature profile with varying values of dimensionless heat and mass parameters H and M. The internal heat transfer parameter, H, was first varied between 40-150 in Figure 7.6 to represent increasing internal heat transfer rates within the system. An artificially high fixed M value of 25 was used, chosen to minimise mass transfer limitations from the gas to the catalyst particles.

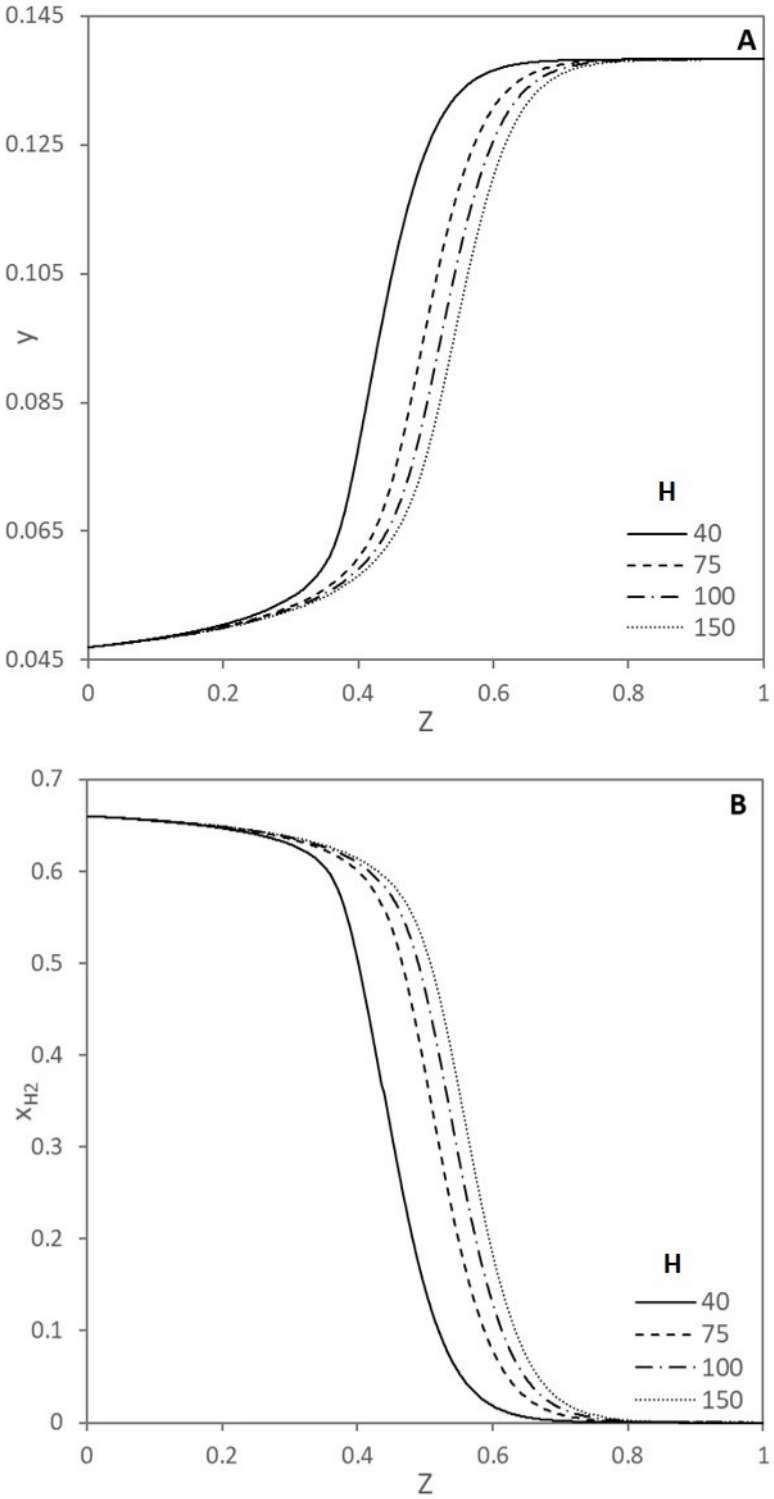


Figure 7.6: Varying H for M = 25 (A) dimensionless temperature, y, and (B) H_2 mol fraction, x_{H2} .

The FT reaction modelled in Figure 7.6 is not markedly heat transfer limited. Increasing values of H represent reduced heat transfer resistances, however varying H has little influence on the shape of the reaction front, with all values giving very similar profiles.

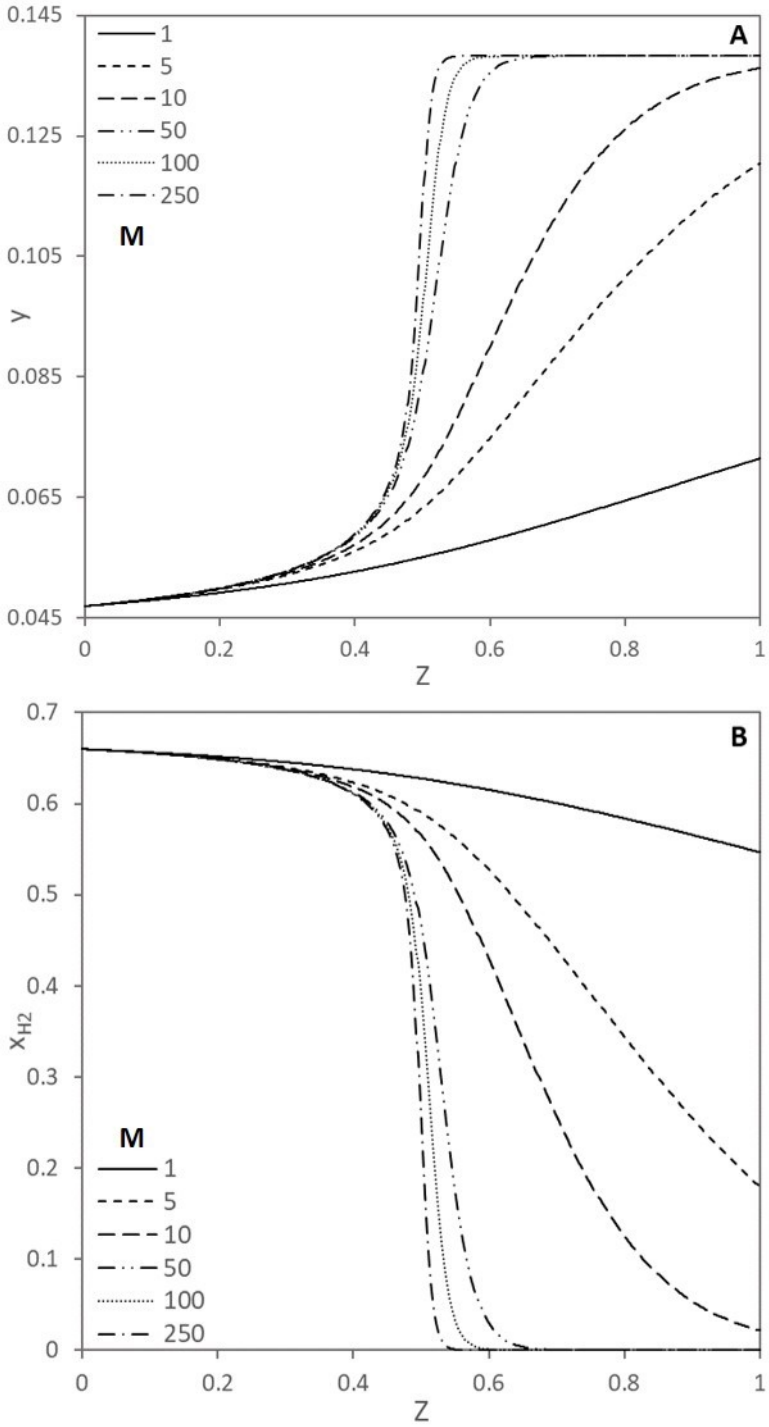


Figure 7.7: Varying M for H = 150 (A) dimensionless temperature, y, and (B) H_2 mol fraction, x_{H2} .

The effect of mass transfer resistances were investigated in Figure 7.7. M was varied between 1 and 250 to simulate high to low mass transfer resistance. For this a fixed H value of 150 was used, to remove any effects of heat transfer limitations. Thus, the FT reaction using the values in Table 7.1 was

mass transfer limited, with increasing M, and hence mass transfer rates, resulting in the reaction front within the bed spreading out over a longer bed length. Since a typical fixed bed FT value for M can easily be less than 5, clearly the reaction can experience significant mass transfer limitations.

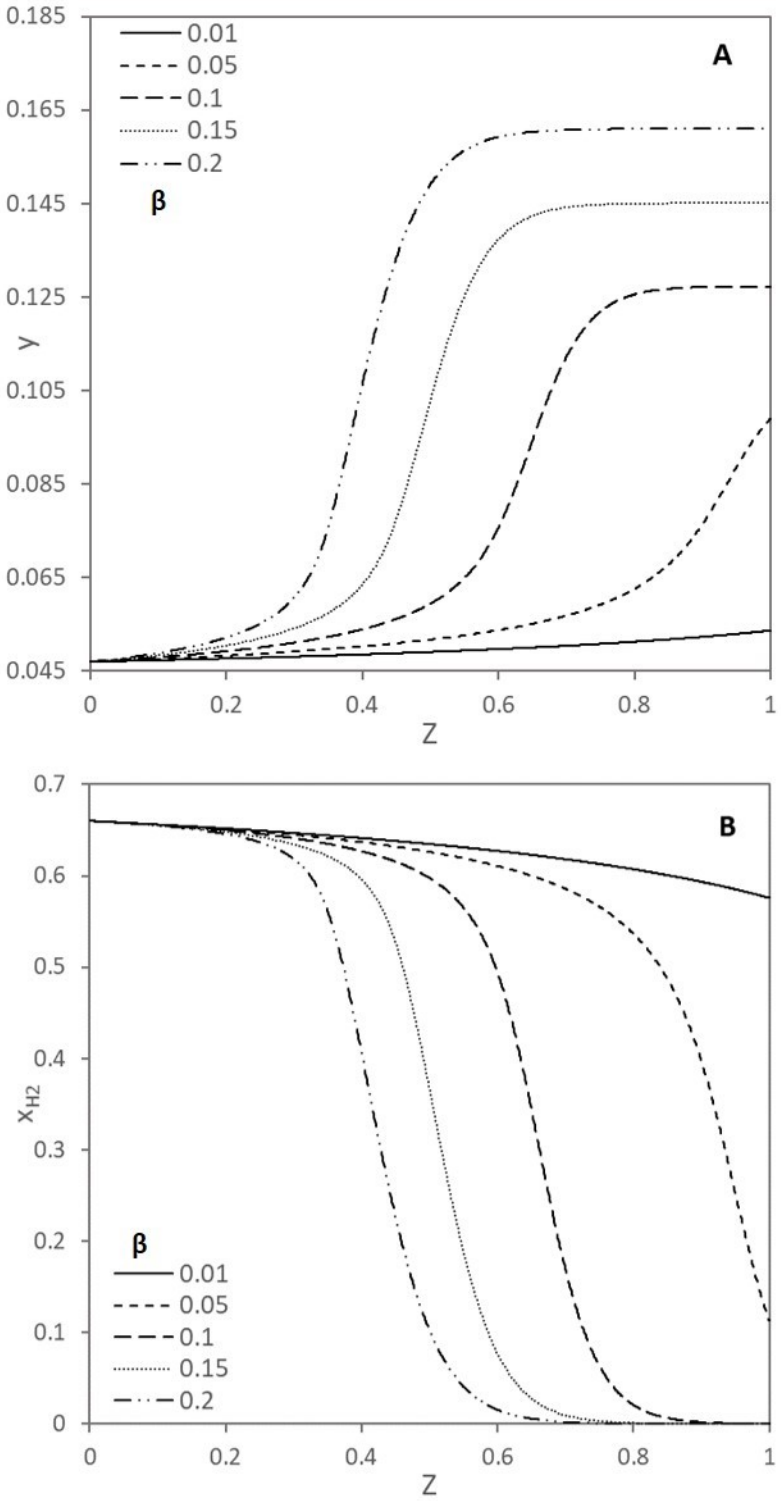


Figure 7.8: Effect of varying β with M = 25, H = 150 on (A) dimensionless temperature, y, and (B) mol fraction of hydrogen, x_{H2}.

If M and H are then taken as 25 and 150 respectively to remove the influence of mass and heat resistances, the effect of varying the dimensionless reaction heat term, β', can be investigated. Unsurprisingly, when this term is increased without other resistances, the reactor length in which the reaction reaches completion was reduced, as shown in Figure 7.8B. This behaviour is an exaggerated version of that seen in Figure 7.6 and shows that the reaction front passes up the bed as β' increases. The dimensionless temperature doesn't behave in the same manner as in that shown in Figure 7.6 however, where a consistent maximum y was reached for each case. In Figure 7.8A as β' was increased, *e.g.* due to an increase in ΔH, the maximum value of y also increases.

The isothermal effectiveness factor, $\eta(y_s)$, was the final dimensionless parameter investigated, representing the relationship between the reaction and diffusion rates within the catalyst particle. The effect of $\eta(y_s)$ on the reaction profile is investigated by varying the reference Thiele modulus, ϕ_0, the ratio of diffusion to reaction rate in the catalyst particle. As seen in Figure 7.9, as ϕ_0 increases the initial value of $\eta(y_s)$ drops and the reaction is increasingly limited by diffusion within the particle. This causes the reaction rate to drop and take place across a wider section of bed.

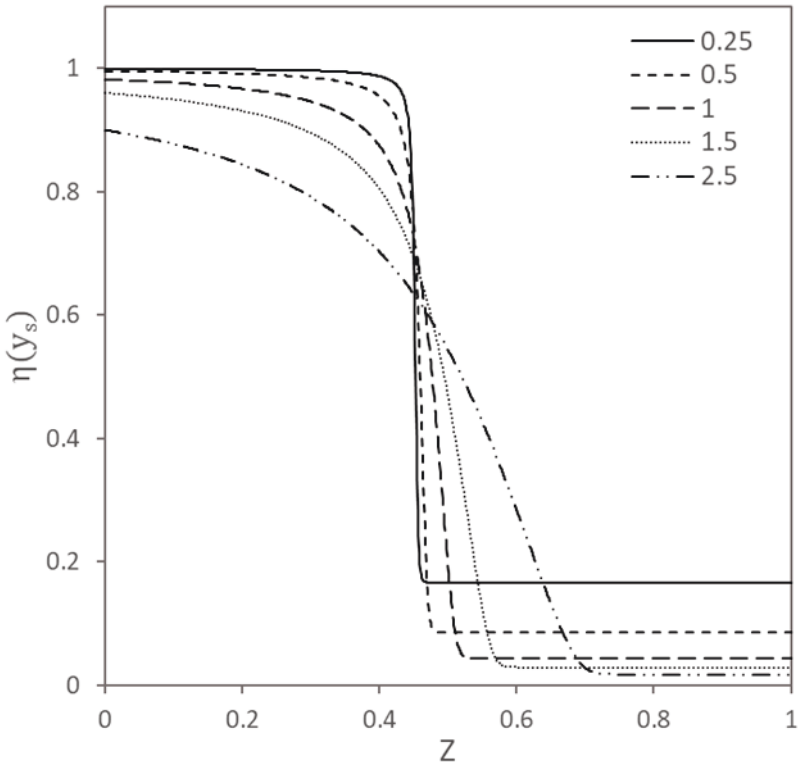


Figure 7.9: Effect of varying ϕ on the isothermal effectiveness factor, $\eta(y_s)$, with M = 500, H = 300 and β = 0.01.

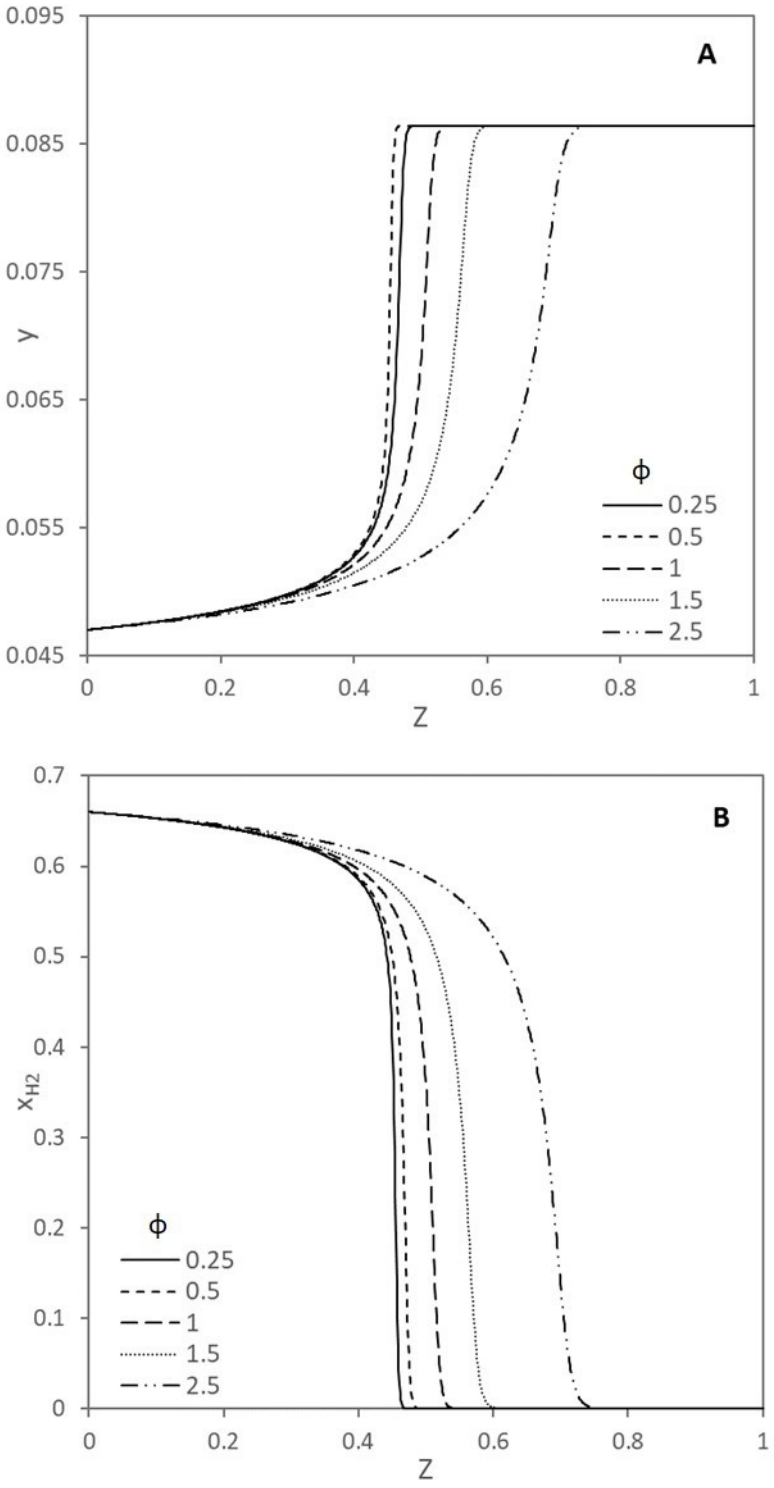


Figure 7.10: Effect of varying ϕ with M = 500, H = 200 and β = 0.01.

Figure 7.10 confirms this diffusion limitation causing the reaction front to occupy a larger bed volume with increasing ϕ, representing increasing diffusion limitations on the reaction within the particle.

7.4.2 Dynamic Model Response – Temperature Variations

Having demonstrated the effect of contraction on reactor profiles at steady state, the behaviour is next investigated dynamically. The phenomenon of wrong way behaviour due to a reduction in feed temperature or flowrate are studied using the dynamic model introduced in section 7.3.

The ability of the model to predict wrong way behaviour in response to a drop in dimensionless feed temperature, y_{in}, is demonstrated in Figure 7.11.

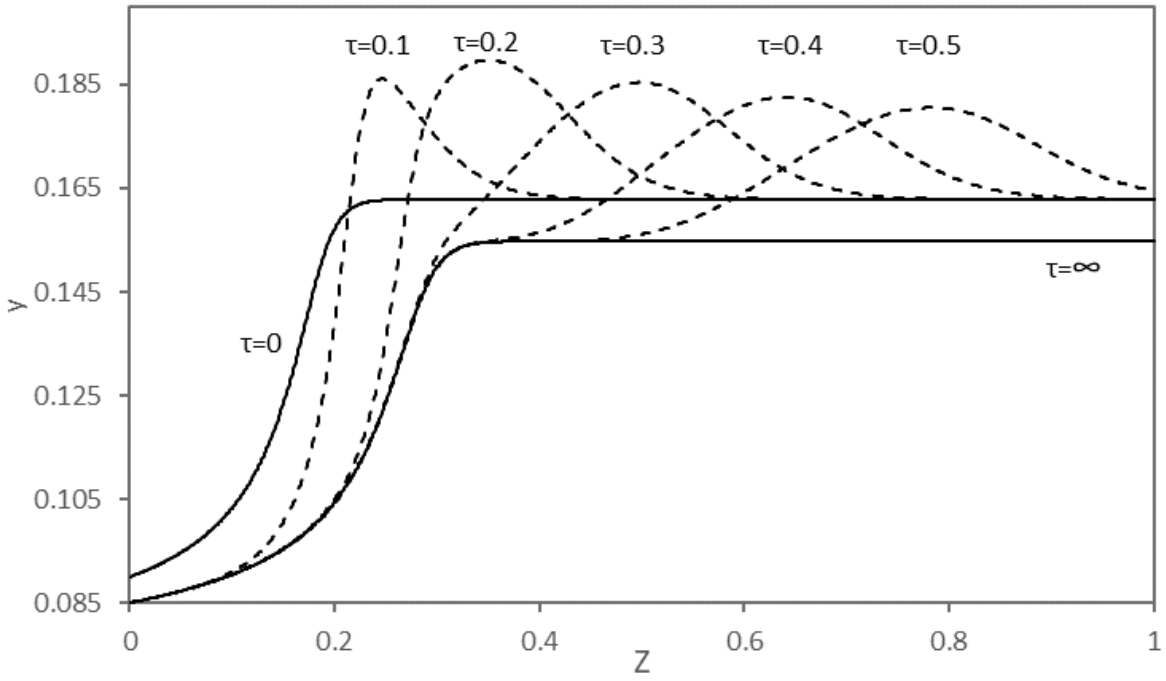


Figure 7.11: Dynamic wrong way response to a drop in inlet feed temperature.
M = 540, H = 180, yr = 0.0833, y_{in1} = 0.09, y_{in2} = 0.085, β = 0.0167, ε = -0.66.

As seen in the work by Luss *et al.* in section 7.3, the drop in dimensionless inlet feed temperature produces a transient temperature peak that travels down the dimensionless bed length, Z, before reaching a new steady state at a lower temperature, y.

This behaviour is seen for both constant and variable velocity reactions, with contraction being expected to exacerbate the inverse response. Figure 7.12 shows the inverse response to a drop in feed temperature at $\tau = 0$ for an adiabatic reactor where the reaction reaches completion within a small section of the bed for both $\varepsilon = 0$ and $\varepsilon = -0.66$, a typical value of contraction for FTS with a stochiometric feed composition. In order to show the scale of the temperature increase the maximum dimensionless temperature reached, y_{max}, is shown as a fraction of the maximum profile temperature at $\tau = 0$. With $\varepsilon = 0$ there is a small amount of wrong way behaviour, with peak temperatures reaching approximately 0.1% above the initial steady state y_{max}. However, when contraction is factored in, not only are the steady state temperatures significantly increased, as previously shown in Figure 7.4, the wrong way

behaviour is also exaggerated with dimensionless temperature peaks reaching almost 4% above y_{max} measured at $\tau = 0$.

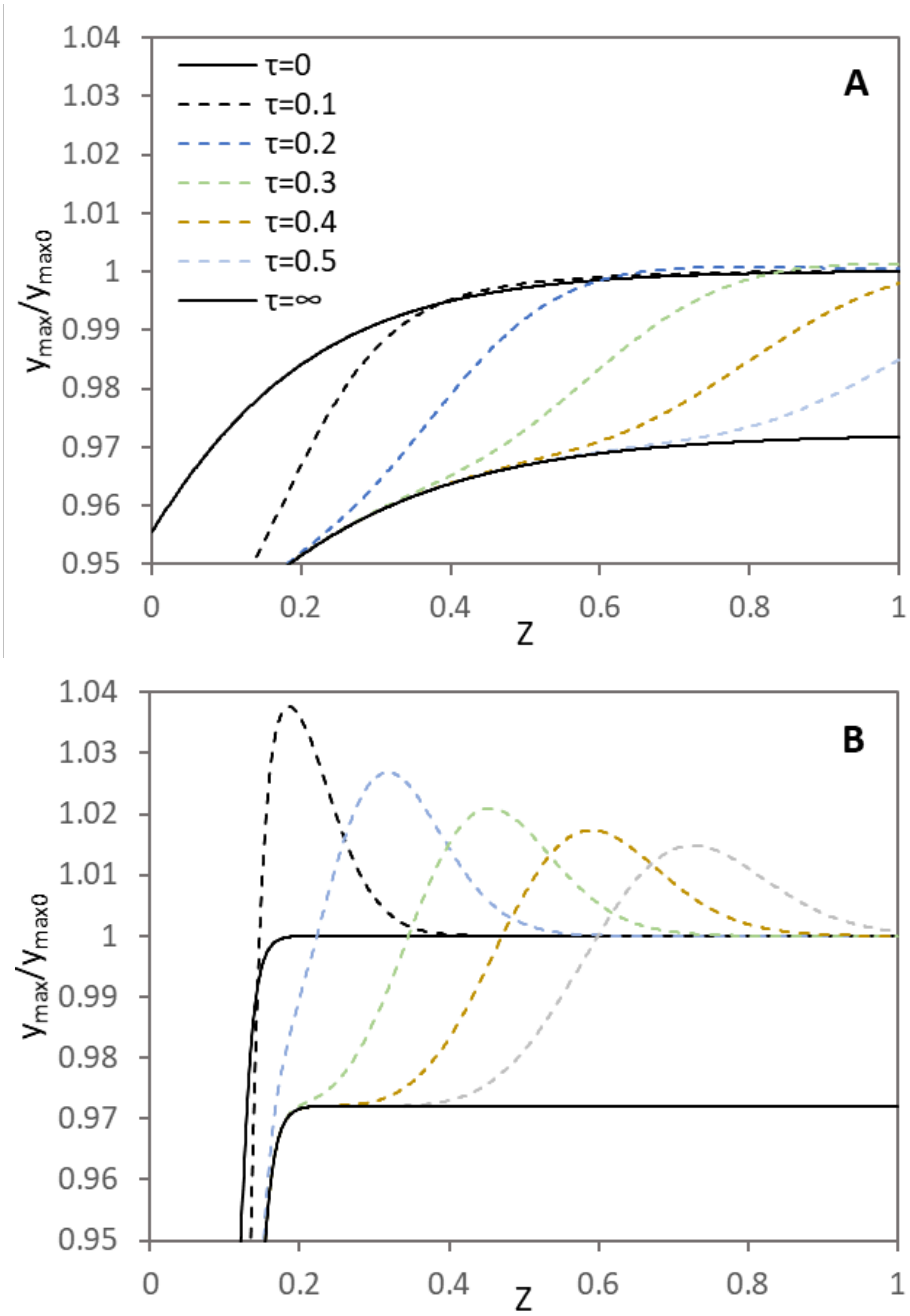


Figure 7.12: Wrong way behaviour due to drop in feed temperature for an adiabatic reactor with (A) ε = 0 and (B) ε = -0.66. Le = 118000, M = 300, H = 135, β = 0.0167, y_{f1} = 0.098, y_{f2} = 0.095.

Figure 7.12 uses modified values of model parameters to more clearly demonstrate the movement of the temperature peak down the bed without mass transfer limitations. When the parameters in Table 7.1 are used the temperature peak is spread through the bed due to the high mass transfer resistances, as shown in Figure 7.13. The peak temperatures achieved however, are higher than those in Figure 7.12, reaching up to 9% above y_{max} at $\tau = 0$ before the peak drops and spreads out through the bed until the new steady state is reached at $\tau = \infty$.

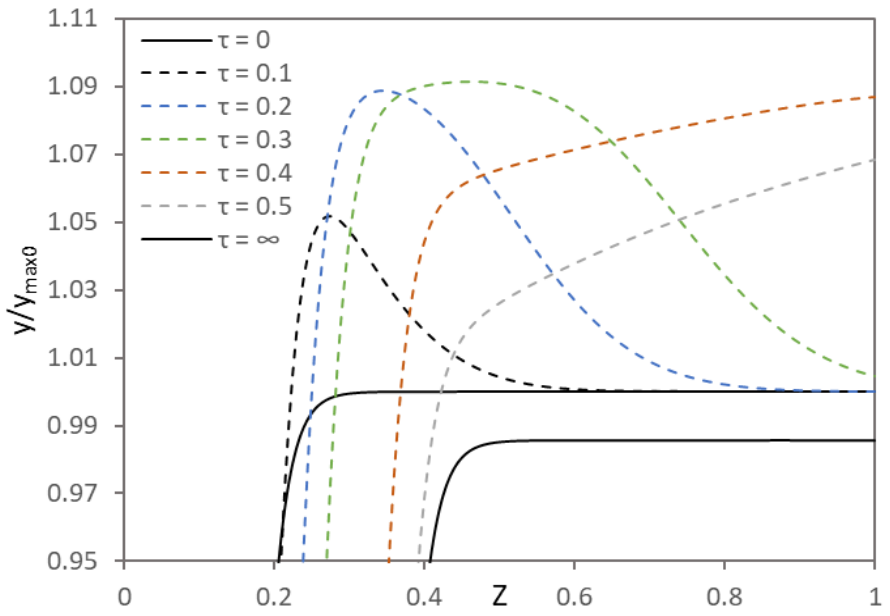


Figure 7.13: Wrong way behaviour due to drop in feed temperature for an adiabatic reactor with ε = -0.66. Le = 169, M = 50, H = 150, β = 0.13, y_{f1} = 0.047, y_{f2} = 0.045.

It is clear that temperature excursions can be orders of magnitude higher when contraction is included. This additional heat must be accounted for when developing models for contracting reactions as it could mean the difference between a manageable hot spot and a catastrophic runaway reaction.

It was found in section 7.4.1 that the dimensionless mass, heat and reaction terms, M, H, β and ϕ, affected the reaction profile to varying extents. The effect of these parameters on peak dimensionless temperatures are investigated in Figure 7.14, Figure 7.15, Figure 7.16 and Figure 7.17.

The influence of M values between 1 and 50 on y_{max} achieved through wrong way behaviour is given in Figure 7.14. A fixed value of H = 150 was used to reduce the effect of heat transfer limitations. The reaction contraction is kept constant with ε = -0.66. The drop in dimensionless feed temperature, y_{f1}-y_{f2}, is taken between 0.001 and 0.005, as larger drops quench the reaction in the downstream bed.

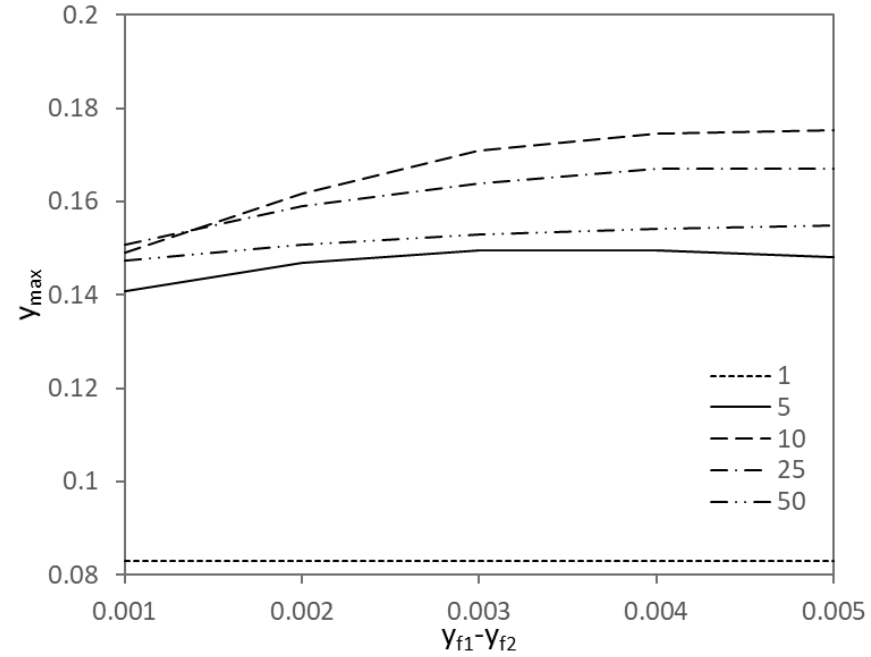


Figure 7.14: Maximum temperatures for M = 1-50 with H = 150 for y_{f1}-y_{f2} = 0.001-0.005, ε = -0.66.

At low values of M the mass transfer resistances are still limiting the extent of reaction, meaning the effect of increasing y_{f1}-y_{f2} is small. Once mass transfer is no longer the limiting factor increasing the magnitude of y_{f1}-y_{f2} increases the scale of wrong way behaviour and peak temperatures, as expected from the findings in section 7.4.1. Larger values of y_{f1}-y_{f2} generally result in a higher y_{max} in this region of M. Interestingly this behaviour then reverses above M = 10, with higher mass transfer coefficients giving lower y_{max} values. It is believed that this is the approach to quenching, achieved at lower values of y_{f1}-y_{f2} as mass transfer limitations are removed with higher values of M. As these values of y_{f1}-y_{f2} are reached the wrong way peak becomes very large, the reaction in the remainder of the bed is quenched and the model displays instabilities. Beyond this y_{f1}-y_{f2} the reaction throughout the bed is quenched and no wrong way behaviour is seen, these values are not plotted on Figure 7.14.

At close to 1, the base effectiveness factor modelled was slightly higher than that calculated for the most active catalyst, 950-106-P, at 0.95. Indicating that, despite having a rate similar to high activity Fe catalysts given in literature and therefore a similar steady state reaction profile to the model, the 950-106-P foamed catalyst would have slightly increased diffusional resistances and hence more moderate temperature peaks during a dynamic response to loss of feed heating.

The effect of heat transfer resistance is shown in Figure 7.15 for H values between 40-150. A fixed value of M = 25 is used to minimise the influence of mass transfer resistance, with feed temperature drops, y_{f1}-y_{f2}, in the range of 0.001-0.005. As with the mass transfer resistances, at low values of H the reaction is heat transfer limited and hence increasing y_{f1}-y_{f2} has little effect on the peak temperature achieved. As the heat transfer resistances reduce the peak temperature increases and the effect of increasing y_{f1}-y_{f2} becomes larger.

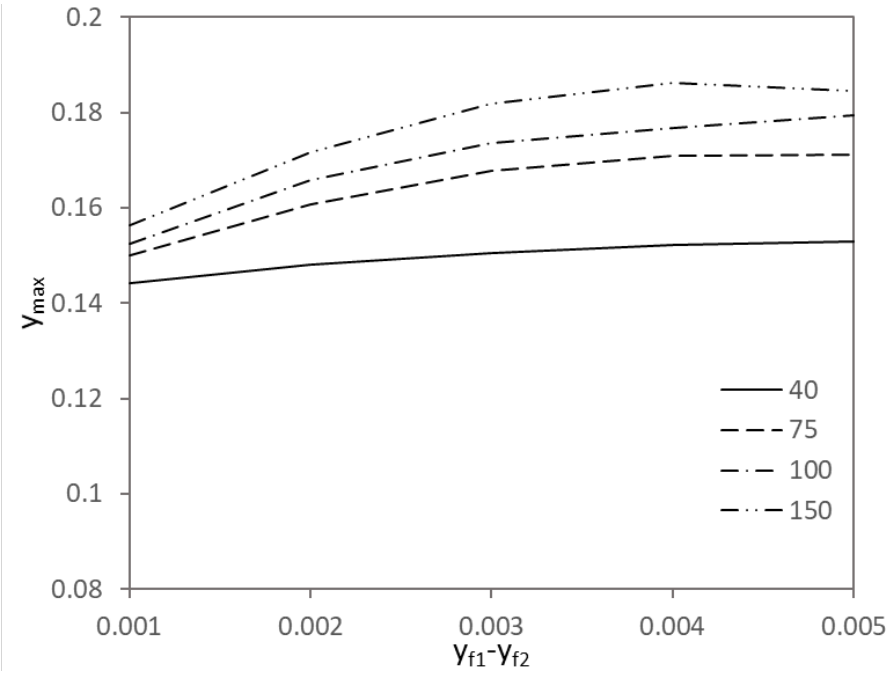


Figure 7.15: Maximum temperatures for H = 40-150 with M = 25 for y_{f1}-y_{f2} = 0.001-0.005, ε = -0.66.

This is in contrast with heat transfer variations during steady state, detailed in Figure 7.6, which had minimal influence on the reaction profile, and none on the maximum temperature achieved. This indicates that the reaction becomes heat transfer limited at the significantly higher y_{max} produced with wrong way behaviour.

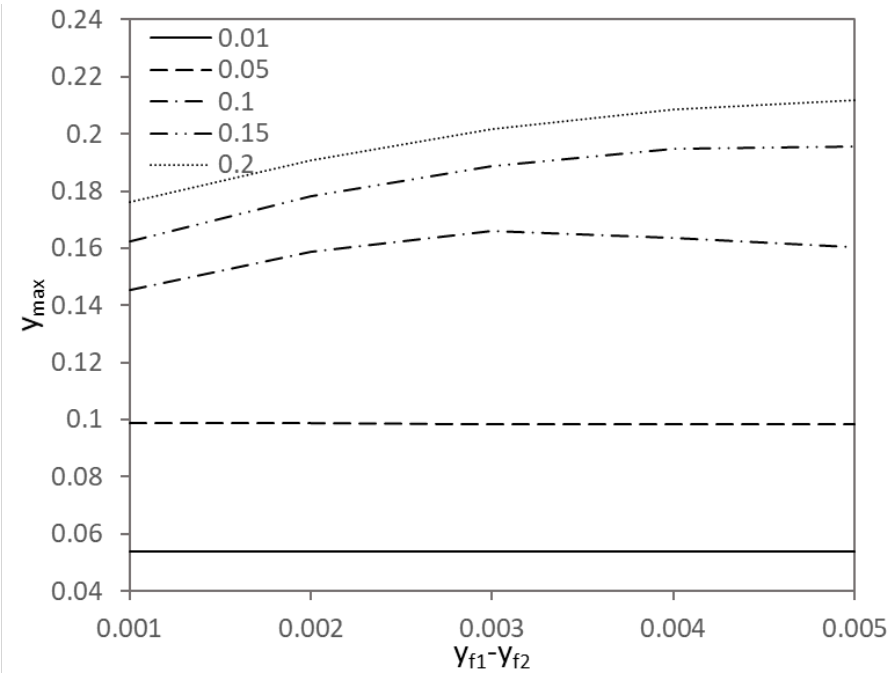


Figure 7.16: Maximum temperatures for β = 0.01-0.2 with y_{f1}-y_{f2} = 0.001-0.005, M=25, H=150, ε = -0.66.

As expected from the results given in Figure 7.8 for varying the dimensionless reaction coefficient, β, at steady state, Figure 7.16 shows that as β is raised the amount of reaction taking place also increases

and y_{max} becomes larger. At low values of β the scale of the temperature drop, y_{f1}-y_{f2}, does not affect y_{max}, however as β becomes larger the wrong way behaviour exaggerates and values of y_{max} increase.

Finally, the effect of the reference Thiele modulus, ϕ_0, on y_{max} is investigated, with the results shown in Figure 7.17 below. As ϕ_0 grows the reaction becomes increasingly diffusion limited, although as shown previously in Figure 7.10, the final extent of reaction does not change. This results in higher values of y_{max} as heat production is maintained but removal *via* convection is reduced. As expected, larger drops in feed temperature, y_{f1}-y_{f2}, give slightly higher peak temperatures as the wrong way behaviour is amplified.

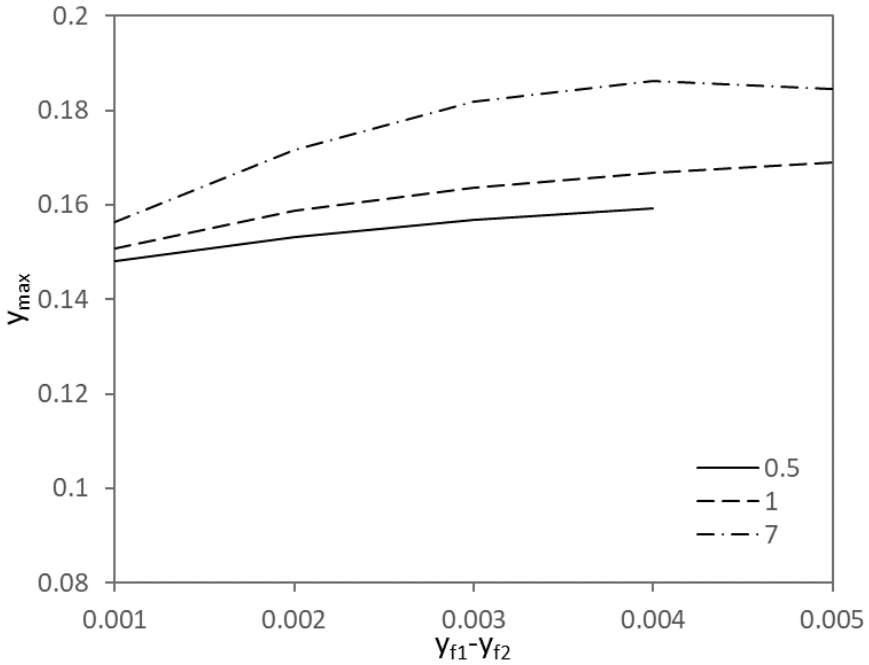


Figure 7.17: Maximum temperatures for ϕ_0 = 0.5-7 with y_{f1}-y_{f2} = 0.001-0.005, M=25, H=150, ε = -0.66.

Realistically however, drops in feed temperature will not be instantaneous. Thermal inertia of large industrial heat exchange units will mean that on a loss of heating the drop in feed temperature will be gradual. In order to more accurately portray this the scheduling tool in gPROMS has been used to model an assumed linear drop in feed temperature of 0.018 over a period τ = 0.25. For reference this equates to a drop in feed temperature over 127 s, with the peak taking approximately 8 minutes to pass through the reactor at these conditions.

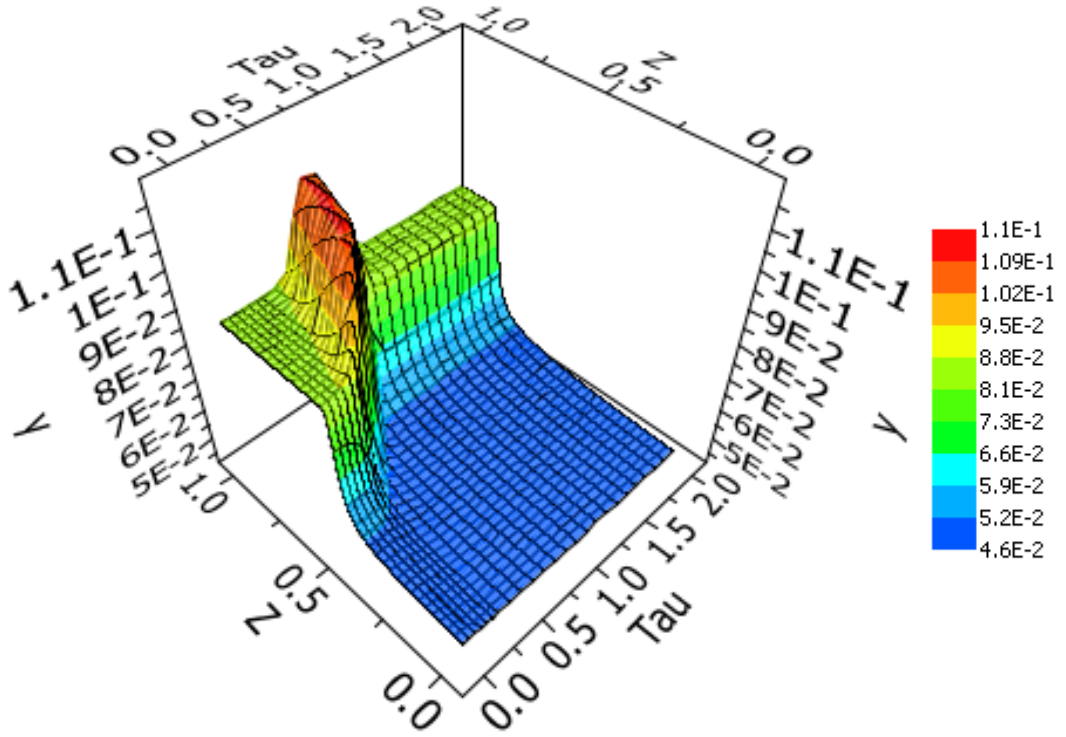


Figure 7.18: 3D plot of gradual drop in dimensionless feed temperature, y_f, of 0.018 linearly over $\tau = 0.25$.

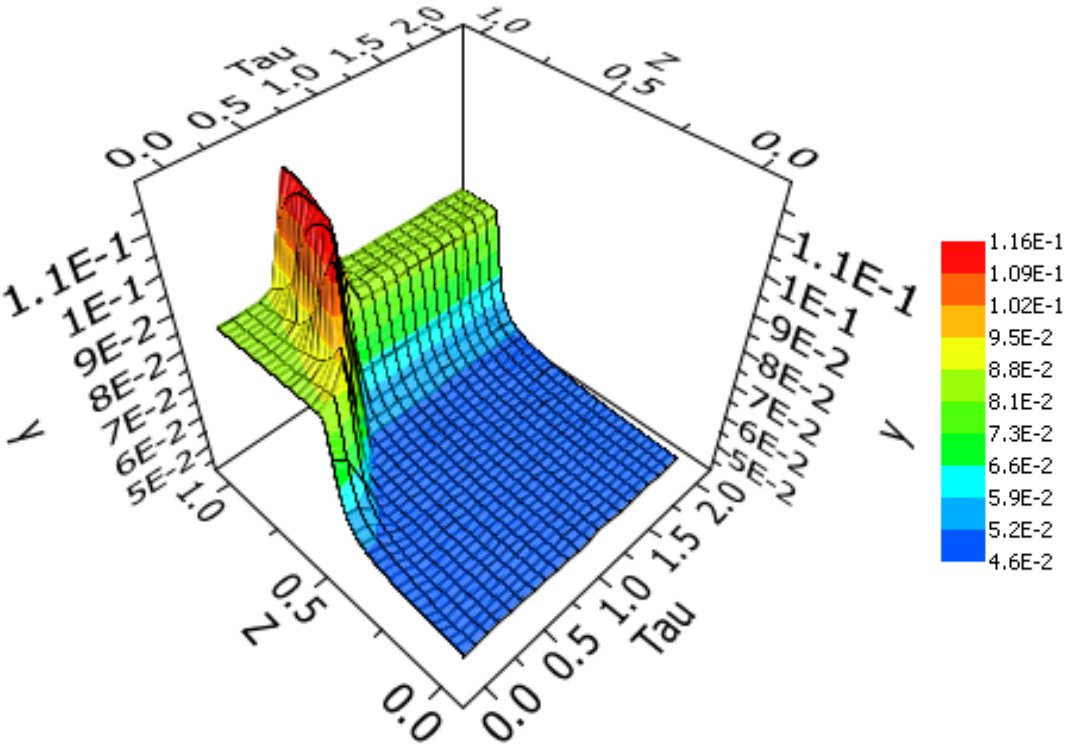


Figure 7.19: 3D plot of instantaneous drop in dimensionless feed temperature.

As shown using a 3D surface plot in Figure 7.18 and Figure 7.19, the gradual feed temperature drop delays the formation of the reactor hot spot and allows it to dissipate. This results in a reduced peak dimensionless temperature, y_{max}, of 0.1092, or 1208 K, compared to 0.1140, or 1261 K, for an

instantaneous drop with the same conditions. For additional clarity the reactor profiles with the maximum y for both gradual and instantaneous drops are shown alongside each other for comparison in Figure 7.20 below.

The additional dissipation of heat achieved with the gradual drop reduces the peak temperature from 34% to 28% above steady-state y_{max}. Although still a significant increase to the steady-state maximum temperature, the reduction in y_{max} for large equipment with sizable thermal inertia could reduce the risk of unsafe temperatues being achieved. However, for this to be accounted for as a mitigating factor the system would require thorough testing and a model generated that matches the individual set-up.

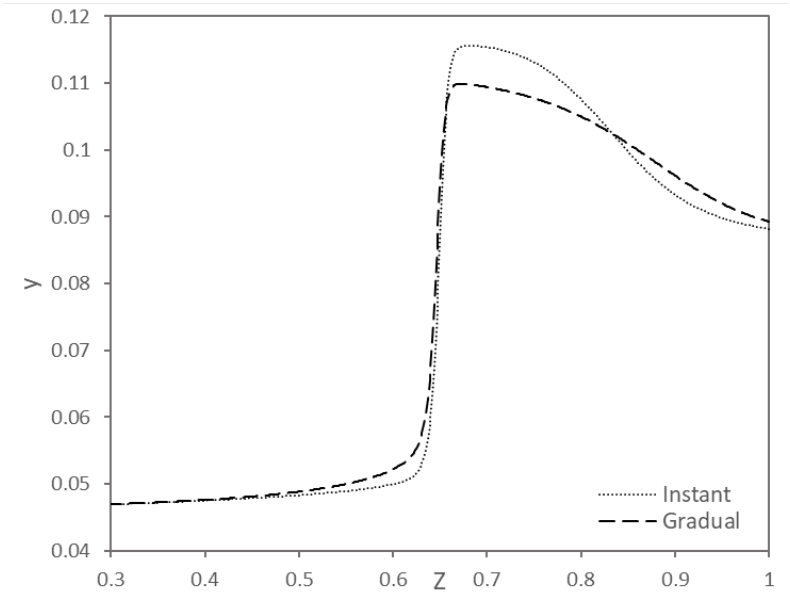


Figure 7.20: Dimensionless reactor temperature, y, against dimensionless bed length, Z, at y_{max} for gradual (0.018 linearly over τ = 0.25) and instantaneous y_f drop.

7.4.3 Dynamic Model Response – Flow Variations

Wrong way behaviour was next investigated for the reduction in feed flowrate case. For computational simplicity an initial feed velocity, u_f, of 1 ms^{-1} was used. The other model parameters were kept as in section 7.4.2. A drop in feed velocity from 1 ms^{-1} to 0.01 ms^{-1}, simulating the transport of reactants from the upstream dead volume into the reactor for both a non-contracting and a mildly contracting reaction, as for a non-stoichiometric FT feed, are shown below in Figure 7.21.

For both cases the temperature at the bed inlet rises immediately after the block-in trip occurs (τ=0.01), as the reaction front becomes much steeper and moves to a new location. For the non-contracting case shown in Figure 7.21A a temperature peak then develops at τ=0.1 before moving down the reactor bed. When contraction is included in Figure 7.21B the temperature peak becomes apparent sooner and, as expected from the results in section 7.4.1, is significantly higher. The contracting case peak also moves through the bed more slowly, again as expected due to the decreasing velocity as the reaction proceeds. These effects combine to intensify the heat produced into a smaller area for an exothermic contracting

reaction, potentially causing unwanted side reactions, carbon laydown and damage to the catalyst and reactor.

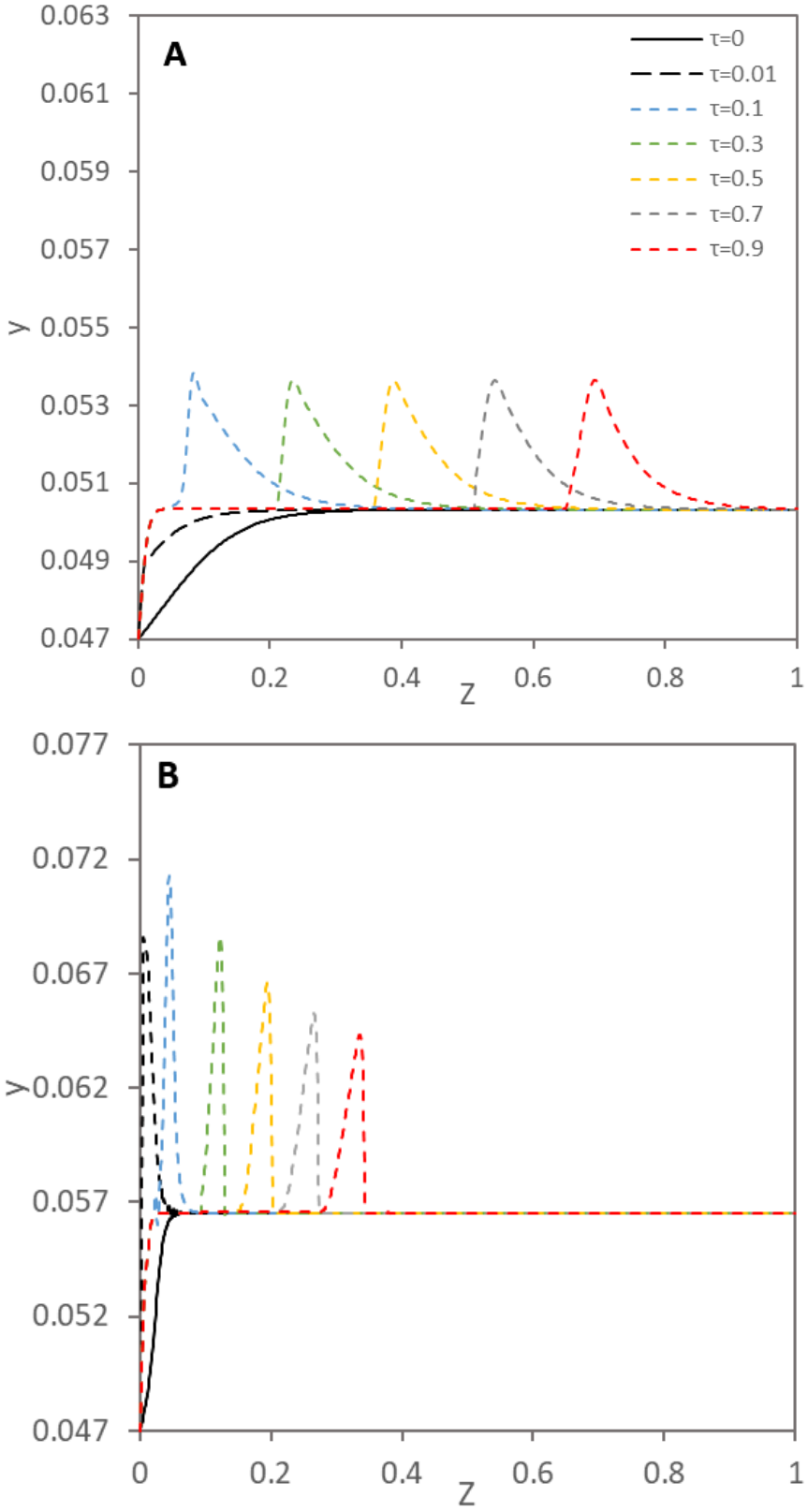


Figure 7.21: Dynamic response to 99% drop in u_f for (A) ε=0 and (B) ε=-0.2. Le=500, M'=540, H'=180, U'=0, β'=0.0167, 1/Pe_M=0, 1/Pe_H=0, y_r=0.0833

Since the reactor is assumed adiabatic and conversion is completed within the bed the final steady-state temperature profile has the same final temperature as the pre-trip profile. In reality the reactor insulation would not be 100% effective and some heat loss to the environment is expected, reducing the final steady state temperature. However, the rate of cooling would be significantly slower than the rate of reaction and therefore this is not expected to alter the value of y_{max} achieved in the peak.

The loss of feed flow model displays some instabilities as the temperature peak moves along the reactor bed which manifest as oscillating y values upstream of the temperature peak. For clarity the oscillations caused by the instability are removed from Figure 7.21, the original plot can be viewed in appendix E.

As previously discussed in section 7.4.1, the dimensionless mass, heat and reaction terms, M', H', β' and ϕ, influence the reaction profile and extent of wrong way behaviour. The sensitivity of the peak dimensionless temperatures to these parameters is investigated in Figure 7.22, Figure 7.23, Figure 7.24 and Figure 7.25 below.

The influence of M' values between 5 and 50 at H' = 150 and ε = -0.2 on y_{max} achieved through wrong way behaviour due to feed loss is given in Figure 7.22. The final dimensionless feed velocity, u_{f2}, is taken between 15% and 2.5% of the initial value, u_{f1}.

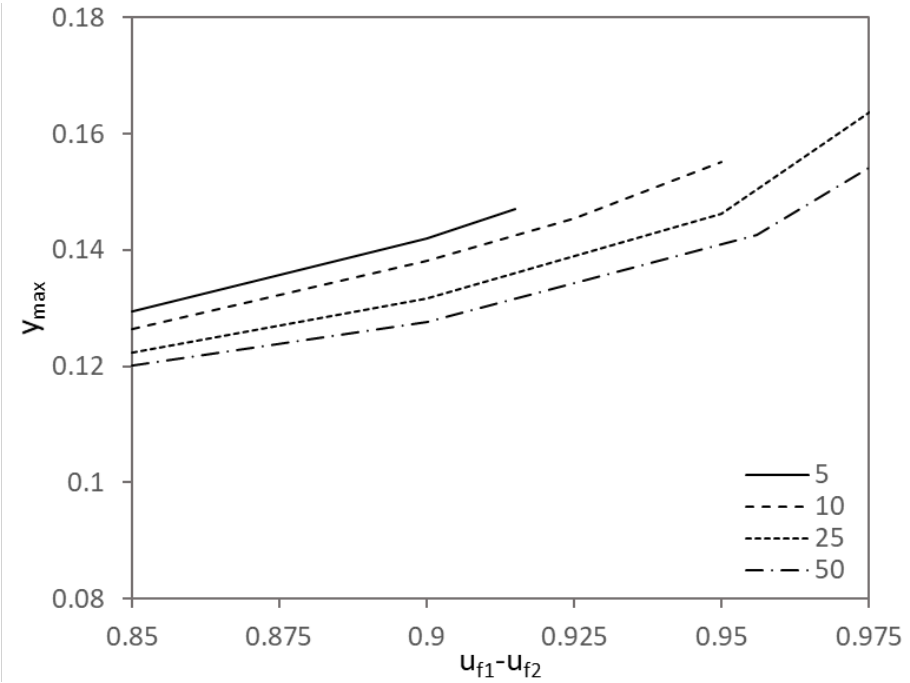


Figure 7.22: Maximum temperatures for M' = 5-50 with H' = 150 for u_{f1}-u_{f2} from 0.85 to 0.975, ε = -0.2.

In contrast to the effect seen in section 7.4.2, where increasing M' values below M' = 10 initially increases the maximum temperature achieved, here the reduction of mass transfer limitations decreases the peak temperature. Since M' is inversely proportional to u_F mass transfer resistances are expected to lower as feed velocity drops, behaving as a system with a higher M' value. Since the system is not mass transfer limited at the low values of v_{f2}, increasing the value of M' allows the heat generated to

dissipate more effectively *via* convection. This effect is seen consistently across the range of velocity drop, with higher losses in feed velocity giving larger values of y_{max}.

The effect of heat transfer resistance is shown in Figure 7.23 for H' values between 40-150. A fixed value of M' = 25 is used to minimise the influence of mass transfer resistance. As with the mass transfer resistances detailed above, y_{max} decreases as H' increases, due to easier dissipation of the heat generated with reduced heat transfer limitations.

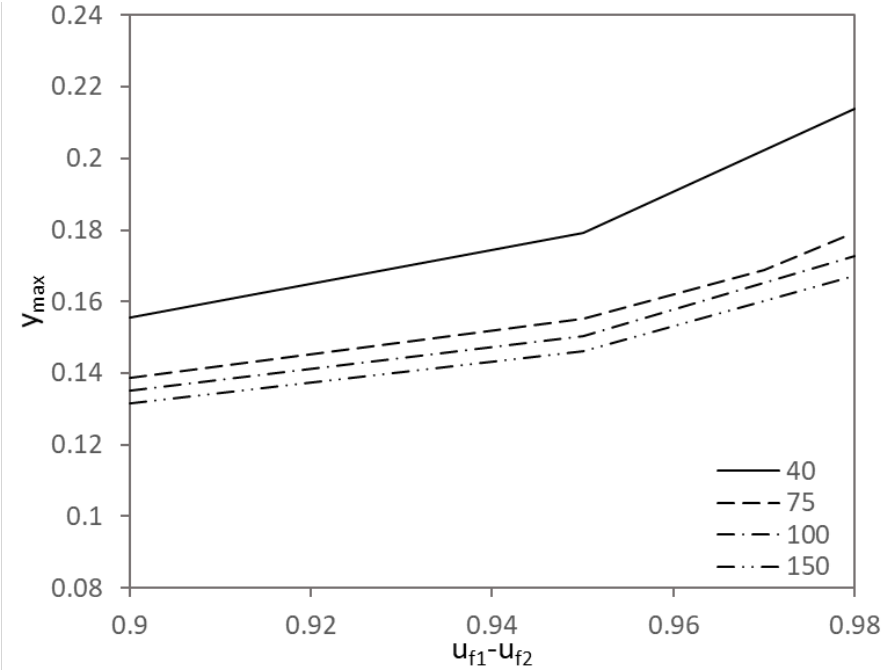


Figure 7.23: Maximum temperatures for H' = 40-150 with M' = 25 for u_{f1}-u_{f2} = 0.9-0.98, ε = -0.2.

As the drop in feed velocity becomes larger the wrong way behaviour and peak temperature are also exaggerated at all values of H', indicating the feed loss case is not heat transfer limited.

Figure 7.24 shows the effect of varying the dimensionless reaction coefficient, β', on peak temperature, y_{max}. As seen in Figure 7.16 for a feed temperature drop, as β' increases the amount of reaction taking place also grows and y_{max} becomes larger. At low values of β' the scale of the velocity drop does not affect y_{max}, however as β' becomes larger the wrong way behaviour exaggerates and y_{max} increases with larger values of v_{f1}-v_{f2}.

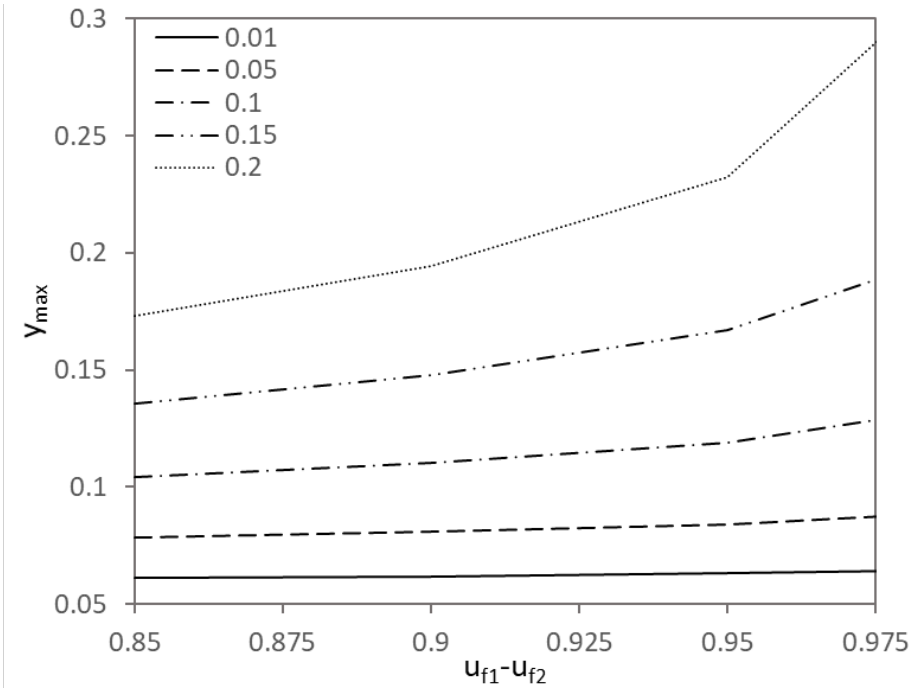


Figure 7.24: Maximum temperatures for β' = 0.01-0.2 with v_{f1}-v_{f2} = 0.85-0.975, M'=25, H'=150, ε = -0.2.

Unlike Figure 7.17 where increasing the Thiele modulus resulted in higher peak temperatures for wrong way behaviour caused by feed cooling, ϕ_0 has negligible effect on y_{max} for loss of feed flow. Figure 7.25 demonstrates that the increase in diffusion resistances as ϕ_0 grows does not limit heat transfer and hence vary y_{max} at the low velocities during a loss of feed.

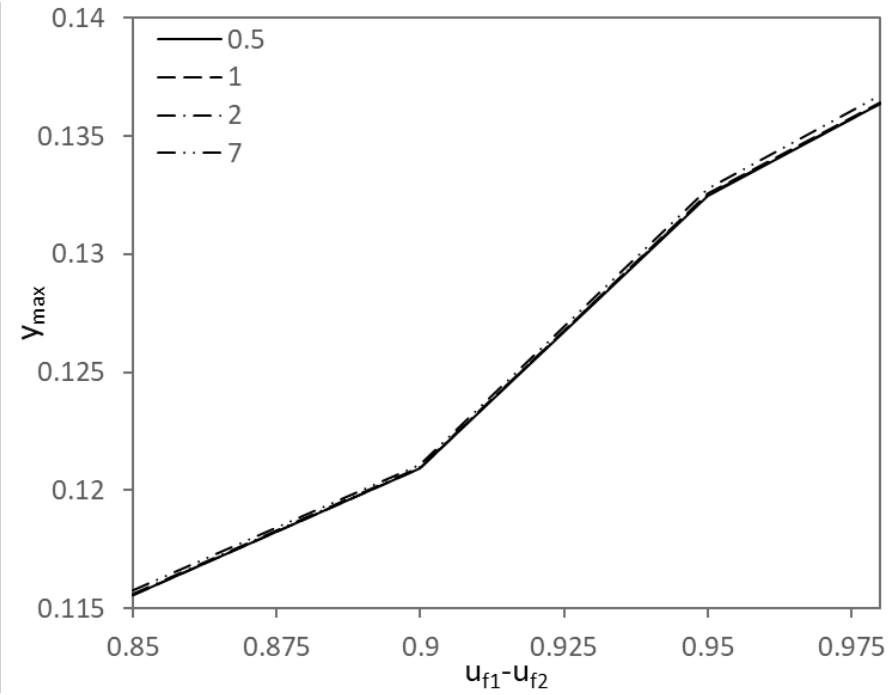


Figure 7.25: Maximum temperatures for ϕ_0 = 0.5-7 with u_{f1}-u_{f2} = 0.85-0.975, M'=25, H'=150, ε = -0.2.

As with the loss of feed heating, loss of feed flow will not be instant and the new feed rate is unlikely to be constant. Large valves take time to completely close and combinations of safety features may

vary rates as they are actuated. The scheduling tool in gPROMS was used to model an assumed linear drop in feed velocity from 100% to 15% at $\tau = 0$ and a further linear drop to 10% over $\tau = 1$, emulating the velocity changes during the seating of a large valve.

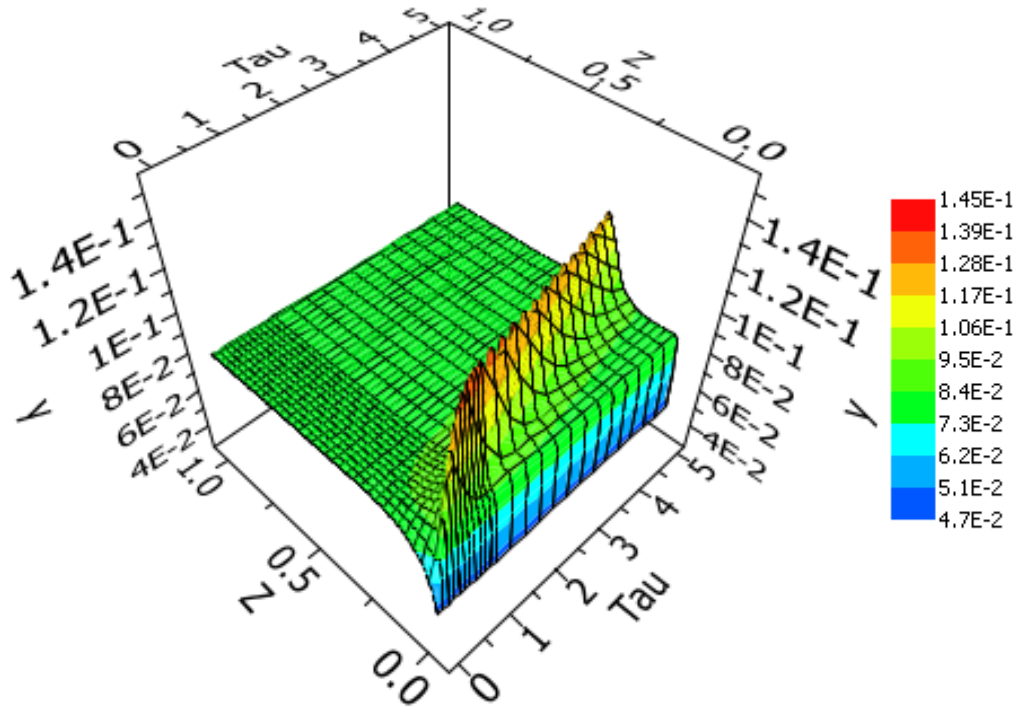


Figure 7.26: 3D plot of dimensionless temperature, y, along dimensionless bed length, Z, during a gradual drop in feed velocity of 100% to 15% at $\tau = 0$ and then to 10% over $\tau = 1$.

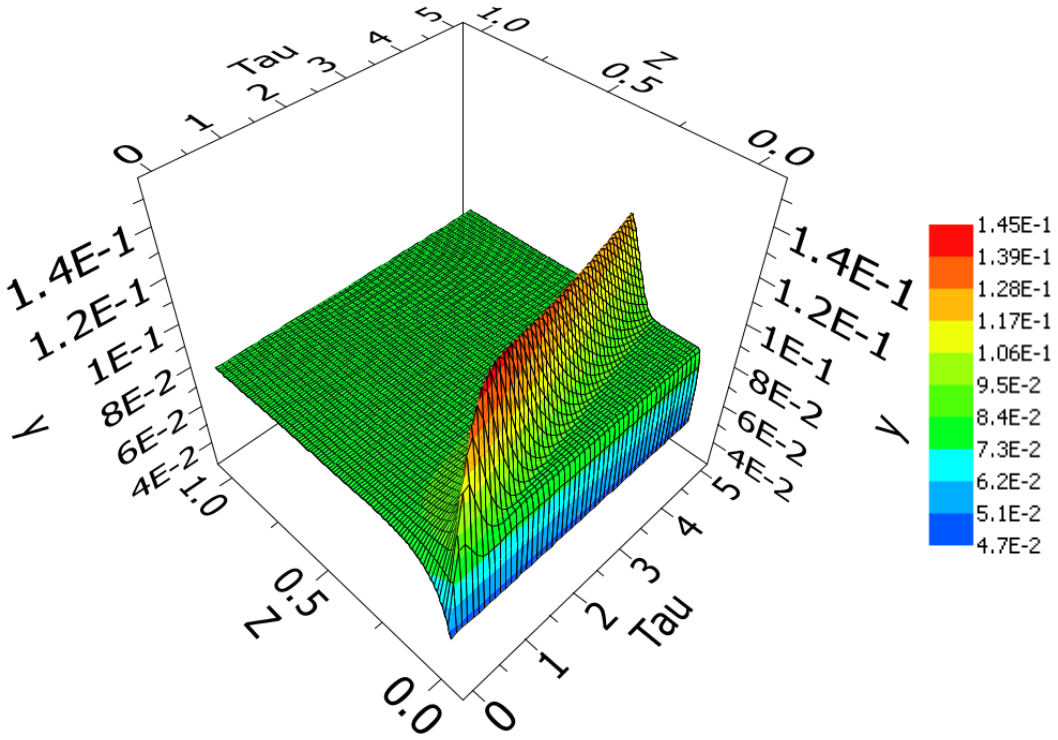


Figure 7.27: 3D plot of dimensionless temperature, y, along dimensionless bed length, Z, during an instantaneous drop in feed velocity to 10%.

Figure 7.26 and Figure 7.27 show that, like the gradual feed temperature loss in Figure 7.20, a slowed rate of feed velocity loss delays the formation of the reactor hot spot and allows it to dissipate. This results in a reduced peak dimensionless temperature, y_{max}, of 0.1360, compared to 0.1447 for an instantaneous drop at the same conditions.

For additional clarity the reactor profiles with the maximum y for both gradual and instantaneous drops are shown alongside each other for comparison in Figure 7.28 below.

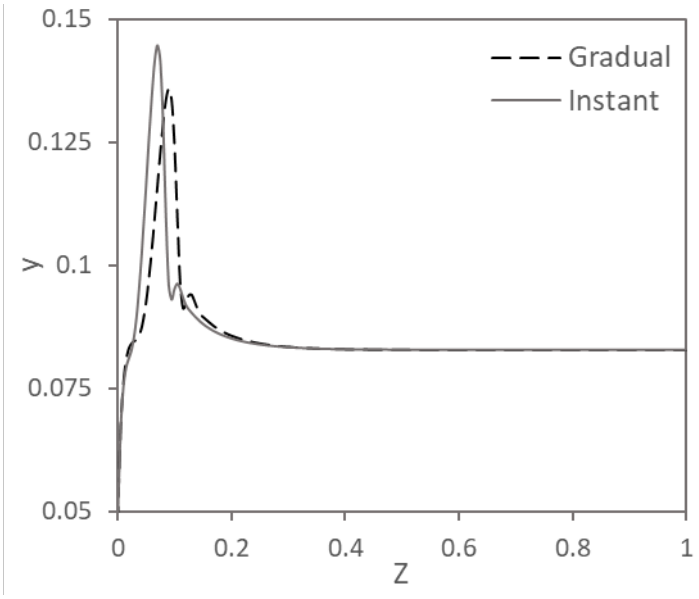


Figure 7.28: Peak dimensionless temperature profile along dimensionless bed length for instant and gradual drops in feed velocity.

The additional dissipation of heat achieved with the gradual drop reduces the peak temperature from 75% to 64% above steady-state y_{max}. As for the wrong way behaviour due to temperature variations, the behaviour of each individual system would need to be accounted for before taking credit in safety assessments for this reduction in peak temperature.

7.5 Conclusions

Both the pseudo-homogeneous and dynamic models reviewed in chapter 7 clearly show that the novel addition of contraction through reaction to fixed bed models results in a varying velocity system with resulting effects on the extent of reaction. The isothermal pseudo-homogeneous model shows the importance of accounting for contraction when modelling, however it is not extensive enough to show anything more than an overall idea of the effects of contraction and does not include temperature profiles. By extending to a non-isothermal heterogeneous model with axial diffusion, more in-depth analysis of the individual factors and their effects on the reaction is possible.

The dynamic heterogeneous model in section 7.3 shows that for FT, a contracting, exothermic reaction, the change in steady state reaction profile by including contraction in the model potentially produces a

significant temperature increase in the range of 100's of degrees C. This is high enough to cause catalyst and equipment damage and should therefore be accounted for.

The model also demonstrates that typical FT reactions over a fixed bed are mass transfer limited. Reducing the mass transfer resistances causes the reaction front to steepen and rapidly reach completion. Increasing internal heat transfer rates has a more limited effect on the reaction profile. Restricting reactant availability at the catalyst surface by varying the reaction term, β, is shown to limit the temperature increase and vary the bed location of the reaction front, but not to alter the reaction profile itself. Finally, increasing the ratio of diffusion and reaction rates within the particle through the Thiele modulus, ϕ, causes the isothermal effectiveness factor, $\eta(y_s)$ to decrease. The drop in $\eta(y_s)$ results in particle diffusion limitations, slowing the reaction in a manner similar to that seen with reducing external mass transfer rates via M.

The intensification of temperature changes on exothermic reactions when contraction is accounted for was also seen when inlet conditions are modified to instigate wrong way behaviour over a fixed bed, using the dynamic model introduced in section 7.3 to simulate loss of feed heating or feed flow.

The dynamic model predicts temperature excursions for exothermic reactions on the loss of feed heating at a variety of initial conditions. In a generic case when a contraction of $\varepsilon = -0.66$ is accounted for the temperature peak increases from 0.1% to almost 4% above the maximum steady state temperature. The magnitude of the temperature peak is dependent on the level of contraction, but also on the mass and heat transfer limitations, reaction coefficient and scale of the inlet change. The same contraction applied to a model with typical FT parameters gives an increased wrong way behaviour peak of 9% above the steady state maximum.

Loss of feed flow in exothermic reactions can also lead to temperature spikes that move down the bed as stagnant gas in the dead volume upstream of the reactor is heated and begins reacting. This has been recognised as an issue with industrial FT reactors during shut in trip situations. A modified pseudo-dimensionless dynamic model has been produced in order to model the dynamic response to feed velocity variations. When contraction is accounted for during a loss of feed flow case the temperature peaks are again exaggerated, from an 8% to a 25% increase, and take longer to pass through the bed due to the reduced volume as the reaction progresses.

As at steady state the dynamic FT model is mass transfer limited. Small increases in the mass transfer parameter, M, result in increases in maximum temperatures increases of over 100% for the loss of feed heating case. At this mass transfer limited stage, the magnitude of the drop in feed temperature has little impact on the peak temperature, however as the mass transfer limitations are reduced the initial change in feed temperature becomes more significant and values of y_{max} begin to decrease again. For the loss of feed flow case the reaction is no longer solely mass transfer limited, as M is inversely

proportional to the lowered feed velocity, u_F. As a result, increasing M decreases the value of y_{max} achieved. Since mass transfer resistances are no longer the only limiting factor, larger drops in u_F give more extreme wrong way behaviour across the range of M values investigated.

A similar effect is seen with varying heat transfer limitations for loss in feed heating cases, where increased values of the heat transfer parameter, H, as well as larger feed temperature drops, result in greater peak temperatures. At steady state it was found that the FT reaction was not significantly heat transfer limited, however, at the higher temperatures seen during wrong way behaviour due to feed cooling some variations in y_{max} with changing heat transfer limitations begin to appear. The magnitude of the rise for loss of feed heating is not as great as for that seen with M, at only approximately 30% increase in peak temperature, but indicates that heat transfer limitations begin to influence the reaction. For drops in feed velocity the behaviour is reversed, with higher H values generating lower peak temperatures. This again suggests that due to the inverse proportionality of H to u_F, the reduced feed flow cases are not significantly heat transfer limited and is corroborated by the consistent increase in y_{max} as u_{F1}-u_{F2} becomes larger across all values of H.

Increasing the reaction parameter, β, for both loss of feed heating and feed flow increases y_{max}, in line with the results seen at steady state. At higher β values the scale of the feed temperature or velocity drop begins to have a greater effect on the extent of wrong way behaviour and y_{max}, with larger drops resulting in higher peak temperatures.

Variations in the Thiele modulus, ϕ, behave in the same manner for loss of feed heating cases, with higher ϕ giving larger y_{max} values as heat transfer *via* convection is reduced. As with the other parameters, the wrong way behaviour is amplified by increased feed temperature drops, particularly at higher values of ϕ. Unlike the reduced feed temperature cases, loss of feed flow situations show negligible changes in peak behaviour with changing Thiele modulus. The reduction in both heat and mass transfer resistances at these conditions means the increased diffusion resistances at higher ϕ values has minimal effect on the dissipation of heat.

The extent of the temperature peak generated due to wrong way behaviour caused by either a loss in feed heating or velocity can be moderated if the feed variation is taken to be gradual, as the heat produced due to the inverse response has an opportunity to dissipate. The extent of spread of the wrong way temperature peak is proportional to the length of time over which the inlet change takes place.

The effect of reduced velocity caused by contraction affects the FT reaction universally. The potentially rapid conversion and large temperature peaks seen when an exothermic reaction undergoes contraction present a significant risk to the catalyst and reactor if unexpected and unprepared for. The FT reaction is also at risk of wrong way behaviour from both loss of feed heating and feed flow trips which can result in peak temperatures far in excess of the steady state maximum. It is therefore suggested that the

benefits gained through the inclusion of variable velocity in a dynamic FT model are well worth the small increase in complexity and processing power.

8 Conclusions

In this thesis foamed iron (III) oxide catalysts were tested for their suitability in the production of liquid fuels from biomass through the BTL *via* FT process. A custom reactor was designed and built in order to test the catalysts at typical industrial conditions.

This closing chapter will review and summarise the important findings of this research, before drawing conclusions on the work as a whole.

8.1 Preparation of Catalysts

Two sets of unsupported Fe_2O_3 based catalysts were produced, a co-precipitated Fe-Zn reference catalyst , and a novel foamed Fe_2O_3 catalyst, produced via a foaming sol-gel method. The foam was calcined at one of two temperatures, 950 °C or 1350 °C, before being crushed into pellets of two size distributions of 106-300 μm and 1000-1250 μm. A portion of all the co-precipitated and foamed catalysts produced were then promoted with 2% K and 1% Cu and calcined again.

XRD analysis found all the catalysts to be composed of predominately hematite. Higher promotion temperatures and longer total calcination times increased crystallinity of the α-Fe_2O_3 catalysts.

Interstitial spaces were formed within the foamed catalysts as part of the production process. This resulted in large pore volumes between 0.29 and 0.98 cm^3g^{-1}, but pore surface areas below 2 m^2g^{-1}. Calcination at the higher temperature of 1350 °C reduced the available surface area significantly, producing a glassy surface devoid of visible grain boundaries and the total loss of the microporous surface seen in all the other catalysts. Secondary calcination periods following promotion resulted in increased grain sizes being measured at the lower calcination temperatures.

8.2 Catalyst Testing

Testing of the foamed catalysts using a simulated bio-syngas containing CO_2 showed that the unpromoted Fe_2O_3 had little inherent FT activity. Promotion with Cu and K increased the conversion of CO for all the foams to between 9-16.5 %.

Rates are higher for the foams calcined at 950 °C than those calcined at 1350 °C, due to the loss of surface area for dissociative adsorption at the higher calcination temperature. Rates are also higher for the 106-300 μm pellets at both temperatures, with correspondingly higher effectiveness factors measured in the smaller catalysts. Low effectiveness factors for the larger particles indicate the 1000-1250 μm pellets are mass transfer limited.

Correspondingly higher hydrocarbon production and CO/H_2 conversion to hydrocarbons rates were also seen with promotion. All the catalysts generated olefins as the primary product and gave similar values of α_1 and α_2 of 0.77-0.84 and 0.86-0.94 in a double ASF distribution model.

The similar ASF distribution seen for all the foams suggests that the reaction mechanism and intrinsic catalyst activity is not drastically altered by the pellet size or calcination temperature. Far more limiting is the reduction in surface sites on catalysts calcined at 1350 °C, and mass transfer limitations introduced with larger pellet size. Despite these limitations the 950 °C catalyst maintained a high level of FT activity with the same sized foam catalyst giving over twice the conversion of the co-precipitated catalyst, showing the foams calcined at 950 °C have potential as unsupported FT catalysts for BTL *via* FT in industry.

8.3 Dynamic Model Allowing for Variable Velocity

Modelling a typical exothermic, contracting, FT reaction at steady state demonstrated the need to include variable velocity in models, with potential temperature increases of over 1000 °C compared to 322 °C when contraction is not accounted for. It showed the fixed bed FT reaction has mass transfer, and to a lesser extent, heat transfer limitations at steady state. Low level diffusional resistances were also apparent within the modelled catalyst particle.

The exaggerated temperatures generated with an exothermic reaction when contraction was accounted for were also seen when investigating dynamic responses to changes in inlet conditions. The phenomenon of wrong way behaviour after a drop in feed temperature or velocity was shown to produce temperature peaks as the reactor moves to the new steady state. These temperature peaks are amplified when contracting reactions are considered.

The dynamic response to decreasing feed temperatures exhibited similar sensitivities to heat and mass transfer parameters to those seen at steady state. The reaction remained predominantly mass transfer limited; however, the heat transfer resistances began to influence the reaction as the peak temperatures increased due to wrong way behaviour.

The behaviour following a drop in feed velocity was slightly different however, with little heat or mass limitation shown, since both the heat and mass parameters are inversely dependant on fluid velocity. The low heat and mass transfer resistances meant that variation in the Thiele modulus had little effect on the peak temperatures since diffusion is no longer a major method for the internal dissipation of heat.

8.4 Future Work

In this final section some future work is proposed. This thesis has shown that the promoted foamed iron oxides are potential FTS catalysts, with high activities compared to the reference catalyst and show promise for use in fixed bed FT reactors. However, more investigation is required into the catalyst behaviour under industrial FTS conditions. The ideas below were considered outside the scope of the work and hence are not included in this thesis, but merit further investigation.

8.4.1 High Temperature Fischer-Tropsch Reactor Conditions

In this work the reactor temperature and pressure were maintained at typical LTFT conditions of 30 barg and 220 °C. One of the benefits of an iron based catalyst is the flexibility in reaction conditions, particularly increased temperatures. Higher temperatures can increase reaction rates and favour smaller products. An additional set of experiments investigating the activity of the foamed iron oxide catalysts at typical HTFT conditions of 300-350 °C would demonstrate how adaptable the catalyst may be for varying fixed bed reactor conditions and desired product ranges.

8.4.2 Catalyst Promotion

The promotors for both the co-precipitated and foamed catalyst were based on those used in the reference catalyst. This work has shown that promotion with K and Cu significantly increases the FT activity of all the Fe based catalysts. Several studies have suggested that increased levels of K promotion have beneficial results on the catalyst activity, an investigation into a range of promotor loadings on the 950-106-P catalyst would show the effect of varying promotion on catalyst activity and product range.

8.4.3 Catalyst Calcination Temperature

Increasing the catalyst calcination temperature form 950 °C to 1350 °C significantly reduced the activity due to a loss of the microporous surface area. High calcination temperatures are often used to increase the crush strength of metal oxides and can help increase catalyst life. A more suitable calcination temperature between 950-1350 °C may exist that optimises available surface area and crush strength. It is suggested that a batch of foamed catalyst is produced and calcined at several temperatures between 950-1350 °C to determine the effect of calcination temperature on both catalyst surface structure and crush strength and identify a possible optimum calcination temperature.

8.4.4 Extended Reaction Periods

Industrially FTS reactors would run continuously for many months. The run times of approximately 100 hours used in this work were chosen to try and demonstrate steady state conditions within the constraints of the experiment, however extended run times >1000 hours need to be carried out to determine the catalyst performance over typical industrial lifespans. The activity, product distribution and catalyst degradation should be monitored over these longer reaction run periods.

8.4.5 Two Dimensional Dynamic Model

The model presented in chapter 7 assumes no radial concentration or temperature gradient, but for large diameter industrial fixed beds this may not be an accurate representation. The inclusion of a second dimension into the model may allow more accurate predictions of potential hot spots and give an indication of optimum thermocouple location.

A Safety Reviews

LOPA

Three of the most serious cases have been reviewed quantitively using LOPA for risk ratings. Risk for serious incidents to be reduced below $1x10^{-6}$ $year^{-1}$.

Case 1: Failure of gas cylinder pressure regulator, loss of containment of toxic syngas, ignition, explosion within fume cupboard, one fatality.

Initiating Event	**Frequency / yr**	**Reference**
Cylinder pressure regulator failure	0.01	A review of Instrument Failure Data, F P Lees, 1976, *Control valve fails open 0.5* Risks associated with the storage and use of chlorine at a water treatment plant, SRD, 1981, *Pressure reducing device release (1kg/s) 10^{-2}*
Mitigating Factors	**Probability**	**Reference**
Occupancy in lab	0.5	Assuming working during extended office hours 7am-7pm
Probability of ignition	1	Worst case
Probability that ignition results in explosion	1	Worst case
Independent Protection Layers	**PFD**	
Pressure control system	0.1	Maximum allowable credit for basic process control system
Gas detection AND ESD valve shutoff	0.01	ASOV failure from HSE failure rates *0.01* Gas detection SIL 2 therefore *0.01*
Local exhaust Ventilation	0.1	Can take credit for SIL 1 only.
Mitigated Event Likelihood / yr	**5.00E-07**	

Case 2: Failure of gas cylinder pressure regulator, loss of containment of toxic syngas to lab, 2-5 fatalities.

Initiating Event	**Frequency / yr**	**Reference**
Cylinder pressure regulator failure	0.01	A review of Instrument Failure Data, F P Lees, 1976, *Control valve fails open 0.5* Risks associated with the storage and use of chlorine at a water treatment plant, SRD, 1981, *Pressure reducing device release (1kg/s) 10^-2*
Mitigating Factors	**Probability**	
Occupancy in lab	0.5	Assuming working during extended office hours 7am-7pm
Independent Protection Layers	**Probability Failed on Demand**	
Pressure control system	0.1	Maximum allowable credit for basic process control system
Gas detection in fume hood and lab AND ESD valve shutoff	0.01	ASOV failure from HSE failure rates *0.01* Gas detection SIL 2 therefore *0.01*
Local exhaust Ventilation, both in fume cupboard and lab	0.01	Can take credit for SIL 1 only, each.
Mitigated Event Likelihood / yr	**5.00E-08**	

Case 3: Leak of fitting to FTIR/MS, loss of containment of toxic syngas to lab, 1 fatality.

Initiating Event	**Frequency / yr**	**Reference**
Leak	0.01	Based on infrequent operator event.
Mitigating Factors	**Probability**	
Occupancy in lab	0.5	Assuming working during extended office hours 7am-7pm
Reduced flowrate	0.356	Max leak rate of syngas 40 ml/min in lab of >75m^3, toxic at 30ppm+
Independent Protection Layers	**Probability Failed on Demand**	
Gas detection at FTIR fitting	0.1	Not SIL tested detection, therefore max RRF of 10.
Gas detection in fume hood and lab AND ESD valve shutoff	0.01	ASOV failure from HSE failure rates *0.01* Gas detection SIL 2 therefore *0.01*
Local exhaust Ventilation	0.1	Can take credit for SIL 1 only.
Mitigated Event Likelihood / yr	**1.78E-07**	

HAZOP

Node 1: Gas Mixing

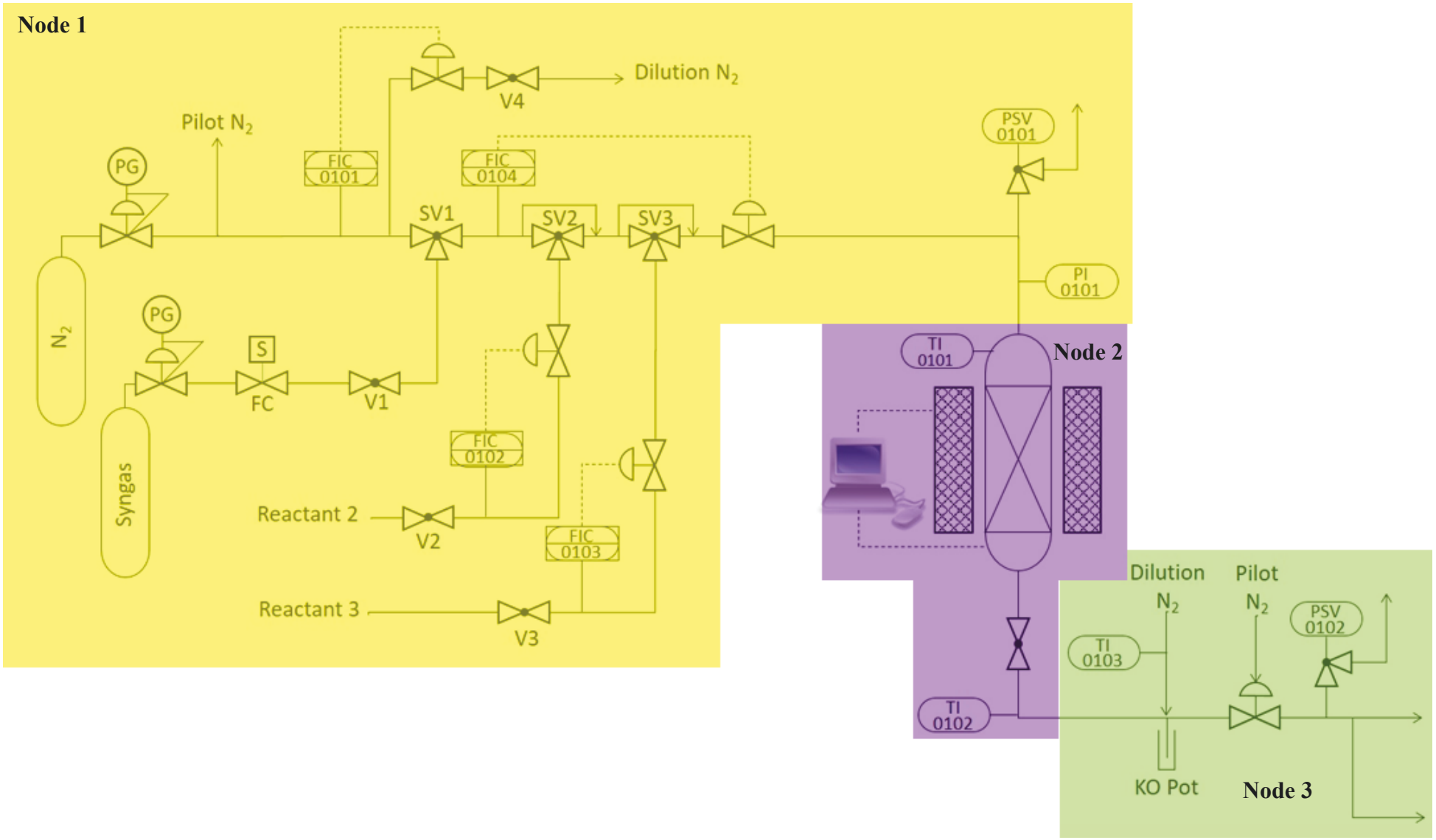
Controlled flowrates of mix gases from cylinders to achieve steady total flowrate of 50mlmin^{-1}, 31.6 barg of mixed gas at inlet to reactor. Tight shutoff for unused reactants via 3-way switching valves (SV1-3). Allows for a N_2 pilot gas and dilution take off of 2000mlmin^{-1}.

Node 2: Heating and Reactor

Preheating of mixed gas via electrical tracing to achieve approx. 200 °C on inlet to reactor. Further controlled heating via PID controlled heater to reaction temperature of 220 °C within reactor. Electrically traced outlet line to maintain temperature above approx. 150 °C to avoid condensing of non-vapour products.

Node 3: Cooling and Analysis

Mixed gases at 31.6 barg and 220 °C are cooled using N_2 dilution flow at approx. 70 °C to knock out condensables. Liquid products removed for GC analysis once KO pot depressurised. Gaseous products maintained at 70 °C via electrical tracing and fed to continuous online FTIR and MS analysis. Pressure control of system via BPR. Vent gases returned to fume cupboard and vented in a safe location.


Node 1
Dilution N_2
V4
Pilot N_2
PG
FIC 0101
FIC 0104
SV1
SV2
SV3
PSV 0101
PI 0101
N_2
PG
S
FC
V1
Syngas
FIC 0102
Reactant 2
V2
FIC 0103
Reactant 3
V3
TI 0101
Node 2
Dilution N_2
Pilot N_2
PSV 0102
TI 0103
TI 0102
KO Pot
Node 3

Node		Parameter	Deviation	Cause	Consequence	Existing safeguards	Prob	Sev	Action
1	i	**Flow - reactor**	No	N2 Cylinder empty/supply valves closed	None				N/A
	ii			Syngas cylinder empty/supply valves closed	Increased τ, resulting in exotherm in reactor, damage/loss of reactor	High T shut down on furnace	4	3	Review extent of exotherm possible Review design conditions for possible exotherm. Independent power and IA (via solanoid valve) shutoff. Also via manual shutdown button.
	iii			IA failure	As ii	As ii			As ii
	iv			Liquid plug downstream of reactor	As ii	As ii			As ii
	v	**Flow - dilution**	No	As No reactor flow	Loss of FTIR acuuracy				N/A
					Concentration of outlet CO increases	Fume cupboard, 2*CO monitor in hood.			Calc max syngas flow through valve with no dilution. With minimum fume cupboard flow calc conc. SOP needs to say about fume cupboard. Move one CO monitor to lab.
	vi	**Flow**	Incorrect	Incorrect cylinder plumbed in	Oxidant in mix	Unused reactants blanked off	3	4	'No oxidants allowed' listed in SOP
	vii	**Flow**	Reverse	Failure of 3 way valve allowing N2 into syngas and vic versa	Mix/release of reactants in un-intended location	cylinder regulators should minimise reverse flow.			Install check valves on all cylinders and reactor inlet
	viii			Higher pressure in one cylinder, allowing reverse flow of reactant 2 or 3 via open route back to syngas or N2	As vii	As vii			As vii
	ix			Loss of syngas cylinder pressure whilst reacting,	Reactants and potentially products upstream of the reactor				As vii

				diffusion of high pressure reactor contents				
	x		High	FIC/PV4 fail on syngas (not an issue with N2, others double jeopardy)	As ii			As ii
	xi			cylinder failure	Release of cylinder content into system	System rated to 288barg, PSV at 35 barg.	1 2	Calc max flow through badger valve Calc max flow through BPR Calc max flow through FTIR & MS
	xii		Low	As no flow				As no flow
	xiii	**Pressure**	High	As high flow		System rated to 288barg, PSV at 35 barg.		As high flow
	xiv		Low	As low/reverse flow				As low/reverse flow
	xv		Negative	Cylinders off, MS on and pulling vacuum	Could vaporise liquid in trap, more likely to pull air through FTIR		1 2	N/A
	xvi	**Temperature**	High	Via reverse flow	As reverse flow			As reverse flow
	xvii		Low	Rapid release via high flow (of CO_2)	Failure of polymer seals, loss of flow control.			Calc min T possible with max CO2 flow and dP
2	xviii	**Flow**	High/Low/No	As ii	As ii	As ii		As ii
	xix		Reverse	PSV lifts /fluidises bed	Solid in valves from fluidised bed			Filter on reactor inlet, considered bursting disk but deemed unnecessary. SOP says to test PSV regularly Balloon on end of PSV vent line to see if lifted

xx	**Temperature**	High	Thermocouple failure	Low/high reading cuts off power via software Watchdog shuts off power if no signal		As ii
xxi			Inner thermocouple not inserted correctly	Power shut down if dT >20 via software		Visual inspection of thermocouples in SOP
xxii		Low	N/A			
	Pressure	High	As ii			As ii
		Low	BRP failure	Loss of reaction		N/A
		Negative	As xv			N/A
	Composition	Air/oxidant	Air in bed, incomplete purge	Exotherm when catalyst oxidises	As ii	Calc max T rise via oxidation, flash point of possible syngas/air mixtures. Set Labview up to not allow pressurisation if no flow through PV4.
	Other	Mis/re-use of reactor body	N/A - all reactors in group made of incaloy			N/A
			Used reactors disposed of. Only change reactor body with Paul's permission.			Mention in SOP Reactor diameter reduced so no other reactors of same dimension. Removal from furnace body is destructive so cannot be reused.

3	**Flow**	High	As nodes 1 & 2	Potentially entrained liquid, damage to FTIR/MS	FTIR/MS have own heated inlets, some resistance to liquids. BPR ok with liquids	N/A
		Low	As xii			As xii
		No	As node 1 Blocked quartz wool liquid knock out			As node 1
	Temperature	High	CW failure	No trapping of liquids	Inherent cooling through lines	Dry ice cooling on inlet to vent Consider removing CW cooling for more inherent air cooling.
			Dry ice trap failure	Condensation in vent, potential flammable liquids released	Inherent cooling through lines, low points before vent	SOP to state to check for liquids in vent and FTIR
	Pressure	High	FTIR valve closed	MS overpressure as all flow diverted to MS		No valve on FTIR inlet - options are only to FTIR or vent

B Temperature Dependent Dynamic Model Full Derivation

Gas Phase Mass Balance

Mass balance in terms of mols^{-1}. All in terms of H_2.

Accumulation = convection in plug – convection out – diffusion out + diffusion in + transfer from particle.

$$\frac{d}{dt}\left(C_{H_2}\epsilon dV_{bed}\right) = u|_z C_{H_2}|_z A_{bed} - u|_{z+\delta z} C_{H_2}|_{z+\delta z} A_{bed} - D\frac{dC_{H_2}}{dz}|_z A_{bed} + D\frac{dC_{H_2}}{dz}|_{z+\delta z} A_{bed} + k_m\left(C_{H_2 S} - C_{H_2}\right) dA_S \quad B.1$$

$$C_i = x_i C_T \qquad C_T = 1/V_m \quad B.2, B.3$$

where C_T is the total concentration and V_m is the molar volume m^3mol^{-1}, giving;

$$C_i = x_i/V_m \quad B.4$$

$$\frac{d}{dt}\left(\frac{x_{H_2}}{V_M}\epsilon dV_{bed}\right) = u|_z \frac{x_{H_2}}{V_M}|_z A_{bed} - u|_{z+\delta z}\frac{x_{H_2}}{V_M}|_{z+\delta z} A_{bed} - D\frac{d\frac{x_{H_2}}{V_M}}{dz}|_z A_{bed} + D\frac{d\frac{x_{H_2}}{V_M}}{dz}|_{z+\delta z} A_{bed} + k_m\left(\frac{x_{H_2 S}}{V_M} - \frac{x_{H_2}}{V_M}\right) dA_S \quad B.5$$

Assuming spherical particles then the surface area, $A_S = 4\pi {r_p}^2$

Volume of the particle $dV_p = (1-\epsilon)dV_{bed} = \frac{4}{3}\pi {r_p}^3$

giving $V_{bed} = {\frac{4}{3}\pi {r_p}^3}\Big/{(1-\epsilon)}$

Divide by dV_{bed}. $\frac{A_{bed}}{dV_{bed}} = 1/dz$ $\frac{dA_S}{dV_{bed}} = \frac{4\pi {r_p}^2}{{\frac{4}{3}\pi {r_p}^3}/{(1-\epsilon)}} = \frac{3(1-\epsilon)}{r_p}$

$$\frac{d}{dt}\left(\frac{x_{H_2}}{V_M}\epsilon\right) = u|_z \frac{x_{H_2}}{V_M}|_z \frac{1}{dz} - u|_{z+\delta z}\frac{x_{H_2}}{V_M}|_{z+\delta z}\frac{1}{dz} - D\frac{d\frac{x_{H_2}}{V_M}}{dz}|_z \frac{1}{dz} + D\frac{d\frac{x_{H_2}}{V_M}}{dz}|_{z+\delta z}\frac{1}{dz} + \left(\frac{x_{H_2 S}}{V_M} - \frac{x_{H_2}}{V_M}\right)\frac{k_m 3(1-\epsilon)}{r_p} \quad B.6$$

$1/V_M$ can be removed from Fick's first law[clxxxix], giving:

$$\frac{d}{dt}\left(\frac{x_{H_2}}{V_M}\epsilon\right) = u|_z \frac{x_{H_2}}{V_M}|_z \frac{1}{dz} - u|_{z+\delta z}\frac{x_{H_2}}{V_M}|_{z+\delta z}\frac{1}{dz} - \frac{D}{V_M}\frac{dx_{H_2}}{dz}|_z \frac{1}{dz} + \frac{D}{V_M}\frac{dx_{H_2}}{dz}|_{z+\delta z}\frac{1}{dz} + \left(x_{H_2 S} - x_{H_2}\right)\frac{k_m 3(1-\epsilon)}{r_p V_M} \quad B.7$$

Limits tending to zero, assuming D is constant along z and can therefore be removed from Fick's second law, however V_M, since it is dependent on T and therefore z, cannot.

$$\epsilon \frac{d\left(\frac{x_{H_2}}{V_M}\right)}{dt} = -\frac{d\left(\frac{x_{H_2}}{V_M}u\right)}{dz} + D\left(\frac{1}{V_M}\frac{dx_{H_2}}{dz}\right)\frac{1}{dz} + \left(x_{H_2S} - x_{H_2}\right)\frac{k_m 3(1-\epsilon)}{r_p V_M} \qquad B.8$$

Divide by ϵ

$$\frac{d\left(\frac{x_{H_2}}{V_M}\right)}{dt} = -\frac{1}{\epsilon}\frac{d\left(\frac{x_{H_2}}{V_M}u\right)}{dz} + \frac{D}{\epsilon}\left(\frac{1}{V_M}\frac{dx_{H_2}}{dz}\right)\frac{1}{dz} + \left(x_{H_2S} - x_{H_2}\right)\frac{k_m 3(1-\epsilon)}{\epsilon r_p V_M} \qquad B.9$$

Dimensionless time, τ, taken as per Chen and Luss paper

$$\tau = \frac{u_f t}{\epsilon L}\frac{1}{Le} \qquad B.10$$

Therefore

$$\frac{d\,\frac{x}{V_m}}{dt} = \frac{d\tau}{dt}\frac{d\,\frac{x}{V_m}}{d\tau} = \frac{u_f}{\epsilon L}\frac{1}{Le}\frac{d\,\frac{x}{V_m}}{d\tau}$$

Dimensionless length, Z, taken as Z=z/L

Therefore

$$\frac{dx}{dz} = \frac{dZ}{dz}\frac{dx}{dZ} = \frac{1}{L}\frac{dx}{dZ}$$

Combining gives

$$\frac{u_f}{\epsilon L}\frac{1}{Le}\frac{d\left(\frac{x_{H_2}}{V_M}\right)}{d\tau} = -\frac{1}{L\epsilon}\frac{d\left(\frac{x_{H_2}}{V_M}u\right)}{dZ} + \frac{D}{L^2\epsilon}\left(\frac{1}{V_M}\frac{dx_{H_2}}{dZ}\right)\frac{1}{dZ} + \left(x_{H_2S} - x_{H_2}\right)\frac{k_m 3(1-\epsilon)}{\epsilon r_p V_M} \qquad B.11$$

Divide by $\frac{u_f}{\epsilon L}$

$$\frac{1}{Le}\frac{d\left(\frac{x_{H_2}}{V_M}\right)}{d\tau} = -\frac{1}{u_f}\frac{d\left(\frac{x_{H_2}}{V_M}u\right)}{dZ} + \frac{D}{u_f L}\left(\frac{1}{V_M}\frac{dx_{H_2}}{dZ}\right)\frac{1}{dZ} + \left(x_{H_2S} - x_{H_2}\right)\frac{k_m 3L(1-\epsilon)}{u_f r_p V_M} \qquad B.12$$

Take M as $M = \frac{3k_m L(1-\epsilon)}{u_f r_p}$ define $Pe_M = \frac{u_f L}{D}$

$$\frac{1}{Le}\frac{d\left(\frac{x_{H_2}}{V_M}\right)}{d\tau} = -\frac{1}{u_f}\frac{d\left(\frac{x_{H_2}}{V_M}u\right)}{dZ} + \frac{1}{Pe_M}\left(\frac{1}{V_M}\frac{dx_{H_2}}{dZ}\right)\frac{1}{dZ} + \left(x_{H_2S} - x_{H_2}\right)\frac{M}{V_M} \qquad B.13$$

However, u still varies with both T, P and reaction. V_M varies with T and therefore Z.

Dimensionless velocity, u', is defined using u_R as a reference velocity (to allow velocity step changes later on). $u' = \frac{u}{u_R}$

$$\frac{1}{Le}\frac{d\left(\frac{x_{H_2}}{V_M}\right)}{d\tau} = -\frac{u_R}{u_f}\frac{d\left(\frac{x_{H_2}}{V_M}u\prime\right)}{dZ} + \frac{1}{Pe_M}\left(\frac{1}{V_M}\frac{dx_{H_2}}{dZ}\right)\frac{1}{dZ} + \left(x_{H_2S} - x_{H_2}\right)\frac{M}{V_M} \qquad B.14$$

Assuming ideal gas $V_M = \frac{V}{n} = \frac{RT}{P}, \qquad V_{M_R} = \frac{RT_R}{P_R}$

$$\frac{V_M}{V_{M_R}} = \frac{T}{T_R}\frac{P_R}{P} \qquad V_M = V_{M_R}\frac{T}{T_R}\frac{P_R}{P}$$

$$\frac{1}{Le}\frac{d\left(\frac{x_{H_2}}{V_{M_R}\frac{T}{T_R}\frac{P_R}{P}}\right)}{d\tau} = -\frac{u_R}{u_f}\frac{d\left(\frac{x_{H_2}}{V_{M_R}\frac{T}{T_R}\frac{P_R}{P}}u\prime\right)}{dZ} + \frac{1}{Pe_M}\left(\frac{1}{V_{M_R}\frac{T}{T_R}\frac{P_R}{P}}\frac{dx_{H_2}}{dZ}\right)\frac{1}{dZ} + \left(x_{H_2S} - x_{H_2}\right)\frac{M}{V_{M_R}\frac{T}{T_R}\frac{P_R}{P}} \qquad B.15$$

Simplify and cancel through V_{MR}

$$\frac{1}{Le}\frac{d\left(x_{H_2}\frac{P}{P_R}\frac{T_R}{T}\right)}{d\tau} = -\frac{u_R}{u_f}\frac{d\left(x_{H_2}u\prime\frac{P}{P_R}\frac{T_R}{T}\right)}{dZ} + \frac{1}{Pe_M}\left(\frac{P}{P_R}\frac{T_R}{T}\frac{dx_{H_2}}{dZ}\right)\frac{1}{dZ} + \left(x_{H_2S} - x_{H_2}\right)M\frac{P}{P_R}\frac{T_R}{T} \qquad B.16$$

With a constant pressure down the bed, assuming pressure loss due to friction is <5% of inlet pressure.

$$\frac{1}{Le}\frac{d\left(x_{H_2}\frac{T_R}{T}\right)}{d\tau} = -\frac{u_R}{u_f}\frac{d\left(x_{H_2}u\prime\frac{T_R}{T}\right)}{dZ} + \frac{1}{Pe_M}\left(\frac{T_R}{T}\frac{dx_{H_2}}{dZ}\right)\frac{1}{dZ} + \left(x_{H_2S} - x_{H_2}\right)M\frac{T_R}{T} \qquad B.17$$

$$\frac{u_R}{u_f} = \frac{1}{u_f'} \qquad T = \frac{yE}{R}$$

$$\frac{1}{Le}\frac{d\left(x_{H_2}\frac{y_R}{y}\right)}{d\tau} = -\frac{1}{u_f'}\frac{d\left(x_{H_2}u\prime\frac{y_R}{y}\right)}{dZ} + \frac{1}{Pe_M}\left(\frac{y_R}{y}\frac{dx_{H_2}}{dZ}\right)\frac{1}{dZ} + \left(x_{H_2S} - x_{H_2}\right)M\frac{y_R}{y} \qquad B.18$$

With no reaction the 3rd and 4th terms are zero, so no change in diffusion or reaction with temperature as expected.

<u>Fluid Energy Balance</u>

Accumulation = convection in– convection out – diffusion out + diffusion in + transfer from particle + transfer from wall. All in terms of Js^{-1}

$$\frac{d}{dt}\left(\rho_f c_f T\epsilon dV_{bed}\right) = \rho_f c_f u|_z T|_z A_{bed} - \rho_f c_f u|_{z+\delta z} T|_{z+\delta z} A_{bed} - \lambda\frac{dT}{dz}|_z A_{bed} + \lambda\frac{dT}{dz}|_{z+\delta z} A_{bed} + h(T_s - T)dA_s + h_w(T_w - T)dA_w \qquad B.19$$

Divide by dV_{bed}. $\frac{A_{bed}}{dV_{bed}} = 1/dz \qquad \frac{dA_s}{dV_{bed}} = \frac{3dV_p/r_p}{dV_p/(1-\epsilon)} = \frac{3(1-\epsilon)}{r_p} \qquad \frac{dA_w}{dV_{bed}} =$

$\frac{2\pi r\, dz}{\pi r^2 dz} = \frac{2}{r}$

$$\frac{d}{dt}\left(\rho_f c_f T\epsilon\right) = \rho_f c_f u|_z T|_z \frac{1}{dz} - \rho_f c_f u|_{z+\delta z} T|_{z+\delta z} \frac{1}{dz} - \lambda \frac{dT}{dz}|_z \frac{1}{dz} + \lambda \frac{dT}{dz}|_{z+\delta z} \frac{1}{dz} + h(T_s - T)\frac{3(1-\epsilon)}{r_p} + h_w(T_w - T)\frac{2}{r} \quad B.20$$

Limits tending to zero

$$\frac{dT}{dt}\left(\rho_f c_f \epsilon\right) = -\rho_f c_f \frac{d(Tu)}{dz} + \lambda \frac{d^2T}{dz^2} + (T_s - T)\frac{3h(1-\epsilon)}{r_p} + (T_w - T)\frac{2h_w}{r} \quad B.21$$

Divide by ϵ

$$\frac{dT}{dt}\left(\rho_f c_f\right) = \frac{-\rho_f c_f}{\epsilon}\frac{d(Tu)}{dz} + \frac{\lambda}{\epsilon}\frac{d^2T}{dz^2} + (T_s - T)\frac{3h(1-\epsilon)}{r_p\epsilon} + (T_w - T)\frac{2h_w}{r\epsilon} \quad B.22$$

Dimensionless time, τ, taken as

$$\tau = \frac{u_f t}{\epsilon L}\frac{1}{Le}$$

Dimensionless temperature, y, and dimensionless bed length, Z, taken as

$$T = \frac{yE}{R} \qquad Z = \frac{z}{L}$$

$$\frac{u_f}{\epsilon L}\frac{1}{Le}\frac{dy}{d\tau}\left(\rho_f c_f\right) = \frac{-\rho_f c_f}{L\epsilon}\frac{d(yu)}{dZ} + \frac{\lambda}{\epsilon L^2}\frac{d^2y}{dZ^2} + (y_s - y)\frac{3h(1-\epsilon)}{r_p\epsilon} + (y_w - y)\frac{2h_w}{r\epsilon} \quad B.23$$

Divide by $\frac{u_f \rho_f c_f}{\epsilon L}$

$$\frac{1}{Le}\frac{dy}{d\tau} = \frac{-1}{u_f}\frac{d(yu)}{dZ} + \frac{\lambda}{u_f L \rho_f c_f}\frac{d^2y}{dZ^2} + (y_s - y)\frac{3hL(1-\epsilon)}{r_p u_f \rho_f c_f} + (y_w - y)\frac{2h_w L}{r u_f \rho_f c_f} \quad B.24$$

Define $H = \frac{3hL(1-\epsilon)}{u_f r_p \rho_f c_f}$ $U = \frac{2h_w L}{u_f r \rho_f c_f}$ $Pe_H = \frac{u_f L \rho_f c_f}{\lambda}$

$$\frac{1}{Le}\frac{dy}{d\tau} = -\frac{1}{u_f}\frac{d(yu)}{dZ} + \frac{1}{Pe_H}\frac{d^2y}{dZ^2} + (y_s - y)H + (y_w - y)U \quad B.25$$

$$u' = \frac{u}{u_r}$$

$$\frac{1}{Le}\frac{dy}{d\tau} = -\frac{u_r}{u_f}\frac{d(yu')}{dZ} + \frac{1}{Pe_H}\frac{d^2y}{dZ^2} + (y_s - y)H + (y_w - y)U \quad B.26$$

$$\frac{1}{Le}\frac{dy}{d\tau} = -\frac{1}{u'_f}\frac{d(yu')}{dZ} + \frac{1}{Pe_H}\frac{d^2y}{dZ^2} + (y_s - y)H + (y_w - y)U \quad B.27$$

Velocity Taking Reaction and T/P into Account

A total mass balance is performed to determine the effect of reaction and conditions on velocity

Velocity in ms^{-1}. All terms in $mols^{-1}$. V_M is specific molar volume m^3mol^{-1}.

Since the reaction is described in terms of H_2 and not total molar concentration, the reaction term must allow for this. A scaling term, f, is used to scale the consumption of H_2 with the overall change in the number of mols in the gas phase. Liquid phase mols are not considered as they take up negligible space compared to the gas phase.

For a reaction aA(g) + bB = cC, where the reaction is described wrt component A the scale factor is given by:

$$f = \frac{c-(a+b)}{a}$$

$$u|_z C_T|_z A_{bed} = u|_{z+\delta z} C_T|_{z+\delta z} A_{bed} + f k_m \left(C_{H_2 S} - C_{H_2}\right) dA_s \qquad B.28$$

As before $C_T = 1/V_M$, $C_i = x_i/V_m$

$$\frac{u|_z A_{bed}}{V_M} = \frac{u|_{z+\delta z} A_{bed}}{V_M} + f k_m \left(\frac{x_{H_2 S}}{V_M} - \frac{x_{H_2}}{V_M}\right) dA_s \qquad B.29$$

Multiply by $\frac{1}{A_{bed}}$, since can't assume V_M is constant, it depends on P and T and is to be left in the derivative for now.

$$\frac{u|_z}{V_M} = \frac{u|_{z+\delta z}}{V_M} + \frac{1}{A_{bed}} f k_m \left(\frac{x_{H_2 S}}{V_M} - \frac{x_{H_2}}{V_M}\right) dA_s \qquad B.30$$

Take, for spherical particles (see fluid MB).

$$dA_s = \frac{A_s}{V_p} dV_p = \frac{3(1-\epsilon)}{r_p} dV_{bed}$$

$$\frac{u|_z}{V_M} = \frac{u|_{z+\delta z}}{V_M} + f k_m \left(\frac{x_{H_2 S}}{V_M} - \frac{x_{H_2}}{V_M}\right) \frac{3(1-\epsilon)}{r_p} \frac{dV_{bed}}{A_{bed}} \qquad B.31$$

As per fluid MB $\frac{A_{bed}}{dV_{bed}} = 1/dz$

$$\frac{u|_z}{V_M} = \frac{u|_{z+\delta z}}{V_M} + f k_m \left(\frac{x_{H_2 S}}{V_M} - \frac{x_{H_2}}{V_M}\right) \frac{3(1-\epsilon)}{r_p} dz \qquad B.32$$

Take limits to zero.

$$-\frac{d\left(\frac{u}{V_M}\right)}{dz} = f k_m \left(\frac{x_{H_2 S}}{V_M} - \frac{x_{H_2}}{V_M}\right) \frac{3(1-\epsilon)}{r_p} \qquad B.33$$

Non-dimensionlise z, u and multiple by -1

$$\frac{u_R}{L}\frac{d\left(\frac{u\prime}{V_M}\right)}{dZ} = fk_m\left(\frac{x_{H_2}}{V_M} - \frac{x_{H_2s}}{V_M}\right)\frac{3(1-\epsilon)}{r_p} \qquad B.34$$

Multiple by L/u_f and take $M = \frac{3k_m L(1-\epsilon)}{u_f r_p}$

$$\frac{u_R}{u_f}\frac{d\left(\frac{u\prime}{V_M}\right)}{dZ} = \frac{Mf}{V_M}\left(x_{H_2} - x_{H_2s}\right) \qquad B.35$$

Assuming ideal gas $V_M = \frac{V}{n} = \frac{RT}{P}$, $V_{M_R} = \frac{RT_R}{P_R}$

$$\frac{V_M}{V_{M_R}} = \frac{T}{T_R}\frac{P_R}{P} \qquad V_M = V_{M_R}\frac{T}{T_R}\frac{P_R}{P}$$

$$\frac{d\left(\frac{u\prime}{V_{M_R}\frac{T}{T_R}\frac{P_R}{P}}\right)}{dZ} = \frac{u_f}{u_R}\frac{Mf}{V_{M_R}\frac{T}{T_R}\frac{P_R}{P}}\left(x_{H_2} - x_{H_2s}\right) \qquad B.36$$

Cancel through V_{MR} , nondimensionalise T and simplify, assuming constant pressure down bed so P = P_R.

$$\frac{d\left(u\prime\frac{y_R}{y}\right)}{dZ} = \frac{u_f}{u_R}Mf\frac{y_R}{y}\left(x_{H_2} - x_{H_2s}\right) \qquad B.37$$

u' = u u_R and f = ε/x_f

$$\frac{d\left(u\prime\frac{y_R}{y}\right)}{dZ} = \frac{u_f}{u_R}Mf\frac{y_R}{y}\left(x_{H_2} - x_{H_2s}\right) \qquad B.38$$

<u>Particle Mass Balance</u>

Accumulation in particle = transfer from fluid phase – reaction in particle.

Assume mass transfer is the limiting step and reaction takes place immediately, hence no accumulation on particle.

Since the heat transfer within the catalyst particle is rapid compared to the interphase transfer, the particle is considered isothermal. Concentration changes within the particle are also faster than both concentration and temperature changes in the bulk, so the particle concentration is also assumed to be in a pseudo-steady state with respect to temperature. An isothermal effectiveness factor is therefore used to model the particle concentration profile, the particles are modelled as spherical.

All in terms of $mols^{-1}$

$$0 = k_m(C_s - C)dA_s - \eta(y_s)k_0 C_s e^{\left(\frac{-E}{RT_s}\right)} dV_{bed} \qquad B.39$$

Particle volume $dV_p = (1-\epsilon)dV_{bed}$

$$k_m(C_s - C)dA_s = \eta(y_s)k_0 C_s e^{\left(\frac{-E}{RT_s}\right)} \frac{dV_p}{(1-\epsilon)} \qquad B.40$$

Divide by $\frac{dV_p}{(1-\epsilon)}$

$$k_m(C_s - C)dA_s \frac{(1-\epsilon)}{dV_p} = \eta(y_s)k_0 C_s e^{\left(\frac{-E}{RT_s}\right)} \qquad B.41$$

$$\frac{A_s}{V_p} = \frac{4\pi {r_p}^2}{4/_3 \pi {r_p}^3} = \frac{3}{r_p}$$

$$k_m(C_s - C)(1-\epsilon)\frac{3}{r_p} = \eta(y_s)k_0 C_s e^{\left(\frac{-E}{RT_s}\right)} \qquad B.42$$

Non-dimensionlise temperature and concentration, $C_i = x_i/V_m$

$$k_m\left(\frac{x_s}{V_M} - \frac{x}{V_M}\right)(1-\epsilon)\frac{3}{r_p} = \eta(y_s)k_0 \frac{x_s}{V_{Ms}} e^{\left(\frac{-1}{y_s}\right)} \qquad B.43$$

As Chen and Luss, take $\frac{u_f}{Lk_0} = e^{\left(\frac{-1}{y_r}\right)}$

Divide through and cancel k_0

$$k_m\left(\frac{x_s}{V_M} - \frac{x}{V_M}\right)(1-\epsilon)\frac{3L}{u_f r_p} = \eta(y_s)\frac{x_s}{V_{Ms}} e^{\left(\frac{-1}{y_s} - \frac{-1}{y_r}\right)} \qquad B.44$$

Take $M = \frac{3k_m L(1-\epsilon)}{u_f r_p}$

$$M\left(\frac{x_s}{V_M} - \frac{x}{V_M}\right) = \eta(y_s)\frac{x_s}{V_{Ms}} e^{\left(\frac{1}{y_r} - \frac{1}{y_s}\right)} \qquad B.45$$

As previously; $V_M = V_{M_R}\frac{T}{T_R}\frac{P_R}{P}$

$$M\left(\frac{x_s}{V_{M_R}\frac{T}{T_R}\frac{P_R}{P}} - \frac{x}{V_{M_R}\frac{T}{T_R}\frac{P_R}{P}}\right) = \eta(y_s)\frac{x_s}{V_{M_R}\frac{T_s}{T_R}\frac{P_R}{P}} e^{\left(\frac{1}{y_r} - \frac{1}{y_s}\right)} \qquad B.46$$

Cancel through Vm_R and assume $P=P_R$. non-dimensioinalise T.

$$M\left(\frac{x_s}{\frac{y}{y_R}} - \frac{x}{\frac{y}{y_R}}\right) = \eta(y_s)\frac{x_s}{\frac{y_s}{y_R}} e^{\left(\frac{1}{y_r} - \frac{1}{y_s}\right)} \qquad B.47$$

$$\frac{M}{y}(x_s - x) = \eta(y_s)\frac{x_s}{y_s}e^{\left(\frac{1}{y_r}-\frac{1}{y_s}\right)} \qquad B.48$$

Particle Energy Balance

All in terms of Js-[1], assumed isothermal particle as for particle mass balance.

Accumulation = transfer from gas phase + heat released by reaction on particle

$$\frac{d}{dt}\left(\rho_p c_p T_s(1-\epsilon)dV_{bed}\right) = h(T - T_s)dA_s + \eta(y_s)k_0 C_s e^{\left(\frac{-E}{RT_s}\right)}(-\Delta H)dV_{bed} \qquad B.49$$

Divide by dV_{bed}

$$\frac{d}{dt}\left(\rho_p c_p T_s(1-\epsilon)\right) = h(T - T_s)\frac{dA_s}{dV_{bed}} + \eta(y_s)k_0 C_s e^{\left(\frac{-E}{RT_s}\right)}(-\Delta H) \qquad B.50$$

Particle volume $dV_p = (1-\epsilon)dV_{bed}$ $\qquad \frac{A_s}{V_p} = \frac{4\pi {r_p}^2}{4/_3\pi {r_p}^3} = \frac{3}{r_p} = \frac{A_s}{V_{bed}(1-\epsilon)}$

$$\frac{A_s}{V_{bed}} = \frac{3(1-\epsilon)}{r_p}$$

$$\frac{d}{dt}\left(\rho_p c_p T_s(1-\epsilon)\right) = h(T - T_s)\frac{3(1-\epsilon)}{r_p} + \eta(y_s)k_0 C_s e^{\left(\frac{-E}{RT_s}\right)}(-\Delta H) \qquad B.51$$

Non-dimensionlise temperature and concentration.

$$\frac{d}{dt}\left(\rho_p c_p \frac{E}{R} y_s(1-\epsilon)\right) = \frac{E}{R}(y - y_s)\frac{3h(1-\epsilon)}{r_p} + \eta(y_s)k_0 \frac{x_{H_2S}}{V_{Ms}} e^{\left(\frac{-1}{y_s}\right)}(-\Delta H) \qquad B.52$$

As previously, divide through by $\frac{u_f}{Lk_0} = e^{\left(\frac{-1}{y_r}\right)}$

$$\frac{\rho_p c_p(1-\epsilon)Lk_0}{u_f}\frac{E}{R}\frac{d}{dt}(y_s) = \frac{E}{R}(y - y_s)\frac{3h(1-\epsilon)Lk_0}{r_p u_0} + \eta(y_s)k_0 \frac{x_{H_2S}}{V_{Ms}} e^{\left(\frac{-1}{y_s}-\frac{-1}{y_r}\right)}(-\Delta H) \qquad B.53$$

Cancel k_0, divide by E/R and $\rho_f c_f$

$$\frac{\rho_p c_p(1-\epsilon)L}{\rho_f c_f u_f}\frac{d}{dt}(y_s) = (y - y_s)\frac{3h(1-\epsilon)L}{\rho_f c_f r_p u_f} + \frac{R}{E\rho_f c_f}\eta(y_s)\frac{x_{H_2S}}{V_{Ms}} e^{\left(\frac{1}{y_r}-\frac{1}{y_s}\right)}(-\Delta H) \qquad B.54$$

$$H = \frac{3hL(1-\epsilon)}{\rho_f c_f u_f r_p} \qquad \beta = \frac{R(-\Delta H)}{V_{Ms}E\rho_f c_f}$$

$$\frac{\rho_p c_p(1-\epsilon)L}{\rho_f c_f u_f}\frac{d}{dt}(y_s) = (y - y_s)H + \beta\eta(y_s)x_{H_2S} e^{\left(\frac{1}{y_r}-\frac{1}{y_s}\right)} \qquad B.55$$

$$Le = 1 + \frac{\rho_p c_p (1-\epsilon)}{\rho_f c_f \epsilon} \qquad \tau = \frac{u_f t}{\epsilon L} \frac{1}{Le}$$

$$(Le - 1)\frac{1}{Le}\frac{d}{d\tau}(y_s) = (y - y_s)H + \beta\eta(y_s)x_{H_2S}e^{\left(\frac{1}{y_r} - \frac{1}{y_s}\right)} \qquad B.56$$

$$\left(1 - \frac{1}{Le}\right)\frac{d}{d\tau}(y_s) = (y - y_s)H + \beta\eta(y_s)x_{H_2S}e^{\left(\frac{1}{y_r} - \frac{1}{y_s}\right)} \qquad B.57$$

Since β contains V_{Ms} which varies with T, need to remove T variable.

$$\beta = \beta' \frac{y_r}{y_s}$$

$$\left(1 - \frac{1}{Le}\right)\frac{d}{d\tau}(y_s) = (y - y_s)H + \beta' \frac{y_r}{y_s}\eta(y_s)x_{H_2S}e^{\left(\frac{1}{y_r} - \frac{1}{y_s}\right)} \qquad B.58$$

$$\left(1 - \frac{1}{Le}\right)\frac{d}{d\tau}(y_s) = (y - y_s)H + \beta' \frac{y_r}{y_s}\eta(y_s)x_{H_2S}e^{\left(\frac{1}{y_r} - \frac{1}{y_s}\right)} \qquad B.59$$

Boundary Conditions

Danckwert's boundary conditions are used for the fluid. Assuming no accumulation at Z=0:

$$0 = u|_f C|_f Abed - u|_0 C|_0 Abed - D_L \left.\frac{\partial C}{\partial z}\right|_f Abed + D_L \left.\frac{\partial C}{\partial z}\right|_0 Abed$$

Cancel through Abed, replace C=x/V_M, non-dimensionalise z.

$$u_f \frac{x_f}{V_M} - u_0 \frac{x_0}{V_M} = \frac{-D_L}{L}\frac{\partial \frac{x_0}{V_M}}{\partial Z}$$

Take $Pe_M = \frac{Lu_R}{D}$, u = u_Ru' and $V_M = V_{M_R}\frac{T}{T_R}$ as above

$$u'_f \frac{x_f}{y_f} - u'_0 \frac{x_0}{y_0} = \frac{-1}{Pe_M}\frac{\partial \frac{x_0}{y_0}}{\partial Z}$$

Energy boundary conditions

$$0 = \rho_f c_f u|_f T|_f \frac{1}{dz} - \rho_f c_f u|_0 T|_0 \frac{1}{dz} - \lambda \left.\frac{\partial T}{\partial z}\right|_f \frac{1}{dz} + \lambda \left.\frac{\partial C}{\partial z}\right|_0 \frac{1}{dz}$$

Cancel 1/dz, divide through by $\rho_f c_f$, make z and T dimensionless

$$u'_f y_f - u'_0 y_0 = -\frac{\lambda}{\rho_f c_f L u_R}\frac{\partial T_f}{\partial z}$$

Take $Pe_H = \frac{\rho_f c_f L u_R}{\lambda}$ as above

$$u'_f y_f - u'_0 y_0 = -\frac{1}{Pe_H}\frac{\partial y_f}{\partial Z}$$

At Z=1 the mass and energy differentials are taken to be zero:

$$\frac{\partial x}{\partial z} = \frac{\partial y}{\partial z} = 0$$

C Temperature Dependant Dynamic Model with Feed Flow Adjustment

Dimensionless fluid mass balance from dynamic model, before simplification.

$$\frac{u_f}{\epsilon L}\frac{1}{Le}\frac{d\left(\frac{x_{H_2}}{V_M}\right)}{d\tau} = -\frac{1}{L\epsilon}\frac{d\left(\frac{x_{H_2}}{V_M}u\right)}{dZ} + \frac{D}{L^2\epsilon}\left(\frac{1}{V_M}\frac{dx_{H_2}}{dZ}\right)\frac{1}{dZ} + \left(x_{H_2S} - x_{H_2}\right)\frac{k_m 3(1-\epsilon)}{\epsilon r_p V_M} \quad C.1$$

Multiply through by ϵL.

$$u_f\frac{1}{Le}\frac{d\left(\frac{x_{H_2}}{V_M}\right)}{d\tau} = -\frac{d\left(\frac{x_{H_2}}{V_M}u\right)}{dZ} + \frac{D}{L}\left(\frac{1}{V_M}\frac{dx_{H_2}}{dZ}\right)\frac{1}{dZ} + \left(x_{H_2S} - x_{H_2}\right)\frac{Lk_m 3(1-\epsilon)}{r_p V_M} \quad C.2$$

Take new values for M and Pe_M without u as $M' = \frac{3k_m L(1-\epsilon)}{r_p}$ $Pe'_M = \frac{L}{D}$

$$\frac{u_f}{Le}\frac{d\left(\frac{x_{H_2}}{V_M}\right)}{d\tau} = -\frac{d\left(\frac{x_{H_2}}{V_M}u\right)}{dZ} + \frac{1}{Pe'_M}\left(\frac{1}{V_M}\frac{dx_{H_2}}{dZ}\right)\frac{1}{dZ} + \left(x_{H_2S} - x_{H_2}\right)\frac{M'}{V_M} \quad C.3$$

However, u still varies with both T, P and reaction. V_M varies with T and therefore Z.

$$u' = \frac{u}{u_R}$$

$$\frac{u_f}{Le}\frac{d\left(\frac{x_{H_2}}{V_M}\right)}{d\tau} = -u_R\frac{d\left(\frac{x_{H_2}}{V_M}u'\right)}{dZ} + \frac{1}{Pe'_M}\left(\frac{1}{V_M}\frac{dx_{H_2}}{dZ}\right)\frac{1}{dZ} + \left(x_{H_2S} - x_{H_2}\right)\frac{M'}{V_M} \quad C.4$$

Assuming ideal gas, constant pressure $V_M = \frac{V}{n} = \frac{RT}{P}$, $V_{M_R} = \frac{RT_R}{P_R}$

$$\frac{V_M}{V_{M_R}} = \frac{T}{T_R} \qquad V_M = V_{M_R}\frac{T}{T_R} = V_{M_R}\frac{y}{y_R}$$

$$\frac{u_f}{Le}\frac{d\left(x_{H_2}\frac{y_R}{y}\right)}{d\tau} = -u_R\frac{d\left(x_{H_2}\frac{y_R}{y}u'\right)}{dZ} + \frac{1}{Pe'_M}\left(\frac{y_R}{y}\frac{dx_{H_2}}{dZ}\right)\frac{1}{dZ} + \left(x_{H_2S} - x_{H_2}\right)M'\frac{y_R}{y} \quad C.5$$

<u>Dimensionless Fluid Energy Balance</u>

$$\frac{u_f}{\epsilon L}\frac{1}{Le}\frac{dy}{d\tau}\left(\rho_f c_f\right) = \frac{-\rho_f c_f}{L\epsilon}\frac{d(yu)}{dZ} + \frac{\lambda}{\epsilon L^2}\frac{d^2y}{dZ^2} + (y_s - y)\frac{3h(1-\epsilon)}{r_p\epsilon} + (y_w - y)\frac{2h_w}{r\epsilon} \quad C.6$$

Divide by $\frac{\rho_f c_f}{\epsilon L}$

$$\frac{u_f}{Le}\frac{dy}{d\tau} = -\frac{d(yu)}{dZ} + \frac{\lambda}{L\rho_f c_f}\frac{d^2y}{dZ^2} + (y_s - y)\frac{3hL(1-\epsilon)}{r_p\rho_f c_f} + (y_w - y)\frac{2h_w L}{r\rho_f c_f} \qquad C.7$$

Define $H' = \frac{3hL(1-\epsilon)}{r_p\rho_f c_f}$ $U' = \frac{2h_w L}{r\rho_f c_f}$ $Pe'_H = \frac{L\rho_f c_f}{\lambda}$

$$\frac{u_f}{Le}\frac{dy}{d\tau} = -\frac{d(yu)}{dZ} + \frac{1}{Pe'_H}\frac{d^2y}{dZ^2} + (y_s - y)H' + (y_w - y)U' \qquad C.8$$

$$u' = \frac{u}{u_R}$$

$$\frac{u_f}{Le}\frac{dy}{d\tau} = -u_R\frac{d(yu\prime)}{dZ} + \frac{1}{Pe'_H}\frac{d^2y}{dZ^2} + (y_s - y)H' + (y_w - y)U' \qquad C.9$$

<u>Dimensionless Particle Mass Balance</u>

$$k_m\left(\frac{x_s}{V_M} - \frac{x}{V_M}\right)(1-\epsilon)\frac{3}{r_p} = \eta(y_s)k_0\frac{x_s}{V_{Ms}}e^{\left(\frac{-1}{y_s}\right)} \qquad C.10$$

As Chen and Luss, take $\frac{u_f}{Lk_0} = e^{\left(\frac{-1}{y_r}\right)}$

Divide through and cancel k_0

$$k_m\left(\frac{x_s}{V_M} - \frac{x}{V_M}\right)(1-\epsilon)\frac{3L}{u_f r_p} = \eta(y_s)\frac{x_s}{V_{Ms}}e^{\left(\frac{-1}{y_s}-\frac{-1}{y_r}\right)} \qquad C.11$$

Take $M' = \frac{3k_m L(1-\epsilon)}{r_p}$

$$\frac{M\prime}{u_f}\left(\frac{x_s}{V_M} - \frac{x}{V_M}\right) = \eta(y_s)\frac{x_s}{V_{Ms}}e^{\left(\frac{1}{y_r}-\frac{1}{y_s}\right)} \qquad C.12$$

As previously; $V_M = V_{M_R}\frac{T}{T_R}$

Cancel through Vm_R and assume $P=P_R$. non-dimensioinalise T.

$$\frac{M\prime}{u_f}\left(\frac{x_s}{\frac{y}{y_R}} - \frac{x}{\frac{y}{y_R}}\right) = \eta(y_s)\frac{x_s}{\frac{y_s}{y_R}}e^{\left(\frac{1}{y_r}-\frac{1}{y_s}\right)} \qquad C.13$$

$$\frac{M\prime}{u_f y}(x_s - x) = \eta(y_s)\frac{x_s}{y_s}e^{\left(\frac{1}{y_r}-\frac{1}{y_s}\right)} \qquad C.14$$

Dimensionless Particle Energy Balance

$$\frac{u_f}{\epsilon L}\frac{1}{Le}\frac{d}{d\tau}\left(\rho_p c_p \frac{E}{R} y_s(1-\epsilon)\right) = \frac{E}{R}(y-y_s)\frac{3h(1-\epsilon)}{r_p} + \eta(y_s)k_0\frac{x_{H_2S}}{V_{Ms}}e^{\left(\frac{-1}{y_s}\right)}(-\Delta H) \qquad C.15$$

As previously, divide through by $\frac{u_f}{Lk_0} = e^{\left(\frac{-1}{y_r}\right)}$

$$\frac{\rho_p c_p(1-\epsilon)k_0}{\epsilon Le}\frac{E}{R}\frac{d}{d\tau}(y_s) = \frac{E}{R}(y-y_s)\frac{3h(1-\epsilon)Lk_0}{r_p u_f} + \eta(y_s)k_0\frac{x_{H_2S}}{V_{Ms}}e^{\left(\frac{-1}{y_s}-\frac{-1}{y_r}\right)}(-\Delta H) \qquad C.16$$

Cancel k_0, divide by E/R and $\rho_f c_f$

$$\frac{\rho_p c_p(1-\epsilon)}{\rho_f c_f \epsilon Le}\frac{d}{d\tau}(y_s) = (y-y_s)\frac{3h(1-\epsilon)L}{\rho_f c_f r_p u_f} + \frac{R}{E\rho_f c_f}\eta(y_s)\frac{x_{H_2S}}{V_{Ms}}e^{\left(\frac{1}{y_r}-\frac{1}{y_s}\right)}(-\Delta H) \qquad C.17$$

$$H' = \frac{3hL(1-\epsilon)}{\rho_f c_f r_p} \qquad \beta = \frac{R(-\Delta H)}{V_{Ms}E\rho_f c_f}$$

$$\frac{\rho_p c_p(1-\epsilon)}{\rho_f c_f \epsilon Le}\frac{d}{d\tau}(y_s) = (y-y_s)\frac{H'}{u_f} + \beta\eta(y_s)x_{H_2S}e^{\left(\frac{1}{y_r}-\frac{1}{y_s}\right)} \qquad C.18$$

$$Le = 1 + \frac{\rho_p c_p(1-\epsilon)}{\rho_f c_f \epsilon}$$

$$\left(1-\frac{1}{Le}\right)\frac{d}{d\tau}(y_s) = (y-y_s)\frac{H'}{u_f} + \beta\eta(y_s)x_{H_2S}e^{\left(\frac{1}{y_r}-\frac{1}{y_s}\right)} \qquad C.19$$

Since β contains V_{Ms} which varies with T, need to remove T variable.

$$\beta = \beta'\frac{y_r}{y_s}$$

$$\left(1-\frac{1}{Le}\right)\frac{d}{d\tau}(y_s) = (y-y_s)\frac{H'}{u_f} + \beta'\frac{y_r}{y_s}\eta(y_s)x_{H_2S}e^{\left(\frac{1}{y_r}-\frac{1}{y_s}\right)} \qquad C.20$$

Velocity Term

$$\frac{u_R}{L}\frac{d\left(\frac{u'}{V_M}\right)}{dZ} = f k_m\left(\frac{x_{H_2}}{V_M} - \frac{x_{H_2S}}{V_M}\right)\frac{3(1-\epsilon)}{r_p} \qquad C.21$$

Multiple by L and take $M' = \frac{3k_m L(1-\epsilon)}{r_p}$

$$u_R\frac{d\left(\frac{u'}{V_M}\right)}{dZ} = \frac{Mf}{V_M}\left(x_{H_2} - x_{H_2S}\right) \qquad C.22$$

Assuming ideal gas $V_M = V_{M_R}\frac{T}{T_R}$

Cancel through V_{MR} , nondimensionalise T and simplify, assuming constant pressure down bed so P = P_R.

$$\frac{d\left(u\prime\frac{y_R}{y}\right)}{dZ} = \frac{1}{u_R} M' f \frac{y_R}{y}\left(x_{H_2} - x_{H_2 S}\right) \qquad C.23$$

f = ε/x_f

$$\frac{d\left(u\prime\frac{y_R}{y}\right)}{dZ} = \frac{1}{u_R} M \frac{\varepsilon}{x_{H_{2f}}} \frac{y_R}{y}\left(x_{H_2} - x_{H_2 S}\right) \qquad C.24$$

Boundary Conditions

Danckwert's boundary conditions are used for the fluid. Assuming no accumulation at Z=0:

$$0 = u|_f C|_f Abed - u|_0 C|_0 Abed - D_L \frac{\partial C}{\partial z}\Big|_f Abed + D_L \frac{\partial C}{\partial z}\Big|_0 Abed \qquad C.25$$

Cancel through Abed, replace C=x/V_M, non-dimensionalise z.

$$u_f \frac{x_f}{V_M} - u_0 \frac{x_0}{V_M} = \frac{-D_L}{L} \frac{\partial \frac{x_0}{V_M}}{\partial Z} \qquad C.26$$

Take $Pe'_M = \frac{L}{D}$ and $V_M = V_{M_R} \frac{T}{T_R}$ as above

$$u_f \frac{x_f}{y_f} - u_0 \frac{x_0}{y_0} = \frac{-1}{Pe_{M'}} \frac{\partial \frac{x_0}{y_0}}{\partial Z} \qquad C.27$$

Make velocity dimensionless

$$u'_f u_R \frac{x_f}{y_f} - u_0{}' u_R \frac{x_0}{y_0} = \frac{-1}{Pe_{M'}} \frac{\partial \frac{x_0}{y_0}}{\partial Z} \qquad C.28$$

Energy boundary conditions

$$0 = \rho_f c_f u|_f T|_f \frac{1}{dz} - \rho_f c_f u|_0 T|_0 \frac{1}{dz} - \lambda \frac{\partial T}{\partial z}\Big|_f \frac{1}{dz} + \lambda \frac{\partial C}{\partial z}\Big|_0 \frac{1}{dz} \qquad C.29$$

Cancel 1/dz, divide through by $\rho_f c_f$, make z and T dimensionless

$$u'_f u_R y_f - u'_0 u_R y_0 = -\frac{\lambda}{\rho_f c_f L} \frac{\partial T_f}{\partial z} \qquad C.30$$

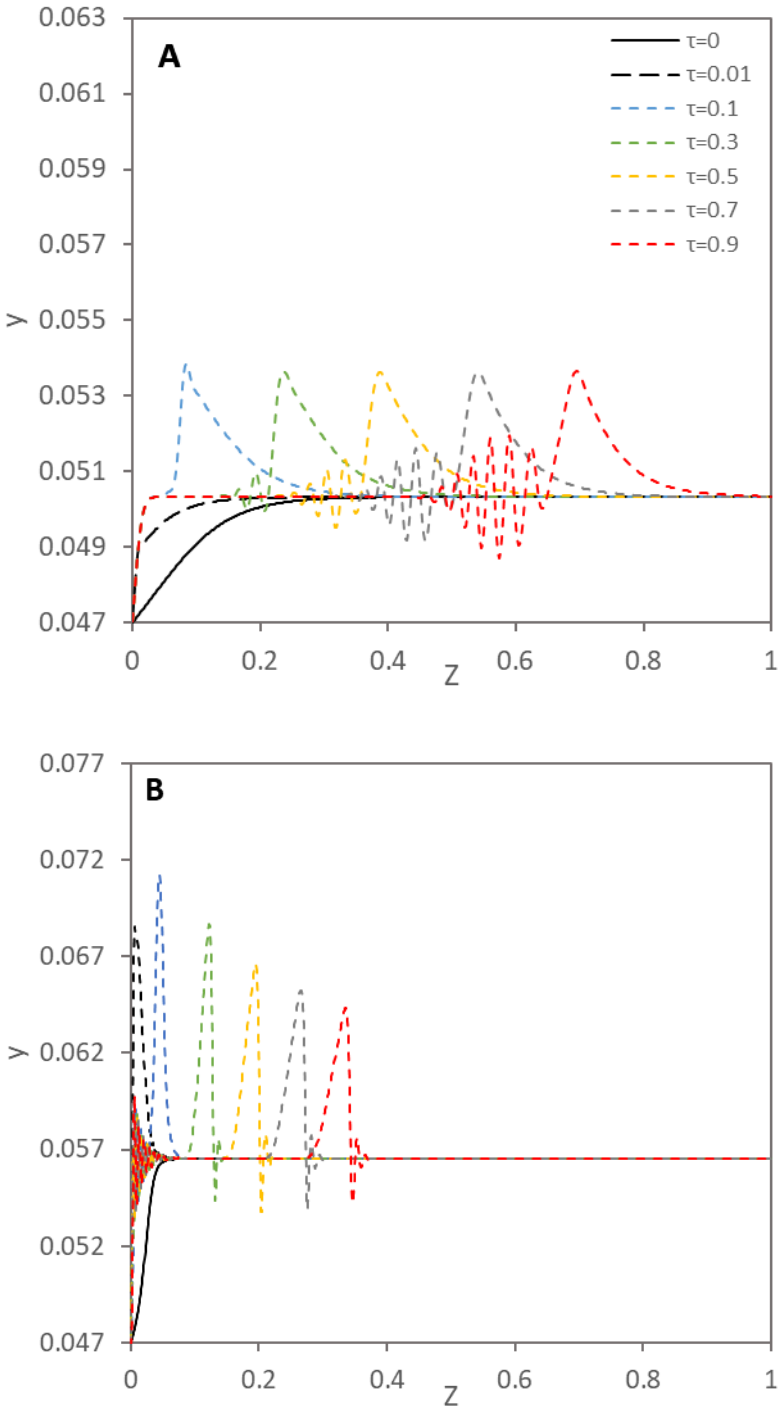
Take $Pe'_H = \frac{\rho_f c_f L}{\lambda}$ as above

$$u'_f u_R y_f - u'_0 u_R y_0 = -\frac{1}{Pe\prime_H} \frac{\partial y_f}{\partial Z} \qquad C.31$$

At Z=1 the mass and energy differentials are taken to be zero:

$$\frac{\partial x}{\partial z} = \frac{\partial y}{\partial z} = 0$$

D Oscillations



Oscillations in loss of feed flow model caused by model instability, see Figure 7.21.

E Published Work

Khoo, Benjamin, and Janet Skitt. 'The 1973 Summerland Disaster — Lessons to the Building Industry from the Process Industry' 269 (October 2019): 3–6 https://www.icheme.org/media/12440/lpb269_pg03.pdf.

Bibliography

[1] Fourier J (1824). Remarques Générales Sur Les Températures Du Globe Terrestre Et Des Espaces Planétaires. *Annales de Chimie et de Physique*. 27, 136–67

[2] Summary for Policymakers. In: Climate Change 2014: Mitigation of Climate Change. Contribution of Working Group III to the Fifth Assessment Report of the Intergovernmental Panel on Climate Change

[3] Global Warming of 1.5°C, an IPCC special report on the impacts of global warming of 1.5°C above pre-industrial levels and related global greenhouse gas emission pathways, in the context of strengthening the global response to the threat of climate change, sustainable development, and efforts to eradicate poverty.

[4] C Le Quéré et al. (2018) Global Carbon Budget 2018. *Earth System Science Data*. 10, 1-54.

[5] IPCC. (2012) Climate Change 2013 The Physical Science Basis. WHO UNEF. AR5.

[6] Stern, N. (2006) *Stern Review Report on the Economics of Climate Change,* Government of the United Kingdom, Part 1.

[7] Global Carbon Project (2018). *Supplemental data of Global Carbon Budget 2018 (Version 1.0) [Data set],* Global Carbon Project, https://doi.org/10.18160/gcp-2018.

[8] Dudley, B. (2019) *BP Statistical Review of World Energy*. BP. 2019 Edition.

[9] Dudley, B. (2016) *BP Energy Outlook - Outlook to 2035*. BP. 2016 Edition.

[10] European Environment Agency. (2017) Data viewer on greenhouse gas emissions and removals, sent by countries to UNFCCC and the EU Greenhouse Gas Monitoring Mechanism (EU Member States). Accessed at https://www.eea.europa.eu/data-and-maps/data/data-viewers/greenhouse-gases-viewer.

[11] Folkstone, R (ed). (2014) Alternative Fuels and Advanced Vehicle Technologies for Improved Environmental Performance. Woodhead Publishing.

[12] IEA. (2009) Transport, Energy and CO2, Moving towards Sustainability, IEA, 2009

[13] Pan European. Directive 2009/28/EC of the European Parliament and of the Council of 23 April 2009 on the promotion of the use of energy from renewable sources. (2009) Europe. European Parliament and Council.

[14] Grove, J. (2017) *Vehicle Licensing Statistics: 2016*. Department of Transport.

[15] Luque, R. de la Osa, A. Campelo, J. Romero, A. Valverde, J. Sanchez, P. (2012) Design and development of catalysts for Biomass-to-Liquid-Fischer-Tropsch (BTL-FT) processes for biofuels production, *Energy & Environmental Science,* 5, 5186-5202.

[16] United States Environmental Protection Agency. (2002) *Clean Alternative Fuels: Fischer-Tropsch*. EPA. EPA420-F-00-036.

[17] Hakawati, R. Symth, B. Daly, H. McCullough, G. Rooney, D. (2019) Is the Fischer-Tropsch Conversion of Biogas-Derived Syngas to Liquid Fuels Feasible at Atmospheric Pressure?, *Energies,* 12, 1031-1059.

[18] total.com. (2020). *BioTfueL: Developing Second-Generation Biofuels*. [online] Available at: https://www.total.com/en/energy-expertise/projects/bioenergies/biotfuel-converting-plant-wastes-into-fuel [Accessed 14 Jan. 2020].

[19] Tri-inc.net (2017). *TRI announces partnerships with Velocys PL.* [online] Available at: https://tri-inc.net/2017/01/26/tri-announces-partnership-with-velocys-plc/ [Accessed 14 Jan. 2020].

[20] Dalai, A. Davis, B. (2008) Fischer-Tropsch synthesis: A review of water effects on the performances of unsupported and supported Co catalysts, *Applied Catalysis A,* 348, 1-15.

[21] Dry, M. (2001) High quality diesel via the Fischer-Tropsch process – a review, *Journal of Chemical Technology and Biotechnology,* 77, 43-50.

[22] Laan, G. Beenackers, A. (1999) Kinetics and Selectivity of the FTS: A Literature Review. *Catalysis Reviews*. 41 (3&4), 255-318.

[23] Todic, B. Ma, W. Jacobs, G. Davis, B. Bukur, D. (2014) C)-insertion mechanism based kinetic model of the Fischer-Tropsch synthesis reaction ove Re-promoted Co catalyst, *Catalysis Today,* 228 (1), 32-39.

[24] Santen, R. Markvoort, A. Filot, J. Ghouri, M. Hensen, E. (2013) Mechanism and microkinetics of the Fischer-Tropsch reaction, *Phys. Chem. Chem. Phys.,* 15, 17038-17063.

[25] Pour, A. Khodabandeh, H. Izadyar, M. Housaindokht, M. (2014) Detailed kinetics of Fischer-Tropsch synthesis on a precipitated iron catalyst, *React Kinet Mech Cat,* 111, 29-44.

[26] Filot, I. Zijlstra, B. Broos, R. Chen, W. Pestman, R. Hensen, E. (2017) Kinetic aspects of chain growth in Fischer-Tropsch synthesis, *Faraday Discussions,* 197, 153-164.

[27] Herrington, E. (1946) The Fischer-Tropsch synthesis considered as a polymerization reaction. *Chem. Ind*. 65, 346

[28] Fortsch, D. Pabst, K. Groß-Hardt, E. (2015) The product distribution in Fischer-Tropsch synthesis: An extension of the ASF model to describe common deviations, *Chemical Engineering Science,* 138, 333-346.

[29] Dictor, R. Bell, A. (1985) Fischer-Tropsch Synthesis over Reduced and Unreduced Iron Oxide Catalysts. *Journal of Catalysis*. 97, 121-136.
[30] Donnelly, T. Satterfield, C. (1989) Product Distributions of the Fischer-Tropsch Synthesis on Precipitated Iron Catalysts. *Applied Catalysis*. 52, 93-114.
[31] Clark, D. Pazdernik, N. (2015) *Biotechnology (2nd edition): Applying the Genetic Revolution,* Elsevier, chapter 13.
[32] UKpia. (2015) *Statistical Review 2015*. UKpia.
[33] Brazil. MINISTRY OF AGRICULTURE, LIVESTOCK AND FOOD SUPPLY
DECREE No. 143 OF 27 JUNE 2007, Art. 1 º Fix in twenty-five percent of the mandatory percentage of anhydrous ethanol to gasoline fuel. (2007) Brasilia. National Printing Office.
[34] Kalnes, T. Marker, T. Shonnard, D. Koers, K. (2008) Green diesel production by hydrorefining renewable feedstocks, *Biofuels Technology*, 7-11.
[35] Echim, C. Maes, J. De Greyt, W. (2012) Improvement of cold filter plugging point of biodiesel from alternative feedstocks, *Fuel,* 93, 642-648.
[36] Pala, L. Want, Q. Kolb, G. Hessel, V. (2017) Steam gasification of biomass with subsequent syngas adjustment using shift reaction for syngas production: An Aspen Plus model, *Renewable Energy,* 101, 484-492.
[37] Ravaghi-Ardebilia, Z. Manentia, F. Pirolab, C. Soaresc, F. Corbettaa, M. Pieruccia, S. Ranz, E. (2014) Influence of the Effective Parameters on H2:CO Ratio of Syngas at Low-Temperature Gasification. *Chemical Engineering Transactions*. 37, 253-258.
[38] Nanda, S. Mohammad, J. Reddy, S. Kozinski, J. Dalai, A. (2014) Pathways of lignocellulosic biomass conversion to renewable fuels, *Biomass Conversion and Biorefinery,* 4-2, 157-191.
[39] Monir, M. Aziz, A. Kristanti, R. Yousuf, A. (2018) Gasification of lignocellulosic biomass to produce syngas in a 50kW downdraft reactor, *Biomass and Bioenergy,* 119, 335-345.
[40] Abello, S. Montano, D. (2011) Exploring iron based multifunctional catalysts for FTS: a review. *ChemSusChem*. 4, 1538-1556.
[41] Lv, P. Yuan, Z. Wu, C. Ma, L. Chen, Y. Tsubaki, N. (2006) Bio-syngas production from biomass catalytic gasification, *Energy Conversion & Management,* 48, 1132-1139.
[42] U.S. Department of Energy (2002) *Benchmarking Biomass Gasification Technologies for Fuels, Chemicals and Hydrogen Production,* National Energy Technology Laboratory. Available from https://www.netl.doe.gov/sites/default/files/netl-file/BMassGasFinal.pdf [Accessed 16th January 2020].
[43] Dry, M. (1981) The Fischer-Tropsch Synthesis. *Catalysis—Science and Technology*. 1, 160–255.
[44] Jun, K. Roh, H. Kim, K. (2004) Catalytic investigation for Fischer Tropsch synthesis from bio-mass derived syngas. Aplied Catalysis A: General. 259 (2), 221-226.
[45] Krishnamoorthy, S. Li, A. Iglesia, E. (2002). Pathways for CO_2 formation and conversion during Fischer-Tropsch synthesis on iron-based catalysts. *Catalysis Letters*. 80 (1-2), 77-86.
[46] Hall, K. Kokes, R. Emmett, P. (1957). Mechanism studies of the Fischer-Tropsch synthesis. The addition of radioactive methanol, carbon dioxide and gaseous formaldehyde. *American Chemical Society.* 79 (12), 2983-2989.
[47] Xu, L. Bao, S. Houpt, D. Lambert, s. Davis, B. (1997). Role of CO_2 in the initiation of chain growth and alcohol formation during the Fischer-Tropsch synthesis. *Catalysis Today.* 36, 347-355.
[48] Sie, S. Krishna, R (1999) Fundamentals and selection of advanced FT reactors. *Applied Catalysts A: Gen*. 186, 55–70.
[49] Stenberg, A. Dry, M. (ed) (2004) *Studies in Surface Science and Catalysis Vol. 152 - Fischer-Tropsch Technology*, Elsevier.
[50] Eigenberger, G. (1992) *Ullmann's Encyclopaedia of Industrial Chemistry, Vol. B4*. VCH Publishers Inc. Available from: http://elib.uni-stuttgart.de/bitstream/11682/1848/1/eig16.pdf [Accessed 6th December 2016].
[51] Vergunst, Th. Kapteijn, F. Moulijn, J. (1998) Carbon Coating of Ceramic Monolithic Substrates. *Studies in Surface Science and Catalysis*, 118, 175-183.
[52] Saeidi, S. Nikoo, M. Mirvakili, A. Bahrani, S. Amin, N. Rahimpour, R. (2015) Recent advances in reactors for low-temperature Fischer-Tropsch synthesis: process intensification perspective. *Reviews in Chemical Engineering.* 31 (3), 209-238.
[53] J.W.A. de Swart, R.E. van Vliet, R. Krishna. (1996) Size, structure, structure and dynamics of 'large' bubbles in a two-dimensional slurry bubble column. *Chem. Eng. Sci*. 51, 4619–4629.
[54] Wojciechowski, B. (1988) The Kinetics of the Fischer Tropsch Synthesis, *Catalyst Reviews Sci. Eng.,* 30, 629-702.
[55] HSE (2001) *Reducing risks, protecting people,* HSE. Available from: https://www.hse.gov.uk/risk/theory/r2p2.pdf [Accessed 17th January 2020].
[56] Tighe, C. (2009) *Reactions of the Oxides of Nitrogen with Carbonaceous Particles*, PhD thesis, University of Cambridge.

[57] Geankoplis, E. Stahel, C. (1964) Axial Diffusion and Pressure Drop of Liquids in Porous Media, *A.I.Ch.E. Journal*, 10, 174-179.
[58] Zhang, ZZ, *The effect of sulfur on chemical looping combustion with iron oxides*, PhD thesis, 2014.
[59] Swagelok (2010), *Tubing Data Sheet*, Available from https://nordival.swagelok.com/Services/~/media/6AF5082D9E4F4B9BA3B94FF1E338C661.ashx [Accessed 5th October 2020]
[60] Swagelok (2017), *Proportional Relief Valves*, available at https://www.swagelok.com/downloads/webcatalogs/en/MS-01-141.pdf [Accessed 5th October 2020]
[61] HSE (2018) *EH40/2005 Workplace exposure limits,* 3rd Edition, HSE TSO. Available from https://www.hse.gov.uk/pubns/priced/eh40.pdf [Accessed 22nd December 2019]
[62] Bartholomew, C. (2001) Mechanisms of catalyst deactivation, *Applied Catalysts A: General,* 212, 17-60.
[63] Khodakov, A. Chu, W. Fongarland, P. (2007) Advances in the development of Novel Cobalt Fischer Tropsch Catalysts for Synthesis of Long-Chain Hydrocarbons and Clean Fuels. Chemical Reviews. 107 (5), 1692-1744.
[64] Vannice, M. (1975) The Catalytic Synthesis of Hydrocarbons from H2/CO Mixtures over the Group VIII Metals. *Journal of Catalysis*, 37, 449-461.
[65] Davis, B. (2003) Fischer-Tropsch synthesis: relationship between iron catalyst composition and process variables. *Catalysis Today*. 84, 83-98.
[66] Dasappa, S. (2016) Biomass to liquid transportation fuel via Fischer Tropsch synthesis – Technology review and current scenario, *Renewable and Sustainable Energy Reviews,* 58, 267-286.
[67] Xie, J. Yang, J. Dugulan, A. Holmen, A. Chen, D. Jong, K. Louwerse, M. (2016) Size and promoter effects in supported iron Fischer-Tropsch catalysts: Insights from experiment and theory, *ACS Catalysis,* 6, 3147-3157.
[68] Liu, R. Xu, Y. Qiao, Y. Li, Z. Ma, X. (2015) Factors influencing the Fischer-Tropsch sysnthesis performance of iron-based catalyst: Iron oxide dispersion, distribution and reducibility, *Fuel Processing Technology,* 139, 25-32.
[69] Luque, R. de la Osa, A. Campelo, J. (2012) Design and development of catalysts for Biomass-To-Liquid-Fischer-Tropsch (BTL-FT) processes for biofuels production. *Energy and Environmental Science*. 5 (1), 5186-5202.
[70] Lee, J. (ed.). (2012) *Advanced biofuels and bioproducts*. New York, Springer. Available from: https://play.google.com/store/books/details?id=Xe2-uZrSOPUC&rdid=book-Xe2-uZrSOPUC&rdot=1&source=gbs_vpt_read [Accessed 7th December 2016].
[71]Abelló, S. Montanø, D. (2011) Exploring Iron-based Multifunctional Catalysts for Fischer– Tropsch Synthesis: A Review. *ChemSusChem*. 4, 1538-1556.
[72] Davis, B. (2007) Fischer-Tropsch Synthesis: Comparison of Performances of Iron and Cobalt Catalysts. *Ind. Eng. Chem. Res*. 46, 8938-8945.
[73] Lu, Y. Yan, Q. Han, J. Cao, B. Street, J. Yu, F. (2017) Fischer-Tropsch synthesis of olefin-rich liquid hydrocarbons from biomass-derived syngas over carbon-encapsulated iron carbide/iron nanoparticles catalyst, *Fuel,* 193, 369-384.
[74] Riberiro, M. Jacobs, G. Davis, B. Cronauer, D. Kropt, A. Marshall, C. (2010) Fischer-Tropsch Synthesis: An in-situ TPR-EXAFS/XANES investigation of the influence of group I alkali promotors of the local atomic and electronic structure of carburized iron/silica catalysts, *J. Phys. Chem. C,* 114 (17), 7895-7903.
[75] Li, S. Li, A. Krishnamoorthy, S. Igelasia, E. (2001) Effects of Zn, Cu, and K promotors on the structure and on the reduction, carburization, and catalytic behaviour of iron-based Fischer-Tropsch synthesis catalysts. *Catalyst Letters.* 77 (4), 197-205.
[76] Li, S. Li, A. Krishnamoorthy, S. Meitzner, G. Iglesia, E. (2002) Promoted Iron-Based Catalysts for the Fischer-Tropsch Synthesis: Design, Synthesis, Site Densities, and Catalytic Properties. *Journal of. Catalysis*. 206, 202–217.
[77] Tao, Z. Yang, Y. Zhang, C. Li, T. Ding, M. Xiang, H. Li, Y. (2007) Study of manganese promotor on a precipitated iron-based catalyst for Fischer-Tropsch synthesis, *Journal of Natural Gas Chemistry,* 16, 278-285.
[78] Aluha, J. Abatzoglou, N. (2017) Promotional effect of Mo and Ni in plasma-synthesized Co-Fe/C bimetallic nano-catalysts for Fischer-Tropsch synthesis, *Journal of Industrial and Engineering Chemistry,* 50, 199-212.
[79] Mangaloglu, D. Baranak, M. Atac, O. Atakul, H. (2018) Effect of the promotor presence in catalysts on the compositions of Fischer-Tropsch synthesis products, *Journal of Industrial and Engineering Chemistry,* 66, 298-310.
[80] Van Berge, P. Barradas, S. Van de Loodsrecht, J. Visagie, J. (2001) Advances in the cobalt catalysed Fischer-Tropsch synthesis, *Erdoel Erdgas Kohle,* 117, 138-142.
[81] Eilers, J. Posthuma, S. Sie, S. (1990) The Shell Middle Distillate Synthesis Process (SMDS), *Catalysis Letters,* 7, 253-270.
[82] Iglesia, E. (1997) Design, synthesis, and use of cobalt-based Fischer-Tropsch synthesis catalysts, *Applied Catalysis A: General,* 161, 59-78.

[83] Jermwongratanachai, T. Jacobs, G. Ma, W. Shafer, W. Gnanamani, M. Gao, P. Kitiyanan, B. Davis, B. Klettlinger, J. Yen, C. Cronauer, D. Kropf, A. Marshall, C. (2013) Fischer-Tropsch synthesis: Comparisons between Pt and Ag promoted Co/Al_2O_3 catalysts for reducibility, local atomic structure, catalytic activity and oxidation-reduction (OR) cycles, *Applied Catalysis A: General,* 166-180.
[84] Batley, G. Ekstrom, A. Johnson, D. (1975) Studies of topochemical heterogeneous catalysis: 3. Catalysis of the reduction of metal oxides by hydrogen. *Journal of Catalysis*. 34 (3), 368-375
[85] Jacobs, G. Das, T. Patterson, P. Li, J. Sanchez, L. Davis, B. (2003) Fischer -Tropsch synthesis XAFS XAFS studies of the effect of water on a Pt-promoted Co/Al_2O_3 catalyst. *Applied Catalysis A: General*. 247, 335-343.
[86] Jacobs, G. Das, T. Zhang, Y. Li, J. Racoillet, G. Davis, B. (2002) Fischer–Tropsch synthesis: support, loading, and promoter effects on the reducibility of cobalt catalysts. *Applied Catalysis A: General*. 233 (1-2), 263-281.
[87] He, J. Liu, Z. Yoneyama, Y. Nishiyama, N. Tsubaki, N. (2006) Multiple-functional capsule catalysts: A tailor made confined reaction environment for the direct synthesis of middle isoparaffins from syngas. *Chemistry – A European Journal.* 12 (32), 8296-8304.
[88] Takeuchi, K. Matsuzaki, T. Arakawa, H. Hanaoka, T. Sugi, Y. (1989) Synthesis of C_2-oxygenates from syngas over cobalt catalysts promoted by ruthenium and alkaline earths *Applied. Catalysis*. 48 (1), 149-157.
[89] Takeuchi, K.; Matsuzaki, T.; Arakawa, H.; Sugi, Y. (1985) Synthesis of ethanol from syngas over Co-Re-Sr/SiO_2 Catalysts. *Applied. Catalysis*. 18 (2), 325-334.
[90] Girardon, J. Constant-Griboval, A. Gengembre, L. Chernavskii, P. Khodakov, A. (2005) Optimization of the pretreatment procedure in the design of cobalt silica supported Fischer–Tropsch catalysts. *Catalysis Today*. 106 (1-4), 161-165.
[91] Okabe, K. Li, X. Wei, M. Arakawa, H. (2004) Fischer–Tropsch synthesis over $Co–SiO_2$ catalysts prepared by the sol–gel method *Catalysis Today*. 89 (4), 431-438.
[92] Feller, A. Claeys, M. van Steen, M. (1999) Cobalt Cluster Effects in Zirconium Promoted Co/SiO2 Fischer–Tropsch Catalysts. *Journal of Catalysis.* 185 (1), 120-130.
[93] Jacobs, G. Das, T. Zhang, Y. Li, J. Racoillet, G. Davis, B. (2002) Fischer–Tropsch synthesis: support, loading, and promoter effects on the reducibility of cobalt catalysts. *Applied. Catalysis. A: General*. 233 (1-2), 263-281.
[94] Xiong, H. Zhang, Y. Liew, K. Li, J. (2005) Catalytic performance of zirconium-modified Co/Al2O3 for Fischer–Tropsch synthesis. *Journal of Molecular Catalysis A: Chemical*. 231 (1-2), 145-151.
[95] Ledford, J. Houalla, M. Proctor, A. Hercules, D. Petrakis, L. (1989) Influence of lanthanum on the surface structure and carbon monoxide hydrogenation activity of supported cobalt catalysts. *Journal of Physical Chemistry.* 93 (18), 6770-6777.
[96] Colley, S. Copperthwaite, R. Hutchings, G. van der Riet, M. (1988) Carbon monoxide hydrogenation using cobalt manganese oxide catalysts: initial catalyst optimization studies. *Ind. Eng. Chem. Res*. 27 (8), 1339-1344.
[97] Morales, F. de Groot, F. Glatzel, P. Kleimenov, E. Bluhm, H. Havecker, M. Knop-Gericke, A. Weckhuysen, B. (2004) In Situ X-ray Absorption of Co/Mn/TiO2 Catalysts for Fischer−Tropsch Synthesis. *Journal of Physical Chemistry B*. 108 (41), 16201-16207.
[98] Withers, H. Eliezer, K. Mitchell, J. (1990) Slurry Phase Fischer-Tropsch Synthesis and Kinetic Studies over Supported Cobalt Carbonyl Derived Catalysts. *Ind. Eng. Chem. Res*. 29, 1807-1814.
[99] Suo, H. Wang, S. Zhang, C. Xu, J. Wu, B. Yang, Y. Xiang, H. Li, Y. (2012) Chemical and structural effects of silica in iron-based Fischer-Tropsch synthesis catalysts, *Journal of Catalysis*, 286, 111-123.
[100] Bukur, D. Sivaraj, C. (2002) Supported iron catalysts for slurry phase Fischer-Tropsch synthesis, *Applied Catalysis A: General,* 1-2, 201-214.
[101] Keyvanloo, K. Mardkhe, M. Alam, T. Bartholomew, C. Woodfield, B. Hecker, W. (2014) Supported iron Fischer-Tropsch catalyst: Superior activity and stability using a thermally stable silica-doped alumina support, *ACS Catalysis,* 1017-1077.
[102] Ernst, B. Libs, S. Chaumette, P. Kiennemann, A. (1999) Preparation and characterization of Fischer–Tropsch active Co/SiO2 catalysts. *Applied Catalysis A: General*. 186 (1-2), 145-168.
[103] Wang, W. Chen, W. (1991) Influence of metal loading on the reducibility and hydrogenation activity of cobalt/alumina catalysts. *Applied Catalysis*. 77, 223-233.
[104] Chin, R. Hercules, D. (1982) Surface spectroscopic characterization of cobalt-alumina catalysts. *Journal of Physical Chemistry.* 86 (3), 360-367.
[105] O'Brien, R. Xu, L. Bao, S. Raje, A. Davis, B. (2000) Activity, selectivity and attrition characteristics of supported iron Fischer-Tropsch catalysts, *Applied Catalysts A: General,* 196, 173-178.
[106] Jun, K. Roh, H. Kim, K. Ryu, J. Lee, K. (2004) Catalytic investigation for Fischer–Tropsch synthesis from bio-mass derived syngas. *Applied Catalysis A: General*. 259 (2), 221-226.
[107] Shaikhutdinov S. (2018) Strong metal-support interaction and reactivity of ultrathin oxide films, *Catalysis Letters,* 148, 2627-2635.
[108] Li, Y. Fan, Y. Yang, H. Xu, B. Feng, L. Yang, M. Chen, Y. (2003) Strong metal-support interaction and catalytic properties of anatase and rutile supported palladium catalyst Pd/TiO_2, *Chemical Physics Letters,* 372, 160-165.

[109] Cheng, K. Ordomsky, V. Virginie, M. Legras, B. Chernavskii, P. Kazak, V. Cordier, C. Paul, S. Wang, Y. Khodakov, A. (2014) Support effects in high temperature Fischer-Tropsch synthesis on iron catalysts, *Applied Catalysis A: General,* 488, 66-77.
[110] Chen, W. Fan, Z. Pan, X, Bao, X. (2008) Effect of confinement in carbon nanotubes on the activity of Fischer-Tropsch iron catalyst, *Journal of the American Chemical Society,* 130, 9414-9419.
[111] Costa, J. Marchetti, G. Rangel, M. (2002) A thorium-doped catalyst for the high temperature shift reaction, *Catalyst Today,* 77 (3), 205-2013.
[112] Zhakenovich, A. Stepanovoa, Y. Tatyana, S. Nessipbay, T. Kylysh, I. Maxat, B. Evgeniy, B. (2015) Getting and X-Ray Diffraction Analysis of the Microsphere Magnetic Catalyst of the Thorium-Uranium Catalyst for Fischer-Tropsch Synthesis, *J. Chem. Chem. Eng.,* 9, 145-148.
[113] Sineva, L. Asalieva, E. Mordkovich, V. (2015) The role of zeolite in the Fischer-Tropsch synthesis over colbalt-zeolite catalysts, *Russian Chemical Reviews,* 84, 1176-1189.
[114] Sano, T. Okabe, K. Kohtoku, Y. Shimazaki, Y. Saito, K. Takaya, H. Bando, K. (1985) A new metal zeolite catalyst for the Fischer-Tropsch reaction, *Zeolites,* 3, 194-196.
[115] Li, J. Xu, L. Keogh, R. Davis, B. (2000) Fischer–Tropsch synthesis. Effect of CO pretreatment on a ruthenium promoted Co/TiO_2. *Catalysis Letters*. 70 (3) 127-130.
[116] Pan, Z. Bukur, D. (2011) Fischer–Tropsch synthesis on Co/ZnO catalyst—Effect of pretreatment procedure. *Applied Catalysis A: General.* 404 (1-2) 74-80.
[117] Khangale, P. Meijboom, R. Jalama, K. (2014) Reduction Behaviour for Co/Al_2O_3 FischerTropsch Catalyst in Presence of H_2 or CO. In: *WCE2014*: Proceedings on the World Congress on Engineering 2014 Vol. II. London.
[118] Jalama, K. (2016) Fischer–Tropsch synthesis over Co/TiO_2 catalyst: Effect of catalyst activation by CO compared to H_2. *Catalyst Communications*. 74, 71-74.
[119] Chun, D. Park, J. Hong, S. Lim, J. Kim, C. Lee, H. Yang, J. Hong, S. Jung, H. (2014) Highly selective iron-based Fischer-Tropsch catalysts activated by CO_2-containing syngas, *Journal of Catalysis,* 317, 135-143.
[120] Post, M. van't Hoog, A. Minderhoud, J. Sie, S. (1989) Diffusion Limitiation in Fischer-Tropsch Catalysts. *AIChE Journal.* 35 (7), 1107-1114.
[121] Gulf Research & Development Company (1985) Conversion of Synthesis Gas to Diesel Fuel in Controlled Particle Size Fluid System. 855317 (Patent).
[122] Rane, S. Borg, O. Rytter, E. Holmen, A. (2012) Relation between hydrocarbon selectivity and cobalt particle size for alumina supported cobalt Fischer-Tropsch catalysts, *Applied Catalysis A: General,* 437-438, 10-17.
[123] Bezemer, G. Bitter, J. Kuipers, H. Oosterbeek, H. Holewijn, J. Xu, X. Kapteijn, F.Dillen, A. de Jong, K. (2006) Cobalt Particle Size Effects in the Fischer−Tropsch Reaction Studied with Carbon Nanofiber Supported Catalysts. *J. Am. Chem. Soc.* 128 (12), 3956-3964.
[124] Barkhuisen, D. Mabaso, I. Viljoen, E. Welker, C. Claeys, M. van Steen, E. Fletcher, J. (2006) Experimental approaches to the preparation of supported metal nanoparticles. *Pure Applied Chemistry*. 78 (9), 1759-1769.
[125] Ma, W. Jacobs, G. Sparks, D. Todic, B. Bukur, D. Davis, B. (2019) Quantitative comparison of iron and cobalt based catalysts for the Fischer-Tropsch synthesis under clean and poisoning conditions, *Catalysis Today,* DOI.
[126] Anderson, R. Karn, F. Shultz, J. (1964) Factors in sulfur poisoning of iron catalysts in Fischer-Tropsch synthesis, *Journal of Catalysis,* 4, 56-63.
[127] Li, J. Coville, N. (2001) Effect of boron on the sulfur poisoning of Co/TiO2 Fischer-Tropsch catalysts, *Applied Catalysis A:General,* 1-2, 177-184.
[128] Borg, O. Hammer, N. Enger, B. Myrstad, R. Lindvag, O. Eri, S. Skagseth, T. Rytter, E. (2011) Effect of biomass-derived synthesis gas impurity elements on cobalt Fischer-Tropsch catalyst performance including in-situ sulphur and nitrogen addition, *Journal of Catalysis,* 279 (1), 163-173.
[129] Pendyala, V. Gnanamani, M. Jacobs, G. Ma, W. Shafer, W. Davis, B. (2013) Fischer-Tropsch synthesis: effect of ammonia impurities in syngas feed over a cobalt/alumina catalyst, *Applied Catalysis A: General,* 468, 38-43.
[130] Ma, W. Jacobs, G. Thomas, G. Shafer, W. Sparks, D. Hamdeh, H. Davis, B. (2015) Fischer-Tropsch synthesis: Effects of hydrohalic acids in syngas on a precipitated iron catalyst, *ACS Catalysis,* 5, 3124-3136.
[131] Sikarwar, V. Zhao, M. Clough, P. Yao, J. Zhong, X. Memon, M. Shah, N. Anthony, E. Fennell, P. (2016) An overview of advances in biomass gasification. *Energy & Environmental Science,* 9, 2939-2977.
[132] J. Werther; J. Reppenhagen, *Fluidization, Solids Handling, and Processing - Industrial Applications: Chapter 7 - Attrition in Fluidized Beds and Pneumatic Conveying Lines*. William Andrew Publishing/Noyes: 1998.
[133] Davis, B. (2003) Fischer-Tropsch synthesis: Relationship between iron catalyst composition and process variables. *Catalysis Today*. 84 (1-2), 83-98.
[134] Bartholomew, C. (2001) Mechanisms of catalyst deactivation, *Applied Catalysis A: General,* 212, 17-60.
[135] Lee, J. Bonte, W. Corthals, S. Krumeich, F. Ruitenbeek, M. Bokhoven, J. (2019) Zeolite nanoreactor for investigating sintering effects of cobalt-catalyzed Fischer-Tropsch synthesis, *Ind. Eng. Chem. Res.* 58 (3) , 5140-5145.

[136] Xie, J. Galvis, H. Koeken, A. Kirilin, A. Dugulan, A. Ruitenbeek, M. de Jong, K. (2016) Size and promotor effects on stability of carbon-nanofiber-supported iron-based Fischer-Tropsch catalysts, *ACS Catalysis,* 6, 4017-4024.
[137] Thune, P. Moodley, P. Scheijen, F. Fredriksson, H. Lancee, R. Kropf, J. Miller, J. Niemantsverdriet, J. (2012) The effect of water on the stability of iron oxide and iron carbide nanoparticles in hydrogen and syngas followed by in-situ X-ray absorption spectroscopy, *J. Phys. Chem. C,* 116 (13), 7367-7373.
[138] Loosdrecht, J. Balzhinimaev, B. Dalmon, J. Niemantsverdriet, J. Tsybulya, S. Saib, A. Berge, P. Visagie, J. (2007) Cobalt Fischer-Tropsch synthesis: Deactivation by oxidation?, *Catalysis Today,* 1-4, 293-302.
[139] Lancelot, C. Ordomsky, V. Stephan, O. Sadeqzadeh, M. Karaca, H. Lacroix, M. Cuurulla-Ferre, D. Luck, F. Fongarland, P. Griboval-Constant, A. Khodakov, A. (2014) Direct evidence of surface oxidation of cobalt nanoparticles in alumina-supported catalysts for Fischer-Tropsch synthesis, *ACS Catalysis,* 4 (12), 4510-4515.
[140] Jahangiri, H. Bennett, J. Mahjoubi, P. (2014) A Review of Catalyst Development for Fischer-Tropsch synthesis from Biomass Derived Syngas. *Catalysis Science and Technology*. 4, 2210-2229.
[141] Dry, M. (2004) FT Catalysts. In: Steynberg, A. (ed) *Fischer-Tropsch Technology.* Studies in surface science and catalysis. Elsevier. 152, 533-600.
[142] Khassin, A. (2001) Cobalt–aluminum co-precipitated catalysts and their performance in the Fischer–Tropsch synthesis. *Journal of Molecular Catalysis A: Chemical.* 168(1-2), 193-207.
[143] Schwarz, J. Contescu, C. Contescu, A. (1995) Method for preparation of catalytic materials. *Chemical Reviews*. 95(3), 477-510.
[144] Iglesia, E. Soled, S. Baumgartner, J. Reyes, S. (1995) Synthesis and Catalytic Properties of Eggshell Cobalt Catalysts for the Fischer-Tropsch Synthesis. *Journal of Catalysis*. 153 (1), 108-122.
[145] Rothenberg, G. (2008) *Catalysis: Concepts and Green Applications*. Weinheim, Wiley-VCH Verlag GmbH & Co. KGaA. Available from: http://onlinelibrary.wiley.com/doi/10.1002/9783527621866.ch1/summary [Accessed 6th December 2016].
[146] Martinelli, M. Viscontia, C. Lietti, L. Forzatti, P. Bassanob, C. Deianab, P. (2014). CO_2 reactivity on Fe-Zn-Cu-K Fischer-Tropsch synthesis catalysts with different K-loadings. *Catalysis Today*. 228, 77-88.
[147] C. Patzschke. (2018) *Copper manganese oxides as oxygen carries for chemical looping air separation for near-zero emission power generation*. PhD. Imperial College London.
[148] M. Boot-Handford. (2015) *The Utilisation of Biomass as a fuel for Chemical Looping Combustion,* PhD. Imperial College London.
[149] Yale University (2020) XRD Principle [online] Available at: https://ywcmatsci.yale.edu/principle-0 [accessed 29th January 2020]
[150] Brunauer, S. Emmett, P. Teller, E. (1938) Adsorption of gases in multimolecular layers, *Journal of the American Chemical Society,* 60 (2), 309-319.
[151] Sing, K. (2001) The use of nitrogen adsorption for the characterisation of porous materials. *Colloids and Surfaces*. 187-188, 3-9.
[152] Barrett, E. Joyner, L. Halenda, P. (1951) The determination of pore volume and area distributions in porous substances Computations from nitrogen isotherms, *Journal of the American Chemical Society,* 73, 373-380.
[153] Webb, P. Orr, C. (1997) *Analytical methods in fine particle technology*, Micromeritics Instrument Corporation, Norcross.
[154] Schuth, F. Unger, K. (1999) Preparation of Solid Catalysts, chapter 3.4: Precipitation and Coprecipitation, John Wiley and Sons, New York. Available at:
https://www.onlinelibrary.wiley.com/doi/pdf/10.1002/9783527619528.ch3d [accessed 29th January 2020].
[155] Gnanamani, M. Shafer, W. Sparks, D. Davis, B. (2011) Fischer-Tropsch synthesis: Effect of CO_2 containing syngas over Pt promoted Co/γ-Al_2O_3 and K-promoted Fe catalysts. *Catalysis Communications*. 12, 936-939.
[156] Riedel, T. Claeys, M. Schulz, H. Schaub, G. Nam, S. Jun, K. Choi, M. Kishan, G. Lee, K. (1999) Comparative study of Fischer-Tropsch synthesis with H_2/CO and H_2/CO_2 syngas using Fe and Co based catalysts, *Applied Catalysis,* 186, 201-213.
[157] Wang, D. Chen, B. Duan, X. Chen, D. Zhou,X. (2016) Iron-based Fischer-Tropsch synthesis of lower olefins: The nature of χ-Fe5C2 catalyst and why and how to introduce promoters, *Journal of Energy Chemistry,* 25, 911-916.
[158] Okeson, T. KEyvanloo, K. Lawson, J. Argyle, M. Hecker, W. (2016) On the kinetics and mechanism of Fischer-Tropsch synthesis on a highly active iron catalyst supported on silica-stabilized alumina, *Catalysis Today,*261, 67-74.
[159] Tu, J. Ding, M. Zhang, Y. Li, Y. Wang, T. Ma, L. Wang, C. Li, X. (2015) Synthesis of Fe2O4-nanocatalysts with different morphologies and its promotion on shifting c5+ hydrocarbons for Fischer-Tropsch synthesis, *Catalysis Communications,* 59, 211-215.
[160] Sadeqzadeh, M. Chambrey, S. Hong, J. Fongarland, P. Luck, F. Curulla-Ferre, D. Schweich, D. Bousquet, J. Khodakov, Effect of Different Reaction Conditions on the Deactivation of Alumina-Supported Cobalt

Fischer−Tropsch Catalysts in a Milli-Fixed-Bed Reactor: Experiments and Modelling, *Ind. Eng. Chem. Res.* 53, 6913-6922.

[161] Hooshyar, N. Vervloet, D. Mudde, R. van Ommen, J. (2012) Intensifying the Fischer–Tropsch Synthesis by reactor structuring – A model study, *Chemical Engineering Journal,* 207–208, 865–870.

[162] Jess, A. Popp, R. Hedden, K. (1999) Fischer–Tropsch-synthesis with nitrogen-rich syngas: Fundamentals and reactor design aspects, *Applied Catalysis A: General,* 186, 321–342.

[163] Bub, G. Baerns, M. (1980) Prediction of the performance of catalytic fixed bed reactors for Fischer-Tropsch Synthesis, *Chemical Engineering Science,* 35, 348-355.

[164] Guettel, R. Turek, T. (009) Comparison of different reactor types for low temperature Fischer-Tropsch synthesis: A simulation study, *Chemical Engineering Science,* 64, 955-964.

[165] Mamonov, N. Alkhimov, S. Mikhailov, M. (2013) One-dimensional heterogeneous model of a Fischer-Tropsch synthesis reactor with a fixed catalyst bed in the isothermal granules approximation, *Catalysis in Industry,* 5, 223-231.

[166] Adesina, A. (1991) Non-isothermal reactor design for variable-density systems. *The Chemical Engineering Journal*, 47, 17-24.

[167] Knochen, J. Güttel, R. Knobloch, C. Turek, T. (2010) Fischer–Tropsch synthesis in milli-structured fixed-bed reactors: Experimental study and scale-up consideration, *Chemical Engineering and Processing*, 49, 958–964.

[168] Crider, J. Foss, A. (1966) Computational Studies of Transients in Packed Tubular Chemical Reactors, *AIChE Journal,* 12, 514.

[169] Sharma, C. Hughes, R. (1978) The behaviour of an adiabatic fixed bed reactor for the oxidation of carbon monoxide – II Effect of perturbations, *Chemical Engineering Sciences,* 34, 625-634.

[170] Van Doesburg, H. De Jong, W. (1976) Transient behaviour of an adiabatic fixed-bed methanator – II Methanation of mixtures of carbon monoxide and carbon dioxide, *Chemical Engineering Sciences,*31, 53-58.

[171] Sinai, J. Foss, A. (1970) Experimental and Computational Studies of the Dynamics of a Fixed Bed Chemical Reactor, *AIChE Journal,* 16 (4), 658-669.

[172] Kulkarni, M. Dudukovic, M. (1996) Dynamics of gas phase and solid phase reactions in fixed bed reactors, *Chemical Engineering Science,* 51 (11) 3083-3088.

[173] Zhu, K. Bos, R. Hellgardt, K. (2020) Activation of catalysts in commercial scale fixed-bed reactors: Dynamic modelling and guidelines for avoiding undesired temperature excursions, *Chemical Engineering Journal,* 382, 122962.

[174] Il'in, A. Luss, D. (1992) Wrong way behavior of packed bed reactors: Influence of reactant adsorption on support, *AIChE Journal*, 38 (10), 1609-1617.

[175] Almeida-Costa, C. Ferreira, R. (1994) Wrong-way behavior in packed bed reactors with "large-pore" catalysts, *Chemical Engineering Science,* 49 (24B), 5571-5583.

[176] Pinjala, V. Chen, Y. Luss, D. (1988) Wrong-Way Behavior of Packed-Bed Reactors: II. Impact of Thermal Dispersion. *AIChE Journal*. 34 (10), 1663-1672.

[177] Mehta, P. Sams, W. Luss, D. (1981) Wrong-Way Behavior of Packed-Bed Reactors: 1 The Pseudo-Homogeneous Model., *AIChE Journal*, 27 (2), 234-246.

[178] Simons, M. (2015) *Dynamic modelling of the shutdown behaviour of a Fischer-Tropsch reactor*, MSc Dissertation, Imperial College London.

[179] Post, M. van't Hoog, A. Minderhoud, J. Sie, S. (1989) Diffusion Limitiation in Fischer-Tropsch Catalysts. *AIChE Journal.* 35 (7), 1107-1114.

[180] Ruthven, D. (1984) Principles of Adsorption and Adsorption Processes. John Wiley and Sons. New York.

[181] Levenspiel, O. (1999) *Chemical Reaction Engineering*. John Wiley and Sons. New York. 3rd Edition.

[182] Chen, Y. Luss, D. (1989) Wrong-Way Behavior of Packed-Bed Reactors: Influence of Interphase Transport. *AIChE Journal*. 35 (7), 1148-1156.

[183] Danckwerts, P. (1958) Continuous Flow Systems, *Chemical Engineering Science,* 2 (1), 1-13.

[184] Govindarao, V. Froment, G. (1986) Voidage Profiles in Packed Beds of Spheres, *Chemical Engineering Science,* 41 (3), 533-539.

[185] ThermoFischer Scientific (2019) *Safety Data Sheet Iron (III) Oxide - Calcined Rev. 4.* Available at: https://www.fishersci.co.uk/store/msds?partNumber=10020190&productDescription=1KG+Iron%28III%29+oxide%2C+pure%2C+calcined&countryCode=GB&language=en, [accessed 6th March 2020].

[186] Speight, J. (2014) Chapter 5 – The Fischer-Tropsch Process, *Gasification of Unconventional Feedstocks,* 118-134.

[187] Nassr, L. (2013) *Simulation of Fischer-Tropsch Fixed-Bed Reactor in Different Reaction Media,* MSc Dissertation, Texas A&M University.

[188] Odunsi, A. O'Donovan, T, Reay, D. (2014) Temperature Stabilisation in Fischer-Tropsch Reactors Using Phase Change Material (PCM), *4th Micro and Nano Flows Conference,* available at: https://bura.brunel.ac.uk/bitstream/2438/9342/1/MNF2014_Full-Ademola_Odunsi_corrected.pdf [accessed 8th March 2020].

[clxxxix] Wenst, R. Mundy, J. Weissman, S. Mason, E. (1963) Gaseous Self-Diffusion in a temperature Gradient, *The Physics of Fluids,* 6(4), 572-578.